THE BELL SYSTEM
TECHNICAL JOURNAL

VOLUME XXXIII MARCH 1954 NUMBER 2

Traffic Engineering Techniques for Determining Trunk Requirements in Alternate Routing Trunk Networks

By C. J. TRUITT

(Manuscript received November 23, 1953)

In 1945 the Bell System embarked on an extensive study with the purpose of developing a program for operator toll dialing on a nationwide basis. Operator toll dialing had been done, of course, on a limited scale in various parts of the country for many years, but the concept of this program was one of nationwide proportions carried on with a uniform numbering plan arrangement and a completely integrated trunking system which would handle traffic at a high speed between any two points in the United States and Canada, even in the busier hours of the day.*

Implementation of this program required the development of new switching mechanisms and the exploitation of carrier transmission potentialities to a degree never before achieved. Great strides had already been made in these fields, resulting in the practical development of the coaxial cable system and the first toll crossbar switching office installed at Philadelphia in 1943. But the very core of the nationwide dialing plan was the proposal to revolutionize the method of traffic distribution so as to combine high speed handling over the intertoll trunk network with a highly efficient use of facilities. The method of accomplishing is called "engineered alternate routing"

---

* W. H. Nunn, Nationwide Numbering Plan, Communication and Electronics, **2,** Sept., 1952 and B. S. T. J., **31,** Sept., 1952.

The capacity of this particular grade is precisely 334 CCS and its efficiency is 16.7 CCS per trunk or only 12 per cent below the single trunk group efficiency. Here the common trunks serve as an alternate route for such portions of the loads a, b, and c, respectively, as can not be handled by the five trunks which are individual to each. Because it is not likely that a, b, and c will overflow equal amounts of traffic at the same time, the common trunks are kept busy by a more or less complementary pattern of greater and lesser overflows at any given moment, emerging from the three subgroups. It is this action of the overflows, amply substantiated by experience, which accounts for the efficiency of graded multiples. Looked at another way, it may be said that all trunks above five in each subgroup of the split-multiple case have been pooled for the common use of all subgroups and that in so doing, it is possible to reduce the number of pooled trunks from 9.9 to five without impairing the speed of service. This very brief discussion of graded multiples serves merely to point out by familiar example, some of the potentialities of the alternate routing principle in the economical handling of telephone traffic.

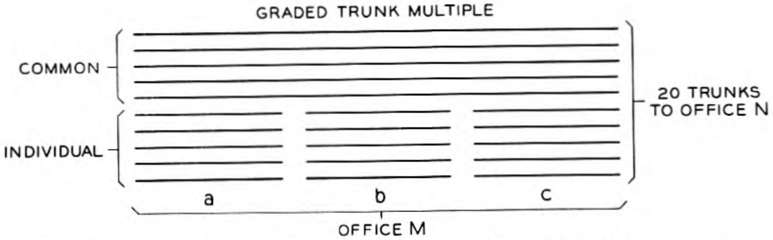

Fig. 1 — Typical graded arrangement of 20 trunks on 10 terminals.

ALTERNATE ROUTING IN LOCAL INTEROFFICE TRUNK NETWORKS

The effectiveness of alternate routing as illustrated by its action in graded multiples suggests the possibility of improving the efficiency of trunking between central offices by arranging the offices themselves in a sort of grade. Let us carry the analogy as far as practicable and assume that the loads a, b, and c in Fig. 1 are now emanating from central offices A, B, and C and still destined for office N. Let us assume that A, B, and C are typical offices in a multi-office city which has a tandem office, T, and further, that every office in the city has a group to and a group incoming from the tandem office. Fig. 2 illustrates these conditions with respect to offices A, B, C, and N and for simplicity indicates carrying the load from the originating office to each distant office would be at a minimum. This required some means of determining how much load would be carried by the direct trunks when offered a given load and consequently how much of that load would be overflowed to the alternate route. For this purpose, a formula* known as the Erlang B "lost-calls-cleared" assumption was used. This formula states for a given random offered load, the amount of load which will be carried by each of a number of trunks, n, tested in succession provided that the calls failing to be carried on the first attempt (the lost calls) *are not reoffered within the hour during which the first offering took place.* The condition italicized is extremely important to the problem since it requires that calls lost on the direct high usage group, i.e., the calls overflowed to the alternate route, must be disposed of without delay on the alternate route or routes. In the New York City trials it was assumed that the then current basis of provision of trunks in each leg of the alternate route (final groups AT and TN, Fig. 2) namely, with a probability of delay of one per cent. (P.01) would, as a practical matter, satisfy the condition that calls overflowing from AN should be cleared. It should be mentioned in passing that the results of the trials substantiated the reasonableness of this assumption.

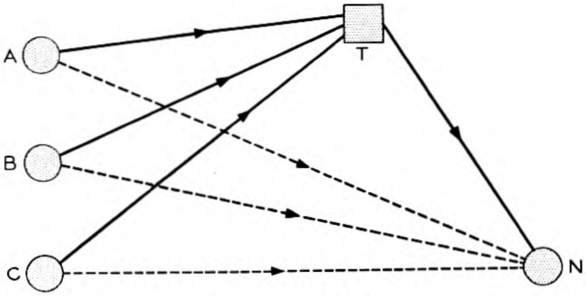

FIG. 2 — Illustration of simple interlocal trunk network arranged for alternate routing.

A typical Erlang B distribution is shown in Fig. 3, Curve A wherein the load carried by each of n=14 trunks is shown for the condition of 240 offered CCS. Thus, assuming the load to be offered in succession to trunks 1, 2, 3, etc., in that order, it will be seen that the first trunk carries the most load, the second trunk somewhat less, the third still less until the fourteenth trunk carries about 0.5 per cent of the total. By

---

* A. K. Erlang, Solution of Some Problems in the Theory of Probabilities of Significance in Automatic Telephone Exchanges, Post Office Electrical Engineers' Journal, **10,** 1917.

is a function of the number of trunks provided to handle a given load on a lost-calls-cleared basis.

Referring once more to Fig. 2, let us assume that the ratio of the cost of an incremental path in ATN to the cost of an incremental path in AN is 1.4. It may then be stated that it costs 1.4 times as much to handle traffic on the alternate route as on the direct route. The cost ratio is computed on the basis of values of incremental trunks because the ultimate question in the economical separation of load between a direct and an alternate route is whether one more trunk should be added to the direct route or should more trunk capacity be provided in the alternate route to handle a marginal portion of the total load. Let us assume further that the offered load, A to N, is 240 CCS and that the efficiency of incremental trunks in the alternate route is 28 CCS per trunk.

With these three factors, the offered load, the cost ratio and the efficiency of incremental trunks in the alternate route, the most economical arrangement of trunks for carrying traffic from A to N may now be determined. The first step is to make sure that any trunk in the direct (HU) group will carry load at a cost per CCS equal to or less than the cost per CCS which is characteristic of the incremental trunks in the alternate route. Since the last trunk in a high usage group carries the least traffic, as previously discussed, the significant comparison is the ratio of the load carried by a trunk added to the alternate route to the load carried by the last trunk in the high usage group. The numerator of that ratio is 28 (CCS) and the denominator could be any one of 14 values shown on Curve A of Fig. 3, depending upon the number of trunks provided. If that ratio is made equal to the cost ratio (ATN/AN) there will be determined a value of load to be carried by a last trunk which in turn will determine the most economical number of trunks for the direct high usage group. This value is referred to as the "economic CCS" of the problem and is determined as follows:

$$\text{Cost ratio } \frac{1.4}{1.0} = \text{Efficiency ratio } \frac{28}{X}$$

$$X = 20, \text{ the economic CCS}$$

On Curve A it will be seen that the sixth trunk will carry 22.5, the seventh, 19.6 and the eighth, 16.4 CCS. Since the loading of the seventh trunk is closest to the economic CCS just computed, the conclusion is that seven trunks should be provided in the high usage group for the minimum overall cost of handling traffic from A to N. Since the seven trunks as a group will carry 185 CCS (Curve B), there will be 55 CCS value of 1.12. With the latter ratio the economic CCS would be (28 ÷ 1.12) or 25. On Curve A of Fig. 3 it will be seen that trunk No. 5 (the last trunk of a 5-trunk group) carries 25 CCS. So, if the lower cost ratio had been used instead of the correct one, the effect upon overall trunking costs would have been 1 per cent in excess of the most economical arrangement. Had a cost ratio of 1.25 been used, six trunks would have been provided in the HU group and no cost penalty would have been incurred. On the other side of the optimum point an eight trunk HU group would meet the requirements of a cost ratio as high as 2.0 with a resulting cost penalty of about 2 per cent. As can be seen from Table I, the cost penalties mount more rapidly when more than the optimum number of high usage trunks are provided than when less are provided.

The principles of alternate routing and certain of the techniques used by traffic engineers in determining quantities and arrangements of interoffice trunks have just been described with particular reference to the trials that have been carried on in New York City. The latter were very extensive undertakings in which not only single alternate routes were provided but for a majority of items, multiple alternate routes. This was possible because New York City had two tandem systems each with a completing field to all city offices as well as other tandem systems (office selector tandems) each with a completing field to about 20 offices. Thus it was possible in many cases for an originating office to test a direct

TABLE I — COMPARATIVE COSTS OF ALTERNATE ROUTING SYSTEM FOR VARIOUS ASSUMPTIONS AS TO NUMBER OF HU TRUNKS

Given: Offered load in CCS 240
Efficiency of trunks added to alternate route 28
Cost ratio, alternate to direct (HU) route 1.4

No. of HU Trunks	Nominal Costs					% Deviation from Optimum
	HU trunks		Alternate trunks		All trunks	
	Per trunk	Total	Per trunk	Total added*		
3	1.0	3	1.4	7.50	10.50	7.70
4	1.0	4	1.4	6.10	10.10	3.59
5	1.0	5	1.4	4.85	9.85	1.03
6	1.0	6	1.4	3.75	9.75	0.00
7	1.0	7	1.4	2.75	9.75	0.00
8	1.0	8	1.4	1.95	9.95	2.05
9	1.0	9	1.4	1.30	10.30	5.64
10	1.0	10	1.4	.80	10.80	10.75

* $\dfrac{\text{Overflow CCS from HU Group} \times 1.4}{28}$

of more than two million items of traffic between toll offices, would need to be devised.

Over the years since 1945 practical solutions to the problems raised by the conditions have been attained by Bell System engineers and the fruits of their efforts will be put to the test in 1954 during which year the first practical application of "engineered" alternate routing in the intertoll network will be undertaken.

The remainder of this paper will be devoted to the more important aspects of the traffic engineering techniques used in determining the arrangement and numbers of intertoll trunks required in a multi-alternate routing system.

GENERAL TOLL SWITCHING PLAN

A brief description of the General Toll Switching Plan* will be appropriate here since any discussion of the alternate routing methods necessarily presumes an understanding of the basic pattern for routing traffic.

The plan under which transmission had been designed and traffic routings determined since 1930 comprehended a maximum connection of 5 intertoll trunks in tandem. Early studies of the alternate routing possibilities in toll networks led to the conclusion that a total of 8 intertoll links would provide a more economical arrangement of trunks by shortening some very long final groups that would otherwise be required. Fig. 4 illustrates schematically the arrangement of switching centers in a maximum connection currently in use.

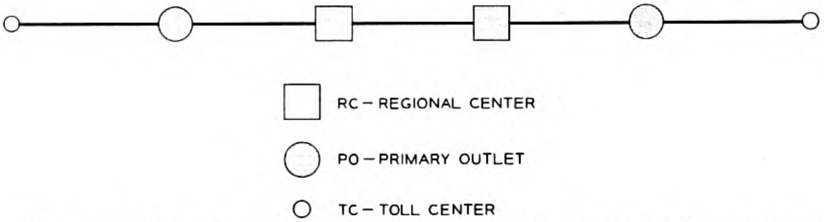

FIG. 4 — Illustration of present basic intertoll network showing maximum intertoll trunk linkage.

Fig. 5 shows a schematic of the proposed General Toll Switching Plan in which a connection involving 8 links is possible between TC1 and TC2. Such a route would constitute the final route between those TC's and each group in the route would be a low delay final group similar to

---

* J. J. Pilliod, Fundamental Plans for Toll Telephone Plant, Communications and Electronics, No. 2, Sept., 1952 and B. S. T. J., **31,** Sept., 1952.

Each regional center (RC) homes on, ie., has a final group to the NC, and has one or more sectional centers homing upon it;

Each sectional center (SC) homes on an RC (or the NC) and has one or more primary outlets homing upon it;

Each primary outlet (PO) homes on an RC, NC or SC and has one or more ordinary toll centers homing upon it; and

Each ordinary toll center (TC) is so called because it performs no through switching function but merely serves as the connecting point between the intertoll network and local central offices or tributaries.

Thus each toll center (and in the generic sense this phrase includes all CSP's as well as ordinary toll centers) was classified with respect to the area served: the TC serving a group of local offices or tributaries, the PO serving a group of TC's, the SC serving a group of PO's, the RC serving a group of SC's and lastly the NC serving all the RC's. Under this arrangement any toll center could home on another of higher rank or classification. Thus a TC or PO, for example, could home upon an RC if so dictated by geographic and economic considerations. Before proceeding with a detailed study of trunk requirements the classification of toll centers and the homing relationships had first to be established. This was done in a manner which reflected the known densities and flow of traffic between the larger cities and the relative cost of final routes which in turn reflected the differences in lengths of haul to one CSP as opposed to another, etc. With the classification and homing of each toll center established it was possible to trace the final route, the route of last resort, between any two toll centers in the entire system. Thus was the stage set for determining the location of and number of trunks to be provided in high usage groups whose function would be to move traffic more economically by direct connection between points than could be done by following the final route.

It is apparent at once from the illustration in Fig. 5 that the problem of determining the most economical alternate for a given HU group is different from that encountered in the interlocal situation of Fig. 2 inasmuch as the latter had only one intermediate switching point in each final route. A further difference not specifically indicated is that intertoll trunk groups handle traffic in both directions whereas interlocal trunk groups handle traffic in only one direction, i.e., there are separate outward and inward groups between any pair of local offices. There are special circumstances under which one-way intertoll groups also are established but these may be ignored for purposes of our discussion.

While this paper is not specifically concerned with the transmission aspects of an alternate routing network some mention should be made costs of the direct and alternate routes are controlling. Since load carried by a high usage group is a function of the load offered, under the Erlang B assumption, it is apparent that the size of the load between any two toll centers will also limit the possible range of economic CCS values which can be realized. In other words a high usage group to exist at all must have at least one trunk and that one trunk must carry not less than the economic number of CCS required by the cost ratio applying to the case. For example, if a busy-hour load of 60 CCS is to be carried between offices A and B and the cost ratio indicates an economic CCS of 25 it can be shown that when one trunk is offered 60 CCS it will carry only 23 of the 60 CCS with the balance 37 CCS being overflowed. Under these conditions no direct (HU) group could be economically established since the efficiency of even the first trunk of such a group would fail to meet the requirement of the case.

This immediately suggests that a prime requirement in determining whether or not there should be a direct group of any size between two toll centers is a level of load at and above which a group will prove in and below which, of course, it will fail to prove in. As previously stated the cost ratio between the alternate route and the potential direct group is also a controlling factor. Thus, to determine the economic propriety of establishing a direct (HU) group it is necessary to know the following:

Cost of path in the alternate route;
Cost of path in the direct route;
Efficiency of trunks added to the alternate route; and
Load offered between toll centers.

The last three of these items were available to the engineer but the first item could not be known in all cases because the groups comprising the logical alternate routes in some cases were themselves hypothetical. For example, a high usage group between TC1 and TC2 in Fig. 5 might have an alternate route via P01 or via P02 which routes in turn would depend upon the existence of groups P01-TC2 and TC1-P02, respectively. Therefore, it was necessary to "cut-and-try" in the process of locating high usage groups. This was accomplished by choosing an average cost ratio (and hence an average economic CCS value) which could be used with the known offered loads between toll centers to test the feasibility of at least one high usage trunk. With this tentative pattern of high usage groups the potentially available alternate routes could then be identified. For each high usage-alternate route triangle thus tentatively selected the test of relative costs was applied to verify the economy of the case. Some proposed high usage groups failed to prove in under such test in which cases the uneconomic high usage groups were load offered to the PO1-PO2 group is composed in part of the overflow traffic from TC1-PO2. It is likewise clear that the final group TC1-PO1 will be offered overflow traffic from both TC1-TC2, TC1-PO2 and TC1-SC and hence the final group can not be engineered until the overflows from all high usage groups terminating at TC1 have been determined. This transfer of load from group to group with each succeeding high usage group serving as the base of a new triangle in orderly procession from TC to RC is the essence of the multi-alternate routing system and, therefore, a precise order of group load computation was necessary to assure proper accounting of the load offered to each group. In practice the order of group load computation requires that all TC-TC high usage groups be established first, then TC-PO groups, TC-SC and so on. The process involves selecting a particular TC as a "reference" and examining all traffic involving that TC to determine what (if any) high usage groups should terminate there.

The second rule, affecting the concentration of switched traffic, is related to the order of group load computation in that it postulates a starting point for the process of examining HU group possibilities. The need for such a rule may be best explained by reference to Fig. 7 representing a simple intertoll network in which PO, a CSP serving four TC's, homes on SC, another CSP, serving four other TC's. The question, answered by the second rule, is which of the eight TC's should be used as the first reference TC. The choice will determine the sizes of, i.e., the number of trunk terminations to be provided at, PO and SC, respectively. Let us examine the reason for this. Assume the TC's homing on PO are to be used as the first set of reference TC's (it makes no difference which TC is first chosen). Assume that the investigation showed an economical HU group between TC2 and SC but that no HU groups proved into any of the TC's (5, 6, 7, and 8) dependent upon SC. The load offered

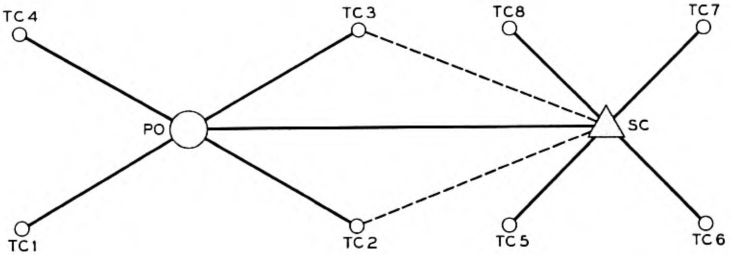

FIG. 7.

administration and engineering have been obtained with that end in view. However, in alternate-routing networks the significant level of a trunk group load is not that which is characteristic of its own busy hour but rather that which is characteristic of the hour in which all trunk groups in a given network are collectively carrying the greatest aggregate traffic volume. For each group the former level is referred to as the group busy-hour (GBH) load and the latter, for convenience, as the office busy-hour (OBH) load.

The reason for using office busy-hour loads between toll centers rather than group busy-hour may be explained with reference to Fig. 8. Here is a represented part of an intertoll trunk network showing 4 HU groups connecting TC with four other toll offices a, b, c and d. TC homes on SC and for simplicity it may be assumed that the alternate route of each such group is the final group to SC.

In the hour during which the greatest volume of traffic is leaving and entering TC, i.e., the office busy-hour, the demand for trunk capacity in the TC-SC group will also be greatest since by design the final group to the home CSP of any TC is the route of last resort for all traffic to and from the TC. Thus the group busy-hour of the TC-SC group coincides with the busy-hour of TC as a whole.

The group busy hours of the respective HU groups (TC-a, TC-b, etc.) may occur outside of the office busy-hour for TC and during such hours the amount of traffic offered to and hence overflowed by each of the HU groups is greater on the average than that occurring in the office busy-hour. But at any other hour than the office busy-hour there is less total load on the network and hence there is some spare capacity in the final group available for handling the group busy-hour overflow of one or more of the high usage groups. By properly evaluating the average ratio between any given toll center-toll center load in its group busy-hour and its value in the office busy-hour it would be practicable to start with basic data in group busy-hour terms and convert it to equivalent office busy-hour levels before undertaking the procedures for separating loads between direct (HU) and alternate routes.

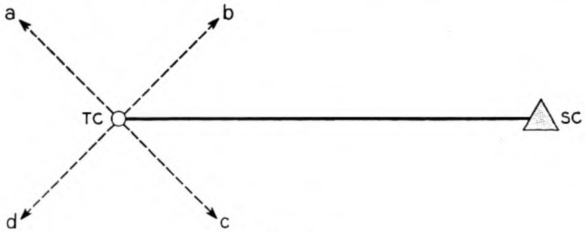

FIG. 8.

loads was arrived at through an averaging process. The ratio values are conservative, i.e., there was some evidence that in large toll offices the higher ratio values apply to larger loads than indicated by the curve. However, no attempt was made to develop separate sets of ratios for offices of different size since the use of the common set of values would tend merely to increase slightly the number of HU trunks required in a relatively few groups. The elimination of this small distortion did not appear to warrant the effort required to achieve it. The study data also showed that for a given toll office the sum of the respective group busy-hour loads for all groups was approximately 10–14 per cent greater than the sum of their respective loads in the office busy-hour.

The significance of this difference in the GBH and OBH aggregates is at once apparent. The intertoll trunk network designed on the alternate routing principle is required to handle from 10–14 per cent less busy-hour traffic than is required under the arrangement in which each toll center-toll center load stands alone and must be trunked for its own busy-hour. It is the pooling of trunk group capacities during the hour of maximum traffic flow for a given office plus the increased efficiency due to larger size of final groups that result in a requirement of fewer trunks in the network as a whole than would be required with any non-alternate routing trunking system of comparable service characteristics. The alternate routing system will enable the handling of normal busy-hour traffic on virtually a no-delay basis in so far as trunk provision may be controlling. The matter of speed of service potentialities and relative costs of alternate routing versus non-alternate routing systems will be treated later.

SOME UNANSWERED QUESTIONS

There are three questions upon the answers to which depend ultimate judgment of the adequacy and economy of a nationwide toll dialing network constructed upon the principles and with the techniques already described. These are:

1. What will be the effect upon trunk requirements of a proper evaluation of the non-random characteristic of lost calls, i.e., of the calls overflowed from high usage groups to other high usage or to final groups?
2. What will be the effect upon trunk requirements of a proper evaluation of the effect of non-coincidence of busy hours and busy seasons among the various toll centers?
3. What are the relative net costs of a nationwide intertoll dialing system engineered for multi-alternate routing and one designed without engineered alternate routing?

Non-coincidence of Busy Hours and Busy Seasons

With respect to the second question involving the non-coincidence of busy hours among toll centers it should be noted first that trunk requirements estimated in the nationwide alternate routing trunk study were predicated on a common busy season and a common office busy hour for all toll offices and all intertoll groups. This premise resulted in system-wide requirements which were patently incorrect since it is known that different toll centers have different busy hours and that the busy season for toll traffic in New England for example is in the summer while that for Florida is in the winter. While it was possible to identify the busy season and the average busy hour of each toll center the statistical problem of incorporating such information for some 2,500 toll centers in a completely integrated nationwide study appeared insuperable.

The seriousness of the error introduced by the above premise is not as great as might at first appear since the New England Company should know the requirements for the busy season of its territory and the Southern Bell Company is equally interested in the busy season requirements for Florida. It is only in the trunks required for handling traffic between these two areas that a distortion of requirements could be readily demonstrated as a result of assuming the two busy seasons to be coincidental when in fact they are months apart. The example cited is an extreme case which serves to point up the problem. While no evaluation has been made of this distortion, and none seems statistically practicable, it is evident that the direction of distortion is toward over-estimation of trunk requirements.*

Thus it may be confidently stated that the general effect of assuming premise regarding the coincidence of busy seasons and busy hours upon the network as a whole was to compute trunk requirements in some groups more liberally than a precise evaluation of all significant factors would indicate as adequate. Proper evaluation of the effect of non-coincidence of busy seasons and busy hours will likely await the findings of field experience.

Costs — Alternate Routing Versus No Alternate Routing

In planning extensive and radical changes in the methods of handling toll traffic on a nationwide basis it was necessary to explore the economic

---

* In the New York City studies previously discussed, a similar assumption was made with respect to the coincidence of busy hours and busy seasons of the local offices. Due to the homogeneity of intra-office traffic the degree of distortion in individual trunk group requirements was considered, except for a very few cases, to be insignificant.

levels can and do change with the years for a variety of reasons thus automatically changing the cost comparison.

In spite of the difficulties in obtaining a true and stable comparison of the overall costs of the two methods the weight of evidence indicated the desirability of proceeding with the plans for achieving an ultimate goal of nationwide toll dialing employing the techniques of multi-alternate routing in the design of the intertoll trunk network.

With the completion of the study of the various intertoll trunk requirements for nationwide operator toll dialing there was established for the first time a bench-mark against which many of the assumptions, theories and procedures which went into its making could be measured for accuracy and practicability. Among these was the early question regarding the cost of operator toll dialing with engineered alternate routing compared to its cost without alternate routing. To arrive at a complete answer it would be necessary to restudy the entire network on the current basis of trunking, compare costs of dial switching equipment without CSP features with the cost of CSP switching equipment, evaluate changes in the location and types of trunk facilities and so on. The undertaking of a study and analysis of this scope would require a larger expenditure of engineering time and effort than would seem justified by the usefulness of the results. It should be noted, however, that analysis of the alternate routing trunk study indicated that the original premise as to trunk economies to be expected were substantially correct. In any event the advent of customer toll dialing with its peremptory requirement for high speed trunking has rendered the original question of the relative costs of operator toll dialing, with and without engineered alternate routing, somewhat academic. It can be safely assumed that a high speed intertoll trunking system suitable for customer dialing and engineered without alternate routing would be prohibitive in cost.

CONCLUSION

The transition from ringdown (wholly manual) handling of long haul toll traffic to operator dialing of such traffic has been proceeding for many years and at an increasingly greater rate during the last five years until now some 45 per cent of such traffic is dialed by operators. This has been accomplished almost exclusively on trunk networks operated without benefit of engineered alternate routing. Along with this, increasing use of dialing by destination code has been achieved as various cities and areas have converted to the nationwide numbering plan.

The second phase of the transition, now under way, involves the change from non-alternate routing to alternate routing trunking. With

Intertoll Trunk Concentrating Equipment

By D. F. JOHNSTON

(Manuscript received August 25, 1953)

This article describes the Intertoll Trunk Concentrating Equipment which is a special purpose common-control type switching system. Its function is to combine, at a central point, small groups of trunks serving traffic originating at various outward toll switchboards and to route the combined traffic to a toll or tandem crossbar office in a distant toll center. The operators at the outward toll switchboards are thereby provided with the equivalent of direct access to the intertoll trunk circuits.

Both operating and equipment savings are realized by the use of this concentrating equipment as compared to handling the same traffic via a toll crossbar office at the originating toll center.

INTRODUCTION

This article deals with a method of handling traffic from outward toll switchboards in a metropolitan toll center to a specific distant toll center with the objectives of (1) providing the equivalent of direct access to intertoll circuits from the individual switchboards, for traffic for which direct circuits cannot be justified, (2) giving relief to the No. 4 type toll switching system in the metropolitan toll center, and (3) providing a means for the dispersion of toll switching facilities.

A metropolitan toll center may contain a number of outward toll switchboards. Some of these are situated in the central toll building and others in decentralized locations. An individual outward switchboard may have a sufficient amount of traffic to a specific distant toll center to justify a group of intertoll circuits direct from the switchboard to the No. 4 type toll or crossbar tandem office in the distant center. It has been the practice to provide such direct access to intertoll circuits at centralized toll switchboards. Traffic exceeding the capacity of such intertoll trunk groups is handled over tandem trunks from the toll switchboards via the No. 4 type toll crossbar office in the originating center. The decentralized switchboards in general have reached intertoll circuits only via tandem trunks to the No. 4 type toll crossbar office in the home toll center.

Handling such traffic through the toll crossbar office involves greater operating effort than handling it by direct trunks since three additional digits per call must be keyed by the operator to direct the call through the toll crossbar office. Also the cost for an intertoll connection is higher with the tandem trunk method than with the direct circuit method, due to the greater number of switching facilities used in establishing the connection. Fig. 1 shows the components used in both cases up to the point where they join common facilities.

INTERTOLL TRUNK CONCENTRATING EQUIPMENT

General

The intertoll trunk concentrating equipment has been developed to provide the equivalent of direct access to intertoll trunks for the traffic, from individual outward toll switchboards, which cannot justify the use of direct trunks. It is a small special purpose common control type switching system located at a central point. It gathers small traffic loads, to a specific destination and automatically routes this traffic to a common group of intertoll trunk circuits which terminate in a toll or tandem crossbar office in the distant toll center.

The maximum capacity of a trunk concentrating equipment is 100 incoming trunks and 40 outgoing trunks. It may be furnished in smaller sizes. If more than 40 outgoing trunks are required to a particular destination, additional concentrating equipments may be furnished.

The field of use for this equipment lies between that of direct trunks and trunks reached through the toll crossbar switching system.

The concentrating equipment is arranged only for multifrequency pulsing from the switchboard. This is a system of pulsing in which combinations of two frequencies within the voice frequency band are transmitted over the talking path to the distant end. Each digit from 0 to 9 employs a different pair of frequencies.

The intertoll trunk concentrating equipment consists of 4 basic circuit components, namely, incoming trunk, trunk selection switches, controller and outgoing trunk circuits.

The detached contact form of circuit presentation is employed in the figures because of its simplicity. In this method the core and winding of a relay may be shown in one location and the associated contacts in other convenient locations. The core and contacts are related by the common designation which appears at the symbols which represent them.

Incoming Trunk Circuits

Several types of incoming trunk circuits are provided to meet the various switchboard conditions where a switchboard and concentrating equipment are located in the same building or to meet the interoffice trunk loop conditions where the switchboard and concentrating equipment are in separate locations. In all cases the incoming trunk circuit receives signals from the switchboard, directly or indirectly and transmits them to the outgoing trunk circuit and to the controller. The incoming trunk circuit also receives signals from the outgoing trunk circuit and transmits them to the switchboard. The incoming trunk circuits, where necessary, also convert the two-wire transmission circuit from the switchboard to a four-wire transmission circuit to meet the intertoll trunk facilities. Fig. 2 shows a typical incoming trunk circuit.

Trunk Selection Switches

The trunk selection switches are the elements which, under the direction of the controller, connect the incoming trunks, requesting service, to the outgoing trunks. Crossbar switches having 20 verticals and 10 horizontals, providing 200 crosspoints, are used. A crosspoint is the intersection of a vertical and a horizontal element of the switch. The incoming trunks are connected to the verticals and the outgoing trunks to the horizontals of the switch. By the switch operation any of the 20 incoming trunks may thus be connected to any of the 10 outgoing trunks.

A single switch will accommodate 20 incoming and 10 outgoing trunks. To increase the number of incoming trunks a similar switch is added for each additional 20 trunks with the verticals connected to the new incoming trunks and the horizontals connected to the corresponding horizontals of the first switch. To increase the number of outgoing trunks switches are added with the horizontals connected to the new group of outgoing trunks and the verticals connected to the corresponding verticals associated with other groups of incoming trunks. The switch arrangement may be envisioned as one large switch having as many verticals as there are incoming trunks and as many horizontals as there are outgoing trunks.

Outgoing Trunk Circuit

Only one type of outgoing trunk circuit is required, as shown in Fig. 3. All outgoing trunks from a particular concentrating equipment terminate in the same distant toll center. The outgoing trunk circuit receives are made a part of the incoming trunk circuits rather than a part of the less numerous outgoing trunks to which they may be switched. Switching between incoming and outgoing trunks is therefore performed on a four-wire basis.

Controller Circuit

The controller circuit is the control element of the trunk concentrating equipment. Its primary function is to select the incoming and outgoing trunks to be interconnected and to operate the proper select and hold magnets of the associated switches to close the required crosspoint. Since the controller circuit is described in some detail later, only the general principles of it will be dealt with at this time.

The controller divides the incoming trunks into ten groups, (0 to 9), of ten trunks each. When idle it admits calls for a very short interval and then closes gates which exclude all other groups until calls recognized, within the gate, have been served. The controller serves the groups and trunks within the gate in one of two orders depending upon the direction of selection existing at the time. In one case selection will start with the lowest numbered trunk in the lowest numbered group and progress to the highest numbered trunk in the highest numbered group. In the other case the order will be reversed starting with the highest numbered trunk in the highest numbered group and progressing to the lowest numbered trunk in the lowest numbered group

The controller also divides the outgoing trunks into four groups, (0 to 3), of ten. The outgoing trunks are served in order, either from low numbered to high numbered trunks or vice-versa. Once selected, the outgoing trunk remains locked out, after use, until all trunks have been used, or until a trouble condition causes a reversal of the direction of selection of the outgoing trunks.

To avoid connecting an incoming trunk to two outgoing trunks or connecting two incoming trunks to an outgoing trunk the controller tests both the select and hold magnets for possible trouble conditions, such as crosses, before operating them.

Each intertoll trunk concentrating equipment has but one controller. If the controller ceased to function the entire concentrating equipment would be out of service. To insure reliability the philosophy was adopted in the design that no single trouble should disable the controller. This accounts for some of the features, the reasons for which otherwise are not obvious.

Completion of Calls

The basic circuit components of the intertoll trunk concentrating equipment are shown in Fig. 4. Three incoming trunks in different groups and from different switchboards are shown. Two outgoing trunks in different groups are also shown. Assume that the controller is conditioned to serve both incoming and outgoing trunks in the low to high order, that a call is placed on incoming trunk 14 and a short time later on incoming trunk 21, and that outgoing trunks 04 and 36 only are available for selection. Seizure of trunk 14 at the originating switchboard causes the incoming trunk to place a ground on the start lead of incoming trunk group 1. This ground indicates to the controller that a trunk in incoming group 1 is calling for service. The controller then closes the gate to all other ten groups, tests the select magnets associated with horizontal 04 for crosses (since outgoing trunk 04 is first in order for selection) and finding none operates the select magnets. It then tests the hold magnets associated with vertical 14 and finding no crosses operates the hold magnets, thus closing the crosspoint whose coordinates are (04, 14) connecting incoming trunk 14 to outgoing trunk 04. The outgoing trunk transmits a seizure signal over the intertoll facilities to the distant end which then transmits a signal back to incoming trunk 14, which relays the information to the controller. The controller then releases from that connection, opens the gates and admits the call waiting on incoming trunk 21. It proceeds to complete this call to outgoing trunk 36 which is next in order of selection in a similar manner.

If in the assumed case outgoing trunk 36 was the last trunk then available for selection the controller would, at the completion of selection of trunk 36, proceed as follows:

(1) If any of the other outgoing trunks which had been locked out were idle the controller would now make these trunks available for selection.

(2) If no trunks were idle the controller would wait, and cause a signal to be transmitted to all associated outward switchboards. This signal will prevent the lighting of idle trunk indicating lamps at each switchboard. When one or more outgoing trunks become idle the controller will make them available for selection and will permit the idle trunk indicating lamps at the associated switchboards to light as an indication that trunks are available.

Component Circuits of the Controller

In the following paragraphs the component circuits of the controller will be described individually. The descriptions of these circuits contain the minimum of detail required to understand how they function.

"Tens Group" and "Tens Gate" Relays for Incoming Trunks

The incoming trunk associated with each controller are divided into groups of ten. These groups are designated 0, 1, 2, etc. Each trunk in the group has a unit designation 0, 1, 2, etc. which corresponds to the vertical of the switch to which it is connected. For instance, an incoming trunk in group 2 which is connected to the number 3 vertical on the switch is designated 23. Each group of trunks has a common start lead, (ST), (See Fig. 2) to the controller which is grounded when any trunk in the group is calling for service. Each trunk in the group of ten supplies an individual lead US to the controller which is also grounded when the particular trunk is calling for service. This lead serves to identify the units designation of the trunk.

In the controller there is a group of three relays associated with each group of 10 incoming trunks (Fig. 5). These are (1) the TENS relay (TN-) which responds to the ground on the ST lead from the trunk group when a trunk in that group is calling for service providing that the TENS gate is open as discussed below, (2) the UNITS CONTROL relay (UC-) which when operated connects the common group of UNITS relays (U0–U9) to the US leads of the grunk group, (3) the HOLD CONNECT (HC-) which when operated steers the hold magnet operating path to the hold magnets associated with the trunks in the particular group. The UC- and HC- relays do not operate until it is the turn of that associated trunk group to be served.

Two series chains, carried through transfer contacts on all of the TENS relays, control the operation of the UNITS CONTROL and HOLD CONTROL relays. The operation of these relays and the manner of advancing selections from one group to another is best explained by the use of the following example. Assume that incoming trunks in groups 1 and 3 have originated calls resulting in the operation of the TN1 and TN3 relays. Assume also that the controller is conditioned for the low to high direcrion of selection for incoming trunks. When the TN1 and TN3 relays operate, they cause the release of the TENS GATE relays (TG1 and TG2) which close the gates to the operation of any other TN relays and operate the UC1 and HC1 relays. When the UNITS gates close as described later, the TN1 relay is released and the trunks in group 1 will be served. When the last trunk in this group has been served the UC1 and HC1 relays release and the UC3 and HC3 relays operate advancing the selections into group 3. The TN3 and UC3 and HC3 relays then function in the same manner as described for the TN1, UC1 and HC1 relays. If the direction of selection had been from high to low instead of from low to high, group 3 would have been served first instead of group 1.

associated with that incoming trunk is released advancing the selection path to the next incoming trunk to be served. When the last incoming trunk within the gate has been selected the END relay releases, signifying the end of selections in that group and enabling the controller to advance to the next group. The release of the END relay releases the UNITS GATE relay restoring the operating path for all U relays.

Select Magnet Operating Circuit

The select magnet operating circuit is shown in Fig. 7. Two of these circuits are provided in accordance with the philosophy that no single trouble should block the concentrator. One of these circuits is associated with each direction of selection. When the UNITS GATE relay operates as described in the preceding paragraph, battery is connected through the windings of the XS and SS relays, chains on the group relays (GP-), chains on the OT relays, to the select magnet associated with the lowest

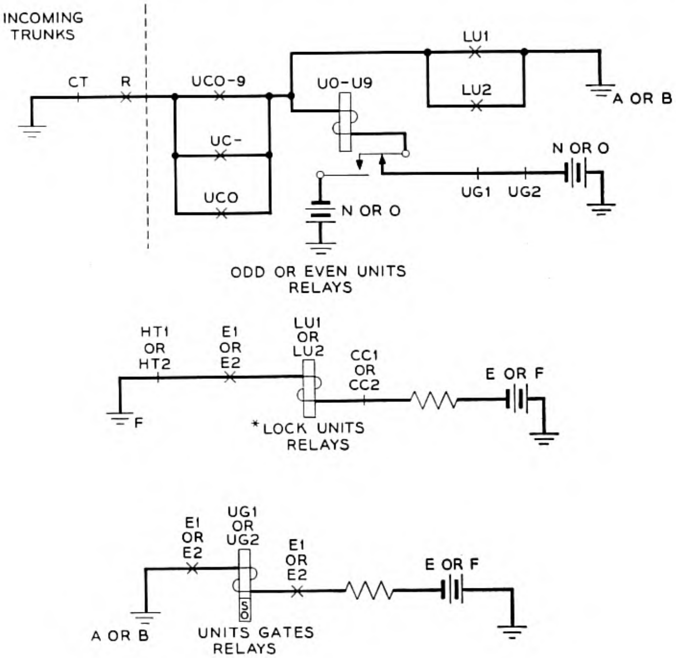

* LOCK UNITS RELAY DESIGNATIONS:
--1 ARE INCOMING LOW TO HIGH
--2 HIGH TO LOW

Fig. 6 — Units, unit gates and lock unit relays.

or highest unoperated OT relay in the group depending on the direction of selection. If the path is found to be closed to ground the SS relay will operate. The XS relay is a polar relay. The resistance shown in series with the secondary winding will have a value depending upon the number of select magnets which are multipled together on each level of the particular concentrator, which number is a function of the number of incoming trunks. The XS relay will operate on every normal connection since the current in the S winding, which is in the direction to operate the relay, will be larger than that in the primary winding. When the resistance to ground on the select magnet lead is less than it should be, due to a cross with another select magnet lead or to a direct ground, the current in the primary winding will be greater than that in the secondary winding and the resultant ampere turns will be sufficient in the non-operate direction to prevent the operation of the XS relay. This would cause the selection to be halted, the controller to time out and the trouble registered. A reversal in the direction of selection would occur and selections would then be resumed. If no fault is found with the select magnet operating path the select magnets operate. The controller then introduces a small time interval to permit all parts of the selecting bar operated by the select magnet to come to rest. The hold magnet operating path is then closed as discussed below and the crosspoint is closed. The closure of the crosspoint operates a relay OS in the outgoing trunk which in turn releases the select magnets and SS relay which releases the XS relay.

Hold Magnet Operating Circuit

The hold magnet operating circuit is shown in Fig. 8. Two circuits are provided, one for each direction of selection to insure against blocking in case a trouble in this portion of the controller. The cross detection part of this circuit is an unbalanced wheatstone bridge, the galvanometer element of which is the polar relay XH. Three of the arms of the bridge are resistances, the values of which are tailored to each particular concentrator depending upon the number of hold magnets to be encountered on a normal connection. This number is a function of the number of outgoing trunks. The fourth arm consists of the hold magnets. When the TENS GATES relays released as previously described the XH relay operated (at this time the hold magnets are not connected and the bridge is not formed). Later in the progress of the call, when the UNITS relays operate, the hold magnets are connected and the bridge is formed. If the resistance of the hold magnet arm of the bridge is as expected, the bridge is unbalanced so as to keep current flowing through the XH relay in the direction to maintain it operated. This will permit a relay HT, which furnishes cessfully completed except as stated above where a continuity check has failed. When the TA relays release, the OT relay associated with the trunk selected, or passed by, is operated and advances the selection to the next idle trunk. The operated OT relay locks to its own GROUP relay GP until the last OT relay in that group has operated. When the last trunk in that group is selected the GP relay of that group is released, advancing the selection path into the next group. The OT relays in the first group are then controlled only from the individual outgoing trunk with which they are associated and will be released when the trunk becomes idle. The trunks in that group cannot be selected again until the group relay has been reoperated which can not occur until all of the outgoing trunks on the concentrator have been selected in turn or until the controller times out. In both of these cases the controller will go through END OF CYCLE operation and reoperate the group relays as later described. With the above arrangement the traffic is spread evenly over the whole group of outgoing trunks.

End of Cycle and Guard Timing

When a connection through the concentrating equipment is released by an operator, the outgoing trunk sends a disconnect signal to the other end, to release the equipment there. It may take approximately 0.75 seconds for the distant equipment to release after it has received the disconnect signal. If this equipment should be reseized before it is released the new call would be connected to the same subscriber. A guard time could be incorporated in every outgoing trunk to prevent the transmission of a seizure signal for this 0.75 seconds, but this would be relatively expensive. To avoid this procedure the end of cycle and guard timing feature has been incorporated in the controller. This feature, shown in Fig. 11, together with the outgoing trunk lock out feature insures that no outgoing trunk can be seized for at least 0.8 of a second after it has been released from a previous call.

When the last available idle outgoing trunk on the concentrator has been selected the last operated group relay GP releases, and two END OF CYCLE relays EC1, EC2 which are normally operated also release. Either one of these relays released operates both the GROUP RESTORE relay GR and an ALL BUSY relay AB. Both the GR and AB relays cause the idle indicating lamp associated with trunks to the concentrator at all originating switchboards to remain dark as an indication that all trunks are busy. If no trunk outgoing from the concentrator is idle at this time nothing else will happen in the controller. When any outgoing trunk in any group becomes idle the GROUP relays associated with such groups control gap breaks down (which is minimum 63 volts for this tube) R is the value of resistance in ohms, and C is the value of the capacitor in farads. The timing circuits measure an interval of about 0.8 seconds which is sufficient to permit the distant end of any trunk, which has just been released, to restore to normal. When the timing interval is complete the GUARD TIME relays release, the direction of selections is reversed, and selections are resumed.

Direction of Selection Control

Two directions of selection are provided for both incoming and outgoing trunks to (1) by-pass incoming and out-going trunks which are in trouble, (2) to guard against blocking due to a single trouble in the controller itself. (See Fig. 12.) The directions of selection are controlled by two combinations of relays, plus three other relays controlled by these combinations. The AOW and AOZ relays control the outgoing directions of selection. With these relays in the unoperated condition the outgoing trunks will be selected in the low to high order and with them operated selections will be made in the high to low order. The outgoing trunks, in the normal course of events, are served starting with lowest or highest numbered trunks and proceeding to the highest or lowest numbered trunk depending upon the direction of selection at the time. When the last trunk has been selected the direction is reversed by either operating or releasing the AOW and AOZ relays depending upon the status quo ante. In case a short time-out is due to failure to close the crosspoint the direction of selection of outgoing trunks is reversed immediately. It is also reversed whenever a long time-out occurs, whatever the cause.

The AW and AZ relays form the combination which controls the incoming direction of selection. Controlled by them are the CONTROL relays C1 and C2 associated with the low to high and high to low directions respectively. With the AW relay unoperated the C1 relay is operated and the direction of selection is from low to high. With the AW relay operated the C1 relay is released, the C2 relay is operated and the direction of selection is from high to low. The incoming direction of selection is reversed under the following conditions:

1. When the outgoing direction is reversed upon the last outgoing trunk being selected the incoming direction is also reversed if and when there are no more incoming trunks within the gate waiting to be served.
2. When a short time-out occurs due to the failure of the END relay to operate or failure of continuity check.
3. When a second failure to close crosspoint occurs.
4. When a long time-out occurs.

the next idle trunk lights. The lamp does not necessarily move progressively thru the group but is always lighted on the lowest numbered idle trunk in the group.

The direct intertoll trunks and the trunks to a concentrating equip-

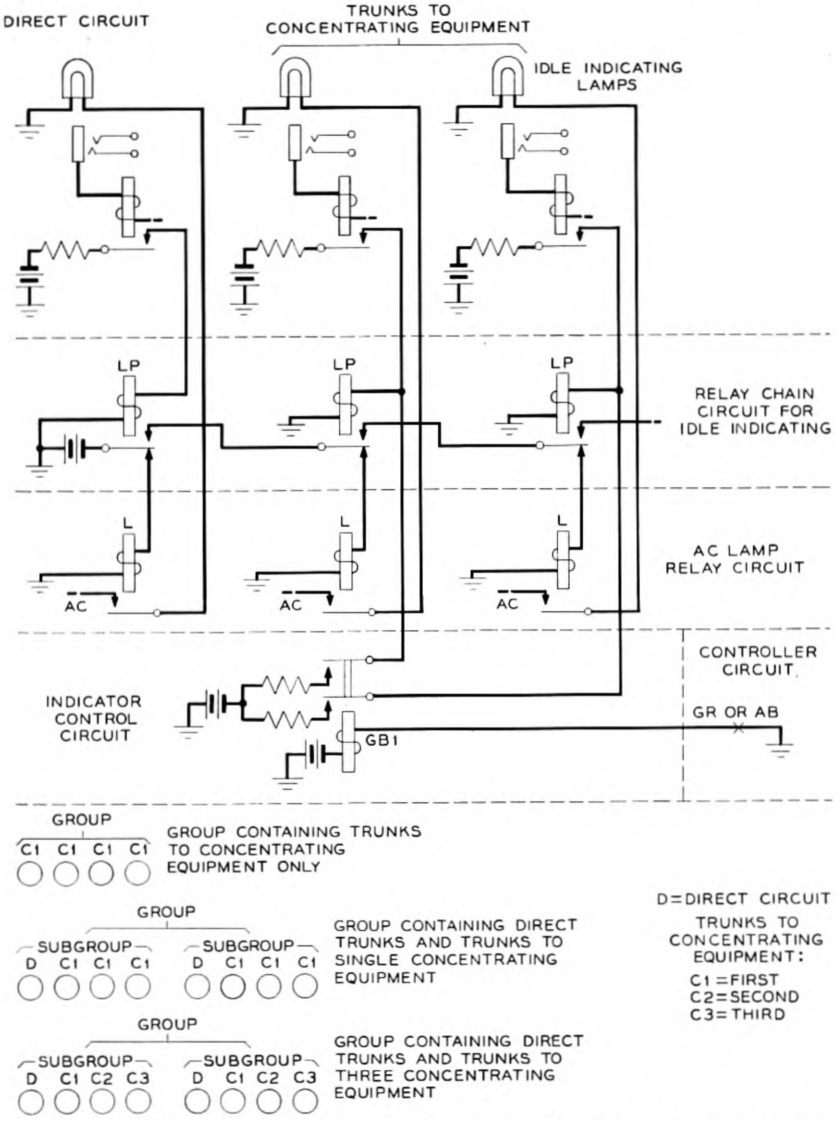

Fig. 13 — Idle trunk indicating control and some examples of groups containing direct trunks and trunks to concentrating equipment.

However, it should be remembered that it contains a single controller which could be disabled by compound trouble, a condition which could be serious if the concentrating equipment were the sole means of handling traffic from any switchboard. It is intended that the concentrating equipment be used in conjunction with direct intertoll circuits and/or tandem trunks to a No. 4 type toll crossbar switching system. When used with direct circuits an operator alternate routing system ensues. Referring back to the paragraph which dealt with idle trunk indicating, it is noted that the direct trunks and the concentrator trunks form a single group or subgroup of trunks to a common destination. The direct trunks appear in the multiple at the head end of the group and are followed by concentrator trunks. The idle indicating lamps direct the operator to a direct trunk, when available, as first choice, and automatically direct the operator to a concentrator trunk when the direct trunks are in use. If the operator also has access to trunks to the toll crossbar office these trunks become third choice for use when the direct and concentrator trunks are busy. Fig. 14 illustrates this situation. The concentrating equipment may be located apart from the central toll building without losing the advantages of the alternate routing discussed above. Thus it is available for dispersing the toll plant to minimize the effect of disaster.

ACKNOWLEDGMENT

The development of the Intertoll Trunk Concentrating Equipment was the combined effort of many people. Important contributions were made by M. Posin and W. L. Shafer, Jr.

The Transistor as a Network Element*

By J. T. BANGERT

(Manuscript received October 7, 1953)

The development of the transistor has provided an active element having important advantages in space and power. As a result, the question arises whether strategic insertion of such active elements in passive networks might lead to interesting results. This paper gives a theoretical analysis confirmed by experiment, of certain possible network applications of transistors. Four general areas are considered in which transistors are used as follows: to reduce the detrimental effects of dissipative reactive elements, to eliminate the necessity for inductors in frequency selective circuits, to produce two terminal envelope delay structures having zero loss, and to invert the impedance of reactive structures. The conclusion is drawn that judicious interspersion of transistors in a transmission network enables performance to be achieved which would otherwise be unobtainable or uneconomical.

INTRODUCTION

It has become customary through the years to classify linear circuits as either active or passive. This convenient, but arbitrary, division has encouraged a philosophy that regards each as a separate and distinct domain. The recent spectacular advances in active devices suggest that in some cases the traditional boundaries should be erased and that a unified approach should be made.

In particular the development of the transistor offers the possibility of interspersing small active elements throughout a passive network to achieve certain desirable effects. This paper intends to survey a few of the ways in which a transistor can be used to advantage in transmission networks. The discussion is divided into four parts as follows:

1. Reduction of dissipation.
2. Elimination of inductance.
3. Production of delay.
4. Inversion of impedance.

---

* Presented in part at the Radio Fall Meeting, Toronto, Ontario, Oct. 28, 1953.

The first portion offers a new approach to the everpresent problem of imperfect reactive elements. The second portion discusses a method of combining resistance and capacitance with transistors to produce characteristics conventionally realized by inductance and capacitance. The third portion proposes a technique for obtaining any specified delay characteristic with a two terminal active structure. The fourth portion considers means of using a transistor to transform passive elements of ordinary size into passive elements of greatly reduced size.

I. REDUCTION OF DISSIPATION

For simplicity in the treatment of network problems it is frequently assumed that purely reactive elements will be used. In many cases this approximation is satisfactory; other times it is worthless, and a more realistic analysis must be made. In this latter case one possibility is to nullify the unwanted dissipation by means of a bridge balance.[1] This will entail the acceptance of some flat loss. Another possibility is to insert active elements within the network in order to supply just enough energy to offset the inherent dissipation of the elements. This second approach, until now relatively unexplored, is being tried with promising results. To avoid introducing new terminology the discussion will employ the concept of negative resistance which has been studied with interest by many investigators.[2-18]

Negative Resistance

Negative resistance is a misleadingly simple name applied to a complex phenomenon. The term implies behavior in some opposite sense to that of an ordinary positive resistance. This is true only for a limited range of frequencies and signal levels. As generally used negative resistance refers to a two terminal active network or electronic device in which the voltage-current ratio has a negative real part and negligible imaginary part.

TABLE I — NEGATIVE RESISTANCE

Parameter	Shunt Type	Series Type
Independent variable	Voltage controlled	Current controlled
Required external impedance	Short circuit stable	Open circuit stable
Effect of internal gain reduction	Increased magnitude of R_N	Decreased magnitude of R_N
Associated reactance	Parallel capacitance	Series inductance

For convenience the simple forms of negative resistance may be divided into two general classes which are duals in a network sense. Since these classes have been identified in the literature in several different ways, it seems desirable to summarize the major characteristics in the form given in Table I.

Therefore a shunt negative resistance is one whose magnitude is controlled mainly by the voltage across its terminals. It is short circuit stable which means it must operate into a low impedance. When the internal gain used to produce the effect is reduced, the magnitude of a shunt negative resistance increases. In addition it should be associated with a parallel capacitance to predict its behavior outside the working band of frequencies.

One method of producing a two terminal shunt negative resistance is to arrange a transistor as shown in Fig. 1(a). To facilitate prediction of the behavior of this combination it is desirable to derive an equivalent circuit.

Equivalent Circuit of a Transistor Shunt Negative Resistance

An equivalent circuit of the transistor and its associated network is shown in Fig. 1(b). By denoting each condenser reactance as jX, the circuit determinant, Δ, can be written as follows.

$$\begin{vmatrix} j2X & -jX & -jX & 0 \\ -jX & r_b + r_e + R_f + jX & -R_f & -r_e \\ -jX & -R_f & R_f + R_a + jX & -R_a \\ 0 & r_m - r_e & -R_a & r_e + r_c - r_m + R_a \end{vmatrix}$$

Next the input impedance is determined as Δ/Δ_{11}.

From this formula the exact general expression for the input impedance is found to be very cumbersome and will not be given. A useful approximation can be found by making some simplifying assumptions

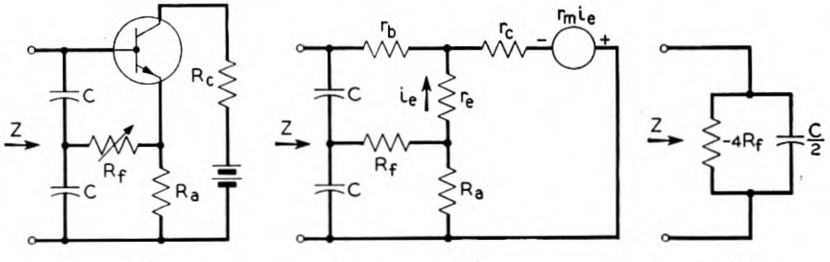

(a) (b) (c).

Fig. 1 — Equivalent circuit of transistor shunt negative resistance.

as follows:

$$\text{Let } r_c >> r_b \qquad r_m >> r_b$$
$$r_c >> r_e + R_a \qquad r_m >> r_e + R_a$$

Under these conditions the network can be represented by the equivalent circuit shown in Fig. 1(c). This circuit consists of a parallel combination of resistance and capacitance in which the capacitance is that of the original two capacitances in series and the resistance is negative and equal to four times the feedback resistor, R_f. Hence the magnitude of the generated shunt negative resistance can be controlled by adjustment of R_f. One measure of the accuracy of this approximation is how much the "constants" of the equivalent circuit change with frequency. Calculations of a typical case show that deviations in frequency of ±5 per cent cause deviations in both capacitance and negative resistance of ±0.05 per cent. Hence this approximation is very accurate for narrow band applications.

This circuit can now be used to advantage in a band filter.

Confluent Band Filter

A conventional confluent band filter is shown in Fig. 2(a). In this structure the presence of dissipation in the series branches impairs performance by introducing flat loss, whereas any dissipation in the shunt branch not only produces flat loss, but, worse still, causes rounding of the transmission characteristic at the edges of the band. For narrow filters having a small percentage band width, any appreciable dissiptation in the shunt arm can degrade the transmission characteristic beyond a reasonable tolerance. One good answer to this problem is to use elements having an extremely low resistive component such as quartz crystals. However, quartz is expensive and has other limitations. Another solution is to build a negative resistance into the filter so as to reduce the inherent element dissipation to zero or at least to a tolerable value. In the present case a shunt negative resistance will be used to compensate the shunt branch. This is done by splitting the shunt capacitance of Fig. 2(a) and inserting the circuit of Fig. 1(a). This can be illustrated by an example. When the filter of Fig. 2(a) is designed to give a 5 per cent band at a midfrequency of 10 kc and impedance level of 600 ohms the shunt branch offers an undesirably low impedance to the compensating transistor circuit and in addition requires cumbersome element values. Both difficulties can be corrected by using capacitative impedance transformations on each side of the shunt branch, thereby

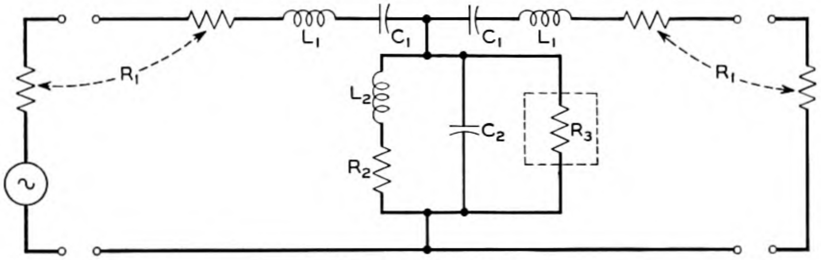

(a) CONVENTIONAL

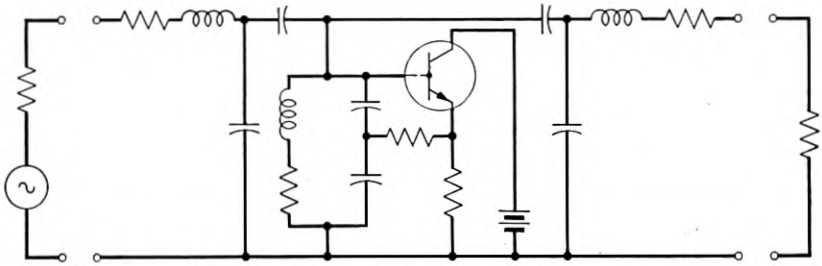

(b) ACTIVE

Fig. 2 — Confluent band filters. (a) Conventional. (b) Active.

raising the impedance of the shunt branch without changing the impedance level at the input and output terminals. At the same time the elements assume much more reasonable values. The modified configuration together with the active portion is shown in Fig. 2(b).

Using the filter described above, a series of transmission curves were calculated and are shown in Fig. 3. When ideal elements are assumed, the transmission is

$$e^{-\theta} = \frac{k^3p^3}{(p^2 + kp + 1)\,[p^4 + kp^3 + (k^2 + 2)\,p^2 + kp + 1]}$$

where $k = \dfrac{f_2 - f_1}{\sqrt{f_2 f_1}}$ and $p = j\omega$

Calculation of this expression results in the classical characteristic labeled "Ideal Passive". When, however, typical values of element resistance are introduced, the transmission is

$$e^{-\theta} = \frac{2R_1\,(\delta_1 p + \delta_2 p^2)\,(\beta_1 p + \beta_2 p^2 + \beta_3 p^3)}{(\alpha_0 + \alpha_1 p + \alpha_2 p^2 + \alpha_3 p^3 + \alpha_4 p^4)^2 - (\delta_1 p + \delta_2 p^2)^2}$$

where

$$\begin{aligned}
\alpha_0 &= R_1(1 + g) \\
\alpha_1 &= R_1[T_1(1 + g) + T_2 + T_{23}] + R_2T_1 \\
\alpha_2 &= R_1[A_1(1 + g) + T_1(T_2 + T_{23}) + A_2] + R_2T_1T_{22} \\
\alpha_3 &= R_1[A_1(T_2 + T_{23}) + A_2T_1] \\
\alpha_4 &= R_1A_1A_2 \\
\delta_1 &= R_2T_1 \\
\delta_2 &= R_2T_1T_{22} \\
\beta_1 &= T_1(1 + g) \\
\beta_2 &= T_1(T_2 + T_{23}) \\
\beta_3 &= T_1A_2
\end{aligned}$$

$$\begin{aligned}
g &= \frac{R_2}{R_3} \\
T_1 &= R_1C_1 \\
T_2 &= R_2C_2 \\
T_{22} &= \frac{L_2}{R_2} \\
T_{23} &= \frac{L_2}{R_3} \\
A_1 &= L_1C_1 \\
A_2 &= L_2C_2
\end{aligned}$$

This expression with the compensating negative resistance $R_3 = \infty$ produces the characteristic labeled "Practical Passive".

The dotted curves show the effect of adding various amounts of negative resistance to the shunt branch by letting R_3 assume negative values. The number on each dotted curve is the ratio of the resistive component of the shunt arm at anti-resonance to the magnitude of the compensating negative resistance. For example, for the curve labeled $\rho = 1$, the resistance in the shunt arm is entirely compensated so that the loss is only that due to the resistance in the series arms. By increasing the amount of compensation in the shunt arm so that $\rho > 1$, called overcompensation it is possible effectively to nullify the losses in the series arm as well. Comparison of the active curve labeled $\rho = 1.21$ with the "ideal passive" curve shows that this technique of resistance compensation can produce a practical filter having a characteristic equal to that of a filter having ideal elements. Filters of this type have already been successfully used in field test equipment.

When the degree of compensation is increased still further, the filter begins to provide gain in the band as shown by the $\rho = 1.36$ curve. It is clear that continued increases in the compensation will eventually absorb the terminations causing the structure to become unstable.

Although the curves given in Fig. 3 are all calculated, tests on experimental models show excellent agreement. To a reader having long experience with passive filters the development of negative insertion loss may seem a little surprising. In order to lend an air of authenticity to this midband gain it is instructive to consider the behavior of a resistive tee section having a negative element. This is a reasonable analogue, because at midfrequency the reactive component becomes zero in each branch of the filter.

Transmission of Symmetrical Tee

The insertion loss of a symmetrical tee section with positive resistance is a well known concept. It is doubtful, however, if the behavior of a tee with a negative element is equally well known. Consider the section shown in Fig. 4 operating between terminations R and having series arms, R_A and a shunt arm, R_B. Normalize by letting $a = R_A/R$ and $b = R_B/R$. Insertion loss is plotted vs. b with a as the third parameter. For b positive the usual loss pattern results; for b negative, a more complex situation develops. When b is very large and negative, the section is still producing a small loss, but as b becomes smaller in magnitude the loss drops to zero and finally becomes a gain. There is a lower limit on the magnitude of b beyond which oscillations will occur. This limit is reached when $2b = -(a + 1)$.

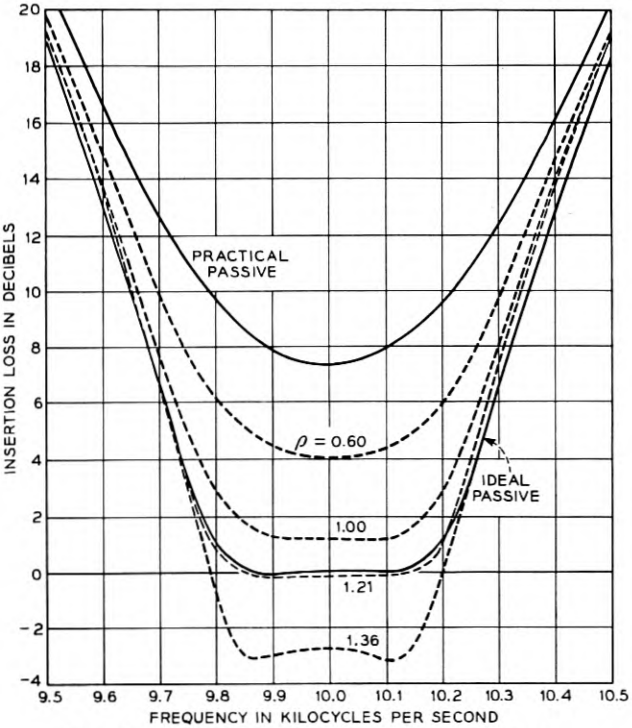

Fig. 3 — Transmission of confluent band filters.

Singularities of Confluent Band Filter

Recent work on insertion loss design and potential analog methods by S. Darlington and others has fostered the practice of characterizing a network by plotting its natural modes and infinite loss points in the complex frequency plane. In the present case it is instructive to study the effect that reducing dissipation will have on the singularities. A full section confluent band filter has five infinite loss points and eight natural modes. In Fig. 5 the singularities of the passive, confluent band filter discussed earlier are plotted in the complex frequency plane and identified by the digit one. A single infinite loss point or zero lies on the negative sigma axis, a pair falls at the origin, and a conjugate pair is located near the midband frequency. The natural modes or poles consist of two conjugate double pairs situated at about the upper and lower cut off frequencies of the filter. The distance of the complex singularities from

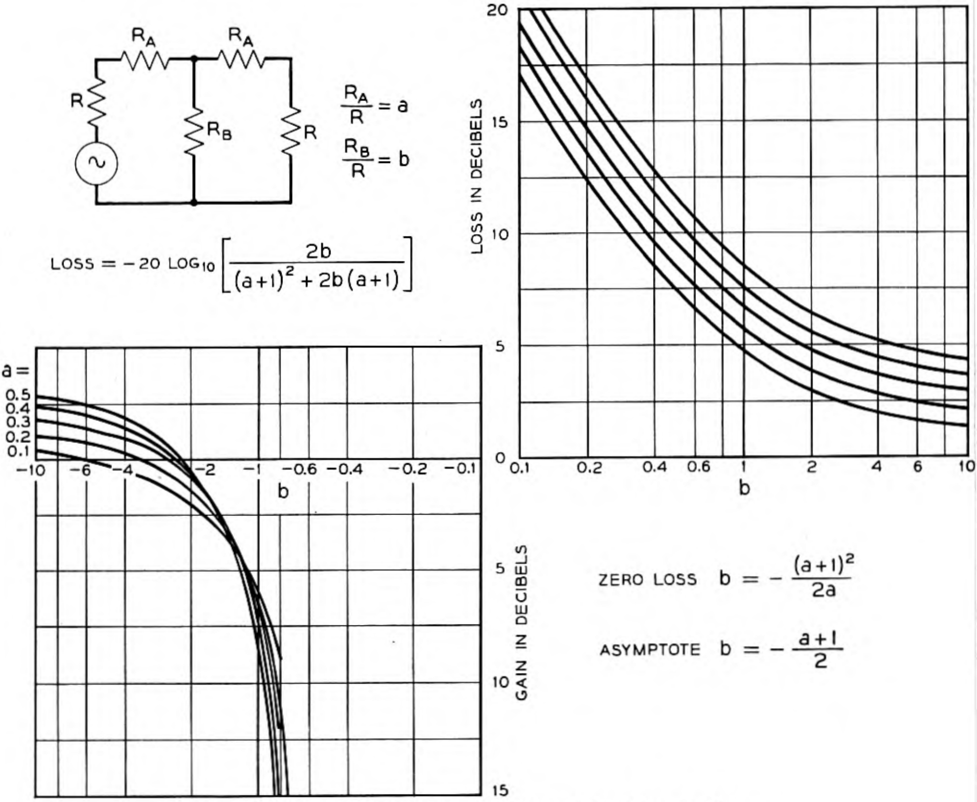

Fig. 4. Transmission of symmetrical tee section.

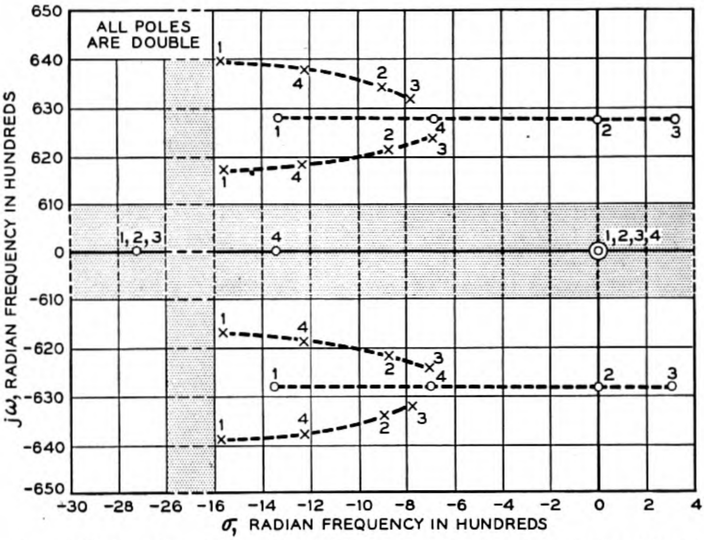

Fig. 5 — Effect of reducing dissipation on singularities of confluent band filter.

the real frequency axis is a function of the amount of dissipation in the elemets. When a value of negative resistance corresponding to the $\rho = 1$ curve in Fig. 3 is added to the passive filter, the singularities move from positions marked 1 to those marked 2 in Fig. 5. Adding a larger amount of negative resistance corresponding to the $\rho = 1.21$ curve in Fig. 3 produces the singularities marked 3. It should be noted that the infinite loss point on the negative sigma axis as well as the two at the origin have not moved. If the dissipation in the shunt branch is reduced by removing the coil and replacing by one having half as much resistance, the singularities change from position one to position four. In this case the infinite loss point on the sigma axis does move. This illustrates that the change in pattern of singularities resulting from use of negative resistance is similar to, but not the same as, that resulting from use of passive inductors having higher values of Q.

M-Derived Band Pass

In order to provide a sharp cut-off in a filter use is often made of *m*-derived peak sections. In the configuration shown in Fig. 6 loss peaks will occur at selected frequencies above and below the pass band provided the elements are nearly free of dissipation. The closer the attenuation peaks are to the pass band the more nearly free from dissipation the elements must be for good performance. As in the previous case, a transistor negative resistance is used to compensate the anti-resonant portion of the shunt arm. The magnitude of this resistance can also be adjusted to serve the additional purpose of compensating for resistance in the series resonant circuit in the shunt arm, as well as the series resonant circuits in the series arms.

The transmission of a non-dissipative m-derived band filter between unit resistive terminations is

$$e^{-\theta} = \frac{kp[(1 - m^2)p^4 + (2 - 2m^2 + k^2)p^2 + (1 - m^2)]}{(mp^2 + kp + m)[p_4 + kmp^3 + (k^2 + 2)p^2 + kmp + 1]}$$

where $m = \sqrt{1 - \left(\frac{f_c}{f_\infty}\right)^2}$

Assuming no dissipation a peak section with an m of 0.86 will give the characteristic shown in Fig. 7 labeled "Ideal Passive". However, when this filter is constructed with typical elements the curve labeled "Practical Passive" results. By introducing a suitable amount of negative resistance the transmission of the practical filter can be made comparable to that of the ideal filter, as illustrated by the curve labeled "Practical Active".

For maximum utility active filter sections must be capable of being connected in tandem to form composite filters without instability, reflections, or interactions. Fig. 8 shows that these filters meet this requirement by giving the measured transmission of a band filter composed of two dissimilar peak sections. On the basis of attainable electrical charac-

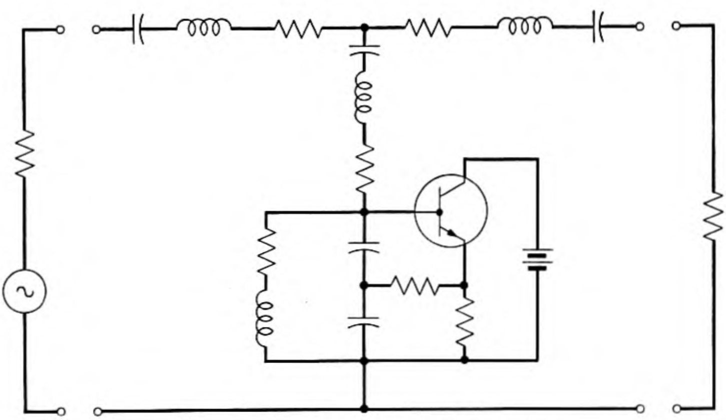

Fig. 6 — Active M-derived band filter.

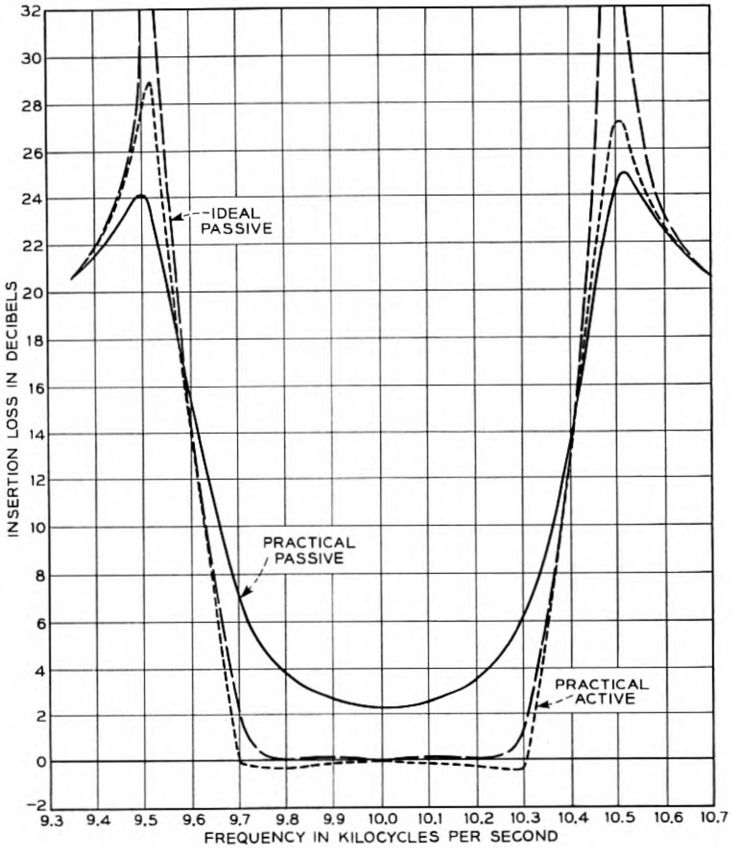

Fig. 7 — Transmission of M-derived band filters.

teristics, active filters of this kind appear to offer potential competition to the crystal channel filters used in broad band carrier systems.

Working Model

To further emphasize this fact the photograph of Fig. 9 shows a model of a composite band filter designed to transmit a 4-kc band at a midfrequency of 98 kc. This model contains seven miniature, adjustable, ferrite inductors, miniature capacitors, and two *n-p-n* junction transistors. The transmission characteristic is shown in Fig. 10. Hence in some cases by employing active circuitry it is possible to use miniature components thereby gaining at least an order of magnitude in the size and weight of structure.

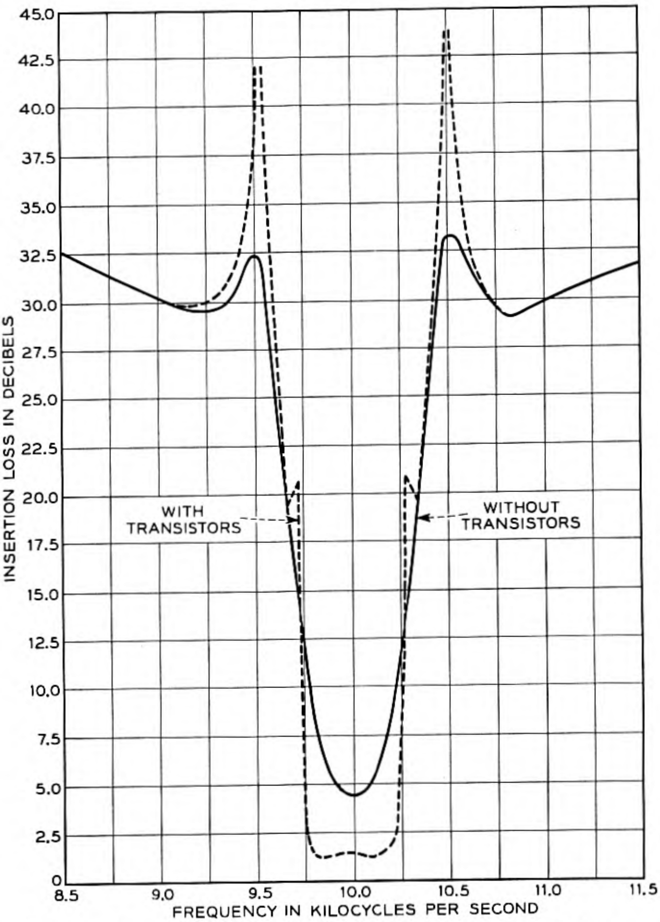

Fig. 8 — Resistance compensation of multi-section filter.

Series Negative Resistance

For satisfactory performance in many applications a series resonant circuit should approach zero impedance at the resonant frequency. To reduce the residual dissipation in an ordinary tuned circuit a series negative resistance, consisting of two transistors, can be used. This technique is illustrated in Fig. 11 which shows how a purely reactive shunt branch can be achieved in either an m-derived low pass filter or a confluent band elimination filter.

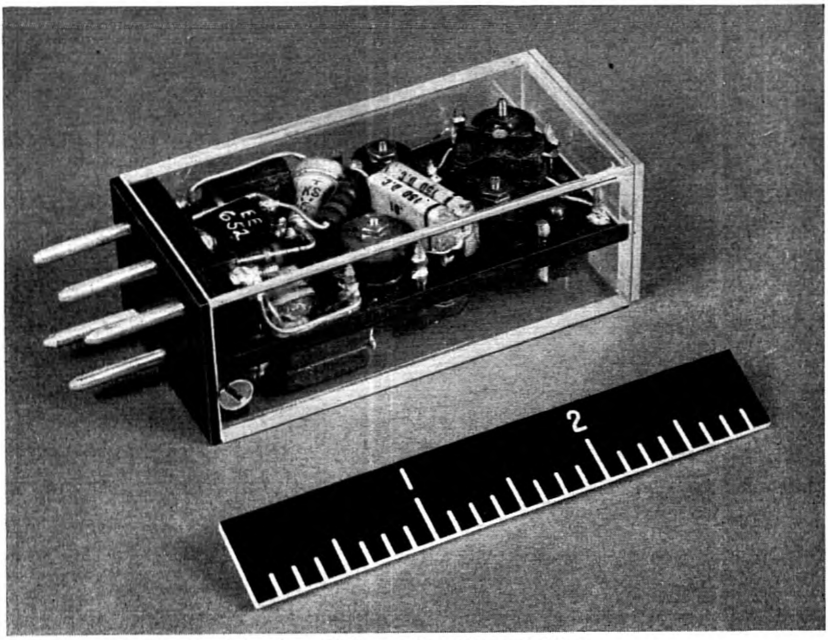

Fig. 9 — 98-kc active channel filter.

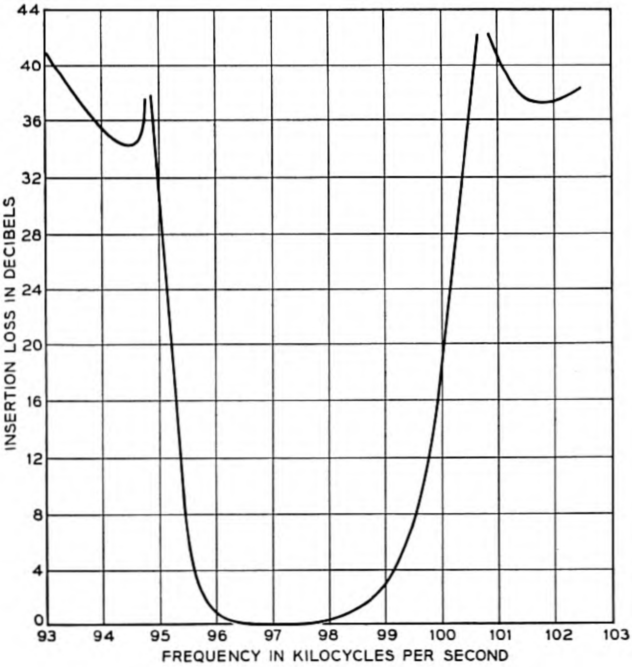

Fig. 10 — Active channel filter.

II. ELIMINATION OF INDUCTANCE

In the practical realization of frequency selective networks it is sometimes awkward, difficult, or even impossible to make effective use of coils as inductive elements. This is true, because of severe limitations on space, exacting tolerances on undesired modulation, or necessity for operation at extremely low frequencies.

It has been well known for some time that inductive elements can be eliminated without restricting the repertoire of the network designer provided he is willing to purchase this freedom by introducing active elements to supply gain.[19, 20]

It can be easily shown that the transmission through a high gain feedback amplifier is proportional to the product of the short circuit transfer admittance of the input network and the short circuit transfer impedance of the feedback network:

$$e^{-\theta} = Y_i Z_f$$

In addition it is also known from energy relations that passive networks containing only one kind of reactance cannot produce complex poles in the short circuit transfer admittance. It is instructive to consider the application of these principles to some familiar kinds of transmission networks. These networks can be logically divided into two classes: those which are primarily concerned with amplitude such as filters, and those mainly concerned with phase such as delay equalizers.

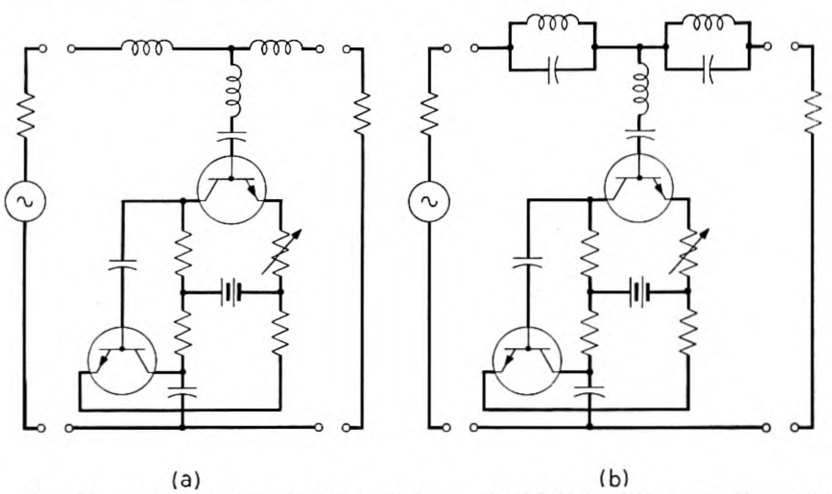
(a) (b)

Fig. 11,— Use of series negative resistance. (a) M-derived low pass filter. (b) Band elimination filter.

Non-inductive Filters

Low Pass

Consider first an image parameter, constant-k, low pass filter which is usually built as a ladder-type structure of series inductance and shunt capacitance. A full section contains three reactive arms and produces an asymptotic loss that increases 18 db per octave.

The transmission is given by the following expression

$$e^{-\theta} = \frac{1}{(1 + \omega_0^{-1}p + \omega_0^{-2}p^2)(1 + \omega_0^{-1}p)}$$

where $\omega_0 =$ cut-off frequency in radians per second.

The function has three poles, one real and two complex conjugate. The question now arises how this function can be divided between the input and feedback networks so as to be physically realizable. Since we know that a passive R-C structure cannot have complex poles in the short circuit transfer admittance, there is no choice but to use the impedance function in the feedback circuit for this purpose. It is now found that any R-C structure which will provide the complex poles insists on providing a real zero for good measure. This unwelcome zero can be nullified by supplying its counterpart as a pole in the admittance function. The transmission is now rewritten, as follows:

$$e^{-\theta} = \left[\frac{1}{(1 + \omega_0^{-1}p)(1 + ap)}\right]\left[\frac{1 + ap}{1 + \omega_0^{-1}p + \omega_0^{-2}p^2}\right]$$

and the singularities are shown in Fig. 12(a). Since the original transmission function also requires a real pole, the admittance function must now supply two real poles. A simple ladder structure having three series resistances and two shunt capacitances meets this requirement. The complex poles cannot be supplied by a ladder structure, but require some sort of bridge such as shown in Fig. 12(a).

At low frequencies the transmission through the filter depends on the ratio of the total series input resistance to the total resistance in the bridge arm of the feedback network. Therefore any amount of flat loss or a moderate flat gain through the filter can be obtained simply by adjusting the ratio of impedance levels of the input and feedback networks.

Simulation of functions by this technique does not provide a unique solution since there is considerable freedom in choice of configuration and location of the cancelling pole and zero.

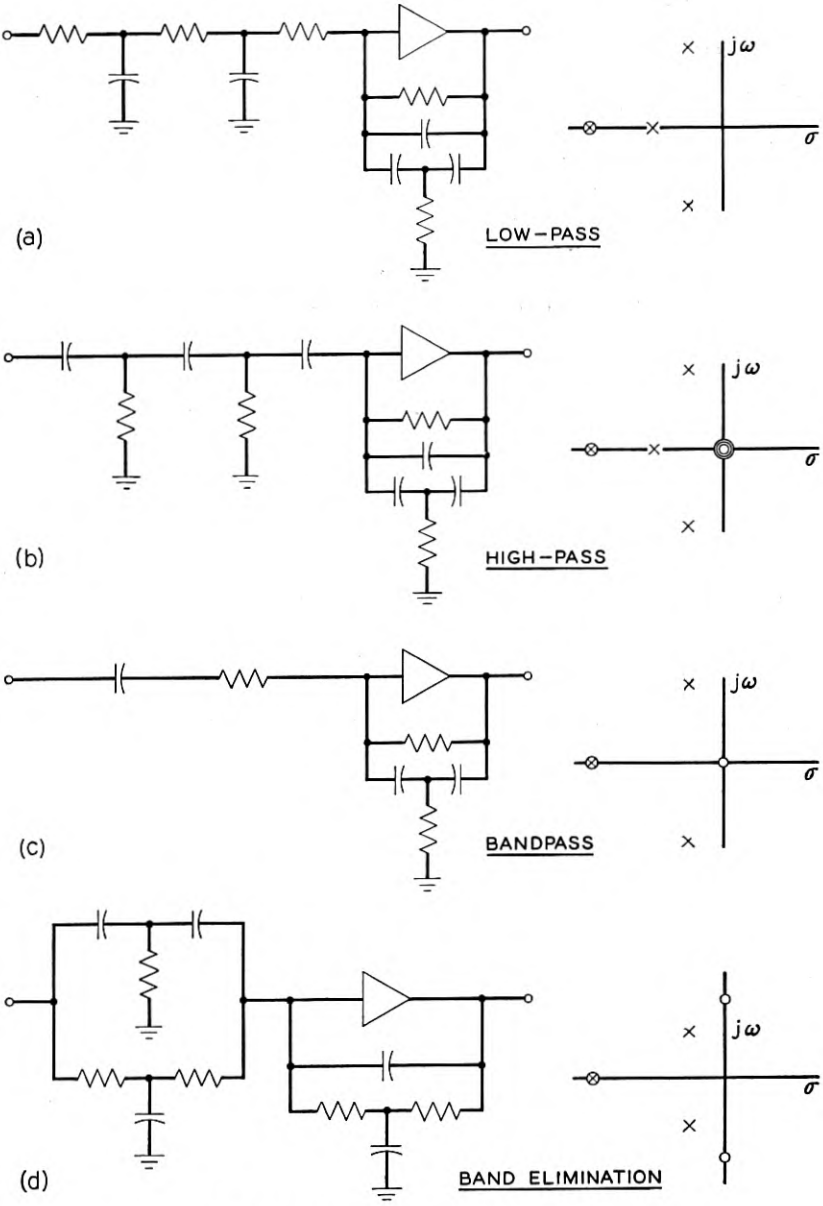

Fig. 12 — Non-inductive active filters.

High Pass

Consider next a high pass filter with cut-off at ω_0. The transmission is

$$e^{-\theta} = \frac{\omega_0^{-3}p^3}{(1 + \omega_0^{-1}p + \omega_0^{-2}p^2)(1 + \omega_0^{-1}p)}$$

$$= \left[\frac{\omega_0^{-3}p^3}{(1 + \omega_0^{-1}p)(1 + ap)}\right]\left[\frac{1 + ap}{1 + \omega_0^{-1}p + \omega_0^{-2}p^2}\right]$$

The complex plane plot in Fig. 12(b) shows exactly the same pattern of singularities as the low pass case with the addition of three zeros at the origin. To realize this function the feedback network remains unchanged, whereas the input network becomes a ladder in which the positions of the resistances and capacitances are interchanged.

Band Pass

A series resonant branch inserted in series between resistive terminations is a simple form of band pass filter having the following transmission:

$$e^{-\theta} = \frac{\omega_m^{-1}Q^{-1}p}{1 + \omega_m^{-1}Q^{-1}p + \omega_m^{-2}p^2} = \left[\frac{\omega_m^{-1}Q^{-1}p}{1 + ap}\right]\left[\frac{1 + ap}{1 + \omega_m^{-1}Q^{-1}p + \omega_m^{-2}p^2}\right]$$

where ω_m is the radian frequency of the peak and Q is a measure of the sharpness of the peak.

The singularities shown in Fig. 12(c) consist of a zero at the origin and two complex conjugate poles. Once again the complex poles are obtained by a bridge circuit in the feedback path. The usual penalty is incurred by the appearance of a real zero which must be cancelled by a real pole. Therefore the admittance function must supply a zero at the origin and one real pole. This is done by a series combination of resistance and capacitance in the input circuit.

Band Elimination

A parallel resonant branch inserted in series between resistive terminations is a simple form of band elimination filter having the following transmission:

$$e^{-\theta} = \frac{1 + \omega_m^{-2}p^2}{1 + \omega_m^{-1}Qp + \omega_m^{-2}p^2} = \left[\frac{1}{1 + ap} + \frac{\omega_m^{-2}p^2}{1 + ap}\right]\left[\frac{1 + ap}{1 + \omega_m^{-1}Qp + \omega_m^{-2}p^2}\right]$$

The singularities consist of two conjugate zeros on the real frequency axis and two complex conjugate poles. A bridge circuit in the feedback path supplies the complex conjugate poles and a parasitic real zero, while a parallel tee in the input path provides the conjugate zeros and a real pole.

It has been found that the experimental performance of the various non-inductive filters described can be predicted with precision from the theory.

Non-inductive Phase Sections

Non-minimum phase networks are used extensively to provide a specified variation in phase with frequency without introducing any change in attenuation. Such all-pass networks consisting only of reactive elements are usually designed as lattices or bridged tee sections. It is theoretically possible and practically desirable to represent any complex all-pass structure by tandem arrangements of two basic all-pass sections called first degree and second degree. The first degree structure pro-

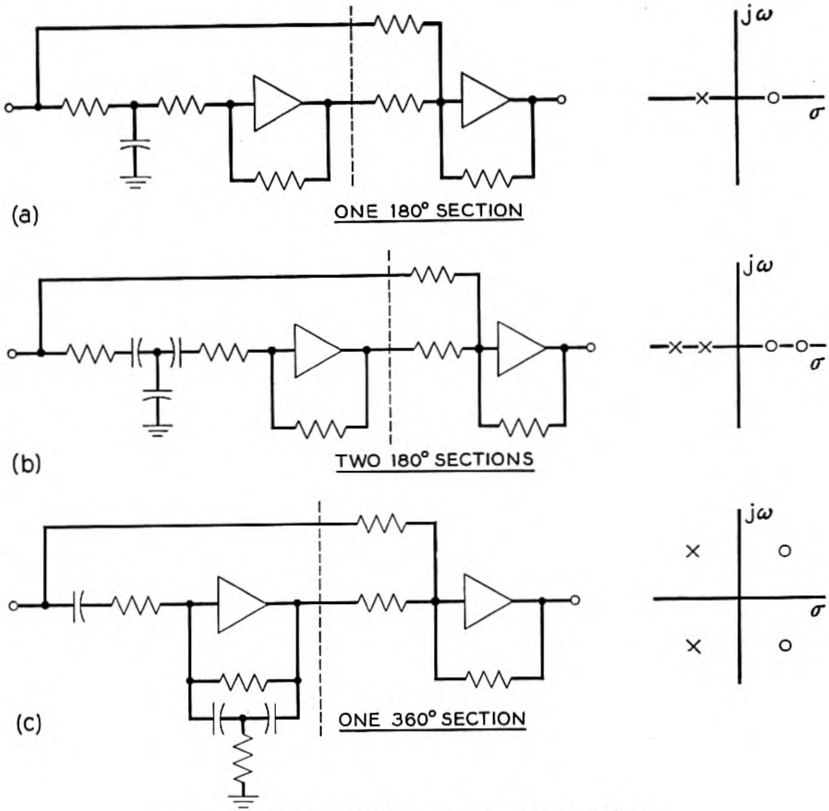

Fig. 13 — Non-inductive active phase sections.

vides a total change in phase of 180° and is characterized by a single pole-zero pair symmetrically located on the σ axis as shown in Fig. 13(a). Only one parameter, the distance from the origin can be chosen. The second degree structure provides a maximum phase shift of 360° and is characterized by two conjugate poles in the left half plane and two symmetrically located zeros in the right half plane shown in Fig. 13(c). The two parameters which can be selected are the rectangular coordinates of one singularity.

It has been suggested that these functions can be realized without benefit of inductance. Here again numerous arrangements are possible, but only a few examples will be given. The basic operation is to perform one division on the original transmission function resulting in a quotient of unity and a fractional remainder of opposite sign. The fractional remainder is then synthesized by a RC network in conjunction with an amplifier.

Single 180° Section

The transmission of a single 180° section is

$$e^{-\theta} = \frac{1 - \omega_0^{-1} p}{1 + \omega_0^{-1} p} = \frac{2\omega_0}{\omega_0 + p} - 1$$

In this case the fractional remainder consists of only one real pole which is realized by the R-C structure shown in Fig. 13(a).

Two 180° Sections

The overall transmission of two 180° sections in tandem is the product of each transmission

$$e^{-\theta} = -\left[\frac{1 - \omega_1^{-1} p}{1 + \omega_1^{-1} p}\right]\left[\frac{1 - \omega_2^{-1} p}{1 + \omega_2^{-1} p}\right] = \frac{2(\omega_1^{-1} + \omega_2^{-1})p}{(1 + \omega_1^{-1} p)(1 + \omega_2^{-1} p)} - 1$$

In this case the fractional remainder consists of one real zero and two real poles which are realized by the R-C structure shown in Fig. 13(b).

Single 360° Section

By far the most common phase corrector is the 360° section whose transmission is

$$e^{-\theta} = -\left[\frac{1 - Q^{-1}\omega_m^{-1} p + \omega_m^{-2} p^2}{1 + Q^{-1}\omega_m^{-1} p + \omega_m^{-2} p^2}\right]$$

$$= 2\left[\frac{Q^{-1}\omega_m^{-1} p}{1 + ap}\right]\left[\frac{1 + ap}{1 + Q^{-1}\omega_m^{-1} p + \omega_m^{-2} p^2}\right] - 1$$

In this case the fractional remainder consists of a zero at the origin and two conjugate complex poles which are realized by the R-C structure shown in Fig. 13(c).

III. PRODUCTION OF DELAY

It has also been proposed that a two terminal active delay equalizer can be constructed with the help of a negative resistance. As shown in Fig. 14 a two terminal network Z is connected between a resistive source and load, each of magnitude, one quarter R_0. The network Z consists of a parallel combination of a reactive network jX and a negative resistance $(-R_0)$. The transmission through Z is

$$e^{-\theta} = \frac{\dfrac{R_0}{2}}{\dfrac{R_0}{2} + Z} = \frac{\dfrac{R_0}{2}}{\dfrac{R_0}{2} + \dfrac{jR_0X}{R_0 - jX}} = \frac{R_0 - jX}{R_0 + jX}$$

This is the desired function, because the amplitude of the transmission

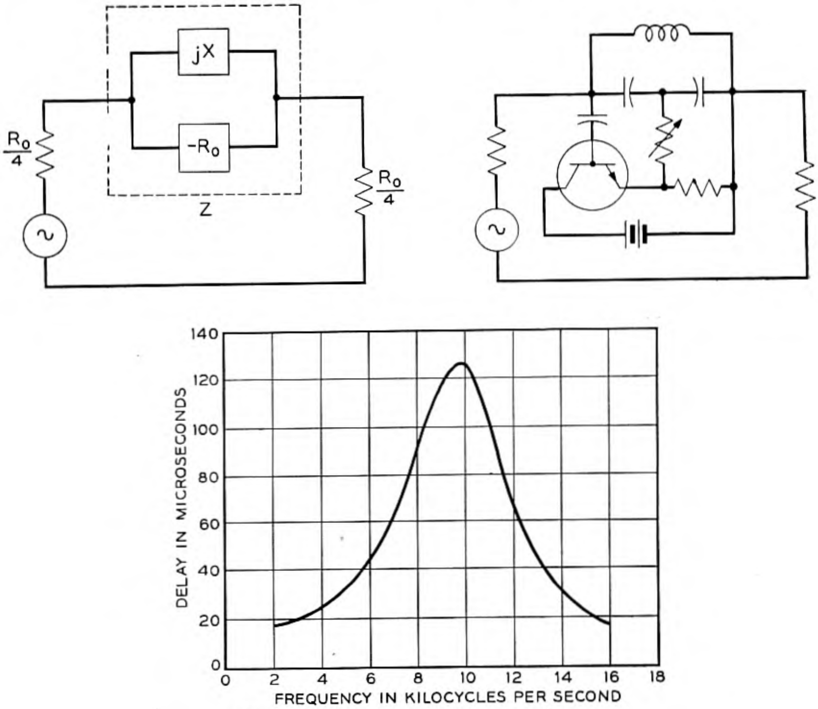

Fig. 14 — Active all-pass section.

is unity regardless of the size of X, and the phase and resultant delay are frequency dependent, because X is a function of frequency. It is theoretically possible to produce the most complicated delay equalizer characteristic by this method provided the negative resistance remains constant over the desired frequency band. As examples only a single 180° section and a single 360° section will be considered.

A 360° section results when the reactance is a single antiresonance given by

$$X = \frac{\omega L}{1 - \omega^2 LC}$$

the transmission is

$$e^{-\theta} = \frac{(p - k)^2 + \omega_m^2}{(p + k)^2 + \omega_m^2} = \frac{1 - Q^{-1}\omega_m^{-1}p + \omega_m^{-2}p^2}{1 + Q^{-1}\omega_m^{-1}p + \omega_m^{-2}p^2}$$

where

$$k = \frac{Q}{2}\,\omega_m \qquad \text{and} \qquad Q = (\omega_m R_0 C)^{-1}$$

In this case there are two degrees of freedom, namely, the width of the delay characteristic and the location of the peak frequency.

The circuit is shown on Fig. 14, where the transistor supplies the negative resistance, the magnitude of which is controlled by the adjustable resistance. A typical delay characteristic is also shown on Fig. 14.

A single 180° section can be obtained by simply omitting the coil in the above circuit. This is equivalent to letting $X = -(\omega C)^{-1}$ so that

$$e^{-\theta} = \frac{p - \omega_0}{p + \omega_0}$$

where $\omega_0 = (R_0 C)^{-1}$

IV. IMPEDANCE INVERSION

Two networks are said to be inverse if the product of their impedance functions is a constant. Given a network of passive elements, there are standard topological methods for finding its structural inverse if it exists. Another method is to use an active circuit in conjunction with the given impedance so that the combination offers an impedance inverse to that of the original impedance. This is a special case of modifying an impedance by feedback.[21] By means of such methods passive circuit elements can be made to appear electrically much larger or much smaller than they really are. For example, as shown in Fig. 15(a), by using an active element a parallel combination of convenient elements such as a 0.1 henry inductance and a 10,000 $\mu\mu f$ capacitance can be made to look like the series combination in Fig. 15(b) of difficult or sensitive elements like a 100 henry inductance and a 10 $\mu\mu f$ capacitance.

This transformation can be made with the transistor circuit of Fig. 15(c) which is also drawn as the equivalent circuit of Fig. 15(d).

In the circuit of Fig. 15(c) the resistor R_A is adjusted so that the

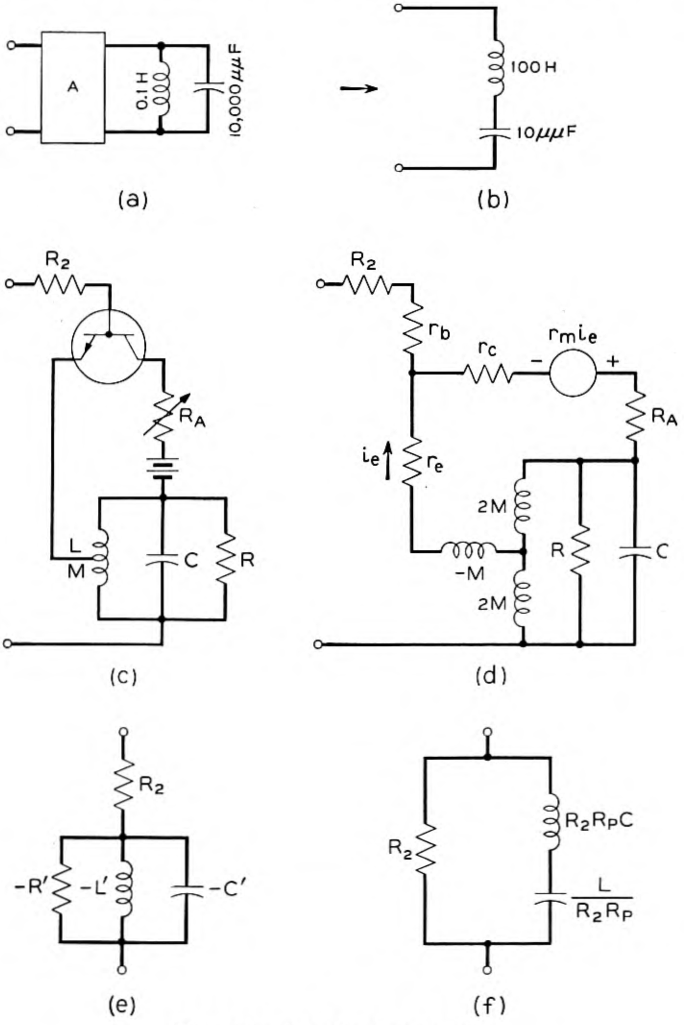

Fig. 15— Impedance inversion.

parameters of the transistor and the associated external circuit will satisfy the following equation

$$\frac{r_c}{2r_0} = \frac{2R_2}{R_P} + 1$$

To eliminate non-essentials it will be assumed that r_b and r_e are negligibly small, and $R_a \ll r_c$. Then by a straightforward, but lengthy, analysis the driving point impedance is found to be

$$Z = R_2 - \frac{pL'}{p^2L'C' + p\frac{L'}{R'} + 1}$$

where $L' = \lambda L$ $\qquad R_P = \frac{4r_0R}{R + 4r_0}$

$R' = \lambda R_P$ $\qquad \lambda = \frac{r_c - 2r_0}{4r_0}$

$C' = \frac{C}{\lambda}$ $\qquad r_0 = r_c - r_m$

The circuit representing this impedance is shown in Fig. 15(e). Since negative elements are not convenient a final transformation is made to the circuit shown in Fig. 15(f).

CONCLUSION

The distinctive properties of the transistor suggest careful consideration of a philosophy which regards the transistor as a circuit element to be introduced at strategic points within a network. Initial work indicates that the judicious interspersion of transistors in a transmission network makes possible performance otherwise unobtainable or uneconomical. This paper has presented examples of how transistors may be used to reduce dissipation, to eliminate inductance, to produce delay, and to invert impedance. Undoubtedly this is only the beginning of exploration which should extend the horizons of network design.

ACKNOWLEDGEMENT

The author is indebted to many associates in Bell Telephone Laboratories, in particular to E. I. Green for basic philosophy and to W. R. Lundry for much helpful advice, and many suggestions, including the novel concepts of non-inductive phase sections and active delay equalizers.

BIBLIOGRAPHY

1. H. Bode, U. S. Patent 2,002,216, May 21, 1935.
2. A. Hull, Description of the Dynatron, Proc. I.R.E., **6,** p. 5, Feb., 1918.
3. A. Bartlett, Boucherot's Constant Current Networks and their Relation to Electric Wave Filters, J. I. E. E., **65,** p. 373, March, 1927.
4. H. Mouradian, Some Long Distance Transmission Problems, Journal Franklin Inst., **207,** p. 165, Feb., 1929.
5. B. van der Pol, New Transformation in Alternating — Current Theory with Application to Theory of Audition, Proc. I.R.E., **18,** p. 221, Feb., 1930.
6. L. Verman, Negative Circuit Constants, Proc. I.R.E., **19,** p. 676, April, 1931.
7. G. Crisson, Negative Impedances and the Twin 21-Type Repeater, B.S.T.J., **10,** p. 485, July, 1931.
8. F. Colebrook, Voltage Amplification with High Selectivity by Means of the Dynatron Circuit, Wireless Eng., **10,** p. 69, Feb., 1933.
9. S. Cabot, Resistance Tuning, Proc. I.R.E., **22,** p. 709, June, 1934.
10. E. Herold, Negative Resistance and Devices for Obtaining It, Proc. I.R.E., **23,** p. 1201, Oct., 1935.
11. L. Curtis, Selectivity Control for Radio, U. S. Patent 2,033,330, March 10, 1936.
12. C. Brunetti, Clarification of Average Negative Resistance with Extension of its Use, Proc. I.R.E., **25,** p. 1595, Dec., 1937.
13. E. Schneider, A. New Type of Electrical Resonance, Phil. Mag., **36,** p. 371, June, 1945.
14. E. Ginzton, Stabilized Negative Impedances, Electronics, **18,** pp. 140, 138, and 140 of July, Aug., and Sept., 1945, respectively.
15. J. Merrill, Theory of the Negative Impedance Converter, B.S.T.J., **30,** p. 88, Jan., 1951.
16. H. Harris, Simplified Q. Multiplier, Electronics, **24,** p. 130, May, 1951.
17. J. Muehlner, Transfer Properties of Single and Coupled Circuit Stages With and Without Feedback, Proc. I.R.E., **39,** p. 939, Aug., 1951.
18. F. B. Llewellyn, Some Fundamental Properties of Transmission Systems, Proc. I.R.E., **40,** p. 271, March, 1952.
19. G. Fritzinger, Frequency Discrimination by Inverse Feedback, Proc. I.R.E., **26,** p. 207, Feb., 1938.
20. R. Dietzold, Frequency Discriminative Electric Transducer, U. S. Patent 2,549,065, April 17, 1951.
21. R. Blackman, Effect of Feedback on Impedance, B.S.T.J., **22,** p. 269, Oct., 1943.

Continuous Incremental Thickness Measurements of Non-Conductive Cable Sheath

By B. M. WOJCIECHOWSKI

(Manuscript received August 5, 1953)

A method has been recently developed for measuring thickness variations of a non-conductive cable sheathing, extruded over a grounded metal jacket. The method translates direct capacitance increments, sensed by probes sliding on the surface of the sheath, into thickness increments. The accuracy of the system based on this method is sufficiently high that the electrical error, which is of the order of a few thousandths of a $\mu\mu F$*, can be disregarded. Experimental data indicate that accuracy of the new system for absolute thickness measurements of homogeneous samples in stationary conditions is of the order of 0.002″.*

The error caused by translating capacitance to thickness depends on manufacturing elements and process tolerances, and can be evaluated on a statistical basis. Thus incremental measurements of the cable sheath thickness on the production line yield accuracies of the order of 0.003″.

Application of this method to absolute sheath thickness measurements involves assumptions directly related to calibration and manufacturing process control. These aspects are rather extraneous to a measuring system per se, and, therefore, are not within the scope of this paper.

1 INTRODUCTION

1.1 The New Cable

A type of telephone cable has been developed in which lead is replaced with a polyethylene sheath extruded over a metal jacket. Since description of various aspects of this development can be found in the technical literature,[1, 2, 3, 4] only some details of the cable construction and production that are pertinent to the understanding of the new measuring system, will be briefly outlined here.

The cable core, Fig. 1, is covered with a thin layer of a highly conductive metal, such as aluminum,[1] or two layers of different metals, such as aluminum and steel,[2, 5] sealed longitudinally. To achieve the desired mechanical properties, the metal jacket is corrugated circumferentially. Between the metal layer and the plastic sheathing, a bonding viscous thermoplastic compound is applied (Fig. 2). Normally, this compound fills the depressions of the corrugations on the metal surface adjacent to the surrounding polyethylene jacket.

The sheathed cable leaves the extruder with an essentially uniform speed, under pulling force of a capstan. For various sizes of cables and production settings, this speed may range from 30 to 80 feet per minute. After leaving the extruder, the cable is cooled in a trough of water and, before reaching the testing position, dried with compressed air.

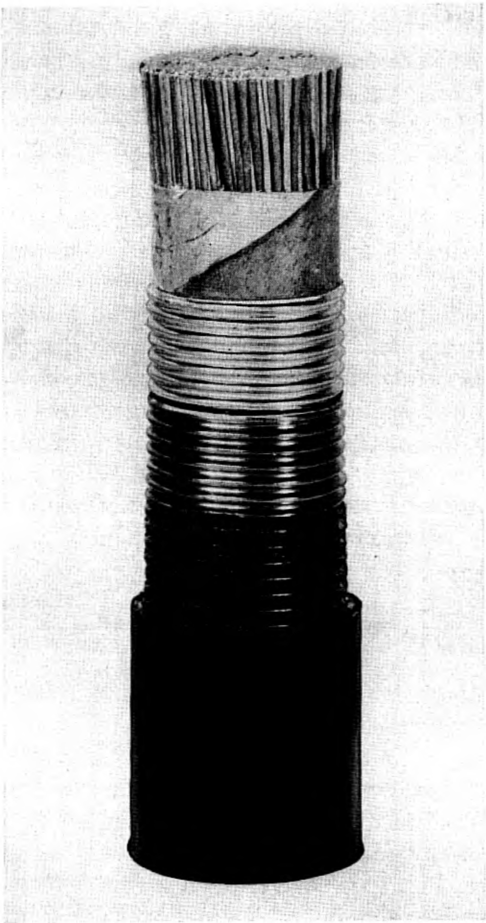

Fig. 1 — Polyethylene sheath telephone cable.

1.2 Measurement Difficulties

Some of the problems encountered in the manufacture of the new cable were related directly to the lack of reliable methods for measuring thickness of the plastic sheathing. Under manufacturing conditions, where sheath thickness cannot be adequately controlled, excess material must be used to assure meeting minimum thickness requirements.

Before the new method was developed, measurements were made by destructive testing of end samples. One or two circumferential strips were taken from each cable length and micrometer measurements were performed on each strip, at four to eight points. Unfortunately, the actual sheath thickness varies in a random way along the cable length, even between points only a few inches apart. It was evident that a method, based on a few point measurements, extrapolating long-cable properties which are describable rather in statistical terms only, left much to be desired.

1.3 Preliminary Considerations

The following methods of cable sheath measurements were considered:

A. Use of an X-ray machine.

B. Ultrasonic echo method (radar techniques).

C. Capacitance measurements.

For practical reasons as well as for anticipated lack of accuracy, the first of these methods was rejected. The success of the second method was judged doubtful, the main reason being the presence of corrugations and of an irregular layer of the filling compound under the polyethylene sheathing, obscuring delimitation of the reflecting boundary surface. The third method, at first, also had discouraging aspects. In the case under discussion only grounded capacitance measurements are involved, since the metal core cannot possibly be insulated from the corrugating and forming machinery. The required long-time capacitance-to-ground stability and accuracy of the measuring system were estimated to be of the

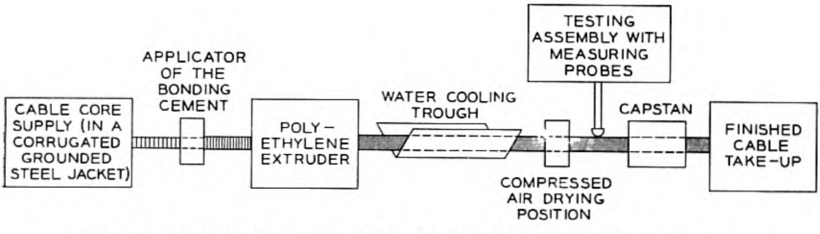

FIG. 2 — Block diagram of the polyethylene extruding process.

order of 0.001 $\mu\mu$F and 0.003 $\mu\mu$F, respectively. Meeting requirements of this order, even under controlled laboratory conditions, presents some difficulties — and yet these requirements had to be met on a production line, on moving cable in the climatic and operational conditions prevailing in a large cable plant.

It was evident, therefore, that conventional grounded-capacitance measurements would not be practical. For instance, a shielded cable connecting the probes with the bridge circuit alone could produce wider random capacitance variations than the capacitance increments under measurement. Thus a new system which would meet all the necessary requirements had to be developed.

2 CIRCUIT DESCRIPTION

The measuring system which was developed consists of an impedance bridge, a phase sensitive detector, an unbalance indicator (recorder), capacitance probes and associated auxiliary equipment (See Figure 3).

2.1 *The Impedance Bridge for Grounded Direct Capacitance Measurements.*

The circuit shown on Fig. 4 employs a bridge having ratio arms[6] magnetically coupled. An application of this type of circuit for capacitance measurements has been known for some time.[7] Such a circuit is capable of performing in one balancing operation direct capacitance measurements while the center point (B) of the transformer ratio-arms winding is grounded. In our case, the "D" corner of the bridge consists of the metal covering of the cable core, which, as was mentioned above, is necessarily at the ground potential. Therefore, the "B" corner cannot be grounded. However, by connecting to this "B"-corner a shielding,[8] surrounding the "A-D" and "C-D" measuring arms, including cables and probes, the following results can be achieved:

(a) Admittances from the measuring electrodes to the "B"-shielding are not critical. These admittances appear across the transformer-arms and, as a result of a close magnetic coupling realizable between these arms, any loading effects across any one of them are symmetrically reflected at the "A" and "C" corners of the bridge, thus essentially not affecting its balance.

(b) Stray admittances from the "B" shielding to ground appear across the opposite corners of the bridge (detector diagonal). Therefore, they also have no essential effects on the circuit balance.

(c) As a result of the "B"-shielding, stray admittances-to-ground

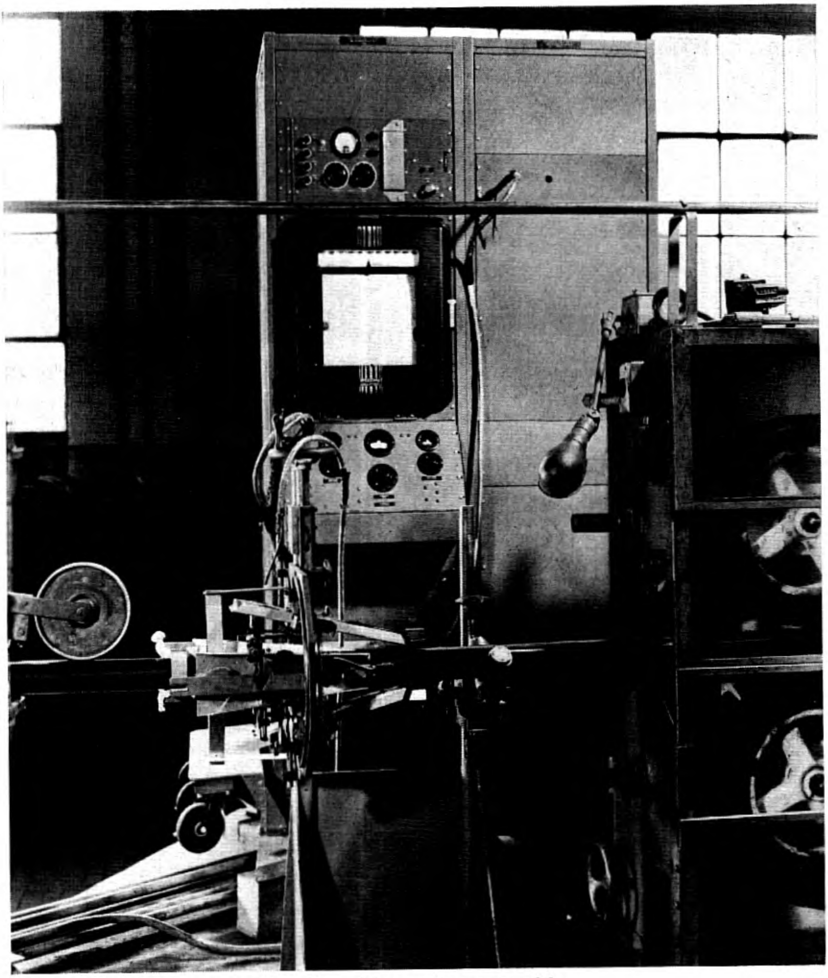

FIG. 3 — Measuring assembly.

from the measuring electrodes and from the connecting leads can be reduced to insignificant quantities.

As a result of the described circuit configuration, the bridge measures capacitance quantities equivalent to direct capacitance, in a particular case where one of two measuring electrodes is grounded. Realization of the grounded direct capacitance measurements is made possible by having within the measuring arrangement a three-electrode system in which stray admittances from the third (ungrounded) electrode to either of the measuring electrodes do not affect the fundamental balance condition of the bridge network.

By the arrangement described not only are the residual effective capacitances between the measuring electrodes and ground reduced to a desirable minimum (actually below one $\mu\mu$F, including calibrating capacitor and balancing networks), but also any adverse capacitance effects of the cables connecting the bridge to the measuring probes are practically eliminated, even though these cables are several feet long.

The calibrated grounded direct capacitance range of the bridge extends over 0.32 $\mu\mu$F in either direction off balance center position. Any unbalances within the $\pm$ 0.25 $\mu\mu$F range can be read in increments of 0.005 $\mu\mu$F per division on a recorder. Since covering such a limited capacitance range directly by an adjustable capacitor could present various practical difficulties, a network, dividing electrically the range of a 100 $\mu\mu$F differential capacitor by the ratio of 150 (approximately), has been applied. Using such a network facilitates calibration and adjustability and greatly reduces effects of the mechanical instability of the variable capacitor. (Similar networks are applied for capacitance and conductance residual balance controls.)

Stationary unbalances of the bridge network can be measured directly in a conventional manner by rebalancing the circuit with the calibrated capacitor. For unbalances rapidly varying in time, however, this null method could not be applied simply. Therefore, a proportional off-balance deflection method had to be used and various means to ascertain overall linearity between incremental capacitance unbalances and indicator deflections were provided, so that eventually variations in linearity no larger than 0.4 db over periods of several days and 0.2 db over several hours have been observed in the actual operating conditions.

Measurements with the bridge depend essentially on the calibrated capacitor. To avoid necessity for frequent and quite elaborate calibration checking (within a few one-thousandths of a $\mu\mu$F) of this capacitor in a laboratory, a set of supplementary, high stability auxiliary standards has been provided in the test set assembly. The capacitance values (1.05 $\mu\mu$F; 1.20 $\mu\mu$F; 1.35 $\mu\mu$F) of these capacitors are so chosen that differences between any pair of them can be compared directly with the calibrated capacitor in the bridge circuit. Reliability of this system is based on a reasonably high probability that change in the calibrated value of any single capacitor will be revealed in the process of mutually comparing all four capacitors. It was felt that this method of ascertaining calibration accuracy at the operating position was particularly recommended in the case of this circuit as its sensitivity to incremental capacitance unbalances is actually higher than the sensitivity of the usually available laboratory equipment.

The bridge network is supplied by a 10-kc ac power source.

2.2 Phase Sensitive Detector

For eccentricity measurements and control of the sheathing process it is essential to register the direction of incremental deviations from an arbitrary level. For this purpose a phase sensitive detector[9, 10] has been provided. Its simplified version is shown on Fig. 4.

By proper adjustment of the phase-shifter, the reactive component of the bridge unbalance signal can be oriented to be in-phase with the reference potential (b-a). In this condition, the capacitance unbalance sensitivity of the discriminator is at its maximum, and for a certain range of capacitance unbalances, linearity of the indicator may be assured. Also, when the above phase condition is fulfilled, the circuit is not sensitive to limited conductance unbalances (this fact also renders the circuit remarkably more stable than a similar circuit using a conventional null detector).

The dc output from the discriminator is fed through a balanced output stage (V2a and V2b), and an attenuator to a Leeds & Northrup zero-centered recorder. At the operating sensitivity level, each of the 100 divisions of the recorder scale corresponds to 0.005 $\mu\mu$F, or approximately to 0.001 inch of the incremental sheath thickness. The rôle of the attenuator is two-fold: it provides control of the over-all sensitivity of the measurements (in steps of 0.2 db), and it introduces more than 20 db attenuation into the dc output signal path. This loss is compensated by an added gain within the feedback-controlled ac amplifier (AC-A) preceding the phase discriminator. The net result of this "ac for dc gain-trading" is a considerable improvement of the over-all circuit stability since the range of random drifts, such as usually generated within the phase-discriminator and its direct-coupled output stage, are materially reduced.

2.3 Measuring Probes

As has been mentioned above, two arms of the bridge circuit consist of a pair of admittances between the grounded metal core of the cable (D corner) and the probes sliding on the surface of the plastic cable sheathing. These probes are connected to the "A" and "C" corners of the bridge, respectively, with two shielded flexible conductors (each

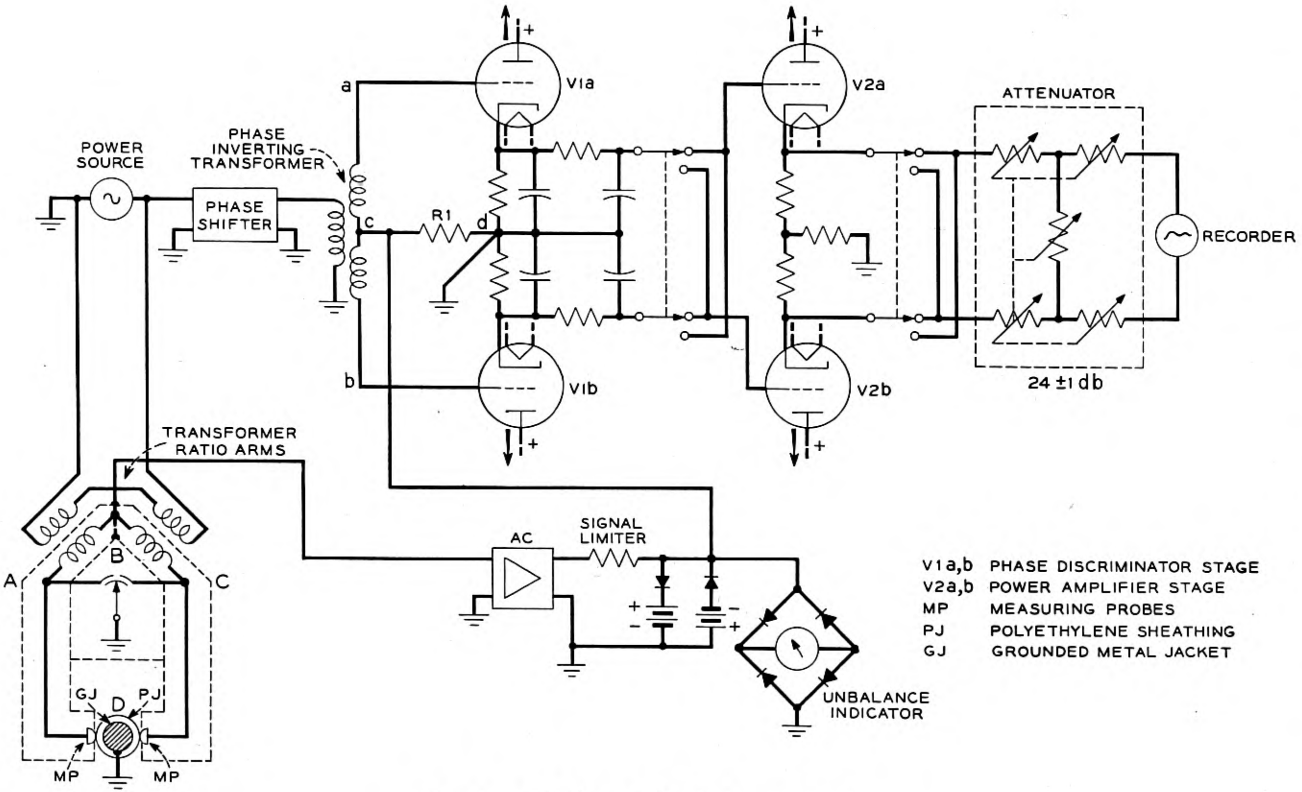

Fig. 4 — Bridge and discriminator circuit.

about 10 feet long) and are maintained mechanically in the testing position by the probe assembly (see Figs. 3 and 5(a)).

In the design of the probes and their assembly, various difficulties had to be overcome. The probes operate on cables subjected to some unavoidable swings and vibrations while moving with speeds up to 80 feet per minute. The capacitance from either of these probes to the metal cable core, in equivalent conditions, should match each other within approximately one-thousandth of a $\mu\mu$F. This capacitance should not be appreciably affected by limited displacements of the probes with respect to the cable plane of symmetry, such as may occur in actual operating conditions.

The first experiments with probes of a conventional design, having flat, or nearly flat, contact surfaces, were quite discouraging. The probe-to-core capacitances fluctuated to an intolerable degree as a result of even minute cable displacements.

Eventually, probes were developed which met all the requirements. Each of these probes is in the form of a cut-off segment of a toroid. The major axis of the cut-off elliptical plane is oriented in the direction essentially parallel to the cable axis, while the convex center part of the probe slides on the cable sheathing. This form of probe has the advantage, common with the spherical form, that the capacitance from the probe to the cable core varies but little as a result of displacements and changes of position caused by the cable motion. But the toroidal form has the following advantages over the spherical: first, for the same residual capacitance to the cylindrical cable core, the transverse dimensions of the former are smaller; and, second, the capacitance of the toroidal form with respect to a cylindrical cable core can be conveniently adjusted by the simple expedient of twisting the probe element in a plane parallel to the cable axis. (Adjustments with a precision exceeding one-thousandth of a $\mu\mu$F were actually performed).

The probe electrodes, surrounded (except for the contacting face) by the B-shielding, are mounted on mechanically balanced light aluminum arms [Figs. 5(a) and 5(b)]. There might be one, two, or four probes to an assembly, which can be turned over 360° around the cable axis. For eccentricity measurements two probes can be simultaneously used, having a spacing of 180° (for measurement of eccentricity across a diameter) or of 90° (for measurement of elipsoidal eccentricity). Also for eccentricity or direct thickness investigations and process settings one probe only may be used, with the other bridge measuring arm connected to an auxiliary standard.

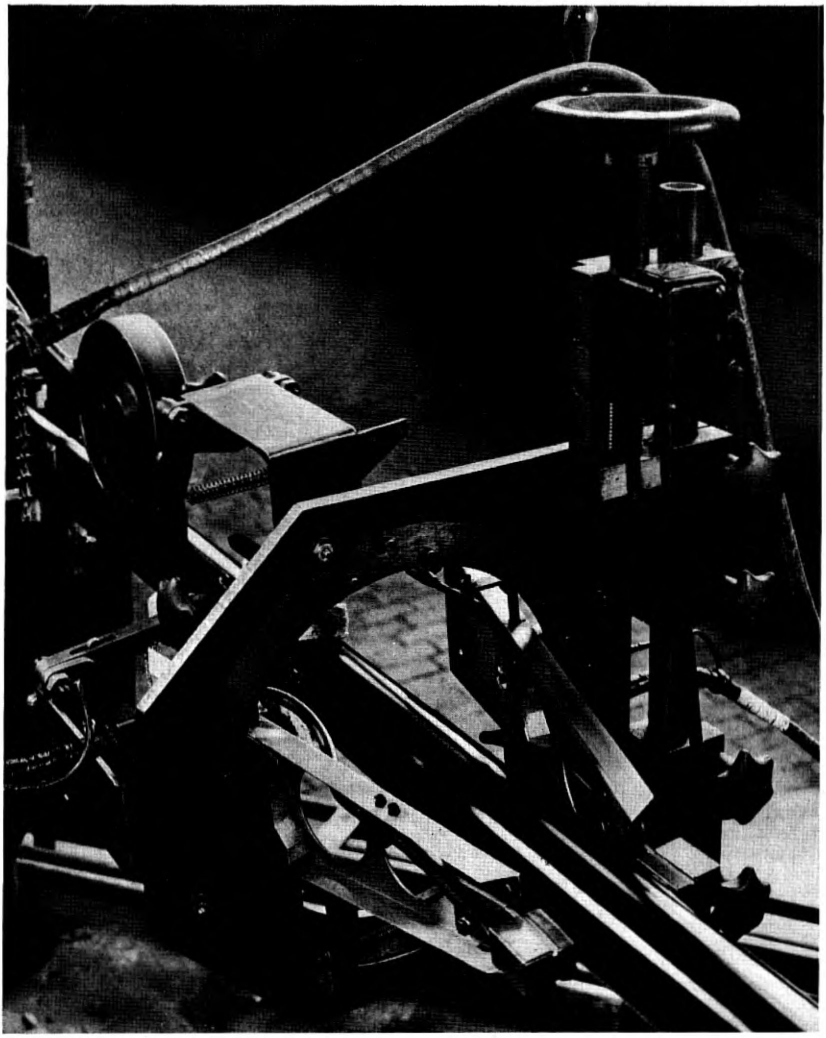

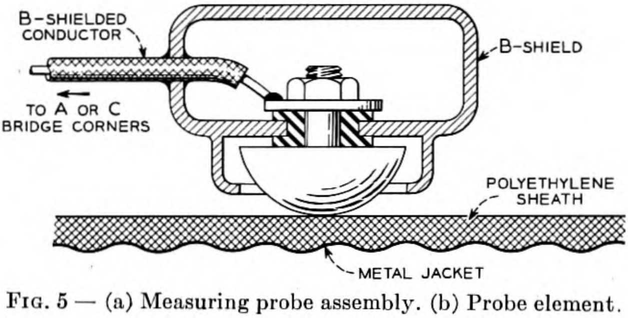

Fig. 5 — (a) Measuring probe assembly. (b) Probe element.

The average capacitance from the probe element to the grounded metal core varies from 1.1 to 1.3 μμF for cables measured.

3 EXPERIMENTAL RESULTS

3.1 Circuit Performance Under Stationary Conditions

Incremental capacitance sensitivity for grounded direct capacitance measurements, in normal operating conditions with the probes in contact with a cable sample: order of 0.001 μμF.

Circuit stability and repeatability for periods over one hour duration: ±0.003 μμF.

Overall linearity of the unbalance indications, as read on the recorder scale within the range of plus or minus 0.25 μμF off center-balance position: ± (3 per cent + 0.003 μμF).

Mechanical Stability: Moving or twisting of the connecting leads has no effect on balance stability. Swinging of the cable under measurement, even beyond the limits encountered in actual working conditions, produces barely noticeable effects on the balance indication.

Capacitance measurements on flat polyethylene samples: One of the measuring bridge arms was connected to the auxiliary standard of 1.20 μμF. The other arm was terminated by the probe in contact with a flat polyethylene sample placed on a grounded metal-plate. Thickness of samples at the point of contact was measured with a micrometer to the nearest 0.0005 inch. Capacitance unbalance readings were taken directly on the recorder scale to the nearest 0.005 μμF. In order to avoid noticeable "air-gap" and "surface" effects, which occur when stacking several samples, in no case were more than two flat samples in a stack measured. Under these conditions, repeatability of readings was within one recorder division (0.005 μμF), equivalent approximately to one-thousandth of an inch. In a typical case shown on Fig. 6, of 38 measurements taken in the thickness range from 0.052 inch to 0.168 inch, only three measurements were off from the averaging curve by more than 0.002 inch. (Further investigation disclosed that these three points, marked "Δ" on Fig. 6, were all associated with a particular sample.)

Capacitance measurements on stationary cable samples. In order to establish statistical reliability of measurements on actual cables by the described capacitance method, a number of cable samples were tested, varying in core diameter, average polyethylene sheathing thickness and mechanical construction.

A typical graph resulting from plotting capacitance increments versus micrometer measurements of a cable sample is shown on Fig. 7. Out of

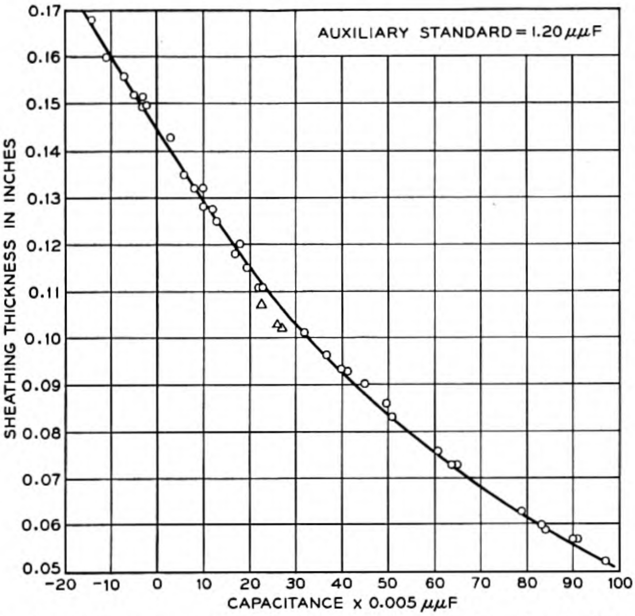

Fig. 6 — Capacitance versus thickness measurements of polyethylene plate samples.

25 measured points, 21 are contained within ±0.003 inch limit off an average curve. Three out of four remaining points (marked "Δ") were found to be from cable areas where application of the thermoplastic cement was excessive (explanation for an extraneous position of the fourth point had not been found by the time these measurements were concluded).

On the basis of over 800 measurements it has been estimated that at least 75 per cent of the plotted points are within the limits of ±0.003 inch deviation from an average capacitance versus thickness curve, for samples taken from the same cable. For samples taken from different cables these deviations ranged sometimes up to ±0.005 inch. A few points (less than 5 per cent) showed deviations larger than 0.01 inch. With some rare exceptions, these extreme deviations indicated larger than actual sheath thicknesses, and in most of the cases they were associated with areas where an excess of the flooding cement was present.

3.2 Incremental Capacitance Measurements on the Production Line

Experimental measurements on over 500 feet of cable length were performed on the production line with one of the bridge arms connected to the probe, and the other arm to an auxiliary standard of nominal value 1.20 μμF. The probe was placed on the surface of a cable moving with a speed of approximately 50 feet per minute. The line, along which the probe was sliding over the sheath, was marked for subsequent measuring purposes. At discrete intervals, the angular position of the probe with respect to the cable circumference was advanced by an angle of 90°. The unbalance signals were traced on the recorder chart with a standard sensitivity of 0.005 μμF per division. After completion of the cable run, the sheath was stripped and washed (to remove flooding compound) and micrometer measurements were taken along the probe route at points six inches apart. Subsequently these micrometer measurements were plotted in scales equivalent to the recorder chart.

A typical example of a measurement performed on a cable section approximately 250 feet long (a total of 500 measured points) is shown on Fig. 8. The upper curve represents a photograph of the recorder tracing. The lower curve was obtained by connecting point-to-point actual thickness readings and plotting them on the non-linear vertical scale following the capacitance versus thickness function (similar to that as shown on Fig. 6), to make both charts graphically equivalent.

From comparison of these graphs a few observations can be made. In fact, these curves represent fundamentally different methods of derivation. The recorder indications are continuous average readings based on an area having a definite width and a length of a few corrugation spaces

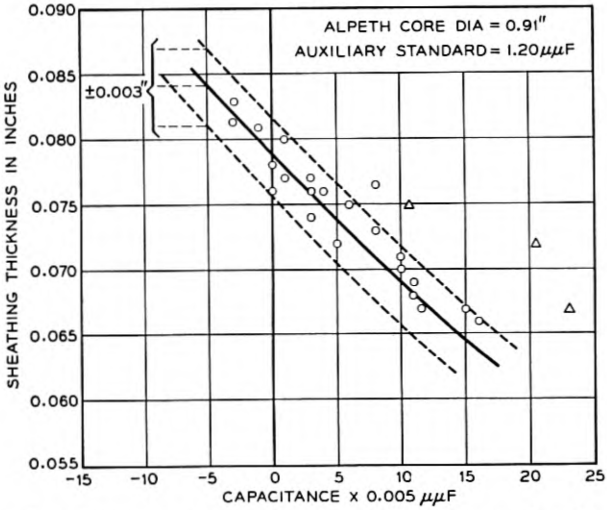

Fig. 7 — Capacitance versus thickness measurements of cable sheathing sample.

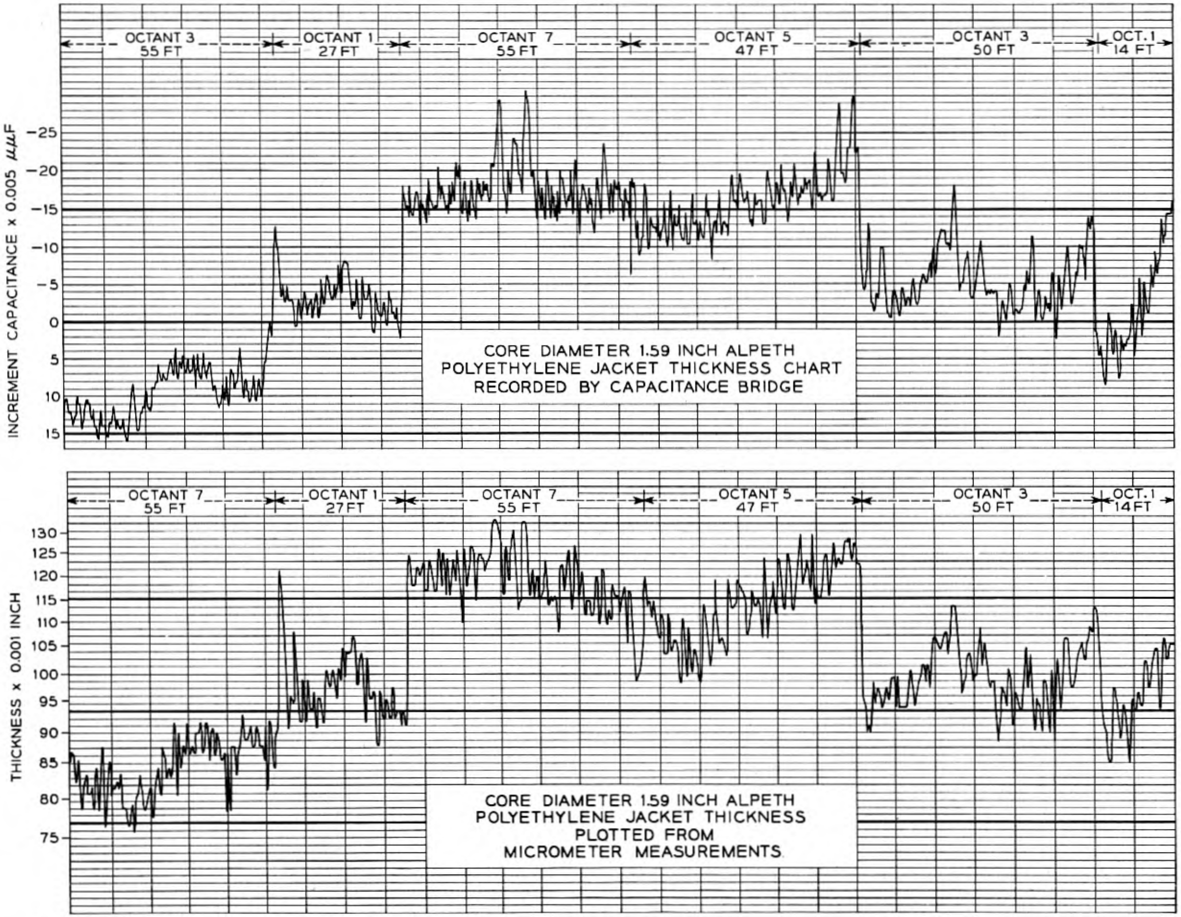

Fig. 8 — Comparison of a recorder graph taken on a production (upper curve) with the micrometer measure-

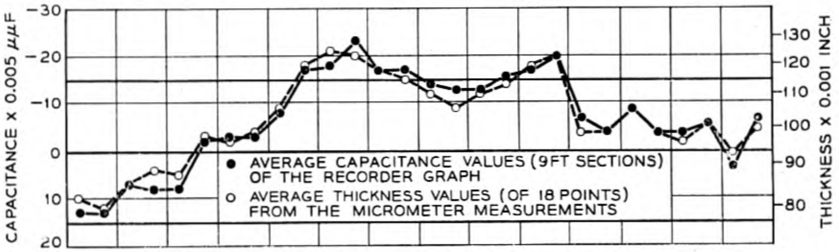

Fig. 9 — Comparison of average values from graphs of Fig. 8.

while the micrometer readings are point measurements taken at discrete distances at the bottom of the corrugation valleys in the polyethylene jacket. Despite this fact, the statistical character of both graphical results is closely similar (See Fig. 9). Assuming an average translation factor of 0.005 μμF per 0.001 inch, and discarding tracing errors, the agreement for incremental measurements between both methods can be estimated to be of the order of 0.003 inch. This accuracy is ample for any practical purpose of incremental thickness control of cable sheathing.

4 CONCLUSIONS

The method presented here for non-conductive sheath thickness measurements yields sufficient stability and translation reliability to be considered an improvement in the art. In particular, the incremental capacitance measurement accuracy of the order of 0.003 μμF (equivalent to less than 0.001 of an inch of incremental sheath thickness) is sufficiently high to disregard, in practical applications, the error of the test set itself. When measuring flat samples in stationary conditions accuracies of the order of 0.002″ for absolute thickness are obtainable.

Reliable differential measurements of cable sheathing on the production line can be realized on a statistical basis. Accuracies of the order of 0.003 of an inch for incremental sheath thickness (eccentricity) measurements were consistently attained in actual manufacturing conditions.

Extensive experience with the described measuring system indicates that it can also be applied for absolute sheath thickness measurements yielding desirable accuracies. This application, however, involves various manufacturing and process control problems extraneous to the measuring system per se. These aspects, therefore, are not discussed in the present paper.*

---

* Development of techniques for absolute sheath thickness measurements, using the described system, is being conducted by W. T. Eppler of Western Electric Co., Inc., Kearny, N. J.

5 ACKNOWLEDGMENTS

In carrying the development work described in this paper, I was helped considerably by fellow engineers as well as men at various supervisory levels of the Western Electric Company. In particular, I would like to thank R. I. Neel for assistance in gathering experimental data at the initial stages of this work, W. T. Eppler for his active part in confronting operation of the system with production line conditions, and D. T. Robb for encouragement and help given me during the development work and in preparation of this paper. A special credit for providing a mass of laborious statistical data concerning accuracy of the method in actual manufacturing conditions belongs to J. L. O'Toole of Bell Telephone Laboratories' group at Kearny.

BIBLIOGRAPHY

1. R. P. Ashbaugh, Alpeth Cable Sheath, Bell Lab. Record, **26,** pp. 441–444, Nov., 1948.
2. R. P. Ashbaugh, Stalpeth Cable Sheath, Bell Lab. Record, **29,** pp. 353–355, Aug., 1951.
3. F. W. Horn and R. B. Ramsey, Bell System Cable Sheath Problems and Designs, Trans. A.I.E.E., **70,** Pt. 1, pp. 1811–1816, 1951.
4. V. T. Wallder, Polyethylene for Wire and Cable, Elec. Eng., **71,** pp. 59–64, Jan. 1952.
5. U. S. Pat. 2,589,700, H. G. Johnstone (1952).
6. J. G. Ferguson, Classification of Bridge Methods of Measuring Impedances, B.S.T.J., **12,** pp. 452–468, Oct. 1933.
7. C. H. Young, Measuring Inter-Electrode Capacitances, Bell Lab. Record, **24,** pp. 433–438, Dec., 1946.
8. L. Hartshorn, *Radio-Frequency Measurements by Bridge and Resonance Methods*, Chapter III, John Wiley & Sons, New York, 1940.
9. A. C. Seletzky, Cross Potential of a 4-Arm Network, Elec. Eng., pp. 861–867, Dec., 1933.
10. U. S. Pat. 2,554,164, B. M. Wojciechowski (1951).

The Application of Designed Experiments to the Card Translator

By C. B. BROWN and M. E. TERRY

(Manuscript received October 27, 1953)

In the course of development of the card translator for use in the No. 4A toll crossbar system it was necessary to evaluate in detail the performance characteristics of all phases of the translator operation. One of the most important phases was that of the action of the translator cards. Since the action of these cards is controlled by the simultaneous influence of many independent variables a study of the card action was made using statistically designed experiments. This study made use of Graeco-Latin Square and Factorial Designs; herewith is presented a detailed description of their application to the problem. Also the method of analysis of the data and resulting conclusions are described in detail.

I. INTRODUCTION

In order to permit circuit designers to use the full capabilities of card translators[1] it has been necessary to conduct tests to determine (1) the time intervals required to drop the cards into reading positions and (2) the maximum number of cards which a translator can operate reliably. It was also desired to establish the maximum and minimum number of cards that could be operated efficiently in a card translator. Early estimates indicated a machine capacity of 1,000 cards but if a higher capacity could be demonstrated, a considerable cost saving in the 4A system would result. Since some differences in card drop time known to exist are due to card position and machine loading this study also was to consider whether or not any special loading instructions were necessary or desirable for field use of card translators. As the study commenced the Western Electric Company Installation Department requested information as to the need for leveling card translators on installation and it was felt that such information could readily be obtained in the course of this study. In investigating the effect of the many variables related to card drop time, a consideration was given to the possibility of the need for any design changes.

All previous tests of card drop time were made on Laboratories' built models of the translators and since tests made after any changes in model design have produced considerable differences in card drop times, it was felt that this study should be made on a sample of the Western Electric product. In addition, previous tests did not encompass all of the known variables over their extreme ranges.

For this study, a new translator was obtained from Western Electric. This translator was one of the regular production and was selected to be a representative unit. Fourteen hundred new 200A blanks were also obtained for use in this translator. Of these, 10 were coded for use as test cards to be observed. One hundred were coded to fill some bins with all coded cards. The balance of the 1,400 cards was left uncoded. This translator was connected to a simplified test set which would cycle the machine through the operation of the 10 coded test cards. Although this test set was simplified in its operation all of the pertinent time relationships involving card dropping were the same as are used in the standard translator circuits.

This study considered all of the variables, with the machine working in a normal cycle of operation as is currently used in the 4A system. These variables are:

1. *Bin* — Some differences in card dropping time had been observed depending on the bin in which the operating card was located.

2. *Position of Card Within Bin* — Earlier tests indicated that the location of the card within its bin made a considerable effect on dropping time.

3. *Code of Card* — Since both three and six digit cards will be used in the translator the code becomes a variable which may affect dropping time.

4. *Coded or Uncoded Cards in Working Bin* — Previous tests were made using only a few coded cards in the bin under observation and it was felt necessary to learn whether or not having all coded cards in a bin made any difference in the dropping time.

5. *Load in Working Bin* — This relates to the number of cards in the bin under observation. A range of from 15 to 105 cards per bin was used.

6. *Load in Machine* — This has to do with the possibility of any effect into the bin under observation from the cards in the other bins of the translator.

7. *Consistency of Data* — This has to do with repeated measurements to observe if the card dropping time is consistent over short periods of time.

8. *Balanced versus Unbalanced Loading* — Since the earlier installations will have machines that are less than full, it was necessary to learn whether or not any special loading considerations with regard to the position of the cards should be specified.

9. *Tilt* — (Machine) This has to do with the accuracy with which the translators should be leveled on installation.

10. *Life* — This variable considers the effect of repeated operations on cards and what effect, if any, these repeated operations have on the dropping time.

The tests on the first nine of the variables have been completed and a discussion of their effect on card dropping time is possible at this time. The tests on the tenth variable, life, are still in progress and have not as yet proceeded far enough to draw any conclusions. Therefore no consideration will be given to the effects of usage in this article. The effect of most of these variables was considered when the translator was operated both with and without the card support bars being used. The card support bars operate at the same time the card is dropped. Their operation is required for every card in the machine. Since their operation is slower than the free fall time of the operating card the card may ride down into the operated position on these bars and the observed drop time will simply be the operate time of the card support bars. This masks the effect of the various friction, gravity, and magnetic forces on the cards. Operating without the card support bars gives information on the free dropping time of the cards uninfluenced by these bars. Thus the masking effect of the card support bars can be removed and the tests made more sensitive to any physical effects which may be taking place at the cards themselves.

II. DESIGN OF EXPERIMENTS

Theory of Designed Experiments

In this problem it was required to evaluate the effect of each of the nine variables independently. It might have been convenient to take one variable at a time and vary it over its range while holding the associated variables at sets of constant values. Then a second independent variable could be chosen, the first variable placed in the group of associated variables, and a new set of runs made. This could be repeated until all the variables had been tested. This is obviously a logical, straightforward but unwieldy procedure.

A simpler procedure would be to vary the chosen variable over its range and at the same time let the associated variables vary over their assigned ranges in such a way that each associated variable is set an equal number of times at each of its possible values. This will cause any effect of the associated variable to be balanced out with respect to the chosen variable. That is, the average response of the system to the chosen variable can be evaluated because the contributions to the response from the associated variables are balanced out with respect to their variations.

Mathematically stated, the purpose of the latter procedure is to allow the independent evaluation of each variable over the observed range of its variation in the presence of the other variables.

Until recent years the standard experimental procedure was to make measurements for several values of one variable while taking great precautions to hold everything else constant. It was early recognized that such a technique was expensive but until the recent development of experimental designs in the field of Statistics there was no known alternative. In the class of designs treated here,[2] the set of numbers representing the respective sums of the measurements taken at the selected values of a given variable has the following properties:

1. If there are K discrete values of the given variables and N measurements made, then each sum contains N/K measurements.
2. If there are K_i values of the i^{th} remaining variable then N/K must be divisible by K_i, for all i.
3. Within each sum, for any given variable, each of the discrete values of the remaining variables must occur the same number of times.
4. The set of values of any of the remaining variables occurring in any sum for a given variable must be identical.

These properties imply that the logical subgroups for the discrete values of any given variable all contain the same number of measurements balanced with respect to the values of all the remaining variables.

The joint simultaneous evaluation of the specified variables can thus be made since it can be shown that the logical subgroups with respect to a given variable are independent of the logical subgroups of any other variable.

One of the difficulties in the use of this new technique is that both an engineer and statistician are required, and only rarely are both these professions found in an individual. It therefore becomes the responsibility of the engineer to outline the major and minor variables of the experiment, the description of the measuring devices to be employed, the accuracies desired in the results and his budget. The statistician must then propose the types of designs that will be appropriate together with their costs, methods of analysis, and salient features. The engineer and statistician must then select the design which best fits the situation.

The design selected for the first experiment of this study combined two basic design types, the Latin Square,[2] and the Factorial Design.[2] A brief discussion of each is in order at this point.

The Latin Square is peculiarly well suited to engineering research problems where many variables exist but the number of discrete levels necessary to describe the variation of any one is small, where relatively great precision is possible in measurements, and where the interaction of the variables is not a factor of the experiment. A key design[2] for a 5x5 Latin Square is as follows:

	Column				
Row	1	2	3	4	5
1	A	B	C	D	E
2	B	C	D	E	A
3	C	D	E	A	B
4	D	E	A	B	C
5	E	A	B	C	D

It will be observed that each Latin letter falls once and only once in every row and column. It is also true that if the logical subgroups A, B, C, D, E are considered, each of these sums has each row and column included once. If to the five row values, column values and letters, the five values of the first, second and third variables are associated respectively, the variables represented by Row, Column, and Letter can be evaluated independently of each other.

On the Key Latin Square, another properly chosen square represented by Greek Letters can be superimposed, and the five values of the fourth variable assigned to these letters at random:

	1	*2*	*3*	*4*	*5*
1	α	β	γ	δ	ϵ
2	γ	δ	ϵ	α	β
3	ϵ	α	β	γ	δ
4	β	γ	δ	ϵ	α
5	δ	ϵ	α	β	γ

The Graeco-Latin Square below is then produced:

	1	*2*	*3*	*4*	*5*
1	$A\alpha$	$B\beta$	$C\gamma$	$D\delta$	$E\epsilon$
2	$B\gamma$	$C\delta$	$D\epsilon$	$E\alpha$	$A\beta$
3	$C\epsilon$	$D\alpha$	$E\beta$	$A\gamma$	$B\delta$
4	$D\beta$	$E\gamma$	$A\delta$	$B\epsilon$	$C\alpha$
5	$E\delta$	$A\epsilon$	$B\alpha$	$C\beta$	$D\gamma$

Note that now each of the variables associated with Row, Column, Latin letter, Greek letter has the property that each element of the four categories contains one and only one element of the remaining three categories. For example, consider the five Latin-Greek letter combinations, or sample cells, containing ϵ:

Row 1 Col 5, *E*; Row 2 Col 3, *D*; Row 3 Col 1, C; Row 4 Col 4, B; Row 5 Col 2, *A*.

Then the sum of these five cells will contain the contribution of the 5 Rows, 5 Columns, and 5 Latin letters.

It should be noted that the rows and columns can be permuted without affecting the properties of the square. Indeed to protect against systematic effects which may be detrimental, it is usual to assign at random the row and column number, as well as the Latin and Greek letters to the values of variables represented by them. A notable exception to randomization occurs when time is a variable and those measurements made under essentially the same conditions within the same unit of time become the experimental unit. In the first experiment, all measurements made on one Run become the experimental unit with respect to time.

The Factorial Design serves a different purpose. In this discussion only two independent variables X, Z will be predicated but the extension to more variables follows directly. The XZ plane is the plane of the independent variables and we seek the point (X_0, Z_0) which gives a value of y (the dependent variable), $Y = \varphi(X, Z)$, which is optimum in some sense. That is, min Y, max Y may be sought, or the surface $f(X, Y, Z)$ shown to be a plane.

Generally only the region in the neighborhood of y (optimum) is of interest to the experimenter. Hence it is imperative (1) to bracket this point with respect to each independent variable and (2) to have a method of estimating y (optimum). If a factorial experiment has l_x different values of X and l_z different values of Z, then each replication of the experiment will require $l_x \cdot l_z$ units or points (X, Z). The first repetition of an experiment is called the second replication in the same way that the first overtone in music is called the second harmonic by engineers. Since the number of units available for test is usually limited, this places a practical ceiling on the magnitude of l_x and l_z. As a practical limit in general l should be 7 or less and the values 2, 3, or 4 are far more common. It is generally better to use the smaller values of l and repeat the experiment, than to conduct an experiment involving only a single replication. In addition to evaluating one variable averaged over the second, we are interested in evaluating the interaction of the variables on each other, when such interaction exists and is of interest. In a sense this interaction measures the departure of the system y, X, Z from linearity.

Once the basic designs have been selected and appropriately combined to fit most efficiently the requirements of the proposed experiment, and the values of the variables randomly assigned to the schematic layout, a detailed experimental layout must be drawn up. This layout must show concisely and clearly each experimental unit and the makeup of every basic element giving its assigned value of each variable. Explicit directions must be drawn up as to the order of selection of the elements of the unit. It is generally advisable for simplicity to assign the elements at random to the M possible consecutive order integers of the experimental unit.

Performance Study

The first seven variables listed in the Introduction are:

1. The Bin in use, *Bins*.
2. Position of Test card pair within the bin, *Position*.
3. The use of 3 digit or 6 digit Cards, *Code*.
4. Arrangement of Coded and Uncoded Cards, *Runs*.
5. Load of Bins containing Test Cards, *Load*.
6. Load of Bins not containing Test Cards, *Idlers*.
7. Order of repeated measurement, *Look*.

These constitute a system — that is, any or all can be varied at will and hence a design involving all of them simultaneously can be sought.

The test set can operate ten test cards; 5 with a 3 digit code and 5 with a 6 digit code. This immediately suggests 5 packages of two coded card pairs, each pair containing a 3 and a 6 digit card. Five pairs can also be handled neatly in 5 bins. The combination of the standard load of 85 cards, with two overloads and two underloads would give a fair evaluation of load criterion. Budget restrictions force the use of only a limited number of coded cards, with blanks used to fill out the experiment. Hence the type of card making up the load must be varied over the loads. It was further found that 5 positions of test cards within the bin covers the range of positions adequately.

The pairs of 3 and 6 digit cards now are associated with the Graeco-Latin Square design with Columns identified with Bins; Rows with distribution of coded cards; or Runs; Latin letters with Load; and Greek letters with position within the bin. Now if the position of the 3 digit card is randomly assigned in the pairs, the design absorbs the first five

TABLE I — DESIGN OF GRAECO-LATIN SQUARE EXPERIMENT

Each run made with the "x" bins loaded with 0, 50, 85 and 100 cards and consists of four operations (A, B, C, D) of each coded card.

BIN NO.

Photocell Mounting	I	II	III	X	IV	V		X	X	X	X	X	X	Lamp

POSITION IN BIN

		Bin I	Bin II	Bin III	Bin IV	Bin V
	Card →	1 6	2 7	3 8	4 9	5 10
Run #1	Pos. in Bin	*d g*	*f g*	*a b*	*a d*	*c e*
	No. of Coded Cards	2	41	50	15	2
	No. of Blank Cards	98	44	0	0	103
Run #2	Pos. in Bin	*c e*	*d g*	*f g*	*a b*	*a d*
	No. of Coded Cards	85	9	15	2	2
	No. of Blank Cards	0	41	0	103	98
Run #3	Pos. in Bin	*f g*	*a b*	*a d*	*c e*	*d g*
	No. of Coded Cards	2	100	2	2	7
	No. of Blank Cards	103	0	83	48	8
Run #4	Pos. in Bin	*a d*	*c e*	*d g*	*f g*	*a b*
	No. of Coded Cards	2	2	105	2	2
	No. of Blank Cards	48	13	0	98	83
Run #5	Pos. in Bin	*a b*	*a d*	*c e*	*d g*	*f g*
	No. of Coded Cards	2	2	2	85	22
	No. of Blank Cards	13	103	98	0	28

variables of the list. The layout of these variables in the Graeco-Latin Square design is given in Table I.

The remaining two variables are functions of different portions of the machine. The rows of the Square, involving distribution of coded and uncoded cards, represent distinct machine set-ups, and hence if for every set-up the load of the seven not-measured bins is varied, and for every variation in this load 4 observations of the 5 pairs are taken, consideration of the remaining two variables is achieved. Yet the tedious part of handling the test cards has been reduced to a very reasonable amount. These last two variables, considered by themselves, form a factorial design and where 4 loads and 4 measurements per load are used, 16 measurements being taken for each machine set-up. Similarly any of the other five variables considered pairwise with one of the latter two forms another factorial design. This resulting complex overall pattern is shown in Table I.

TABLE II — TRANSLATOR TILT TEST — DESIGN OF EXPERIMENT

TEST CARDS LOCATION

Bin	I	II	III		IV	V
Cards.	6, 1	2, 7	8, 3		4, 9	10, 5

POSITION OF TEST CARDS IN BINS

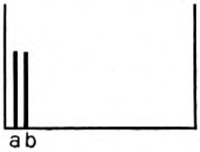

Total number of cards in each bin: 100
Bin # I contains all coded cards.

	Description of Tilt
Tilt #0	Lamp end lower than photocell end by 1/16″ in 3 feet. Translator resting on table at all four points. North Lamp end higher than South Lamp end by 1/16″ in 22″. North Photocell end higher than South Photocell end by 1/16″ in 22″
Tilt #1	Lamp end higher than photocell end by 9/16″ in 3″ ft. Lamp end supports blocked up 1/4″ North Lamp end higher than South Lamp end by 1/8″ in 22″ North Photocell end higher than South Photocell end by 1/8″ in 22″
Tilt #2	Lamp end higher than photocell end by 15/16″ in 3 ft. Lamp end supports blocked up 1/2″ North Lamp end higher than South Lamp end by 3/16″ in 22″ North Photocell end higher than South Photocell end by 3/16″ in 22″
Tilt #3	Lamp end higher than photocell end by 1 1/8″ in 3 ft. Lamp end supports blocked up 5/8″ North Lamp end higher than South Lamp end by 3/16″ in 22″ North Photocell end higher than Souh Photocell end by 3/16″ in 22″

Tilt Study

Routine field practice for the installation of a card translator calls for leveling the table before positioning of the translator. After a translator was placed it had been found that the level was not maintained, and the question of final level requirements was raised. Accordingly the test machine was run at 0 in., 5/8 in., 1 in., and 1 3/16 in. tilt, Table II. Two test cards were placed in each of five bins. Since the two end card positions on the low side of each bin were suspected as being critical, the two test cards were placed in these positions in the five bins. The experiment is shown schematically below:

	Bins				
	I	II	III	IV	V
Tilt 0	a_6b_1	a_2b_7	a_8b_3	a_4b_9	$a_{10}b_5$
1	a_6b_1	a_2b_7	a_8b_3	a_4b_9	$a_{10}b_5$
2	a_6b_1	a_2b_7	a_8b_3	a_4b_9	$a_{10}b_5$
3	a_6b_1	a_2b_7	a_8b_3	a_4b_9	$a_{10}b_5$

where a is the end position, b is the next-but-end position, and the subscripts identify the actual card number. Considering any bin, the two card positions and the four values of tilt may be considered as a factorial design. Similarly, the five bins combine with the four values of tilt as a factorial design.

Balanced Loading

At the onset of general usage many translators will not be fully loaded. It was desirable to investigate the effects of various patterns of loading at three representative low loads of 200, 400 and 600 cards respectively. Four logical patterns were studied (see Tables III and IV) all of which are shown below for a load of approximately 400 cards. (Similar patterns follow with loads of 200 and 600 cards.):

Bin	1	2	3	4	5	6	7	8	9	10	11	12
W	x	x	x	x								
X	x	x					x	x				
Y	x	x									x	x
Z	0	0	0	0	0	0	0	0	0	0	0	0

x = 100 cards, 0 = 1/12 load (approximately)

The ten test cards were all placed in Bin One.

This experiment involves only two factors; the four loading patterns,

Table III — Loading Patterns in Partially Loaded Card Translator — Balanced versus Unbalanced Load Test

Treatments	Load	No. of Cards in Bins											
		Bin I	Bin II	Bin III	Bin IV	Bin V	Bin VI	Bin VII	Bin VIII	Bin IX	Bin X	Bin XI	Bin XII
W	600	100	100	100	100	100	100	—	—	—	—	—	—
	400	100	100	100	100	—	—	—	—	—	—	—	—
	200	100	100	—	—	—	—	—	—	—	—	—	—
X	600	100	100	100	—	—	—	100	100	100	—	—	—
	400	100	100	—	—	—	—	100	100	—	—	—	—
	200	100	—	—	—	—	—	100	—	—	—	—	—
Y	600	100	100	100	—	—	—	—	—	—	100	100	100
	400	100	100	—	—	—	—	—	—	—	—	100	100
	200	100	—	—	—	—	—	—	—	—	—	—	100
Z	600	50	50	50	50	50	50	50	50	50	50	50	50
	400	33	33	33	33	33	33	33	33	33	33	33	37
	200	16	16	16	16	16	16	16	16	16	16	16	24

Note: All cards in Bin I are coded, see Table IV. Cards in Bins II–XII not coded.

and the three loads of cards. A suitable design is the factorial design with one factor, the loading pattern, at four levels (W, X, Y, Z) and the other factor, the loads of cards at three levels (200, 400, 600) with ten test card measurements taken at each of the twelve points.

III. DATA

The data on card dropping time were obtained by means of shadowgrams of the light output from two of the light channels of the translator. Each shadowgram comprised the operation of the 10 test cards in sequence. Samples of these shadowgrams are shown on Figs. 1 and 2. For the purpose of these experiments the card dropping time is defined as the time from the release of the pull-up magnets until the full closure of the light channels of the translator exclusive of any card rebound. The data from the various experiments were tabulated and are given in Tables V to XI, inclusive.

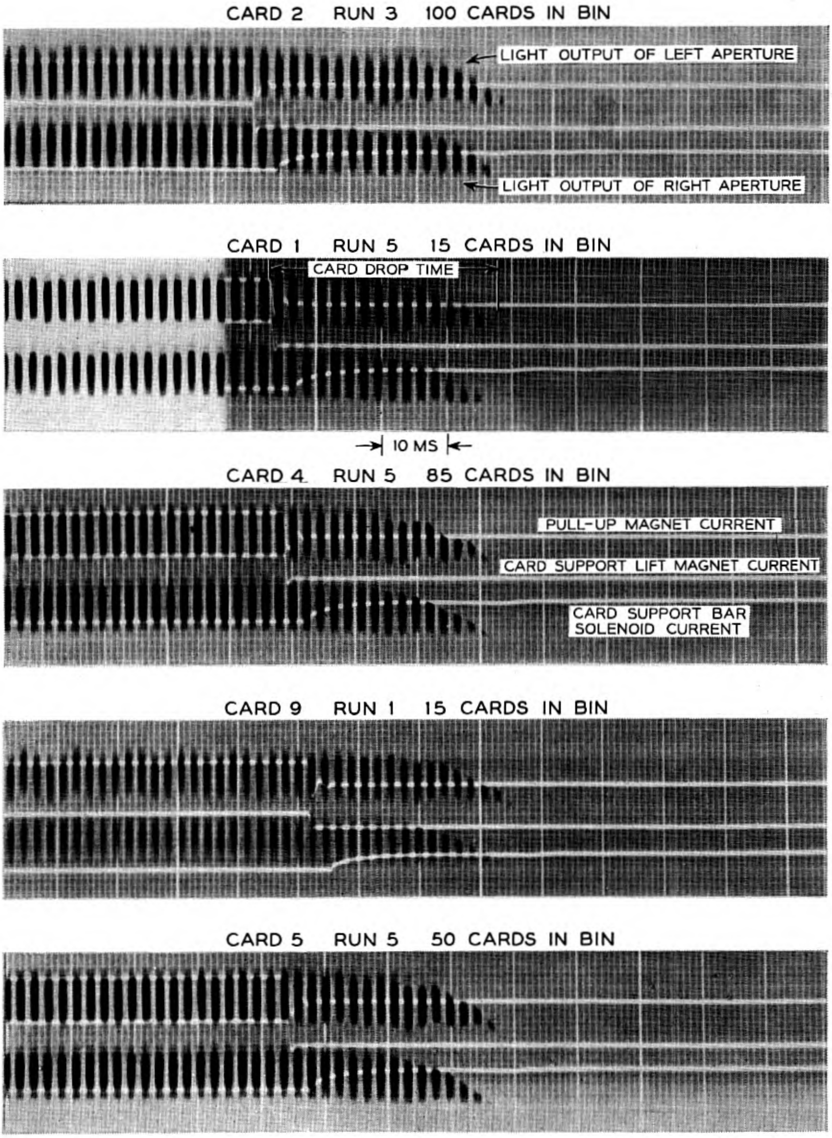

FIG. 1 — Card motion shadowgraphs, card support bars working.

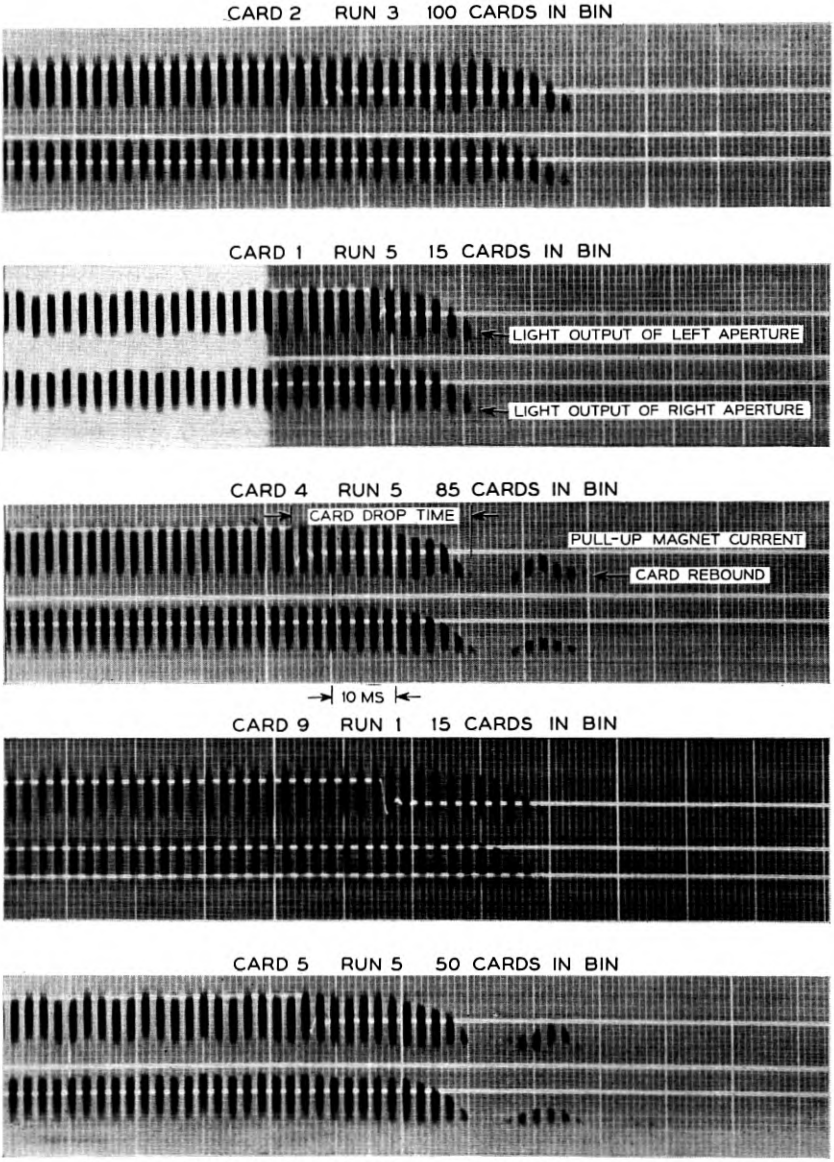

Fig. 2 — Card motion shadowgraphs, card support bars out.

TABLE IV — CARD TRANSLATOR BALANCED VERSUS UNBALANCED LOAD TEST — ARRANGEMENT OF CODED CARDS IN BIN I

No. of Cards	Arrangement of Coded Cards in Bin I																
	← Left end of Bin																Right end of Bin →
100	#1	#2	*10*	#3	*15*	#4	*15*	#5	*10*	#6	*15*	#7	*15*	#8	*10*	#9	#10
50	#1	#2	*5*	#3	6	#4	*7*	#5	*4*	#6	*7*	#7	6	#8	*5*	#9	#10
33	#1	#2	*3*	#3	*4*	#4	*3*	#5	*3*	#6	*3*	#7	*4*	#8	*3*	#9	#10
16	#1	#2	*1*	#3	*1*	#4	*1*	#5	*0*	#6	*1*	#7	*1*	#8	*1*	#9	#10

Note: Numbers preceded by # represent the test cards. Numbers in italics represent quantity of non-test coded cards placed between two consecutive test cards.

IV. ANALYSIS OF THE DATA

After checking the raw data for recording errors, they were analyzed and reduced in three distinct steps as follows:

1. Using the techniques of the analysis of variance* each variable and each measured interaction of several variables was tested as a possible assignable cause of variation.

2. Using the components of variance analysis† on those variables and combinations of variables found to be assignable causes in Step 1 their contributions to the overall variation was estimated, and

3. After tabulating the arithmetic mean for each value of the variables an upper and lower bounds were determined which estimates the allowance, or probable range of means, for similar experiments and operations on card translators having the same residual σ. The technique used was proposed and formulated by J. W. Tukey.[3]

The analysis of variance tables were reduced to the summary in Tables XII and XIII for the seven variable studied.

Proceeding to the tabulation of the means and the calculation of the allowances appropriate to these means, the data was reduced as in Table XIV. The magnitude of the several effects can now be noted. The effect of Idler load is quite meaningful — as the load on the machine is increased to the normal load of 85 we see a decrease in mean dropping time from 36.5 to 34.4 milliseconds. Also the slight increase for the overload of 100 is not significant statistically or engineeringwise. At first glance the results of Idler loads of 0, 50, 85 and 100 might seem to be inconsistent with those of Operating Loads of 15, 50, 85, 100, and 105. The mean dropping time of the Load of 15 (say) is the average dropping time of

---

* See Appendix for Discussion and References 2, 4 and 5.

† See Appendix for Discussion and Reference 6.

TABLE V — CARD DROP TIME IN MILLISECONDS — NO CARDS IN X BINS — CARD SUPPORT BARS OPERATING

		Bin ♯ I		Bin ♯ II		Bin ♯ III		Bin ♯ IV		Bin ♯ V	
Card ♯ →		1	6	2	7	3	8	4	9	5	10
Run ♯1	A	36	38	36	35.5	37	36.5	37	37.5	37.5	40
	B	36.5	38	36.25	37.5	35	37	36.5	37	37	39.5
	C	35.25	37.5	35	36	37	36	36	36	37.5	39
	D	35.5	38	37	36.25	36.5	36.5	36.5	36.5	37	39
	$\bar{X}$	35.8	37.8	36.06	36.32	36.37	36.5	36.5	36.75	37.25	39.37
	R	1.25	0.5	2.0	2.0	2.0	1.0	1.0	1.5	0.5	1.0
Run ♯2	A	34	35	34	33.5	34	34	36	35	37	39
	B	33.5	34.5	34	34	34	34	35.5	33.5	37	38
	C	34	34.5	33.5	34	35	34	36	35	36.5	38.5
	D	35.5	33	33.5	34.5	34.5	34	35.5	34.5	36.5	38
Run ♯2	X	34.25	34.25	33.75	34.0	34.37	34	35.75	34.5	36.75	38.37
	R	2.0	2.0	0.5	1.0	1.0	0	0.5	1.5	0.5	1.0
Run ♯3	A	36.5	37.5	38	36.5	37	37	37	38	37.5	39.5
	B	36	37	36.5	35	36	37	36.5	36.5	38	39
	C	36	36.5	37.5	35.5	36	35	37	36.5	38	39.5
	D	35.5	36.5	37.5	35.5	36	35.5	35.5	36.5	37.5	38.5
Run ♯3	X	36.0	36.37	37.37	35.62	36.25	36.12	36.5	36.37	37.75	39.12
	R	1.0	1.0	1.5	1.5	1.0	2.0	1.5	1.5	0.5	1.0
Run ♯4	A	37	37	35.5	37	36	37	37	37.5	38	38.5
	B	36	37.5	35.5	36	36	37	36.5	37.5	38	38.5
	C	36	37.5	35	36	35.5	36	37	38	37.5	38
	D	35.5	37	36	36	36	36	37	37.5	37.5	37.5
Run ♯4	X	36.12	37.25	35.50	36.25	35.87	36.50	36.87	37.62	37.75	38.12
	R	1.5	0.5	1.0	1.0	0.5	1.0	0.5	0.5	0.5	1.0
Run ♯5	A	36	36	37	37	35.5	36.5	37	36.5	38.5	38.5
	B	36	35.5	37	37	37	37	37	37	38.5	39
	C	36	36	36	36	36	36.5	37	37	38.5	39
	D	36	35	35.5	36	35	36	36.5	37	38	39
	$\bar{X}$	36	35.62	36.37	36.50	35.87	36.50	36.87	36.87	38.37	38.87
	R	0	0.5	1.5	1.0	2.0	1.0	0.5	0.5	0.5	0.5

Cards in Bins loaded with 15 cards in the presence of 4 bins loaded with 50, 85, 100, and 105 cards respectively and of bins loaded as a group with 0, 50, 85, or 100 cards. On the other hand the mean dropping time attributable to an Idler load of 50 cards (say) is the average of all dropping cards in the operating bins when the 7 Idler loads are 50 cards. Hence the statistical conclusion that the effect of loads in the operating bins is slight over the range of loads of 15 to 105 cards is reached, and that the

TABLE VI — CARD DROP TIME IN MILLISECONDS — 50 CARDS IN X BINS — CARD SUPPORT BARS OPERATING

		Bin #I		Bin #II		Bin #III		Bin #IV		Bin #V	
	Card # →	1	6	2	7	3	8	4	9	5	10
Run #1	A	35	36	34	35	34.5	35	33	34	33.5	35
	B	33.5	35	34.25	34	33	33.5	32.5	33.5	33.5	34.5
	C	34.5	34	32.5	34	32.5	32.5	32	33.25	32	34
	D	34	32.5	32	34	33.5	33.5	33.25	32.5	33	33
	$\overline{X}$	34.25	34.37	33.19	34.25	33.37	33.62	32.69	33.31	33	34.12
	R	1.5	3.5	2.25	1.0	2.0	2.5	0.75	1.5	1.5	2.0
Run #2	A	35.5	35	34	34	32.5	35	35	35.5	35	35.5
	B	35.5	35.5	34	33.5	34.5	34.5	35.5	35	35.5	35
	C	35	35	34	35	34.5	34	36	35	34.5	34
	D	34	35	34	34	32.5	34	35.5	34	35	35
	$\overline{X}$	35.0	35.1	34	34.1	33.5	34.4	35.5	34.9	35.0	34.9
	R	1.5	0.5	0	1.5	2.0	1.0	1.0	1.0	1.0	1.5
Run #3	A	35	35	37.5	34	34.5	34.5	34	34	34	34.5
	B	36	36.5	37	36	35.5	35.5	34	34.5	34.5	36
	C	35	35.5	39	35	35.5	35	34.5	34.5	34.5	35.5
	D	35.5	37	39	35	35.5	34	34.5	34.5	34.5	35.5
	$\overline{X}$	35.37	36.0	38.12	35.0	35.25	34.75	34.25	33.37	33.37	35.37
	R	1.0	2.0	2.0	2.0	1.0	1.5	0.5	0.5	0.5	1.5
Run #4	A	37	37	35.5	35.5	36.5	35	35	35.5	36	37
	B	36.5	37	36	36.5	36.5	36	35.5	35.5	36	37
	C	37.5	38	35.5	36	36.5	35	36	35.5	35.5	36.5
	D	37	37.5	35.5	37.5	36.5	36.5	36.5	36	37	38
	$\overline{X}$	37	37.37	35.62	36.37	36.50	35.62	35.75	35.62	36.12	37.12
	R	1.0	1.0	0.5	2.0	0	1.5	1.5	0.5	1.5	1.5
Run #5	A	36	36	35.5	36	35.5	36	34.5	36	34.5	35
	B	35	35.5	35	36	35	35	34	34	34.5	35
	C	35.5	36	35.5	35.5	34.5	35	34	35	34.5	35
	D	36	35.5	35	35.5	34.5	35.5	34	34.5	34	34.5
	$\overline{X}$	35.62	35.75	35.25	35.75	34.87	35.37	34.12	34.87	34.37	34.89
	R	1.0	0.5	0.5	0.5	1.0	1.0	0.5	1.5	0.5	0.5

improvement in dropping time caused by increasing the overall load is generally consistent over the test bin loads.

One last estimate must be made — that of the σ' for a single measurement where*

$$\sigma'^2 = \sigma_s'^2 + \sigma_e'^2 + \sum \sigma'^2_{\text{assignable causes}} .$$

---

* See Appendix for meaning of symbols and discussion.

TABLE VII — CARD DROP TIME IN MILLISECONDS — 85 CARDS IN X BINS — CARD SUPPORT BARS OPERATING

		Bin #I		Bin #II		Bin #III		Bin #IV		Bin #V	
Card # →		1	6	2	7	3	8	4	9	5	10
Run #1	A	34.5	34	32.5	32.5	33	34	32.5	34	33.5	33.5
	B	35	34	34	32	32	34	33	33	33.5	33
	C	33	34	33.5	33.5	32.5	33.5	33	33.5	33.5	33
	D	35	34	34	32	33	33.5	33	33.5	32.5	34
	$\overline{X}$	34.4	34	33.5	32.5	32.9	33.7	32.9	33.5	33.25	33.4
	R	2.0	0	1.5	1.0	1.5	0.5	0.5	1.0	1.0	1.0
Run #2	A	33	34.5	32	34	33	34.5	34	33.25	33.5	33.5
	B	32	35	34.5	34.5	32	33.5	35	34	33.75	34
	C	34	35	33.5	34.5	33	34.5	35.5	35	35	35
	D	34	34	34	34.5	33.5	35	35	34.5	35	33
	$\overline{X}$	33.25	34.62	33.5	33.4	32.9	34.4	34.19	33.55	34.31	33.79
	R	2.0	1.0	2.5	0.5	1.5	1.5	1.5	1.75	1.5	1.5
Run #3	A	35	35	36.5	32.5	34	34.5	33	34.5	34	34
	B	35	35.5	37	34.5	35.5	34	33	34.5	34.5	34
	C	35	34.5	36	34.5	35.5	33	33.5	34	34.75	35
	D	35	35	37	34.5	35	34.5	34	34.5	34	34.5
	$\overline{X}$	35	35	36.62	34	35	34	33.37	34.37	34.31	34.37
	R	0	1.0	1.0	2.0	1.5	1.5	1.0	0.5	0.75	1.0
Run #4	A	37	37	36.5	36.5	36	36	35	35	36.5	36.5
	B	38	37.5	37	36	36.5	37	36	35	36.5	36.5
	C	37	37	37	35	36	36.5	35.5	35	36	36.5
	D	36	35	36	36	36	36	35	35.5	35.5	36.5
	$\overline{X}$	37	36.62	36.62	35.87	36.12	38.37	35.37	35.12	36.12	36.25
	R	2.0	2.5	1.0	1.5	0.5	1.0	1.0	0.5	1.0	1.0
Run #5	A	35	35	34	35	33.5	34	34	33.5	33.5	34
	B	34.5	34.5	34	34	34	33.5	34	33	33.5	33.5
	C	34	34.5	34	34.5	34	33.5	33	32.5	33	34
	D	34	35	33.5	34.5	33.5	34	33	33.5	32.5	34
	$\overline{X}$	34.37	34.75	33.87	34.50	33.75	33.75	33.50	33.12	33.12	33.87
	R	1.0	0.5	0.5	1.0	0.5	0.5	1.0	1.0	1.0	0.5

If the assignable causes contributing to this estimate are not removed then this σ' is the well known parameter for control charts.

The variable Runs may be an experimental variable which will not occur in operational usage since coded cards only will be used in the machines. The joint effect, however, of this variable with all the others is slight, for

$$\sigma'_{w0} = 2.68 \text{ ms without Runs, and}$$
$$\sigma'_{w} = 2.98 \text{ ms with Runs included.}$$

TABLE VIII — CARD DROP TIME IN MILLISECONDS — 100 CARDS IN X BINS — CARD SUPPORT BARS OPERATING

		Bin #I		Bin #II		Bin #III		Bin #IV		Bin #V	
	Card # →	1	6	2	7	3	8	4	9	5	10
Run #1	A	34	35.5	34.5	35	34	35	33.5	34	34.5	35
	B	34	35	35	35	34.5	34.5	34.5	35	35	34
	C	34	35	34	33	35	34.5	33.5	33.5	35	34
	D	35	33.5	34.5	35	35	34	35	33.5	33.5	34.5
	$\bar{X}$	34.75	34.75	34.5	34.5	34.62	34.5	34.12	34.0	34.5	34.37
	R	1.0	2.0	1.0	2.0	1.0	1.0	1.5	1.5	1.5	1.0
Run #2	A	34	36.5	34.5	35.5	33.5	34.5	35.5	36	35	35.5
	B	34.5	35	35	35.5	33.5	35	35.5	36.5	35.5	34
	C	34	34	34	33	34	33.5	34	34	33.5	33
	D	33	32	33.5	32.5	33.5	33.5	34.5	34	33	34
	$\bar{X}$	33.9	34.37	34.25	34.12	33.6	34.12	34.9	35.12	34.25	34.12
	R	1.5	4.5	1.5	3.0	0.5	1.5	1.5	2.5	2.5	2.5
Run #3	A	34.5	34.5	36.5	33.5	35.5	33.5	34	34	34	34
	B	35	34.5	38	34	34.5	33.5	34	33.5	33	34
	C	35	35.5	38.5	34	34.5	34.5	33.5	33.5	34.5	34.5
	D	34.5	35	39.5	34	35	35	34	34	34	35
	$\bar{X}$	34.75	34.87	38.12	33.87	34.87	34.12	38.87	33.75	33.87	34.37
	R	0.5	1.0	3.0	0.5	1.0	1.5	0.5	0.5	1.5	1.0
Run #4	A	37	37	35.5	35.5	36	35.5	35	35.5	36	37
	B	36	36	37	36	36	35.5	35	35.5	37	36
	C	36	36.5	35.5	37	36	36.5	35	36.5	36	37
	D	37	36	35.5	35.5	35.5	35.5	34.5	35	36	37
	$\bar{X}$	36.5	36.37	35.87	36	35.87	35.75	34.87	35.62	36.25	36.75
	R	1.0	1.0	1.5	1.5	0.5	1.0	0.5	1.5	1.0	1.0
Run #5	A	33.5	34	33.5	33.5	33.5	33.5	32.5	33.5	33.5	33
	B	33.5	33	34	34.5	34	34	32.5	33.5	33.5	33.5
	C	35	35	34	34.5	33.5	34	33	33.5	33.5	33
	D	34	34	34.5	33.5	34	34	33	33	33	34
	$\bar{X}$	34	34	34	34	33.75	33.87	32.75	33.37	33.37	33.37
	R	1.5	2.0	1.0	1.0	0.5	0.5	0.5	0.5	0.5	1.0

The overall estimate of Mean dropping time was found to be 35.1 ms. We can predict therefore that the dropping time of a card chosen at random from a normal translator at the beginning of its life will be 35.1 $\pm 3\sigma'$ (without Runs) or between 27 and 43 ms from the well known 3σ limits.

When the analysis of variance with the card support bars out is examined it is found that the sampling error σ_s^2 remains stationary but

TABLE IX — CARD DROP TIME IN MILLISECONDS — 85 CARDS IN X BINS — CARD SUPPORT BARS OUT

		Bin #I		Bin #II		Bin #III		Bin #IV		Bin #V	
Card # →		1	6	2	7	3	8	4	9	5	10
Run #1	A	23.5	27	26.5	26	28	28	25	24	26	26.5
	B	23.5	28	25.5	26.5	28	27	25	24	25.5	26
	C	23	27	26	26	29	28	25	23	26	26.5
	D	24	26.5	26.5	27	29.5	27.5	25	24	26.25	26
	$\bar{X}$	23.5	27.1	26.1	26.4	28.6	27.6	25	23.75	25.94	26.25
	R	1.0	1.5	1.0	1.0	1.5	1.0	0	1.0	1.75	0.5
Run #2	A	24.5	26.5	26	23.5	22	21.5	34	31.5	32	27.5
	B	25	27	25	22	21.5	22	33.5	31	32	28
	C	24	27.5	26.5	23.5	21.5	23	34.5	31.5	31.5	27.5
	D	24.5	26.5	25	22.5	22	22	34	31.5	33	28
	$\bar{X}$	24.5	26.9	25.6	22.9	21.75	22.12	34.0	31.4	34.6	27.75
	R	1.0	1.0	1.5	1.5	0.5	1.5	1.0	0.5	1.5	0.5
Run #3	A	28	29	37.5	28	34	28	29	28.5	24	22
	B	27	29	37	28	33	28	30	28	24	21
	C	28.5	30	37.5	29	32.5	28	28.5	28	23.5	20
	D	28	30	38	29	33	28	29	27.5	24	21
	$\bar{X}$	27.87	29.5	37.5	28.5	33.12	28	34.12	28	23.87	21
	R	1.5	1.0	1.0	1.0	1.5	0	1.5	1.0	0.5	2.0
Run #4	A	16.5	23.5	22	24	28	29	28.5	32	34	34
	B	17	23	22	23.5	28	29	28	33	33.5	33.5
	C	17	23	21	22	28	29	27.5	32	30.5	33
	D	17	23.5	22	22.5	28	29	28	31	33.5	36.5
	$\bar{X}$	16.87	23.25	21.75	23	28	29	28	32	32.87	33.50
	R	0.5	0.5	1.0	2.0	0	0	1.0	2.0	3.5	3.0
Run #5	A	16.5	17	25	25.5	28.5	28	29	30	26	25.5
	B	16	17	26	26.5	28	28	29	29.5	26	25
	C	18	17.5	25	25.5	28	28	28.5	29.5	26	25
	D	16.5	17.5	25	25.5	28	28	29	30	26	25.5
	$\bar{X}$	16.75	17.25	25.25	25.75	28.12	28	28.87	29.75	26	25.25
	R	2.0	0.5	1.0	1.0	0.5	0	0.5	0.5	0	0.5

the experimental error is inflated tenfold. The assignable causes found in the previous experiment are found here, where measured, with one exception — the interaction of Codes on Positions. The estimate of σ' for a single reading with the card support bars out now becomes

$$\sigma' = 8.56 \text{ ms.}$$

Since the overall estimate of mean dropping time with the card support

TABLE X — TILT STUDY DATA — CARD DROP TIME IN MILLISECONDS — CARD SUPPORT BARS OUT

		Bin #I		Bin #II		Bin #III		Bin #IV		Bin #V	
	Card # →	6	1	2	7	8	3	4	9	10	5
Tilt #0	A	21.5	19.5	29	26	30.5	27.5	32.5	32.5	31	29
	B	21.5	19.5	31	25.5	32	28.5	31.5	35	30.5	28.5
	C	21.5	19.0	29.5	26	31	28	31	34	30.5	29
	D	21.5	19.0	29.5	25.5	30.5	28.5	32	34.5	30.5	29.5
	Σ	86	77	119	103	124	112.5	127	136	122.5	116
	$\bar{X}$	21.5	19.25	29.75	29.75	31	28.13	31.75	34	30.63	29
	R	0	0.5	2	0.5	1.5	1	1.5	2.5	0.5	1.0
Tilt #1	A	27.5	21	38	28	38.5	28.5	44	28.5	47	31.5
	B	25	21	37	27.5	38	29	44	29	49	31
	C	25.5	20.5	38	27.5	43	28.5	47	29.5	46	31
	D	25.5	21.5	39	28	42.5	28	43.5	29	46.5	32
	Σ	103.5	84	152	111	162	114	178.5	116	188.5	125.5
	$\bar{X}$	25.88	21	38	27.75	40.5	28.5	44.63	29	47.13	31.38
	R	2.5	1	2	0.5	5	1	3.5	1	3	1
Tilt #2	A	29	23.5	62.5	32	67	32	73	32.5	92.5	38.5
	B	38.5	23	57.5	31	63.5	31.5	72.5	32	62.5	37
	C	33	22.5	58.5	30.5	59	31	68.5	32	66	37.5
	D	33	23	59	31.5	59.5	31.5	75	33	67.5	37.5
	Σ	132.5	92	237.5	125	249	126	289	129.5	288.5	150.5
	$\bar{X}$	33.13	23	59.38	31.25	62.25	31.5	72.25	32.38	72.13	37.63
	R	9.5	1	5	1.5	8	1	6.5	1	30	1.5
Tilt #3	A	58	23	68	33.5	109.5	34	Did not oqerate	34.5	69.5	39.5
	B	41.5	23.5	69	33	95	33.5		34.5	91.5	38.5
	C	34	23	80	33.5	77	34		36	87	39.5
	D	31.5	24.5	80.5	34	86.5	35		36	95	39
	Σ	165	94	297.5	134	368	136.5		141	343	156.5
	$\bar{X}$	41.25	23.5	74.38	33.5	92	34.13		35.25	85.75	39.13
	R	26.5	1.5	12.5	1	32.5	1.5		1.5	25.5	1

bars out was 26.7 ms, it can be predicted that the limits for the dropping time for a single card at the onset of life of a card translator will be 1 and 52 ms. It is to be noted that while the upper limits in both these estimates are reasonably close, the lower limits are quite different. This is to be expected since the card support bars may delay the dropping of a card and thus restrict operations that might be fast.

Tilt Study Analysis

A fundamental assumption underlying any comparison is that the compared elements have been measured with the same precision. Scru-

TABLE XI — BALANCED VERSUS UNBALANCED LOAD — CARD DROP TIME IN MILLISECONDS

Treatment	Load	Look	Test Card									
			1	2	3	4	5	6	7	8	9	10
W	600	A	24.5	21.5	25	21.5	28.5	28	26.5	29	30.5	31.5
		B	24	22	26	27.5	28	27.5	27	29	29.5	31
	400	A	24	22	27.5	29.5	28.5	29	28	30	29	34
		B	24	22.5	28	28	28	28	28	30	30.5	33
	200	A	26	24.5	29.5	30	30	29	29	30	31	33
		B	25.5	24	30	30	30	29.5	28.5	29.5	30	33.5
X	600	A	25	22.5	27	28	27.5	28	27.5	26	30	32
		B	24.5	23	27	28.5	28	28	28	29	30	33
	400	A	25	24.5	29	29	29.5	28	28.5	30	30	33
		B	25	24.5	29.5	29	29.5	28	28	29	30.5	33
	200	A	28	26	29.5	29	29	28.5	27.5	27.5	24.5	26
		B	27	25.5	29.5	29	28.5	27.5	26.5	28	25	26
Y	600	A	24.5	22.5	27	28	28.5	28.5	28	29	30	34
		B	24	23	27	28	28	28	28.5	30	29	32.5
	400	A	25.5	23	29	29.5	29	28	28.5	28.5	28.5	33.5
		B	25	24	29.5	29.5	29	28	28.5	29	29.5	33
	200	A	27.5	26.5	28.5	28.5	27.5	27.5	26	27	25	26
		B	27.5	26	28.5	28.5	27.5	28	26	28	23.5	26
Z	600	A	21	20	23	23.5	25	25.5	26	25.5	26	26.5
		B	21.5	20	23	24.5	25.5	26.5	25.5	25.5	26.5	26.5
	400	A	18	18.5	23	26.5	27	25	24.5	24.5	24.5	27
		B	19	18.5	22	26	27	25.5	25.5	25	25	26
	200	A	19.5	18.5	20	21.5	22	22	22	22	22	22
		B	18	18.5	21	22	22.5	22	21.5	21.5	22.5	22

tiny of the data cast grave doubt on this assumption and each card position was analyzed separately as shown below.

CARD POSITION A

ANALYSIS OF VARIANCE

Source	Degrees of Freedom	Sum of Squares	Mean Square
Bins	4	8947	2238
Tilt	3	25653	8551
(Expt. Error) Bins x Tilt*	11	2882	262
Total	18	37482	

* One observation was lost, and Fisher's Missing Plot Technique was used (5).

CARD POSITION B

ANALYSIS OF VARIANCE

Source	Degrees of Freedom	Sum of Squares	Mean Square
Bins	4	1515	379
Tilt	3	492	164
(Expt. Error) Bins x Tilt	12	168	14
Total	19	2175	

The two estimates of experimental error being 262 and 14 $\overline{\text{ms}}^2$ respectively against a previous estimate (Table XIII) on 24 degrees of freedom of 10.9 $\overline{\text{ms}}^2$, we must accept Position A as coming from a different universe with respect to position B and the previous seven varible experiments. Further Position B on the same evidence has been measured with equivalent precision when compared to the previous study with the card support bars out.

The individual dropping times of Position B cards over the experiment range from 19 to 39.5 ms., well within the predicted dropping times. The mean dropping times for each tilt of card Position B are as follows:

Tilt	0	1	2	3
	27.2 ms	27.5 ms	31.2 ms	33.8 ms

By contrast the mean dropping times for Position A are:

Tilt	0	1	2	3
	28.9 ms	39.2 ms	59.9 ms	73.6 ms

with a range of 21 ms to 109.5 ms on the fourth tilt.

TABLE XII — ANALYSIS OF VARIANCE — SUMMARY — WITH CARD SUPPORT BARS

Source	Degrees of Freedom	Sum of Squares	Mean Squares	Mean Squares is an Estimate of*
1. Looks	3	5.65	1.88 N.S.(+)	
2. Code	1	4.46	4.46†	$\sigma_e^2 + 20(\sigma_{cb}^2 + \sigma_{cp}^2 + \sigma_{cl}^2 + \sigma_{cr}^2) + 100\sigma_c^2$
3. Idlers	3	520.48	173.49‡	$\sigma_e^2 + 10(\sigma_{ib}^2 + \sigma_{ir}^2) + 25\sigma_{ci}^2 + 50\sigma_i^2$
4. Bins	4	53.43	13.35‡	$\sigma_e^2 + 10\sigma_{ib}^2 + 20\sigma_{cb}^2 + 40\sigma_b^2$
5. Runs	4	359.64	89.91‡	$\sigma_e^2 + 20\sigma_{cr}^2 + 10\sigma_{ir}^2 + 40\sigma_r^2$
6. Loads	4	26.07	6.52‡	$\sigma_e^2 + 20\sigma_{cl}^2 + 40\sigma_l^2$
7. Positions	4	35.96	8.99‡	$\sigma_e^2 + 20\sigma_{cp}^2 + 40\sigma_p^2$
8. Codes x Idlers	3	6.58	2.19 N.S.	$\sigma_e^2 + 25\sigma_{ci}^2$
9. Codes x Bins	4	20.34	5.08‡	$\sigma_e^2 + 20\sigma_{cb}^2$
10. Codes x Runs	4	16.78	4.20‡	$\sigma_e^2 + 20\sigma_{cr}^2$
11. Codes x Loads	4	11.99	3.00†	$\sigma_e^2 + 20\sigma_{cl}^2$
12. Codes x Positions	4	25.47	6.37‡	$\sigma_e^2 + 20\sigma_{cp}^2$
13. Idlers x Bins	12	162.52	13.54‡	$\sigma_e^2 + 10\sigma_{ib}^2$
14. Idlers x Runs	12	203.99	17.00‡	$\sigma_e^2 + 10\sigma_{ir}^2$
15. Experimental Error	136	128.76	0.95	σ_e^2
16. Sampling Error	597	224.88	0.39	σ_s^2
	799	1807.00		

* See Appendix and Reference.
† Significant at 5 per cent level.
‡ Significant at 1 per cent level.
(+) N.S. = Not significant at 5 per cent level.

Clearly, Card Position A gives rise to an undesirable assignable cause which must be dealt with, and Card Position B while showing tilt as an assignable cause has a dropping time at the extreme tilt well within the allowable tolerances (see Conclusions).

Balanced Loading

The two main variables were total machine load in numbers of cards (Number) and distribution of cards over bins (Loading). The results of this experiment were so clear that little analysis was necessary. Although the mean dropping time of cards distributed uniformly over the twelve bins was statistically significantly different from the means of cards from the three nonuniform distributions the magnitude of the difference 4.8 ms was not sufficiently large to cause concern. Furthermore a decrease in mean dropping time was observed as the total load in-

TABLE XIII — ANALYSIS OF VARIANCE — SUMMARY — WITHOUT CARD SUPPORT BARS

Source	Degrees of Freedom	Sum of Squares	Mean Square	Mean Square is an Estimate of*
1. Looks	3	1.72	0.57 N.S.	
2. Code	1	3.43	3.43 N.S.	$\sigma_e^2 + 5\sigma_{cb}^2 + 5\sigma_{cr}^2 + 5\sigma_{cl}^2 + 5\sigma_{cp}^2 + 25\sigma_c^2$
3. Idlers				
4. Bins	4	714.69	178.67‡	$\sigma_e^2 + 5\sigma_{cb}^2 + 10\sigma_b^2$
5. Runs	4	275.61	68.90‡	$\sigma_e^2 + 5\sigma_{cr}^2 + 10\sigma_r^2$
6. Loads	4	1695.52	423.88‡	$\sigma_e^2 + 5\sigma_{cl}^2 + 10\sigma_l^2$
7. Position	4	239.42	59.86‡	$\sigma_e^2 + 5\sigma_{cp}^2 + 10\sigma_p^2$
8. Codes x Idlers				
9. Codes x Bins	4	205.39	51.35‡	$\sigma_e^2 + 5\sigma_{cb}^2$
10. Codes x Runs				
11. Codes x Loads				
12. Codes x Positions	4	144.09	36.02‡	$\sigma_e^2 + 5\sigma_{cp}^2$
13. Idlers x Bins				
14. Idlers x Runs				
15. Experimental Error	24	261.28	10.89	σ_e^2
16. Sampling Error	147	48.86	0.33	σ_s^2
	199	3689.01		

* See Appendix and Reference 6.
† Significant at 5% level.
‡ Significant at 1% level.
(+) N.S. = Not significant at 5% level.

creased regardless of the distribution of cards, confirming a conclusion from the first experiment.

V. CONCLUSIONS OF OVER-ALL STUDY

When considered in the normal cycle of translator operation with the card support bars functioning, the range of card drop times was observed to be from 32 to 40 ms with a mean of 35.1 ms. Based on the results obtained in this study it is predicted the dropping time of a card chosen at random in a new translator will be between 27 and 43 ms. This includes all the known variables except the life of the cards. The test on this variable is continuing and all conclusions reached in this report may be modified somewhat by the results of this life study which will be reported at a later date. The relative effect of the several variables is tabulated in Table XIV. The only two variables found to have any sig-

TABLE XIV — MEAN CARD DROPPING TIMES WITH ALLOWANCES SUMMARIZED WITH REGARD TO VARIABLES

Variable	No. Readings in each Mean	Mean Dropping Time Milliseconds					Range of Means	Allowance
Looks		A	B	C	D			
C.S. In	200	35.2	35.2	35.1	34.9		Negligible	
C.S. Out	50	26.8	26.6	26.6	26.8		Negligible	
Codes		3 digit	6 digit					
C.S. In	400	35.0	35.2				Negligible	
C.S. Out	100	26.6	26.8				Negligible	
Idlers		0 cards	50	85	100			
C.S. In	200	36.5	35.0	34.4	34.6		2.1	±0.4
Graeco-Latin Square								
Runs		1	2	3	4	5		
C.S. In	160	34.6	34.5	35.3	36.3	34.8	1.8	±0.5
C.S. Out	40	26.0	26.9	28.6	26.9	25.1	3.5	±3.0
Bins		I	II	III	IV	V		
C.S. In	160	35.3	35.1	34.8	34.8	35.5	0.7	±0.5
C.S. Out	40	23.4	26.3	27.4	29.0	27.5	5.6	±3.0
Positions		ab	ad	ce	dg	fg		
C.S. In	160	35.5	35.3	34.9	35.0	34.9	0.6	±0.5
C.S. Out	40	28.9	26.1	26.2	26.0	26.5	2.9	±3.0
Loads		15 cards	50	85	100	105		
C.S. In	160	34.9	35.0	35.0	35.4	35.3	0.5	±0.5
C.S. Out	40	21.6	25.3	29.1	29.3	28.3	7.7	±3.0
Graeco-Latin Sq. & Codes		Min			Max.			
C.S. In	16	33.6			37.6		4.0	±2.5
C.S. Out	4	16.8			37.5		20.7	±8.4
Idlers & Bins								
C.S. In	40	34.0			38.2		4.2	±1.6
Idlers & Runs								
C.S. In	40	33.4			36.8		3.4	±1.6

nificance when operating in the normal manner were the load in the machine and the number of coded and uncoded cards in the working bin. In a lightly loaded machine the flux from the pull-up magnet is concentrated in the few cards and therefore in each card there is a greater amount of flux to decay before the card is free to drop. When a bin is loaded with all coded cards the dropping time may be increased because the cards are slightly deformed by the coding process which in turn increases the effective thickness of the cards thus reducing their freedom in the bin.

Although these two variables were significantly large they still are included in the range of dropping times mentioned above and are not of sufficient magnitude to warrant special consideration in loading the

TABLE XV — CARD TRANSLATOR — SUMMARY OF DATA ON CARD REBOUND — CARD SUPPORT BARS OUT

No. of operations	200	100%
No. of operations with no rebound	83	41.5%
No. of operations with one rebound	116	58%
No. of operations with two rebounds	1	0.5%
Maximum duration of one rebound	17 ms.	
Minimum duration of one rebound	6 ms.	
Duration of two rebounds	28 ms.	
Maximum magnitude of a rebound	⅓ reopening	

Bins	No. of Operations	No. of Operations with Rebound	Per cent of Operations with Rebound
1	40	28	70
2	40	24	60
3	40	25	62.5
4	40	15	37.5
5	40	25	62.5

Load	No. of Operations	No. of Operations with Rebound	Per cent of Operations with Rebound
15	40	15	37.5
50	40	28	70
85	40	23	57.5
100	40	23	57.5
105	40	28	70

translators. The effect of the load in the machine was further investigated in the balanced vs. unbalanced loading test and although it was found that a balanced load produced a faster drop time, the amount of improvement obtained by balancing the load is not enough to warrant special loading instructions.

The card dropping time as observed with the card support bars out of the circuit ranged from 16 to 40 ms with a mean of 26.7 ms and the predicted total range is from 1 to 52 ms. Although the minimum dropping time is considerably less with the card support bars out, the translator cannot be operated satisfactorily in this manner. The cards rebound on a majority of the operations; in fact, 58 per cent of the operations with the card support bars out had measurable rebound. When operated in the normal manner no card rebound was observed at any time. A summary of the amount of card rebound observed is given in Table XV.

As a result of this study, it was concluded that the requirement for minimum 65 cards per bin should be removed and that the field be permitted to place as few cards as they find convenient in any bin. A second conclusion was that the maximum number of cards per bin be set at 100. This will allow a total of 1,200 cards per machine, an increase of

20 per cent in the capacity of a translator over the design objectives. The requirement that an uncoded card be placed next to each separator should remain until the life test which is currently in progress is concluded. These uncoded cards are to be included in the 100 cards per bin figure. A preliminary analysis of the data indicates that it is probably necessary that this requirement be retained for field use.

With regard to the leveling of the machine, it was found that if the translator table is leveled consistent with the normal practice of the installation department no further leveling is necessary when the translator is installed on the table provided an uncoded card is next to each separator. When only cards that were at least one removed from the separator were considered it was found that the Translator could be tilted 1 inch in 3 feet without seriously affecting the card drop time.

Considering the ranges of the several variables considered and the results of the analysis of the data, it appears that there is no major unknown variable having an effect on the card dropping time. It is also believed that the results of the work on this machine can be considered representative of the results that will be obtained on another new production model translator.

APPENDICES

I. ANALYSIS OF VARIANCE

The general theory of the analysis of variance has been formulated and discussed at length by several authors.[2, 4, 5] Basically it reduces to the concept that in any set of data obtained from a statistically designed experiment the total sum of squares of deviations from the mean can be partitioned into orthogonal components, and that under certain restrictions the distribution of each component falls into known patterns. Hence data taken from designed experiments can be examined for conformance to the known pattern, and a lack of conformity indicates an assignable cause of variation. Further, the distribution of the ratio of mean square deviations under specified conditions has been tabulated as the table of the F ratio. It has also been shown that when a treatment variable is not a parameter or assignable cause of variation in the experiment, the partitioned component for that variable must contain only residual variation. Thus, the analysis of variance tests the hypothesis that the treatment means for a given variable are all equal (i.e., the variable is not a parameter) by testing the ratio of the mean squares of mean deviations for the variable to the residual mean square, i.e., the F ratio. When this F ratio is larger than the critical value at the α^{th} level, the variable is said to be *significant at the* α^{th} *level*. That is, let us assume a null hypothesis that the variable in question is not a parameter or assignable cause, and select a critical value, F^*, such that the probability of observing an F ratio greater than F^* (when the null hypothesis is true) is small (say 0.01). Then if the F ratio is computed from our experimental observations and the null hypothesis rejected when this ratio is larger than F^*, on the average incorrect decisions will be made not more than 1 per cent of the time. This method of evaluation is not trivial and in complex situations reference should be made to the literature or to experts.

II. COMPONENTS OF VARIANCE

A basic difference between the estimation of the Components of Variance[6] and the Analysis of Variance above is the concept of the underlying model or law. The Analysis of Variance tests the hypothesis that the treatment variable is not a parameter. In the estimation of Components of Variance we assume that the observed effect of the several values of a given variable is a random sample from a normal population of effects from these values. If u_{iv} is the true effect of the i^{th} value of the v^{th} variable, then the component of variance due to the v^{th} variable, σ_v^2, is found from

$$\sigma_u^2 = \frac{\sum_{i=1}^{k} \mu_{iv}^2 - \frac{\left(\sum_{i=1} \mu_{iv}\right)^2}{k}}{k - 1}.$$

If $u_{1v} = u_{2v} = \cdots = u_{kv}$, then $\sigma_v^2 = 0$, and the mean square for variable v contains only residual variation. If the variable v is a parameter, $\sigma_v^2 > 0$; and the mean square for variable v contains $\sigma_e^2 + M\sigma_v^2$ (M measurements being made at each of the k levels of the variable). It is desirable to estimate the component of variability of each variable, in order to be able to estimate the variability of a measurement which is affected by these variables. That is, if there are ρ variables whose components of variance are σ_i^2, $i = 1, \cdots, \rho$ respectively and if the measurement, x, is influenced by all of these variables, then

$$\sigma_x^2 = \sum_{i=1}^{\rho} \sigma_i^2 + \sigma_e^2, \qquad \text{and} \qquad \sigma_x = \sqrt{\sum_{i=1}^{\rho} \sigma_i^2 + \sigma_{\text{error}}^2}\,.$$

Referring to Table XII and using the column of mean squares, we make the following inferences:

Since the ratio of mean square for variables to mean square for experimental error is "significantly" large for all the main variables, excluding Looks, these main variables are considered to be assignable causes of variation. It is also evident that the three digit cards are causing an effect quite different from that of the six digit cards when the four variables, Bins, Runs, Loads, and Position are allowed to vary. Since the ratio of the mean square of variables of lines 9, 10, 11, and 12 of Table XII to mean square for experimental error is significantly large, in the same way lines 13 and 14 show that the effect of Idler loads is not independent of the Bins and Runs effects. Statistically then, we have isolated many significant effects, but note that our experimental error, σ^2, for samples of four readings is 0.95 $\overline{\mathrm{ms}}^2$ and σ is then 0.975 ms.

If we compare two means $\bar{x}_1$ and $\bar{x}_2$ each based on N samples of four observations each we will detect as significant, differences as small as

$$3\sigma_{\bar{x}_1-\bar{x}_2} = \frac{3\sqrt{2\sigma}}{\sqrt{N}} \; \frac{4.095}{\sqrt{N}} \, .$$

When N is large we will, therefore detect as significant, differences which may be of no interest engineering-wise. Thus not only is the significance of the effects of interest but also the magnitude of the effect.

When the component of variance attributable to each of the significant effects is estimated only four are so large as to be of interest to the engineer. The four variables are Idlers, Runs, interaction of Idlers on Runs and Bins. The estimates of the components of variance, $\hat{\sigma}^2_{\text{effect}}$, are obtained by equating the linear combinations of the components of variance shown in the right hand column of Table XII to the mean squares which estimate them and solving.

The component estimates are:

	σ^2	
Idlers	3.	$\overline{ms}^2$
Runs	1.55	$\overline{ms}^2$
Idlers x Runs	1.60	$\overline{ms}^2$
Idlers x Runs	1.26	$\overline{ms}^2$

III. SOURCES AND MEASURES OF ERROR

In any experiment a decision must be made as to the number of experimental units to be measured and the number of repeated measurements to be made on each unit.[7] It is important to note that measurements made on the same unit and a measurement made on each of several units give rise to two distinct sources of variation, and that both of these should be estimated. Consider making n measurements on each of k units, where the k units are a random sample of units belonging to a normal universe with mean u and variance σ_b^2. Further a set of measurements on the i^{th} unit is a random sample of measurements from a normal universe of measurements with mean u_i and variance σ_w^2. Clearly, if the set contains only one measurement ($n = 1$), we cannot estimate σ_w^2, and if there is only one unit ($k = 1$) we cannot estimate σ_b^2. When both $n, k > 1$ we can estimate simultaneously both σ_b^2 and σ_w^2. Let Xij be the j^{th} measurement on the i^{th} unit,

$$j = 1, \cdots, n; i = 1, \ldots, k.$$

and $\bar{X}_i$ be the mean of the i^{th} unit,

$\bar{\bar{X}}$ be the mean of all the units.

We can estimate σ_w^2 directly by computing

$$\sigma_w^2 = \frac{\sum_{i=1}^{k} \sum_{j=1}^{n} (X_{ij} - \bar{X}_i)^2}{k(n - 1)}, \qquad \text{but}$$

σ_b^2 can only be estimated indirectly by first estimating $\sigma_w^2 + n\sigma_b^2$ from

$$\frac{n \sum (\bar{X}_i - \bar{\bar{X}})^2}{k - 1}$$

Then the estimate of σ_b^2 is

$$\frac{1}{n}\left(\frac{n \sum_{i=1}^{k} \frac{(\bar{X}_i - \bar{\bar{X}})^2}{k - 1}}{k - 1} - \frac{\sum_{i=1}^{k} \sum_{j=1}^{n} (X_{ij} - \bar{X}_i)^2}{(n - 1)k}\right).$$

Since $\sigma_{\bar{x}}^2 = \frac{1}{k}(\sigma_b^2 + \frac{\sigma_w^2}{n})$, it is clear that if σ_b^2 is large relative to σ_w^2, then $\bar{X}$, for fixed $M = nk$, will have greater precision if k is large and n is small. The estimate of σ_w^2 is called the sampling variance or sampling attributable to repeated measurements. The estimate of σ_b^2 is called the component of variance due to experimental variation free of sampling error. For a given experiment the estimate of $\sigma_w^2 + n\sigma_b^2$ is called the experimental error term and measures the precision of measurement of a unit. In the experiment $\sigma_w^2 = \sigma'^2_s$, and $\sigma_b^2 = \sigma'^2_e$.

BIBLIOGRAPHY

1. L. N. Hampton and J. B. Newsom, The Card Translator for Nationwide Dialing, B.S.T.J., **32,** pp. 1037–1098, Sept., 1953.
2. W. G. Cochran and G. M. Cox, "Experimental Designs", J. Wiley and Sons, New Yor,, 1950.
3. J. W. Tukey, "Comparing Individual Means in the Analysis of Variance", Biometrics, Vol. 5, No. 2, 1949.
4. W. J. Dixon and F. J. Massey, "Introduction to Statistical Analysis", McGraw Hill, New York, 1951.
5. R. A. Fisher, "Design of Experiments", Oliver and Boyd, London, 1950.
6. S. Lee Crump, "The Estimation of Variance Components in the Analysis of Variance", Biometrics, Vol. 2, No. 1, 1946.
7. C. Eisenhart, "Assumptions Underlying the Analysis of Variance", Biometrics, Vol. 3, No. 1, 1947.

Wave Propagation Along a Magnetically-Focused Cylindrical Electron Beam

By W. W. RIGROD and J. A. LEWIS

(Manuscript received August 24, 1953)

This paper analyses the nature of wave propagation along a cylindrical electron beam, focused in Brillouin flow by means of a finite axial magnetic field. Two different types of conducting boundaries external to the beam are treated: (1) the concentric cylindrical tube, forming a drift region; and (2) the sheath helix, forming a model of the helix traveling-wave tube. The field solution of the helix problem is used to evaluate the normal-mode parameters of an equivalent circuit seen by a thin beam, thereby permitting computation of the gain constant of growing waves. The gain constant of the cylindrical beam with Brillouin flow is found to exceed that of a similar beam with rectilinear flow, presumably because of the transverse component of electron motion in the former.

INTRODUCTION

The theory of the helix traveling-wave has been treated in previous papers,[1–4] for cases in which the electrons move along straight lines parallel to the axis of the helix, as though immersed in an infinitely strong magnetic field. In practice, however, the electron beam is focused by a magnetic field of finite intensity,[5, 6] such that the electrons follow spiral paths about the common axis. The purpose of this paper is to extend traveling-wave tube theory to the case of such focused beams, and to compare the gain constants for the two types of electron motion. The motion of the beam in an infinite field is usually described as rectilinear flow; that in a finite focusing field, as Brillouin flow.

The gain constant of the dominant mode in a traveling-wave tube may be computed from the field solution for the electron beam in the presence of its circuit structure. This procedure, however, requires the solution of cumbersome transcendental equations for each particular set of dimensions and operating conditions. A more flexible method of analysis has been provided by Pierce,[1] based on an expansion in terms of normal modes of propagation. For any particular *type* of beam and circuit, three circuit parameters must be evaluated from the field solution. The performance of the traveling-wave tube is then described quite accurately by a cubic equation containing these parameters, over a wide range of dimensions and operating conditions. The usefulness of this normal-mode method has been further enhanced by publication of a nomograph[7] for the calculation of the gain constant.

In its initial form, the normal-modes solution for a helix traveling-wave tube was greatly simplified by the assumption that the electron beam is so thin that the electric field acting on it is constant. Employing the field solution for a beam of finite thickness in a helix, Fletcher[4] was able to compute the circuit parameters for the solid and hollow cylindrical electron beams, respectively, confined to rectilinear flow.

This procedure will now be extended to cylindrical beams in Brillouin flow, in which transverse electron motion occurs. First, it will be necessary to solve the field equations for this type of beam in a helix. As a by-product of this computation, the solution of the field equations for the beam in a concentric drift tube will briefly be given. Finally, with some restrictions, the helix parameters will be evaluated, and the gain of helix amplifiers with such beams compared with that obtained with otherwise identical rectilinear beams.

FIELD EQUATIONS IN THE ELECTRON BEAM

When a small ac field is impressed upon a short length of electron beam, the electrons respond by executing small ac excursions about their steady-state trajectories. These ac motions of charged particles constitute a transverse distribution of ac currents, which in turn excites an ac field distribution. The propagation of an ac signal along a beam depends upon the reciprocal action of these currents and fields.

To find the propagation constants for a particular configuration of electron stream and enclosure, we must therefore solve Maxwell's equations in the presence of the ac driving currents in the beam, subject to the external boundary conditions. When the fields and currents possess circular symmetry, these equations may be formally separated into TE and TM groups.[2] In addition, as we are concerned only with "slow" waves, the equations may be simplified by neglecting all terms of relative magnitude k^2/γ^2, where k is the wave number in free space, and γ the propagation wave number.

TM WAVE

$$\frac{1}{r}\frac{\partial}{\partial r}\left(r\frac{\partial E_z}{\partial r}\right) - \gamma^2 E_z = \frac{\gamma^2}{j\omega\epsilon}J_z + \frac{\gamma}{\omega\epsilon}\frac{1}{r}\frac{\partial}{\partial r}(rJ_r) \qquad (1)$$

$$E_r = \frac{j}{\gamma}\frac{\partial E_z}{\partial r} - \frac{j\omega\mu}{\gamma^2} J_r \tag{2}$$

$$H_\theta = \frac{\omega\epsilon}{\gamma} E_r - \frac{j}{\gamma} J_r \tag{3}$$

TE WAVE

$$\frac{1}{r}\frac{\partial}{\partial r}\left(r\frac{\partial H_z}{\partial r}\right) - \gamma^2 H_z = -\frac{1}{r}\frac{\partial}{\partial r}(rJ_\theta) \tag{4}$$

$$H_r = \frac{j}{\gamma}\left(\frac{\partial H_z}{\partial r} + J_\theta\right) \tag{5}$$

$$E_\theta = -\frac{\omega\mu}{\gamma} H_r = -\frac{j\omega\mu}{\gamma^2}\left(\frac{\partial H_z}{\partial r} + J_\theta\right) \tag{6}$$

Here (r, θ, z) are the polar cylindrical coordinates, ω the angular driving frequency, ϵ the dielectric constant and μ the permeability, of free space, in MKS units. The ac amplitudes of the electric and magnetic fields, and the convection-current density, respectively, are represented by the components of $\underline{E}$, $\underline{H}$, and $\underline{J}$. All ac quantities have been assumed to vary as $\exp j(\omega t\text{-}\gamma z)$.

When the assumption is made that the convection current density in the beam is of the same order of magnitude as the displacement current density, equations (2) and (6) reduce to the following:

$$E_r = \frac{j}{\gamma}\frac{\partial E_z}{\partial r} \tag{7}$$

$$E_\theta = -\frac{j\omega\mu}{\gamma^2}\frac{\partial H_z}{\partial r} \tag{8}$$

In order to evaluate the components of $\underline{J}$ in the beam, it is necessary to determine the velocity and charge distributions, first in the unmodulated, and then in the ac modulated beam.

The focusing of long cylindrical electron beams by axial magnetic fields of moderate strength has been fully described by Brillouin[5] and Samuel[6]. This type of electron motion, called "Brillouin flow", can be established when a parallel electron beam abruptly enters a suitable magnetic field. The electrons thereupon acquire an angular velocity component which leads to a balance of radial forces in the beam.

The equations of motion of electrons in an axial magnetic field B_0 are as follows:

$$\ddot{r} - r\dot{\theta}^2 = \eta(\partial V_0/\partial r - r\dot{\theta}B_0) \tag{9}$$

$$r\ddot{\theta} + 2\dot{r}\dot{\theta} = \eta\dot{r}B_0 \tag{10}$$

$$\ddot{z} = \eta\cdot\partial V_0/\partial z \tag{11}$$

In these equations (r, θ, z) is the position of an electron at time t; dots indicate differentiation with respect to t, following the electrons; $\eta = e/m$, where $-e$ is the electronic charge and m its mass; and V_0 is the potential describing the steady, axially symmetric electric field. Relativistic effects and the magnetic field resulting from electron motion have been neglected, as our interest is confined to beam velocities which are small compared to that of light.

It is readily verified that a solution of the above equation is:

$$\dot{r} = 0, \qquad \dot{\theta} = \dot{\theta}_0 = \eta B_0/2, \qquad \dot{z} = u_0 \tag{12}$$

$$\eta\, \partial V_0/\partial r = r\dot{\theta}_0^{\,2}, \qquad \partial V_0/\partial z = 0 \tag{13}$$

Thus all the particles in the beam have the same angular velocity, equal to the Larmor angular frequency, and the same axial velocity u_0. From Poisson's equation, we find the charge density:

$$\rho_0 = -\,2\epsilon\dot{\theta}_0^{\,2}/\eta \tag{14}$$

It is convenient to introduce the angular plasma frequency ω_p, defined by:

$$\omega_p^{\,2} = -\eta\rho_0/\epsilon = 2\dot{\theta}_0^{\,2} \tag{15}$$

In steady-state flow, an electron with initial position (r_0, θ_0, z_0) has the position $(r_0, \theta_0 + \dot{\theta}_0 t, z_0 + u_0 t)$ at time t. When the beam is modulated by a small ac signal, the electrons suffer small ac displacements from their steady-state trajectories. If we assume that the signal propagates along the axis of the beam as $\exp j(\omega t - \gamma z)$, we can write the perturbed electron coordinates in terms of the Lagrangian coordinates (r_0, θ_0, z_0) as follows:

$$r = r_0 + \tilde{r}(r_0)\cdot\exp j[\omega t - \gamma(z_0 + u_0 t)] \tag{16}$$

$$\theta = \theta_0 + \dot{\theta}_0 t + \tilde{\theta}(r_0)\cdot\exp j[\omega t - \gamma(z_0 + u_0 t)] \tag{17}$$

$$z = z_0 + u_0 t + \tilde{z}(r_0)\cdot\exp j[\omega t - \gamma(z_0 + u_0 t)] \tag{18}$$

where the tildes indicate ac amplitudes, and the dots indicate, as before, time differentiation at fixed r_0, θ_0, z_0. Thus the dots are equivalent to multiplication by $j(\omega - \gamma u_0)$, when applied to ac quantities.

The equations of motion for the ac modulated beam differ from the steady-state equations (9) — (11), in that the particle coordinates are now given by (16) — (18), and there are ac fields present in addition to the dc fields $-\partial V_0/\partial r$ and B_0. As is usual in small-signal theory, only first-order ac quantities are retained in any equation. To this approximation, the ac fields can be evaluated at the unperturbed particle position.

Not all of the ac fields need to appear in the force equations, however. Reference to the field equations shows that the contributions of the ac magnetic fields to the force components are smaller than those due to the electric fields by a factor of the order of $(u_0/c)^2$ or smaller (where c is the velocity of light), and hence may be neglected. In addition, the force exerted by E_θ is of the same order as that due to H_r, and may be neglected too.

Omitting the factor $\exp j[\omega t - \gamma(z_0 + u_0 t)]$ for brevity from all ac terms, we can write the equations of motion as follows:

$$\ddot{r} - (r_0 + \tilde{r})(\dot{\theta}_0 + \dot{\tilde{\theta}})^2 = -\eta[-\partial V_0/\partial r + E_r + (r_0 + \tilde{r})(\dot{\theta}_0 + \dot{\tilde{\theta}})B_0] \quad (19)$$

$$(r_0 + \tilde{r})\ddot{\tilde{\theta}} + 2\dot{\tilde{r}}(\dot{\theta}_0 + \dot{\tilde{\theta}}) = \eta\dot{\tilde{r}}B_0 \quad (20)$$

$$\ddot{\tilde{z}} = -\eta E_z \quad (21)$$

These equations may be simplified with the aid of (12):

$$\eta\, \partial V_0/\partial r = (r_0 + \tilde{r})\dot{\theta}_0^2 \quad (22)$$

and by recalling that the dots may be replaced by multiplication by $j(\omega - \gamma u_0)$. We obtain, finally:

$$\tilde{r} = \eta E_r/(\omega - \gamma u_0)^2 \quad (23)$$

$$\tilde{\theta} = 0 \quad (24)$$

$$\tilde{z} = \eta E_z/(\omega - \gamma u_0)^2 \quad (25)$$

Although the foregoing equations deal with the dynamics of individual electrons, the assumption that the beam behaves like a smoothed-out "fluid" of charge, with a single velocity at each point, enables us to assign values of velocity and all other ac quantities, to *fixed positions* in space, (r, θ, z). In these coordinates, the dc velocity is given by:

$$\underline{v}_0 = (0,\ r\dot{\theta}_0,\ u_0) \quad (26)$$

and the ac velocity by:

$$\begin{aligned} \underline{v} &= (\dot{r},\ r\dot{\tilde{\theta}},\ \dot{\tilde{z}}) \\ &= j(\omega - \gamma u_0)[(\tilde{r},\ r\tilde{\theta},\ \tilde{z})] \end{aligned} \quad (27)$$

Although the ac quantities are defined at r_0, they may be taken to be the same at r, to a linear approximation.

The same result, (27), might have been obtained by stating the equations of motion in terms of Eulerian coordinates, in which the perturbed variables are the components of fluid velocity at any fixed point. In this procedure, the "material" or total time derivative would be used in the expressions for acceleration.

The ac space-charge density ρ is found with the aid of the continuity equation:

$$\frac{\partial}{\partial t}(\rho_0 + \rho) = -\text{div}\,[(\rho_0 + \rho)(\underline{v}_0 + \underline{v})] \tag{28}$$

$$\rho = \frac{j\rho_0}{\omega - \gamma u_0}\,\text{div}\,\underline{v} \tag{29}$$

From (23)–(25) and (27), the ac velocity may be written:

$$\underline{v} = \frac{j\eta}{\omega - \gamma u_0}\,(E_r\,,\,0,\,E_z) \tag{30}$$

Combining these with Poisson's equation, we find:

$$\rho = -\frac{\eta\rho_0}{(\omega - \gamma u_0)^2}\,\text{div}\,\underline{E} = \frac{\omega_p^2}{(\omega - \gamma u_0)^2}\cdot\rho \tag{31}$$

There are two possible solutions to (31):

$$(\omega - \gamma u_0)^2 = \omega_p^2 \tag{32}$$

$$\rho = 0 \tag{33}$$

Solution (32) represents two longitudinal space-charge waves of arbitrary amplitude distribution, with plasma-frequency oscillations about the average beam velocity:

$$\gamma = \frac{\omega}{u_0} \pm \frac{\omega_p}{u_0} \tag{34}$$

The second solution, (33), however, permits us to evaluate the components of the ac convection current density $\underline{J}$, and thereby solve the field equations (1) — (8):

$$\underline{J} = \rho_0\underline{v} + \rho\underline{v}_0 \tag{35}$$

$$J_r = \rho_0 v_r = \frac{\omega_p^2\epsilon}{\gamma(\omega - \gamma u_0)}\,\frac{\partial E_z}{\partial r} \tag{36}$$

$$J_\theta = 0 \tag{37}$$

$$J_z = \rho_0 v_z = -\frac{j\omega_p^2\epsilon}{\omega - \gamma u_0}\,E_z \tag{38}$$

The wave equations (1) and (4) for E_z and H_z now reduce to the following.

$$\frac{1}{r}\frac{\partial}{\partial r}\left(r\frac{\partial E_z}{\partial r}\right) - \gamma^2 E_z = 0 \tag{39}$$

$$\frac{1}{r}\frac{\partial}{\partial r}\left(r\frac{\partial H_z}{\partial r}\right) - \gamma^2 H_z = 0 \tag{40}$$

These equations have solutions for E_z and H_z, which are finite at $r = 0$, of the form $A \cdot I_0(\gamma r)$, where A is an arbitrary constant and I_0 the modified Bessel function of zero-th order.

It is not without interest to remark that the same pair of solutions, given by (32) and (39)— (40), has been found by L. R. Walker for a beam of arbitrary cross-section, with the same longitudinal velocity and space-charge density at every point, in the absence of any impressed dc magnetic field.

Due to the radial component of electron motion, the beam surface is rippled. For a steady-state radius b, this rippling can be expressed, in a linear approximation, by the perturbed radius:

$$r(b) = b + \tilde{r}(b) \exp j(\omega t - \gamma z) \tag{41}$$

The rippled beam is equivalent to a uniform cylindrical beam with an ac surface charge density $\rho_0\tilde{r}$, or a surface current density whose components are:

$$G_z = \rho_0 \tilde{r} u_0 \tag{42}$$

$$G_\theta = \rho_0 \tilde{r} \dot{\theta}_0 b \tag{43}$$

The total ac convection current may be written in a form which applies equally well to the cylindrical beam with purely rectilinear flow:

$$\begin{aligned} I_c &= \int_0^b J_z 2\pi r\, dr + 2\pi b \rho_0 u_0 \tilde{r}(b) \\ &= -j\omega\epsilon \cdot R \cdot 2\pi b \cdot A \cdot I_1(\gamma b)/\gamma \\ &= -j\omega\epsilon R \int_0^b E_z\ 2\pi r\, dr \end{aligned} \tag{44}$$

where R is a beam propagation function which will prove convenient:

$$R = \frac{\omega_p^2}{(\omega - \gamma u_0)^2} = \frac{(\beta_p b)^2}{(\gamma b - \beta_e b)^2} \tag{45}$$

and

$$\beta_e = \omega/u_0\,,\ \beta_p = \omega_p/u_0 \tag{46}$$

Thus we note that wave propagation along a cylindrical beam with Brillouin flow is accompanied by swelling and contracting of its boundary, with constant space-charge density, rather than by space-charge bunching. The second interesting result is that the dynamics and field equations for the focused beam are identical with those for a beam with zero dc magnetic field, except for the angular component of surface current density G_θ.

SPACE-CHARGE WAVES

We now consider the given beam, of radius b, in a concentric conducting tube of radius $a > b$. The boundary problem consists of matching the TM wave admittances inside and outside of the beam, at its boundary. (The TE fields are of no interest in the drift-tube problem, as they are not excited at the ends of the tube, and are not coupled to the TM fields.) Let I refer to the beam region $0 \leq r \leq b$, and II to the space between beam and conductor $b \leq r \leq a$. Then, at $r = b$,

$$\frac{H_\theta^I + G_z}{E_z^I} = \frac{H_\theta^{II}}{E_z^{II}} \tag{47}$$

The beam admittance on the left is evaluated with the aid of (3), (7), (36), and (42):

$$Y_e = \frac{j\omega\epsilon}{\gamma}(1 - R)\frac{I_1(\gamma b)}{I_0(\gamma b)} \tag{48}$$

In region II,

$$E_z = B \cdot I_0(\gamma r) + C \cdot K_0(\gamma r)$$

$$H_\theta = \frac{j\omega\epsilon}{\gamma}[B \cdot I_1(\gamma r) - C \cdot K_1(\gamma r)]$$

where K_0 and K_1 are modified Bessel functions of the second kind. The wave admittance at $r = b$ in II is therefore:

$$Y_c = \frac{j\omega\epsilon}{\gamma}\left[\frac{I_1(\gamma b) - (C/B) \cdot K_1(\gamma b)}{I_0(\gamma b) + (C/B) \cdot K_0(\gamma b)}\right] \tag{49}$$

At $r = a$, $E_z^{II} = 0$ or:

$$C/B = -I_0(\gamma a)/K_0(\gamma a) \tag{50}$$

Equating beam and circuit admittances (48) and (49), we obtain:

$$R = \frac{-\dfrac{I_0(\gamma a)}{K_0(\gamma a)}}{\gamma b \cdot I_1(\gamma b) \cdot \left[I_0(\gamma b) - \dfrac{I_0(\gamma a)}{K_0(\gamma a)} \cdot K_0(\gamma b)\right]} \tag{51}$$

This equation must be solved simultaneously with each of the following:

$$\begin{aligned} \gamma_1 b &= \beta_e b + \beta_p b/\sqrt{R_1} \\ \gamma_2 b &= \beta_e b - \beta_p b/\sqrt{R_2} \end{aligned} \tag{52}$$

Thus, for a given beam and frequency, the solution consists of two unattenuated waves, one faster and the other slower than the beam velocity. The wavelength of the interference pattern is given by:

$$\lambda_s = \frac{4\pi}{\gamma_1 - \gamma_2} \tag{53}$$

For a cylindrical beam,

$$\beta_p b = 174\sqrt{P} \tag{54}$$

where $P = I/V^{3/2}$ amps/(volts)$^{3/2}$, the perveance. In practice, P and hence $\beta_p b$ are usually so small that we can gain a fair estimate of λ_s by assuming $R_1 = R_2$:

$$\lambda_s \simeq \frac{2\pi\sqrt{R}}{\beta_p} \tag{55}$$

Fig. 1 shows the variation of $R^{1/2}$ with γb for several values of b/a. (The "intrinsic" solution (32) is included as a line at $R^{1/2} = 1$.) The ordinates of these curves are approximately proportional to the space-charge wavelength, and the abcissae to the frequency, as $\gamma \simeq \beta_e = \omega/u_0$ for small perveance.

Space-charge waves propagating along a cylindrical beam with rectilinear flow have been treated by Hahn[8] and Ramo[9]. In Fig. 2, their computations have been reformulated in the same way as in Fig. 1, and compared with the results for Brillouin flow, for two values of b/a. The space-charge wavelength is always greater in Brillouin flow, for the principal pair of waves and the same b/a and γb.

HELIX PROBLEM

In place of the drift tube at radius a, we now have a helically conducting sheet of zero thickness and pitch angle ψ. In addition to I $(0 \leq r \leq b)$ and II $(b \leq r \leq a)$, we shall use III to identify fields in the region $(a \leq r < \infty)$. The boundary conditions at $r = b$ are:

$$\begin{aligned} H_\theta^I + G_z - H_\theta^{II} &= 0 \\ E_z^I - E_z^{II} &= 0 \\ H_z^I - G_\theta - H_z^{II} &= 0 \\ E_\theta^I - E_\theta^{II} &= 0 \end{aligned} \tag{56}$$

At $r = a$, the boundary conditions are:

$$\begin{aligned} E_z^{II} + E_\theta^{II} \cot \psi &= 0 \\ E_z^{III} + E_\theta^{III} \cot \psi &= 0 \\ E_z^{II} - E_z^{III} &= 0 \\ H_z^{II} + H_\theta^{II} \cot \psi - H_z^{III} - H_\theta^{III} \cot \psi &= 0 \end{aligned} \tag{57}$$

Inasmuch as $\cot \psi \sim \gamma/k$, the contribution of E_θ to the field at the helix can conceivably be comparable to that of E_z. The TE fields are coupled to the TM group, in addition, through the angular surface current G_θ, which depends on E_z. All 8 equations must therefore be solved simultaneously.

The procedure follows that of Chu and Jackson[2] for the field solution

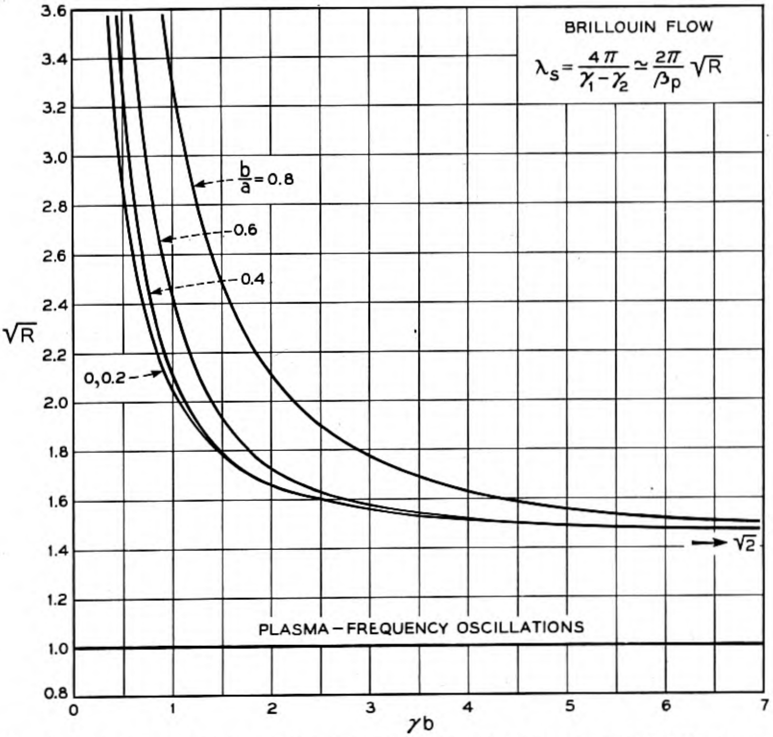

Fig. 1 — Space-charge wavelength λ_s for cylindrical beam with Brillouin flow, in a concentric drift tube. Here b and a are the beam and tube radii, respectively; $R^{1/2}$ is a dimensionless parameter; and the waves propagate as $\exp j(\omega t - \gamma z)$. To compute $\lambda_s \simeq 2\pi R^{1/2}/\beta_p$, use $\beta_p b = 174P^{1/2}$, where P is the beam perveance. The abscissae are approximately given by $\gamma \sim \beta e = \omega/u_0$. (Equations 52–55.)

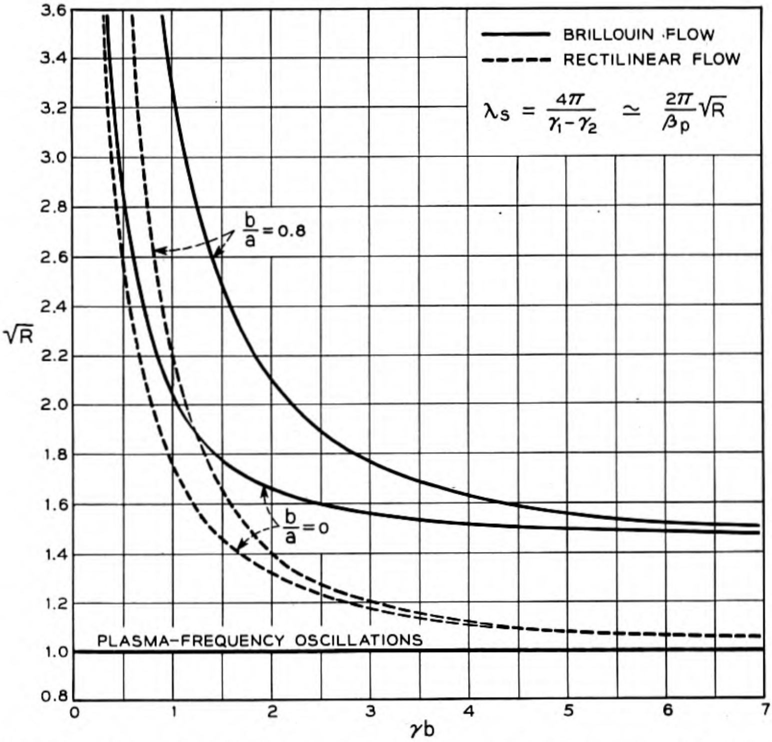

Fig. 2 — Comparison between space-charge wavelengths for cylindrical beams with Brillouin flow and those with rectilinear (confined) flow, respectively.

of the rectilinear beam. The 12 independent variables of (56–57) are reduced to 6 by expressing H_θ and E_θ in terms of E_z and H_z, respectively. The latter, however, require 2 arbitrary constants for a complete description in region II, making a total of 8 constants to be determined.

The eliminant of the 8 boundary-value equations can be written as a TM wave-admittance equation at the beam surface:

$$\frac{j\omega\epsilon}{\gamma}(1 - R)\frac{I_1(\gamma b)}{I_0(\gamma b)} = \frac{j\omega\epsilon}{\gamma}\frac{I_1(\gamma b) - \delta\cdot K_1(\gamma b)}{I_0(\gamma b) + \delta\cdot K_0(\gamma b)} \tag{58}$$

where

$$\delta = \frac{\delta_0 + RF}{1 - \dfrac{K_0(\gamma b)}{I_0(\gamma b)}RF} \tag{59}$$

$$\delta_0 = \frac{1}{K_0^2(\gamma a)}\left[\left(\frac{ka \cot \psi}{\gamma a}\right)^2 K_1(\gamma a)I_1(\gamma a) - K_0(\gamma a)I_0(\gamma a)\right] \tag{60}$$

$$F = (kb \cot \psi)\left(\frac{\dot{\theta}_0 b}{c}\right)\frac{I_1^2(\gamma b)K_1(\gamma a)}{K_0(\gamma a)} \tag{61}$$

In (61), c is the velocity of light.

The right side of (58), which is the admittance H_θ/E_z looking away from the beam surface, contains a term δ which depends on the helix geometry and the amplitude of the TE fields excited by the surface current G_θ. Thus, although the TE fields do not affect the electron paths, they are excited by the beam, and coupled to the TM fields at the helix. If G_θ were zero, δ would reduce to δ_0, and the circuit admittance in (58) would then be the same as for a cylindrical beam with rectilinear flow. In (59), δ is expressed in terms of δ_0 and the product, RF, where R is the beam propagation function, and F a factor dependent on the magnetic field and the geometry.

This is the complete field solution of the problem. Equation (58) has four roots: two complex and two real propagation wave numbers, one of the latter representing a backward wave. In addition, there are two unattenuated space-charge waves, given by (34); or a total of 6 waves in all.

EQUIVALENT THIN-BEAM SOLUTION

Pierce[1] has expressed the admittance equation for an ideally thin beam, interacting with an arbitrary distributed circuit, as follows:

$$\frac{q}{E} = \frac{j\beta_e}{(j\beta_e - \Gamma)^2}\frac{I_0}{2V_0} = -\left(\Gamma^2 K\left[\frac{\Gamma_0}{\Gamma^2 - \Gamma_0^2} + \frac{2jQ}{\beta_e}\right]\right)^{-1} \tag{62}$$

where q = total convection current

E = longitudinal electric field

Γ = propagation constant = $\sqrt{-\gamma^2 - k^2}$

I_0 = dc beam current

V_0 = dc beam potential

Γ_0, K, Q = normal-mode circuit parameters.

For slow waves, $\Gamma \simeq j\gamma$. For moderate values of perveance, the accelerating voltage may be replaced by the beam potential at the axis:

$$u_0 \simeq \sqrt{2\eta V_0}$$

$$\frac{j\beta_e}{(j\beta_e - \Gamma)^2}\frac{I_0}{2V_0} \simeq j\omega\epsilon\pi b^2 R \tag{63}$$

Then, dividing both sides of (62) by $2\pi b$, we may rewrite it as a wave-admittance equation:

$$-\frac{j\omega\epsilon}{\gamma}\cdot\frac{\gamma b}{2}\cdot R = -\left(2\pi b\Gamma^2 K\left[\frac{\Gamma_0}{\Gamma^2 - \Gamma_0^2} + \frac{2jQ}{\beta_e}\right]\right)^{-1} \tag{64}$$

With the aid of (59), we can solve the admittance equation (58) for R, and re-write it as follows:

$$Y_e = Y_B \tag{65}$$

with

$$Y_e = -\frac{j\omega\epsilon}{\gamma}\cdot\frac{\gamma b}{2}\cdot R \tag{66}$$

$$Y_B = \frac{j\omega\epsilon}{\gamma}\cdot\frac{\gamma b}{2}\cdot\frac{I_0(\gamma b)}{I_1(\gamma b)}\left(\frac{\delta_0}{\gamma b\cdot I_0(\gamma b)[I_0(\gamma b) + \delta_0\cdot K_0(\gamma b)] - \dfrac{FI_0(\gamma b)}{I_1(\gamma b)}}\right) \tag{67}$$

The solid-cylindrical Brillouin beam in a helix is thus equivalent to a thin beam whose circuit admittance is Y_B. By equating Y_B to the right side of (64), we can evaluate the normal-mode parameters for this admittance, and thereby use all the results of previous thin-beam calculations.[1,7] The equivalence of the two circuit expressions, however, requires that we replace the transcendental expression (67) by an algebraic one, with no more than three arbitrary constants. This can be done very effectively, in the region of interest, by means of the approximation:[2]

$$Y_B \simeq -(\gamma_p - \gamma_0)\left(\frac{\partial Y_B}{\partial\gamma}\right)_{\gamma=\gamma_0}\cdot\frac{\gamma - \gamma_0}{\gamma - \gamma_p} \tag{68}$$

in which γ_0 and γ_p are the zero and pole, respectively, of Y_B:

$$\delta_0(\gamma_0) = 0$$

$$\delta_0(\gamma_p) = \left(-\frac{I_0(\gamma b)}{K_0(\gamma b)} + \frac{F}{\gamma b\cdot I_1(\gamma b)\cdot K_0(\gamma b)}\right)_{\gamma=\gamma_p} \tag{70}$$

If we were to neglect the term containing F in (70), the error in the magnitude of $\delta_0(\gamma_p)$ would be measured by:

$$\frac{F}{\gamma b\cdot I_1(\gamma b)\cdot I_0(\gamma b)} \equiv (kb\cot\psi)\left(\frac{\dot\theta_0 b}{c}\right)\frac{I_1(\gamma b)\cdot K_1(\gamma a)}{I_0(\gamma b)\cdot K_0(\gamma a)} \tag{71}$$

In most low-power traveling-wave tubes, the first factor in parentheses is usually less than 3; the second factor less than 0.01; and the last factor always less than unity. The error in evaluating γ_p, moreover, is less than this product, for the slope of the curve δ_0 versus γb increases with γb. Putting $F = O$, therefore, leads at most to a very slight error in γ_p and

$$\left(\frac{\partial Y_B}{\partial \gamma}\right)_{\gamma=\gamma_0}$$

Outside of the region (γ_0, γ_p), δ_0 grows large rapidly, and the expression for Y_B is hardly affected at all by this assumption.

Physically, the negligible role played by F in the admittance equation means that $\delta \simeq \delta_0$, i.e., the TM helix admittance is not appreciably perturbed by the TE fields excited by G_θ.

With $F = 0$, (67) may be re-written:

$$Y_B = \frac{\gamma b}{2} \cdot \frac{I_0(\gamma b)}{I_1(\gamma b)} \cdot Y_H \tag{72}$$

$$Y_H = \frac{j\omega\epsilon}{\gamma}\left[\frac{I_1(\gamma b) - \delta_0 \cdot K_1(\gamma b)}{I_0(\gamma b) + \delta_0 \cdot K_0(\gamma b)} - \frac{I_1(\gamma b)}{I_0(\gamma b)}\right] \tag{73}$$

Here Y_H is the helix admittance seen by a thin cylindrical hollow beam, with rectilinear electron flow. As in the case of Y_B, it may be replaced in the vicinity of (γ_0, γ_p), by the approximation:

$$Y_H \simeq -(\gamma_p - \gamma_0)\left(\frac{\partial Y_H}{\partial \gamma}\right)_{\gamma=\gamma_0} \frac{\gamma - \gamma_0}{\gamma - \gamma_p} \tag{74}$$

Fletcher[4] has evaluated the normal-mode parameters for Y_H as follows:

$$\Gamma_0^2 = -\gamma_0^2 - k^2 \tag{75}$$

$$Q_H \frac{\gamma_0}{\beta_e}\left[1 + \frac{k^2}{\gamma_0^2}\right]^{-1/2} = \frac{1}{2}\frac{\gamma_0^2}{\gamma_p^2 - \gamma_0^2} \tag{76}$$

$$\frac{1}{K_H} = -j\pi b \gamma_0^2 \left[1 + \frac{k^2}{\gamma_0^2}\right]^{3/2} \left(\frac{\partial Y_H}{\partial \gamma}\right)_{\gamma=\gamma_0} \tag{77}$$

We have used the subscript H to refer the parameters to the hollow beam, and will use the subscript B to refer to the solid-cylindrical Brillouin beam.

As Y_B and Y_H have the same zero and pole, they have the same natural propagation constant Γ_0, and the same space-charge parameter Q:

$$Q_B = Q_H \tag{78}$$

This quantity can be found plotted in Fig. 1 of Reference 4, or in Fig. A6.1 of Reference 1.

From (68), (72), and (74), we find:

$$\left(\frac{Y_B}{Y_H}\right)_{\gamma=\gamma_0} = \left(\frac{\partial Y_B/\partial\gamma}{\partial Y_H/\partial\gamma}\right)_{\gamma=\gamma_0} = \left[\frac{\gamma b}{2}\frac{I_0(\gamma b)}{I_1(\gamma b)}\right]_{\gamma=\gamma_0} \tag{79}$$

The impedance parameters for the two beams are therefore related to each other by:

$$K_B = K_H \left[\frac{2}{\gamma b}\frac{I_1(\gamma b)}{I_0(\gamma b)}\right]_{\gamma=\gamma_0} \tag{80}$$

Both Pierce[10] and Fletcher[4] have found the impedance parameter of the hollow beam to be related to that of a thin beam along the axis of a helix, K_T, as follows:

$$K_H = K_T[I_0^2(\gamma b)]_{\gamma=\gamma_0} \tag{81}$$

The gain parameter C is defined by: $C^3 = (2K)(I_0/8V_0)$ (82)

Thus, for given I_0 and V_0, the factor by which the gain parameter of a thin beam should be multiplied to give that of a hollow beam, is:

$$(K_H/K_T)^{1/3} = [I_0^{2/3}(\gamma b)]_{\gamma=\gamma_0} \tag{83}$$

This "impedance reduction factor" can similarly be evaluated for the finite cylindrical beam with Brillouin flow:

$$(K_B/K_T)^{1/3} = \left[\frac{2}{\gamma b} I_1(\gamma b)\cdot I_0(\gamma b)\right]^{1/3}_{\gamma=\gamma_0} \tag{84}$$

Cutler,[7] who calls this quantity F_2, has described how it and the parameter Q can be used to compute the gain of traveling-wave tubes. The procedure depends upon the evaluation of C and QC. The expression for C_B, in Cutler's notation, is:

$$C_B \simeq (K_2/K)^{1/3}\ F_1F_2(I_0/8V_0)^{1/3} \tag{85}$$

Here K_2/K is a factor, of the order of 0.5, which corrects the impedance of the ideal sheath helix for the physical dimensions and support elements of the actual helix. It is best found by measurement. The factor F_1 is plotted in Fig. 3.4 of Reference 1, and obeys the empirical relation:

$$F_1(\gamma a) = 7.154 \exp\ (-0.6664\ \gamma a) \tag{86}$$

Finally, the factor F_2 is the impedance reduction factor (84), which is plotted in Fig. 3 of this paper for various ratios of the radii, b/a.

It is of interest to compare the relative gain of beams with rectilinear and with Brillouin flow, respectively. Pierce[10] has computed a first approximation to the impedance reduction factor for the solid-cylindrical beam with rectilinear flow, by averaging E_z^2 over the beam area (with E_z for the empty helix):

$$(K_s/K_T)^{1/3} \sim [I_0^2(\gamma b) - I_1^2(\gamma b)]_{\gamma=\gamma_0}^{1/3} \tag{87}$$

Fletcher[4] has improved upon this calculation by replacing the solid beam with a thin hollow beam of different radius and dc current. This has the same electronic admittance Y_e and derivative $dY_e/d\gamma$ when $R = 1$.

The impedance reduction factors for the three types of beams have been plotted in Fig. 4, using a typical value of b/a. For the same I_0, V_0, and b/a, the gain parameters C are found to be greatest for the hollow beam, and least for the solid rectilinear beam.

The high gain of the hollow beam is due to its concentration in the region of greatest field strength. The greater gain of the beam with Brillouin flow, relative to that of a similar beam with confined flow, is probably due to transverse electron motion, in two ways:[11]

(1) causing electrons to interact with the transverse as well as longitudinal fields; and

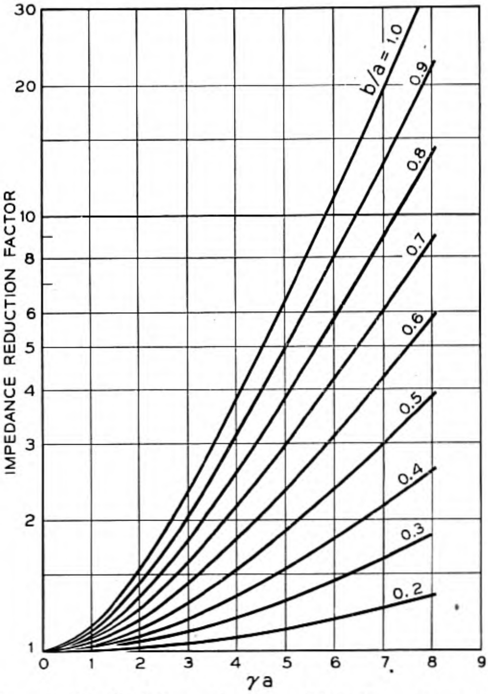

Fig. 3 — The factor $(K_B/K_T)^{1/3}$, or F_2, by which the gain parameter C_T for a thin beam should be multiplied to give C_B, the gain parameter for a cylindrical beam with Brillouin flow, of the same current and voltage. Computation of C_B using this factor is described in text following equation (85).

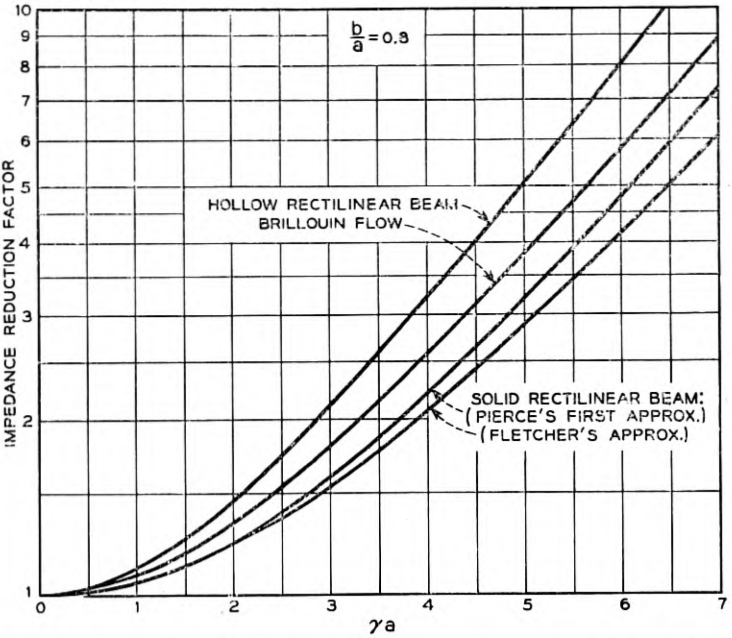

Fig. 4 — Comparative values of impedance reduction factor for several kinds of beams, of the same relative radii b/a.

(2) causing electrons to move preferentially into regions of retarding longitudinal fields, a process analogous to bunching.

CONCLUSIONS

Field solutions have been presented for the magnetically-focused cylindrical beam, when modulated by a small ac signal. Two types of beam enclosure have been treated: the concentric drift tube and the ideally thin (sheath) helix.

There are two pairs of unattenuated space-charge waves in the drift-tube: one with arbitrary amplitude distribution, and another pair which is coupled to the external field (Fig. 1). The space-charge wavelength of the latter pair is greater than that of space-charge waves in a similar beam with rectilinear flow (Fig. 2).

The solution of the helix problem consists of the aforementioned two space-charge waves with arbitrary amplitude, as well as the usual four waves of traveling-wave tube theory, or six waves in all. In order to compute the gain constant of the growing wave, the field solution has been re-written as the admittance equation of a thin beam in an artificial circuit. By means of two approximations, the normal-mode parameters of this circuit have been evaluated.

The first approximation amounts to neglecting the TE fields coupled to the TM wave, and is valid for most low-power traveling-wave tubes. The second approximation consists of replacing the circuit admittance function by an algebraic expression with the same zero and pole, and the same slope at the zero. Although thin-beam theory predicts small deviations of complex roots (of the admittance equation) from the natural propagation wave number, it is difficult to judge whether any such roots might occur outside of the region in which this approximation holds, for the finite beam.

The space-charge parameter Q_B is found to be the same as for a thin hollow beam with rectilinear flow (Fig. 1 of Reference 4, or Fig. A6.1 of Reference 1). The gain parameter C_B can be computed from Equation (85), Fig. 3.4 of Reference 1, and Fig. 3 of this paper. The gain of the cylindrical beam with Brillouin flow is found to be greater than that of a similar cylindrical beam with rectilinear flow, presumably because of transverse electron motion in the former. Its gain, however, is less than that of a thin hollow cylindrical beam with rectilinear flow, for the same radius, current, and voltage (Fig. 4).

ACKNOWLEDGEMENTS

The writers are indebted to J. R. Pierce for suggesting the general approach used in this paper, to H. Suhl and C. F. Quate for their helpful criticisms, and to Mrs. C. Lambert for computing the graph material.

REFERENCES

1. J. R. Pierce, *Traveling-Wave Tubes*, D. Van Nostrand, N. Y., Chapters VII, VIII, (1950).
2. L. J. Chu and J. D. Jackson, Field Theory of Traveling-Wave Tubes, Proc. I.R.E., **36,** p. 853, 1948.
3. E. H. Rydbeck, Theory of the Traveling-Wave Tube, Ericsson Tech. **46,** p. 3, 1948.
4. R. C. Fletcher, Helix Parameters Used in Traveling-Wave Tube Theory, Proc. I.R.E., **38,** p. 413, 1950.
5. L. Brillouin, A Theorem of Larmor and Its Importance for Electrons in Magnetic Fields, Phys. Rev. **67,** p. 260, 1945.
6. A. L. Samuel, On the Theory of Axially Symmetric Electron Beams in an Axial Magnetic Field, Proc. I.R.E., **37,** p. 1252, 1949.
7. C. C. Cutler, The Calculation of Traveling-Wave Tube Gain, Proc. I.R.E. **39,** p. 914, 1951.
8. W. C. Hahn, Small Signal Theory of Velocity-Modulated Electron Beams, G. E. Rev., **42,** p. 258, 1939.
9. S. Ramo, Space Charge and Field Waves in an Electron Beam, Phys. Rev., **56,** p. 276, 1939.
10. J. R. Pierce, *Traveling-Wave Tubes*, D. Van Nostrand, N. Y., App. II.
11. J. R. Pierce, *Traveling-Wave Tubes*, D. Van Nostrand, N. Y., Chapt. XIII.

Diffraction of Plane Radio Waves by a Parabolic Cylinder

Calculation of Shadows Behind Hills

By S. O. RICE

(Manuscript received April 3, 1953)

Expressions are given for the diffraction field far behind, and the surface currents on, a parabolic cylinder. Approximate values for the field strength and current density are given when the radius of curvature of the cylinder is large compared to a wavelength. The formulas may have value in predicting the shadows that are cast by hills in microwave propagation. The idea of representing hills by knife-edges has been used successfully by a number of investigators. The theory of the parabolic cylinder indicates that such a representation is valid even for gently rounded hills when the angle of diffraction is small. On the other hand, when the angle of diffraction is so large that the knife-edge calculations do not apply, the results presented here may be used.

1. INTRODUCTION

A number of investigators have studied the effect of hills on the propagation of short radio waves. Experiment has shown that the field far behind a hill may be computed, to a reasonable degree of accuracy, by assuming that the hill acts like a knife-edge (half-plane)[1]. The question naturally arises as to the conditions under which such an assumption is permissible. Here we attempt to throw some light on this question by taking the hill to be a parabolic cylinder.

Our results indicate that, for small angles of diffraction, even gently curved hills act like knife-edges. However, for larger angles corresponding to points deep in the shadow or to points high in the illuminated region, it may be necessary to use the more exact formulas which take the curvature of the hill into account.

---

[1] See, for example, Ultra-Short-Wave Propagation, J. C. Schelleng, C. R. Burrows and E. B. Ferrell, Proc. I.R.E., **21**, pp. 423–463, 1933.

As an application of our results, a brief study is made of the hypothesis that very short radio waves are transmitted far beyond the horizon by successive diffractions over hills or ridges. The ridges are assumed to be of equal height, to be 40 miles apart, and to have a radius of curvature of 100 meters at their crests. At the frequencies considered (30 and 300 mc) and at the small angles of diffraction required to go from one crest to the next, the ridges act like knife-edges.

At 30 mc and a distance of 280 miles the calculated field is in fair agreement with the observed field[2]. At 300 mc and at the same distance the calculated field is about 50 db below the observed field. This suggests that the 30 mc long distance propagation may possibly be explained by successive diffractions. The discrepancy at 300 mc may be due to any one of a number of reasons. For example, it may be due to the effect of the non-uniformity of the atmosphere, or to the roughness of our approximations (for one thing, we neglect reflections from the ground between the ridges).

The first theoretical work on the diffraction of plane electromagnetic waves by a parabolic cylinder apparently was done by P. S. Epstein.[3] His work makes use of a series of parabolic cylinder functions. When the cylinder is large many terms are required for computation. By "large" we mean that the radius of curvature at the vertex of the cylinder is large compared to the wavelength of the radio wave.

An entirely different approach was used by V. Fock[4,5] in 1946. In the first paper Fock sketches the derivation of an integral for the current density on a large paraboloid of revolution. In the second paper he rederives this integral by considering the form assumed by the field equations when a plane wave strikes a gently curved conductor at grazing incidence. His result gives the change in current density on a large and highly conducting parabolic cylinder as we go from the illuminated region into the shadow.

In 1950 K. Artmann[6] examined the diffraction field far behind a large circular cylinder. He showed that, for small angles of diffraction, the

---

[2] A summary of experimental data is given by K. Bullington, Radio Transmission beyond the Horizon in the 40-400 Megacycle Band, Proc. I.R.E., **41,** pp. 132–135, 1953.

[3] Dissertation, Munich (1914). A more accessible account of this work is given in the Encyklopäedie der Math. Wiss. 5, Part 3 (1909–1926) Phys. p. 511. See also H. Bateman, *Partial Differential Equations of Math. Phys.*, (Cambridge Univ. Press 1932) p. 488.

[4] The Distribution of Currents Induced by a Plane Wave on the Surface of a Conductor, J. Phys. (U.S.S.R.), **10,** pp. 130–136, 1946.

[5] The Field of a Plane Wave Near the Surface of a Conducting Body, J. Phys. (U.S.S.R.), **10,** pp. 399–409, 1946.

[6] Beugung polarisierten Lichtes an Blenden endlicher Dicke im Gebiet der Schattengrenze, Zeitschr. für Phys. **127,** pp. 468–494, 1950.

diffraction pattern is shifted by an amount proportional to the ⅓ power of the radius of curvature. Whether the shift is towards the shadow or in the opposite direction depends upon the polarization of the incident wave.

In this paper we derive some of the results given by Fock and Artmann by starting with Epstein's series. In addition we investigate the diffracted field at a great distance behind the cylinder. The cylinder is assumed to be a perfect conductor in all of our work except for a few equations given near the ends of Sections 4, 6, and 7. The procedure is similar to that used in the smooth-earth theory.[7] The series is converted into an integral and then the path of integration is deformed so as to gain as much simplification as possible. As might be expected, the results for a large parabolic cylinder are similar in some respects to those for a smooth earth. Much of the work requires a knowledge of the behavior of parabolic cylinder functions of large complex order. Although several studies of this behavior have been published, the results are not in the form required. For this reason, and for the sake of completeness, several sections dealing with the properties of parabolic cylinder functions have been included.

Incidentally, W. Magnus[8] has studied the field produced by a line source located at the focus of a parabolic cylinder. However, his problem is somewhat different from the one with which we are concerned.

I am grateful to Prof. Erdélyi of the California Institute of Technology and to my colleagues at Bell Telephone Laboratories for helpful discussions and references which resulted in a number of improvements throughout the paper. I am also indebted to Miss Marian Darville for performing the rather laborious computations upon which the various curves and tables are based.

2. DISCUSSION OF RESULTS

Various expressions are given later for the electromagnetic field in terms of parabolic cylinder functions. In this section we shall confine a good share of our attention to the case in which the cylinder is very large compared to a wavelength so that the cylinder functions may be approximated by Airy integrals. As in the remainder of the paper, we shall be concerned chiefly with the field behind the cylinder and the current density on the cylinder.

---

[7] By "Smooth-earth theory" we mean the formulas for the field produced by a dipole near a large sphere. A complete discussion of the theory is given in the book by H. Bremmer, *Terrestrial Radio Waves* (Elsevier, 1949).

[8] Zur Theorie des zylindrisch-parabolischen Spiegels, Zeitschr. für Physik, **118,** pp. 343–356, 1941.

It turns out that the results for the parabolic cylinder are closely related to those obtained by Sommerfeld[9] for the diffraction of a plane wave by a perfectly conducting half-plane. In fact, the two fields are surprisingly similar in the region of the shadow boundary. More precisely, the fields are similar for values of the angle ψ, defined in Fig. 2.3, such that (roughly)

$$|\,\psi \text{ in radians}\,| < \frac{1}{4}\left[\frac{\text{wavelength}}{\text{radius of curvature of cylinder at its crest}}\right]^{1/3},$$

where the coefficient ¼ has been selected somewhat arbitrarily. For larger values of $|\,\psi\,|$ the difference between the fields becomes pronounced. As we go deeper and deeper into the shadow, i.e. as ψ becomes more and more negative, the field behind a cylinder ultimately decreases exponentially with ψ. On the other hand, the field behind a half-plane decreases roughly as $1/|\,\psi\,|$. Since the exponential function decreases more rapidly than does $1/|\,\psi\,|$, the shadow behind a hill is darker than the one behind a half-plane. High in the illuminated region the field consists of the incident wave plus the wave reflected from the illuminated portion of the cylinder. For the half-plane this reflected wave is negligibly small until ψ reaches 180°.

First we shall review the situation pictured in Fig. 2.1. An incident wave comes in from the left and strikes a perfectly conducting vertical half-plane which casts a shadow as shown. The electric and magnetic intensities are proportional to exp $(i\omega t)$ where t is the time and ω is the radian frequency. The unit of length is chosen so that λ, the wavelength, is equal to 2π. This is done in order to simplify the expressions we have to deal with. For example, a plane wave of unit amplitude traveling in the positive x direction, as shown in Fig. 2.1, is represented by exp $(-ix)$.

Sommerfeld's exact expressions, for the special case of horizontal incidence shown in Fig. 2.1, may be written as

$$\text{(hp)} \qquad E = (e^{-ix} + S_1) + S_2(0), \tag{2.1}$$

$$\text{(vp)} \qquad H = (e^{-ix} + S_1) + S_3(0), \tag{2.2}$$

where (2.1) holds when the electric intensity E is parallel to the edge, and (2.2) when the magnetic intensity H is parallel to the edge. From

---

[9] Math. Annalen, **47,** p. 317, 1896. Sommerfeld's results have been described in a number of texts on optics. The book, *Huygens' Principle* by Baker and Copson (Oxford 2nd edition, 1950) deals with this and many similar problems. See also Chap. 20 of Frank-von Mises, *Die Differential-und Integralgleichungen der Mechanik und Physik,* 2nd edition, Braunschweig: F. Vieweg and Sohn (1935).

the analogy with the radio case, these two polarizations will be termed "horizontal polarization" (hp) and "vertical polarization" (vp), respectively. The incident plane wave for hp is assumed to have an E of unit amplitude. This is indicated by the exp $(-ix)$ in (2.1). For vp the incident wave is assumed to have an H of unit amplitude. The S's are defined by the Fresnel integrals

$$e^{-ix} + S_1 = (i/\pi)^{1/2} e^{-ix} \int_{-\infty}^{t_1} e^{-it^2}\, dt,$$

$$S_1 = -(i/\pi)^{1/2} e^{-ix} \int_{t_1}^{\infty} e^{-it^2}\, dt, \tag{2.3}$$

$$S_2(0) = -S_3(0) = -(i/\pi)^{1/2} e^{+ix} \int_{t_2}^{\infty} e^{-it^2}\, dt,$$

$$t_1 = (2r)^{1/2} \sin\frac{\varphi}{2}, \qquad t_2 = (2r)^{1/2} \cos\frac{\varphi}{2}, \qquad i^{1/2} = \exp(i\pi/4),$$

where (r, φ) are the polar coordinates shown in Fig. 2.1 [S_1 and $S_2(0) = -S_3(0)$ for an arbitrary angle of incidence are given by Equations (5.3), (5.6), and (5.20) of Section 5]. We use the notation $S_2(0)$, $S_3(0)$ to indicate that these functions are special cases of the functions $S_2(h)$, $S_3(h)$ which appear in the analysis for the parabolic cylinder.

The principal part of the field far to the right of the half-plane, where x is positive, is given by exp $(-ix) + S_1$ whose absolute value is plotted in Fig. 2.2. The function S_1 almost cancels the incident wave in the shadow, and then drops down to small values outside the shadow. The function $S_2(0)$ is always small in the region we shall consider. It becomes large only when φ exceeds π. It then corresponds to the wave reflected from the front (left-hand side) of the half-plane.

When we are far enough away from the shadow boundary to make

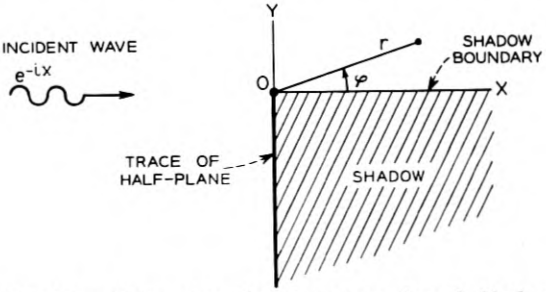

Fig. 2.1 — Diffraction of a plane wave by a half-plane.

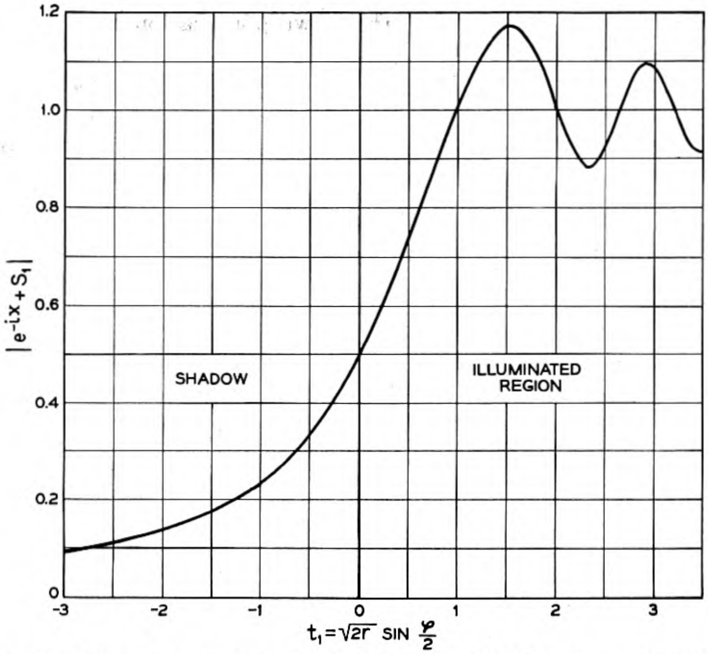

Fig. 2.2 — The approximate value $|e^{-ix}+S_1|$ of $|E|$ for hp and of $|H|$ for vp at a great distance r behind a half-plane. Here, as in all of our work, the wavelength λ is 2π. For an arbitrary wavelength replace r by $2\pi r/\lambda$, etc.

$\varphi^2 r \gg 1$, exp $(-ix) + S_1$ has the asymptotic expressions [see Equations (7.7) and (7.8)]

$$e^{-ix} + S_1 \sim \begin{cases} c(r)/2\sin\frac{\varphi}{2}, & \varphi < 0 \text{ (shadow)} \\ e^{-ix} + c(r)/2\sin\frac{\varphi}{2}, & \varphi > 0 \end{cases} \tag{2.4}$$

$$c(r) = i^{3/2}(2\pi r)^{-1/2}e^{-ir}. \tag{2.5}$$

These expressions lead us to picture the field to the right of the half-plane as the sum of the incident wave and a wave, $c(r)/\varphi$, spreading out from the diffracting edge[10] (for the small φ's of interest, $2\sin\varphi/2 \approx \varphi$ even though $\varphi^2 r \gg 1$). In the illuminated region these two waves interfere with each other to give the oscillations around unity shown in Fig.

---

[10] See, for example, R. W. Wood, *Physical Optics*, 3rd edition, p. 220 (MacMillan, 1935). Curves of equal phase and amplitude have been computed and plotted by W. Braunbeck and G. Laukien, Einzelheiten zur Halbebenen-Beugung, Optik, **9**, pp. 174–179, 1952.

2.2. In the shadow only the edge wave is present and there is no interference. S_1 is not the edge wave in the shadow.

The edge does not radiate uniformly in all directions. The φ in the denominator of $c(r)/\varphi$ indicates that the edge sends out its strongest wave in the direction of the shadow boundary where $\varphi = 0$. This accounts for the decreasing size of the oscillations in Fig. 2.2 as φ becomes more and more positive. It likewise accounts for the steady decrease as φ becomes more and more negative.

That $S_2(0)$ is small in comparison with $\exp(-ix) + S_1$ follows from

$$S_2(0) \sim c(r)/2 \cos \frac{\varphi}{2} \tag{2.6}$$

and the fact that this is small compared to the $c(r)/2 \sin(\varphi/2)$ in (2.4) when φ is small.

So far, we have been discussing a special case of Sommerfeld's results. Now we turn to the case of the perfectly conducting parabolic cylinder shown in Fig. 2.3. Here, as in Fig. 2.1, the incident plane wave $\exp(-ix)$ comes in from the left. The fields for the two kinds of polarization are given by

$$\text{(hp)} \qquad E = (e^{-ix} + S_1) + S_2(h), \tag{2.7}$$

$$\text{(vp)} \qquad H = (e^{-ix} + S_1) + S_3(h), \tag{2.8}$$

where, just as in the half-plane case, the fundamental vectors E and H are perpendicular to the plane of Fig. 2.3 and the incident waves are of unit amplitude.

The $[\exp(-ix) + S_1]$ in (2.7) and (2.8) is exactly the same Fresnel integral (2.3) as for the half-plane. $S_2(h)$ is a rather complicated integral

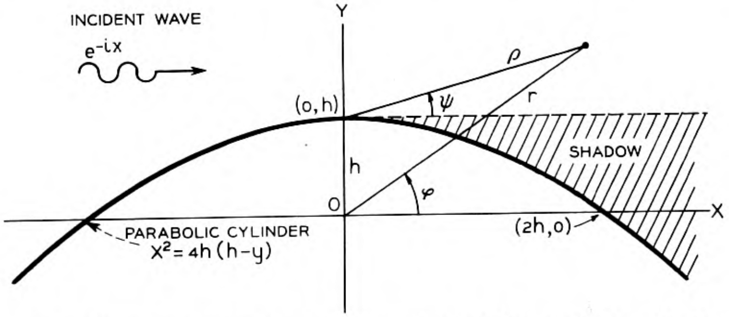

Fig. 2.3 — Coordinates used in the discussion of the parabolic cylinder. The coordinates such as $(0, h)$ refer to (x, y). The origin 0 of coordinates is at the focus of the parabola and h is the height of the vertex or crest, above the origin.

(obtained by setting the angle of incidence θ equal to $\pi/2$ in equation (5.4)) involving parabolic cylinder functions. When $h = 0$ the parabolic cylinder reduces to a half-plane and $S_2(h)$ reduces to the value $S_2(0)$ appearing in (2.3). The symbol $S_3(h)$ represents an integral much like $S_2(h)$ except that it contains derivatives of the parabolic cylinder functions. As we might expect, $S_2(h)$ and $S_3(h)$ behave in much the same way as does $S_2(0)$. In particular, they are small compared to $\exp(-ix) + S_1$ at the shadow boundary, and their asymptotic expressions analogous to (2.6) hold as φ and ψ pass through zero.

$S_2(h)$ and $S_3(h)$ have been put in a form suitable for computation in two cases, (1) when $h = 0$, which is the half-plane case already discussed, and (2) when h and r/h^2 are very large. In the second case it is convenient to introduce new polar coordinates (ρ, ψ) with their origin at the crest of the parabola as shown in Fig. 2.3. In these coordinates a circular cylindrical wave spreading out from the crest is asymptotically proportional to

$$c(\rho) = i^{3/2} (2\pi\rho)^{-1/2} e^{-i\rho}. \tag{2.9}$$

In Section 8 it is shown that

$$E \approx [e^{-ix} + S_1]_\rho - \frac{c(\rho)}{\psi} + c(\rho)h^{1/3}\left[\Psi(\tau) + \frac{1}{\tau}\right] \exp(i\tau^3/3), \tag{2.10}$$

$$\tau = h^{1/3}\psi$$

is an approximation which gives the field (for horizontal polarization) in the region of the shadow boundary far behind a large cylinder. Our τ is an approximation to the g used there. Here the subscript ρ on $[\exp(-ix) + S_1]_\rho$ means that the quantity within the brackets is to be computed as though it corresponded to a half-plane with its edge at the crest of the parabolic cylinder, so that ρ, ψ are to be used in (2.3) instead of r, φ. Also,

$$\Psi(\tau) = 2i^{-1/3} \int_0^\infty \frac{Ai(u) \exp(i^{-1/3}u\tau)\, du}{Ai(u) - iBi(u)} + 2i \int_0^\infty \frac{Ai(u) \exp(iu\tau)\, du}{Ai(u) + iBi(u)} \tag{2.11}$$

where $Ai(u)$ and $Bi(u)$ are Airy integrals defined by equations (13.12) and (13.16), and tabulated in reference.[11] In this paper we find it convenient to use the Airy integrals instead of the related Bessel functions

---

[11] The Airy Integral, Brit. Asso. Math. Tables, Part — Vol. B (Cambridge, 1946).

of order ⅓. As in (2.3), the fractional powers of i are made precise by taking $i \equiv \exp(i\pi/2)$.

Three kinds of approximations have been made in the derivation of (2.10), namely those associated with the assumptions (1) that the angle ψ is small, (2) that h is large, and (3) that r/h^2 is large. The terms in $1/\psi$ and $1/\tau$ do not cause trouble at $\psi = 0$ because their infinities cancel each other.

The counterpart of (2.10) for vertical polarization is obtained from (2.10) by replacing E by H and $\Psi(\tau)$ by $\Psi_v(\tau)$, where the subscript v stands for "vertical"; and $\Psi_v(\tau)$ is given by (2.11) when $Ai(u)$ and $Bi(u)$ are replaced by their derivatives with respect to u.

Series for $\Psi(\tau) + 1/\tau$ and $\Psi_v(\tau) + 1/\tau$ which converge for negative (shadow) values of τ are given by Equations (7.31) and (7.53), respectively, with g in place of τ. Table 2.1 gives values of $\Psi(\tau)$ and $\Psi_v(\tau)$ which were obtained from the series for τ negative, and from numerical integration of (2.11) and its analogue for $\tau \geqq 0$.

When τ is large and positive Equations (7.35) and (7.55) show that

$$\begin{aligned} \Psi(\tau) + 1/\tau &\sim (i\pi\tau)^{1/2} \exp(-i\tau^3/12), \\ \Psi_v(\tau) + 1/\tau &\sim (i\pi\tau)^{1/2} \exp(i\pi - i\tau^3/12). \end{aligned} \tag{2.12}$$

When τ is large and negative the leading terms in (7.31) and (7.53) give

$$\begin{aligned} \Psi(\tau) + 1/\tau &\sim - i^{1/3}\, 2.03 \exp[(2.025 + i\, 1.169)\tau], \\ \Psi_v(\tau) + 1/\tau &\sim - i^{1/3}\, 3.42 \exp[(0.882 + i\, 0.509)\tau]. \end{aligned} \tag{2.13}$$

Now that we have expressions for the field what do they tell us? For one thing, they may be used to show that the field near the shadow

TABLE 2.1 — VALUES OF $\Psi(\tau)$ AND $\Psi_v(\tau)$

τ	$\lvert\Psi(\tau)\rvert$	arg. $\Psi(\tau)$	$\lvert\Psi_v(\tau)\rvert$	arg. $\Psi_v(\tau)$
3	3.13	−93.5°	3.16	+104.3°
2	2.21	−1.8°	2.80	192.4°
1.5	1.945	+21.6	2.44	211.3
1.0	1.715	+32.5	1.985	219.5
0.5	1.486	34.2	1.522	218.6
0	1.254	30.0	1.089	210.0
−0.5	1.030	22.9	0.724	193.7
−1.0	0.823	15.2	0.459	167.8
−1.5	0.648	8.48	0.317	130.6
−2.0	0.511	+3.79	0.281	92.0
−3.0	0.338	+0.12	0.288	45.1
−4.0	0.250	−0.12	0.264	22.3
−5.0	0.200	−0.02	0.221	9.71

boundary is almost the same as for a half-plane. Away from the shadow boundary, the field in the shadow can be interpreted as a "crest wave" which reduces to the "edge wave" for a half-plane. The crest wave decreases as an exponential function of ψ in the shadow instead of as $1/\varphi$ in the case of a half-plane. In other words it is much darker behind a parabolic cylinder than behind a half-plane — and the larger the cylinder the darker it is. (A glance at Fig. 2.8 shows that this statement must be qualified for vertical polarization by requiring the observer to be deep in the shadow.) As Figs. 2.7 and 2.8 show, deep in the illuminated region the crest wave behaves like the wave reflected (as computed by geometrical optics) from the illuminated portion of the cylinder.

Now we consider expressions for the surface currents. Let J and J_v be the densities of the conduction currents which flow on the surface of the perfectly conducting parabolic cylinder for the cases of horizontal and vertical polarizations, respectively. J is parallel to E and is perpendicular to the plane of Fig. 2.3 while J_v flows in the plane of the figure. J_v is positive when the current flows in the direction of increasing x. In Section 6 it is shown that when h is large, J and J_v are given approximately by

$$\zeta_0 J \approx \frac{\exp(-ix - i\gamma^3/3)}{\pi h^{1/3}} \int_0^\infty \left[\frac{i^{-2/3} \exp(-i^{1/3} u\gamma)}{Ai(u) - iBi(u)} + \frac{\exp(-iu\gamma)}{Ai(u) + iBi(u)} \right] du, \tag{2.14}$$

$$J_v \approx \frac{i \exp(-ix - i\gamma^3/3)}{\pi} \int_0^\infty \left[-\frac{\exp(-i^{-1/3} u\gamma)}{Ai'(u) - iBi'(u)} + \frac{\exp(-iu\gamma)}{Ai'(u) + i\,Bi'(u)} \right] du. \tag{2.15}$$

These expressions are obtained when the relations (13.17) for Airy integrals are used in equations (6.16) and (6.23). Here ζ_0 is the intrinsic impedance of free space. In the rational MKS system which we use $\zeta_0 = 120\pi$ ohms. The factor ζ_0 appears in (2.14) but not in (2.15) because we assume the incident wave for vertical polarization ($H = 1$, $E = \zeta_0 H = 120\pi$) to be 120π times stronger than the one for horizontal polarization ($E = 1$). The primes on $Ai(u)$ and $Bi(u)$ denote their derivatives with respect to u. The parameter γ depends upon the coordinate x of the point at which the current is being observed:

$$\gamma = x/2h^{2/3}. \tag{2.16}$$

Equations (2.14) and (2.15) hold only in the region of the crest of the cylinder and for large h. Under these conditions $x + \gamma^3/3$ is very nearly equal to the distance along the surface measured from the crest of the cylinder.

An expression equivalent to the one for J_v in (2.15) has been derived and tabulated by V. Fock.[4]

Series for $\zeta_0 J$ and J_v which converge for positive (shadow) values of γ are given by equations (6.17) and (6.24). When γ is large and negative the application of the method of steepest descent to integrals (6.16) and (6.23) leads to

$$\begin{aligned} \zeta_0 J &\approx -(x/h)e^{-ix}\,[1 + i/4\gamma^3 + \cdots], \\ J_v &\approx 2e^{-ix}\,[1 - i/4\gamma^3 + \cdots], \end{aligned} \tag{2.17}$$

in which $x/h = 2\gamma h^{-1/3}$.

Table 2.2 gives values of $h^{1/3}\zeta_0 J$ exp (ix) and J_v exp (ix). The values of J for $\gamma > 0$ were computed from the series, and the ones for $\gamma \leqq 0$ were obtained by numerical integration of (2.14). The entries for J_v were taken from the more extensive table given by Fock.[4] In order to express his results in our terms it is necessary to use the fact that the radius of curvature at the vertex of the parabola is $2h$. A change in the sign of i is also necessary because the time enters Fock's work through exp $(-i\omega t)$ instead of exp $(i\omega t)$. The values shown were checked for $\gamma > 0$ by the series and for $\gamma \leqq 0$ by numerical integration of (2.15)

Fock's table shows that by the time γ has reached -2 the value of J_v exp (ix) has become 1.982 at an angle of +1.45 degrees. This is close to the limiting value of 2 predicted at $\gamma = -\infty$ by (2.17).

It will be noted that, for large values of h, J is smaller than J_v by

TABLE 2.2 — SURFACE CURRENT DENSITIES

γ	$h^{1/3}\zeta_0 J$ exp $(ix + i\gamma^3/3)$		J_v exp $(ix + i\gamma^3/3)$	
	modulus	Argument in degrees	mod.	Arg.
-1.0	2.16	-25.9	1.861	$-15.43°$
-0.5	1.38	-16.8	1.682	$+1.52$
0.0	0.77	-30.0	1.399	0.00
0.3	0.515	-44.8	1.197	-6.06
0.6	0.327	-62.9	0.991	-14.23
1.0	0.167	-90.1	0.738	-26.63
1.5	0.066	-125.9	0.488	-42.57
2.0	0.025	-161.6	0.315	-57.98
3.0	0.0033	-230.7	0.130	-87.57
4.0	0.00043	-298.0	0.054	-116.75

the order of $h^{-1/3}$ when γ is of moderate size. It will be shown later that the current density decreases exponentially as one moves into the shadow, and that its rate of decrease is related to that of the field as shown in Fig. 2.6.

We now take up the detailed discussion of the expressions for the field and the current density. It is convenient to consider the current density first. When a plane wave strikes a perfectly conducting plane, the surface current is proportional to the tangential component of H in the incident wave, and flows at right angles to it. In the rational MKS units we are using, the surface current density is two times the incident tangential H. When we consider the illuminated side of a large parabolic cylinder and calculate the current density by doubling the tangential component of the incident H we obtain the approximations

$$\begin{aligned} \zeta_0 J &\approx -2x(4h^2 + x^2)^{-1/2} e^{-ix}, \\ J_v &\approx 2e^{-ix}, \end{aligned} \tag{2.18}$$

which hold when x is large and negative. When h is very large but $x/2h$ small these formulas agree with the leading terms of (2.17) which were obtained from our integrals for the current density.

Expressions for the current density deep in the shadow may be obtained from the leading terms of the convergent series by letting γ become large and positive. The exponential decrease is found to be

$$\begin{aligned} |\zeta_0 J| &\approx 1.43h^{-1/3} \exp(-1.013xh^{-2/3}), \\ |J_v| &\approx 1.83 \exp(-0.44xh^{-2/3}), \end{aligned} \tag{2.19}$$

where the numbers appearing in these equations are associated with the smallest zeros of $Ai(u)$ and $Ai'(u)$, respectively. These formulas for a large cylinder are roughly similar to those for propagation over a smooth earth. The radius of curvature at the crest of the cylinder is $2h$. Setting this equal to the radius of the earth gives an exponential rate of decrease for J and J_v which is the same as that over a smooth earth for the two polarizations. Of course, the coefficients multiplying the exponential functions are different. This agreement is not surprising since the Airy integrals are closely related to the Hankel functions of order $\frac{1}{3}$ used in the smooth earth theory.

The surface current densities as a function of the distance $h - y$ below the crest for $h = 1000$ and for $h = 0$ are shown in Fig. 2.4. The equation of the cylinder shows that $h - y = x^2/4h$ so that, from (2.19), $\zeta_0 J$ and J_v decrease in proportion to $h^{-1/3} \exp[-2.025h^{-1/6}(h - y)^{1/2}]$ and $\exp[-.88h^{-1/6}(h - y)^{1/2}]$, respectively, far down in the shadow.

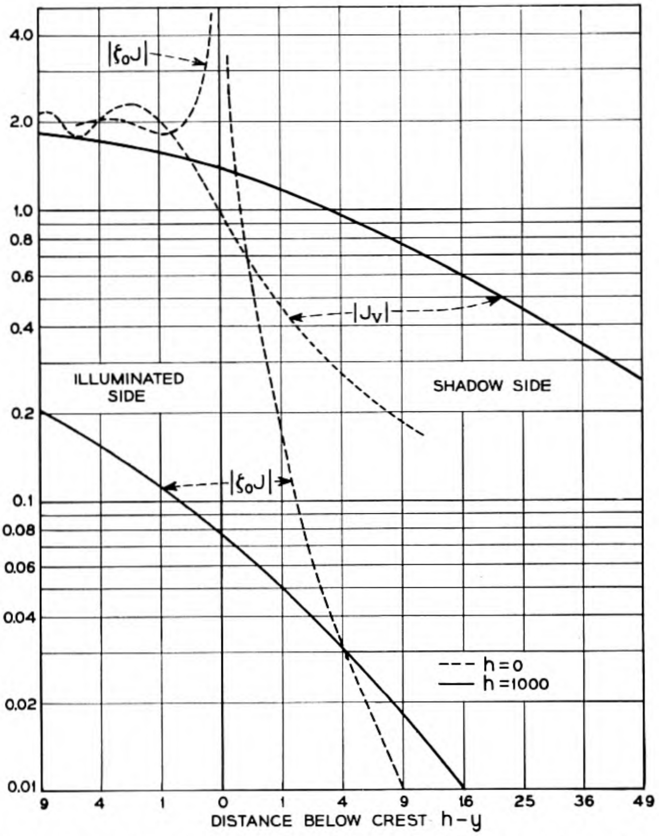

Fig. 2.4 — The surface current density is plotted as a function of the vertical distance below the crest or edge. The curves for $h = 1000$ and $h = 0$ are obtained from Table 2.2 and equations (2.20), respectively. Here, as always, the units are such at $\lambda = 2\pi = 6.28 \ldots$

The equations used to compute the curves marked $h = 0$ are

$$\zeta_0 J = (i\pi r)^{-1/2}\left[e^{-ir} \mp 2ir^{1/2}\int_{\pm\sqrt{r}}^{\infty} e^{-it^2}dt\right], \qquad J_v = 2(i/\pi)^{1/2}\int_{\pm\sqrt{r}}^{\infty} e^{-it^2}dt, \tag{2.20}$$

where the upper signs are for the shadow side and the lower ones for the illuminated side. The computations are made easier by the relations

$$(\zeta_0 J)_- - (\zeta_0 J)_+ = 2,$$
$$(J_v)_- + (J_v)_+ = 2,$$

where the subscripts "$-$" and "$+$" denote opposite points on the illuminated side and shadow side, respectively, of the half-plane. These relations follow from (2.20).* The radius vector r from the origin is equal to $-y$ on the half-plane. Equations (2.20) follow quite readily from (2.3). The values of J and J_v for an arbitrary angle of incidence and $h = 0$ are given by expressions (6.6) and (6.22), respectively.

All of the curves in Fig. 2.4, even $| \zeta_0 J |$ for $h = 1{,}000$, eventually approach the value 2 far down on the illuminated side. It may be shown that $| J_v |$ and $| \zeta_0 J |$ for the half-plane decrease like $(\pi r)^{-1/2}$ and $1/(2\pi^{1/2} r^{3/2})$, respectively, deep in the shadow. Hence as we go to the right in Fig. 2.4, the dashed curves will eventually cross over and lie above the solid curves, which decrease exponentially. The larger h, the lower and flatter is the curve for $| \zeta_0 J |$.

Now we turn to the diffraction field at points far to the right of the cylinder. When $| \psi | \ll 1$, so that we are not too far from the shadow boundary, and h is large, the field is given by (2.10), or by its analogue for vertical polarization. In order to get acquainted with (2.10) we first examine the field when $| \psi | \ll 1$ but $\psi^2 \rho \gg 1$.

When we are so far behind the cylinder that $\psi^2 \rho \gg 1$ even though $| \psi | \ll 1$, the asymptotic expressions (2.4) show that

$$[e^{-ix} + S_1]_\rho \sim \begin{cases} c(\rho)/\psi, & \psi \text{ negative (shadow)} \\[2ex] e^{-ix} + \dfrac{c(\rho)}{\psi}, & \psi \text{ positive} \end{cases} \tag{2.21}$$

Substitution of (2.21) in (2.10) gives

$$E \sim \begin{cases} c(\rho) h^{1/3} \left(\Psi(\tau) + \dfrac{1}{\tau} \right) \exp\,(i\tau^3/3), & \psi < 0 \\[2ex] c(\rho) h^{1/3} \left(\Psi(\tau) + \dfrac{1}{\tau} \right) \exp\,(i\tau^3/3) + e^{-ix}, & \psi > 0 \end{cases} \tag{2.22}$$

The presence of $c(\rho)$ shows that the total wave may be regarded as the sum of the incident wave and a wave spreading out from the crest. The crest wave is the analogue of the edge wave, $c(r)/\varphi$, for the half-plane. In fact, when we are in the region where the $1/\tau$ in (2.22) is the most important term, the crest wave is approximately

$$c(\rho)/\psi \tag{2.23}$$

---

* They also follow from superposition and consideration of the symmetry of the currents produced on the half-plane $y < 0$, $x = 0$ when $-A$ is impressed. Here A denotes the system of currents which flows in the upper half-plane $y > 0$, $x = 0$ when the incident wave falls on a complete plane at $x = 0$.

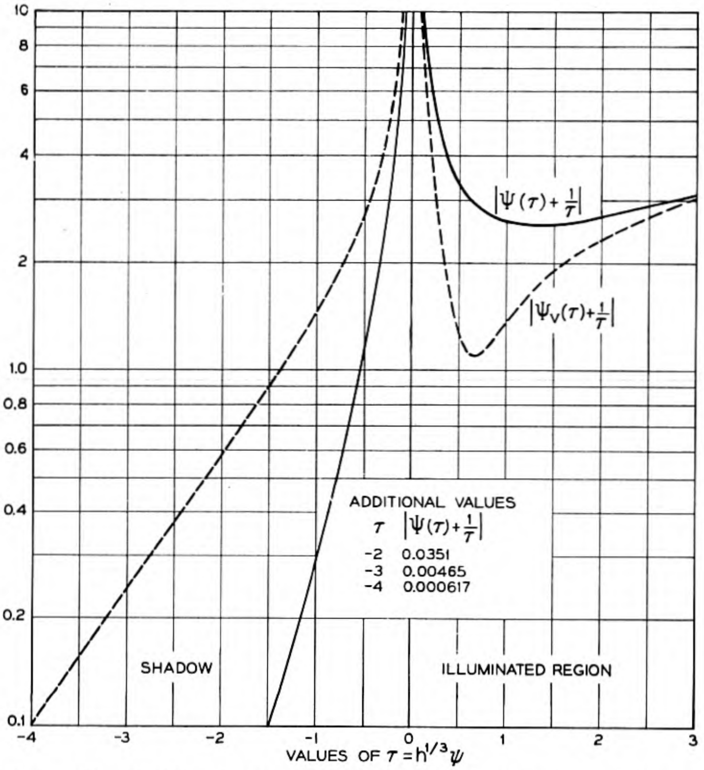

Fig. 2.5 — The amplitude of the crest wave may be obtained from these curves and expressions (2.24). Here $\tau = h^{1/3}\psi$ where ψ is small. However ρ must be large enough to make $\psi^2\rho \gg 1$.

and this corresponds to a half-plane with its edge at the crest of the cylinder. τ may be small even though we are considering $|\psi|$ to be large enough to make (2.21) and (2.22) hold, i.e. large enough to make $|\psi|\rho^{1/2} \gg 1$. Indeed, multiplying by $h^{1/3}$ gives $|\tau|\rho^{1/2} \gg h^{1/3}$ which may be achieved for small values of τ by making ρ large enough.

It follows from (2.22) and its analogue for vertical polarization that the amplitudes of the crest waves are

$$\begin{aligned} &\text{(hp)} \qquad (2\pi\rho)^{-1/2}\, h^{1/3}\, |\Psi(\tau) + 1/\tau|, \\ &\text{(vp)} \qquad (2\pi\rho)^{-1/2}\, h^{1/3}\, |\Psi_v(\tau) + 1/\tau|, \end{aligned} \tag{2.24}$$

where the expression (2.9) for $c(\rho)$ has been used. The last factors in (2.24) may be computed from Table 2.1. They are plotted in Fig. 2.5.

When we go deep down into the shadow where τ is large and negative we see from (2.13) that

$$\begin{aligned} |\,\Psi(\tau) + 1/\tau\,| &\sim 2.03\, e^{2.025\tau}, \\ |\,\Psi_v(\tau) + 1/\tau\,| &\sim 3.42\, e^{0.882\tau}, \end{aligned} \tag{2.25}$$

so that the absolute value of the field is

$$\begin{aligned} &(\mathrm{hp}) \qquad |\,E\,| \sim (2\pi\rho)^{-1/2}\, h^{1/3}\, 2.03 \exp\,(2.025\, h^{1/3}\psi), \\ &(\mathrm{vp}) \qquad |\,H\,| \sim (2\pi\rho)^{-1/2}\, h^{1/3}\, 3.42 \exp\,(0.882\, h^{1/3}\psi). \end{aligned} \tag{2.26}$$

where the angle ψ is negative. Thus, as Artmann[6] has pointed out, the field decreases exponentially as we go into the shadow. The larger h is, the more rapid is the decrease. This supports the statement made earlier that it is darker behind a large cylinder than behind a half-plane.

Comparison of the expressions for the current density and field strength for the shadow regions shows that there is a simple approximate relation between them. Near the crest of the cylinder, where x is small, the radius of curvature is nearly $2h$. Hence the tangent to the parabola drawn from the point P (located at (ρ, ψ) deep in the shadow) touches the parabola at T where x is approximately $-2h\psi$. This is shown in Fig. 2.6. Replacing x by $-2h\psi$ in the expressions (2.19) shows that the current density at T is proportional to the field at P as given by (2.26). It follows that

$$\begin{aligned} &(\mathrm{hp}) \qquad |\,E/\zeta_0 J\,| \sim 1.41\, h^{2/3}\, (2\pi\rho)^{-1/2} \\ &(\mathrm{vp}) \qquad |\,H/J_v\,| \sim 1.87\, h^{1/3}\, (2\pi\rho)^{-1/2}. \end{aligned} \tag{2.27}$$

This leads us to picture the field at P as being produced principally by the surface currents around T. The effect of the stronger currents

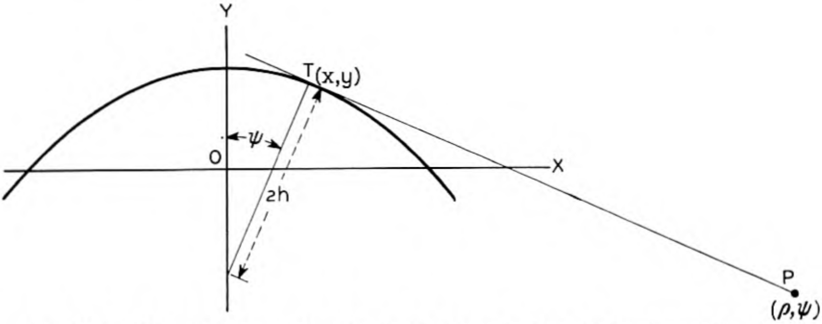

Fig. 2.6 — The field strength at point P (deep in the shadow) specified by the polar coordinates (ρ, ψ) is nearly proportional to the current density at the tangent point T specified by the rectangular coordinates (x, y).

closer to the crest is perhaps blocked out by the curvature of the cylinder. For comparison with the horizontal polarization case we note that E at (ρ, ψ) for an infinitely long current filament at the origin $\rho = 0$ is given by

$$|E/\zeta_0 I| \sim .5(2\pi\rho)^{-1/2} \tag{2.28}$$

where I is the current carried by the filament and the frequency is is such that $\lambda = 2\pi$. There is some difficulty with the picture for vertical polarization because the current element at T points directly towards P and hence should produce very little field there. This is perhaps associated with the fact that the (vp) ratio in (2.27) is smaller than the (hp) ratio by approximately the factor $h^{-1/3}$.

We now leave the shadow region and consider the field at points well inside the illuminated region. Fig. 2.5 shows that for large positive values of τ the amplitude of the crest wave tends to increase with τ. The asymptotic expressions (2.12) show that when τ is large and positive

$$|\Psi(\tau) + 1/\tau| \approx |\Psi_v(\tau) + 1/\tau| \sim (\pi\tau)^{1/2} = (\pi\psi)^{1/2}h^{1/6}, \tag{2.29}$$

and hence the amplitude of the crest wave deep in the illuminated region is, from (2.22) and its analogue,

$$\begin{aligned} &\text{(hp)} \qquad |E - e^{-ix}| \sim (2\pi\rho)^{-1/2}(\pi\psi h)^{1/2}, \\ &\text{(vp)} \qquad |H - e^{-ix}| \sim (2\pi\rho)^{-1/2}(\pi\psi h)^{1/2}. \end{aligned} \tag{2.30}$$

Since (2.30) is derived from the general expression (2.10) it is subject to the restrictions mentioned just below equation (2.11). In particular the angle ψ should be small (but we must still have $\psi^2\rho \gg 1$ as assumed in (2.22)). When ψ is positive, an application of the laws of geometrical optics to determine the reflection from the curved surface of the parabolic cylinder leads to the expressions[12]

$$\begin{aligned} &\text{(hp)} \quad |E - e^{-ix}| \sim \left[\frac{h \tan(\psi/2)}{\rho}\right]^{1/2} \sec(\psi/2), \qquad \psi > 0 \\ &\text{(vp)} \quad |H - e^{-ix}| \sim \left[\frac{h \tan(\psi/2)}{\rho}\right]^{1/2} \sec(\psi/2), \qquad \psi > 0 \end{aligned} \tag{2.31}$$

for the reflected wave. When ψ is small these expressions reduce to (2.30) as they should.

Expressions (2.31) may also be obtained from our analysis by start-

---

[12] In our two-dimensional case the calculation of the required radius of curvature, etc., is not difficult. General theorems dealing with problems of this sort and references to earlier work are given in the paper, A General Divergence Formula, H. J. Riblet and C. B. Barker, J. Appl. Phys. **19**, pp. 63–70, 1948.

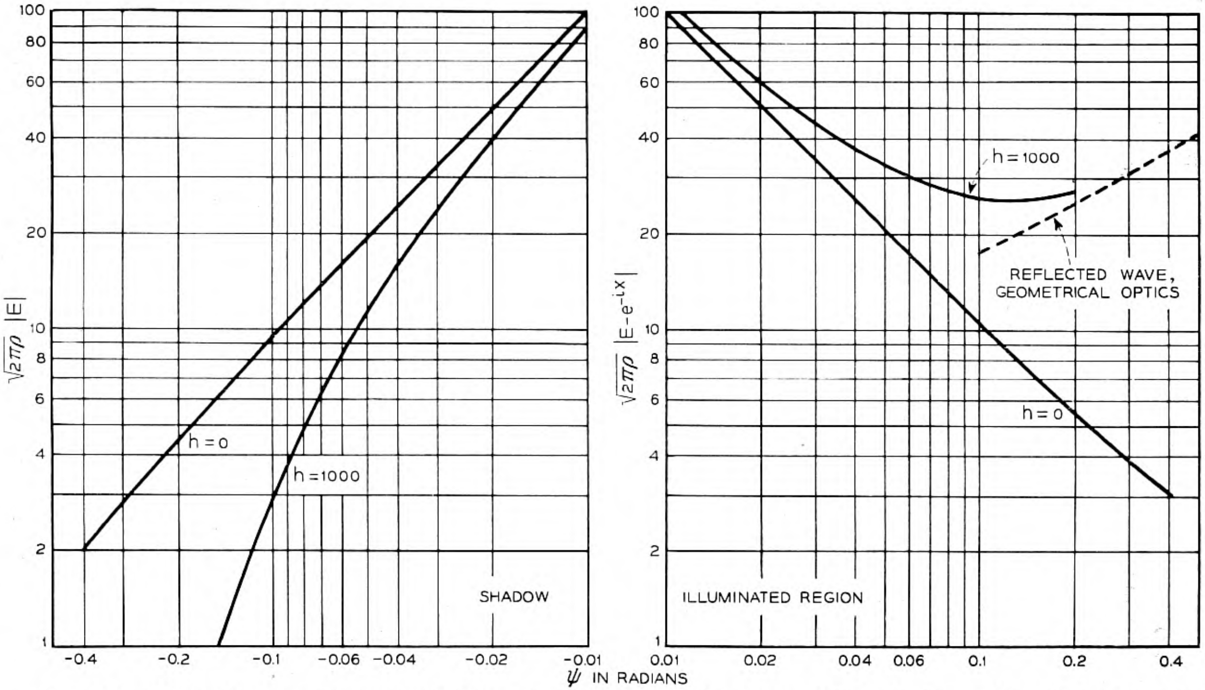

Fig. 2.7 — Strength of crest wave for horizontal polarization. The curves fail for $|\psi| < \rho^{-1/2}$, and the $h = 1000$ curve becomes less reliable as ψ increases. The exponential decrease deep in the shadow is given by equation (2.26). The dashed curve for the reflected wave is computed from equation (2.31).

ing with equations (7.36) and (7.56). Furthermore, it may be verified that the phase angles of the reflected waves as computed from (7.36) and (7.56) agree with those computed from geometrical optics when reflection coefficients of -1 and $+1$ are assumed for hp and vp, respectively.

The amplitudes of the crest waves for $h = 1{,}000$ and $h = 0$ are shown for hp in Fig. 2.7 and for vp in Fig. 2.8. Of course, when $h = 0$ the crest wave reduces to the edge wave from a half-plane. The curves for $h = 1{,}000$ were computed from equations (2.24) and the curves of Fig. 2.5 (or their equivalent when τ is small). The curves for $h = 0$ were computed from

$$\begin{aligned}
&|E| \sim (2\pi\rho)^{-1/2}\left|\frac{1}{2\sin(\psi/2)}+\frac{1}{2\cos(\psi/2)}\right|, \qquad \psi<0\\
&\text{(hp)}\\
&|E - e^{-ix}| \sim (2\pi\rho)^{-1/2}\left|\frac{1}{2\sin(\psi/2)}+\frac{1}{2\cos(\psi/2)}\right|, \qquad \psi>0\\
&|H| \sim (2\pi\rho)^{-1/2}\left|\frac{1}{2\sin(\psi/2)}-\frac{1}{2\cos(\psi/2)}\right|, \qquad \psi<0\\
&\text{(vp)}\\
&|H - e^{-ix}| \sim (2\pi\rho)^{-1/2}\left|\frac{1}{2\sin(\psi/2)}-\frac{1}{2\cos(\psi/2)}\right|, \qquad \psi>0
\end{aligned} \tag{2.32}$$

which follow from (2.1), (2.2), (2.4) and (2.6).

From equation (2.21) onward we have been discussing the field for values of ψ and ρ such that $\rho\psi^2 \gg 1$. For these values the concept of the crest wave is helpful in visualizing the behavior of the field. Now we consider the field at points close to the boundary of the geometric shadow far behind the cylinder. This is the region in which Artmann[6] was especially interested. His results for the shift of the field may be obtained from (2.10) and its analogue by taking $|\psi|$ to be very small.

At the shadow boundary $\psi = 0$ and $[\exp(-ix) + S_1]_\rho = \frac{1}{2}$. Hence the region of interest at present is in the neighborhood of the point point $t_1 = 0$, $|\exp(-ix) + S_1| = \frac{1}{2}$ of Fig. 2.2. A magnified view of this region showing the shift of the field is given in Fig. 2.9. The figure shows that, for a given value of $\rho\psi$, $|E|$ for hp is less than $|H|$ for vp. As Artmann has pointed out, this is to be expected since the reflection coefficient for E (hp) is roughly -1 and the reflected wave therefore

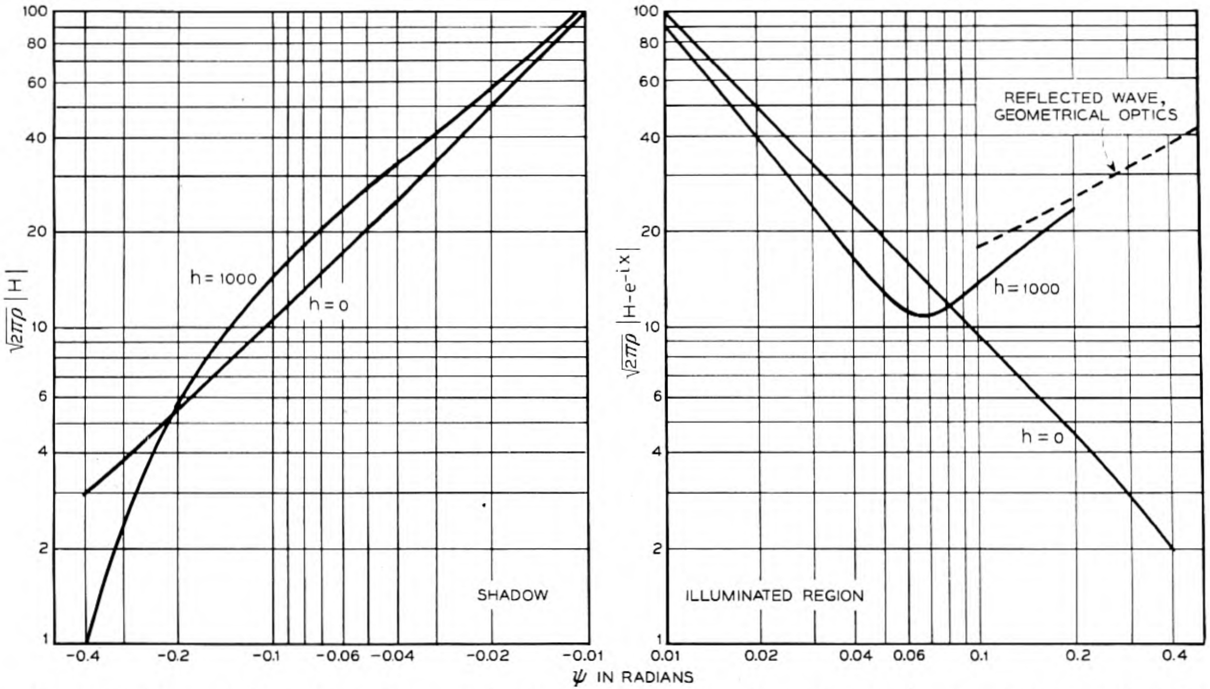

Fig. 2.8 — Strength of crest wave for vertical polarization. The remarks made in the caption of Fig. 2.7 also hold here. Incidentally, a value of $h = 1000$ corresponds to a radius of curvature of $2000/2\pi = 318$ wavelengths at the crest.

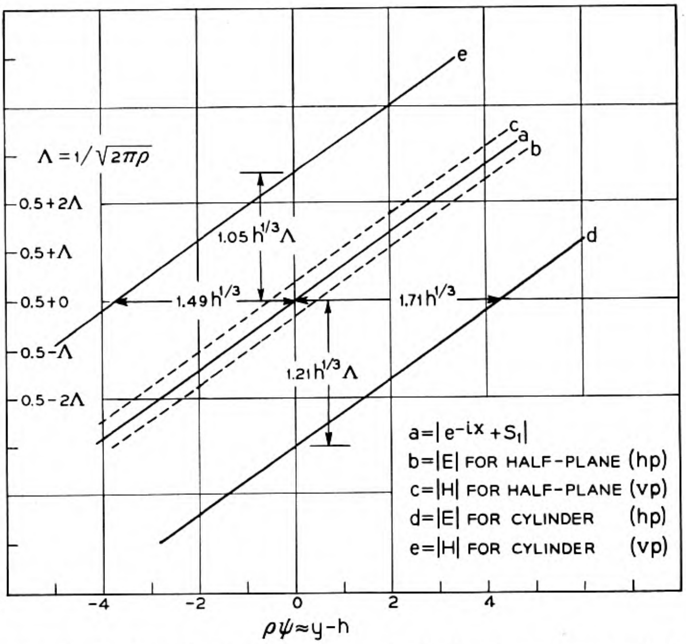

Fig. 2.9 — Behavior of $|E|$ and $|H|$ on the shadow boundary far behind the half-plane or parabolic cylinder. This is a magnified view of the region around $t_1 = 0$, $|\exp(-ix) + S_1| = \frac{1}{2}$ in Fig. 2.2.

tends to cancel the direct wave when ψ is very small. On the other hand, the reflection coefficient for H (vp) is $+1$ and the reflected wave tends to add to the direct wave.

The distances $1.71h^{1/3}$ and $-1.49h^{1/3}$ appearing in Fig. 2.9 are the amounts, measured in units for which the wavelength is 2π, by which $|E|$ and $|H|$ are shifted by the curvature of the parabolic cylinder. If $y' - h'$ is the shift in meters for $|E|$ and if the radius of curvature of the crest is $a = 2h'$ meters, Fig. 2.9 gives $\beta(y' - h') = 1.71\,(\beta h')^{1/3} = 1.71\,(\beta a/2)^{1/3}$ where $\beta = 2\pi/\lambda$. Thus $y' - h' = 0.399\lambda\,(a/\lambda)^{1/3}$ meters. The corresponding shift for $|H|$ is $-0.346\lambda(a/\lambda)^{1/3}$ meters. Artmann gives the values 0.39 and -0.20 for the respective coefficients. The discrepancy between -0.346 and -0.20 is cause for worry because it seems to indicate either a mistake in our work, which I have been unable to locate, or a shortcoming in the approximations made by Artmann for the case of vertical polarization.

As h approaches zero the parabolic cylinder becomes a half-plane and the curves d and e should approach curves b and c, respectively. According to Fig. 2.9 both d and e approach curve a. This failure is an indication of the errors introduced by the approximations used in the derivation of (2.10) and its analogue.

3. RADIO PROPOGATION OVER A SUCCESSION OF RIDGES ON THE EARTH'S SURFACE

The results mentioned in Section 1 concerning propagation over a succession of ridges may be obtained from the expressions and curves of Section 2 as follows: Consider the situation shown in Fig. 3.1. Let a radio wave start out from a transmitter at T. We assume that by the time it arrives at the first ridge at P it has become equivalent to a plane wave of amplitude A/ℓ traveling in the direction TP, where A is a constant depending on the strength of the transmitter. For the sake of simplicity the waves reflected from the ground are neglected. In a more careful study they would have to be included.*

In order to calculate the strength of the wave at the second ridge, we assume it to be a crest wave coming from P. Let G denote the value of $| E |$ (we assume the case of horizontal polarization since the reflection coefficient of physical materials approaches -1 for almost grazing incidence) at Q corresponding to a plane wave of unit amplitude incident on P. From Fig. 3.1 we see that the values of ψ and ρ to be used in computing G are $\psi \approx -\ell/R$, $\rho = 2\pi\ell/\lambda$, $\lambda =$ wavelength, $R =$ radius of earth. The value of h depends upon the radius of curvature of the ridge: $2h = 2\pi$ (radius of curvature)$/\lambda$.

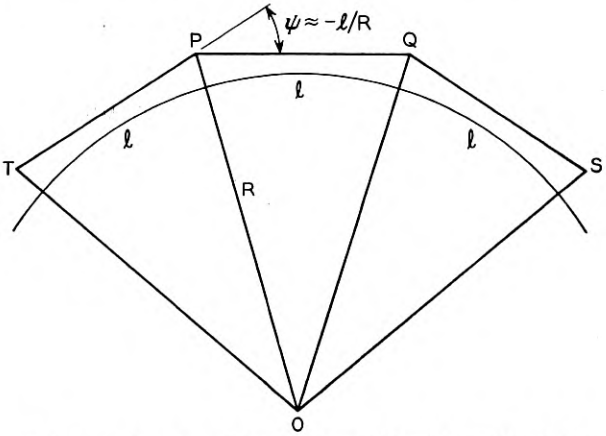

Fig. 3.1 — Diagram showing ridges at P and Q which diffract the radio wave starting from T so that a portion of it is received at S.

---

* A method for doing this (for one hill) is given in Reference 1, page 417.

The amplitude of the wave striking the ridge at Q is $AG/\ell\sqrt{2}$. The $\sqrt{2}$ comes from the horizontal sidewise spreading of the wave in going from ℓ to 2ℓ. If we were dealing with the energy instead of the amplitude, the factor would be 2 instead of $\sqrt{2}$. When this wave is assumed to be plane and traveling in the PQ direction, similar reasoning shows that the amplitude of the disturbance at the receiver S is $AG^2/\ell\sqrt{3}$.

If, instead of two ridges at P and Q, as shown in Fig. 3.1, there are N ridges between the transmitter at T and the receiver at S, the amplitude of the radio wave at S is $AG^N/\ell\sqrt{N+1}$. The distance between T and S is approximately $(N+1)\ell$, and the free space amplitude at S is $A/(N+1)\ell$. Hence

$$\frac{\text{Actual Amplitude at S}}{\text{Free Space Amplitude at S}} = G^N(N+1)^{1/2}. \tag{3.1}$$

The actual field at S is therefore

$$20\,N\log_{10}(1/G) - 10\log_{10}(N+1) \tag{3.2}$$

db below the free space field.

As an example, let us assume a distance of 280 miles between the transmitter and receiver, and a distance of 40 miles between successive ridges. This gives $N = 6$. For a wavelength of 10 meters and a radius of curvature of 100 meters for the diffracting ridges, the formulas of Section 2 show that the ridges behave like half-planes and that $G \approx 0.227$. Equation (3.2) then says that, for a distance of 280 miles and a wavelength of 10 meters the actual field should be about 69 db below the free space field. Although this is in fair agreement with the experimental results, calculations for other distances indicate that the field strengths predicted by (3.2) tend to be smaller than the ones observed.

When the work is carried through for $\lambda = 1$ meter and a distance of 280 miles, (3.2) says that the field is 120 db below free space. The observed fields are 70 ± 15 db below the free space value.

These figures suggest that the roughness of the earth's surface might possibly account for transmission far beyond the horizon for wavelengths of the order of 10 meters. For wavelengths of the order of 1 meter either the approximations leading to (3.2) break down or some other explanation is required.

4. SERIES FOR THE ELECTROMAGNETIC FIELD

Here we set down series for the electromagnetic field when a plane wave strikes a perfectly conducting parabolic cylinder. Since Epstein's classical work deals with the general case of finite conductivity, the series we use are special cases of the ones discussed by him.

The parabolic coordinates (ξ, η) which we shall use are related to the rectangular coordinates (x, y) and polar coordinates (r, φ) as follows:

$$\begin{aligned} x + iy &= (\xi + i\eta)^2/2i = r\,e^{i\varphi}, \\ x &= \xi\eta = r\cos\varphi, \qquad y = (\eta^2 - \xi^2)/2 = r\sin\varphi, \\ r &= (x^2 + y^2)^{1/2} = (\xi^2 + \eta^2)/2, \\ dx^2 + dy^2 &= (\xi^2 + \eta^2)\,(d\xi^2 + d\eta^2) = 2r(d\xi^2 + d\eta^2), \\ \xi &= (2r)^{1/2}\cos(\varphi/2 + \pi/4), \\ \eta &= (2r)^{1/2}\sin(\varphi/2 + \pi/4). \end{aligned} \tag{4.1}$$

The lines η = constant are a series of downward-curving confocal parabolas having their focus at the origin. The parabolic cylinder $x^2 = 4h(h - y)$ is given by $\eta^2 = 2h$. This special value of η will be called η_0:

$$\eta_0 = (2h)^{1/2} \geqq 0, \qquad h = \eta_0^2/2. \tag{4.2}$$

When $\eta_0 = 0$, the cylinder reduces to the half-plane $x = 0$, $y \leqq 0$. The lines ξ = constant are halves of upward-curving confocal parabolas having their common focus at the origin. Outside the cylinder $\eta > \eta_0 \geqq 0$, so η is always positive in our work. ξ is positive in the half-plane $x > 0$ and negative in $x < 0$.

For much of our work we shall assume the incident wave to come in at the angle θ, $0 \leqq \theta \leqq \pi$, as shown in Fig. 4.1. As mentioned in Section

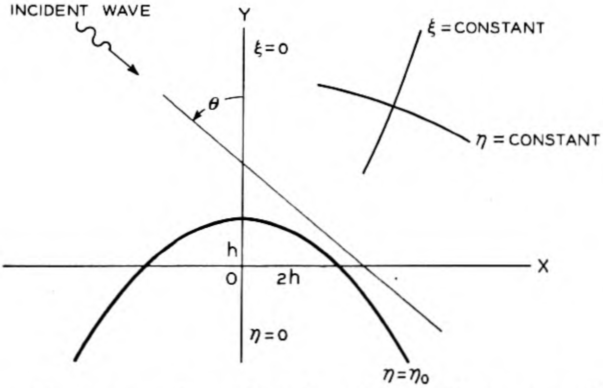

Fig. 4.1 — This diagram shows the angle θ of the incident wave and the surface of the perfectly conducting cylinder $x^2 = 4h(h - y)$ (or $\eta = \eta_0$).

2, the field quantities are assumed to depend upon the time through the factor $\exp(i\omega t)$ where ω is the radian frequency.

The wave equations for horizontal and vertical polarization are, respectively,

$$\frac{\partial^2 E}{\partial \xi^2} + \frac{\partial^2 E}{\partial \eta^2} + (\xi^2 + \eta^2)E = 0 \tag{4.3}$$

$$\frac{\partial^2 H}{\partial \xi^2} + \frac{\partial^2 H}{\partial \eta^2} + (\xi^2 + \eta^2)\, H = 0 \tag{4.4}$$

where, as explained in Section 2, the unit of length has been chosen so that the wavelength $\lambda = 2\pi$. On the surface of the perfectly conducting cylinder, i.e. for $\eta = \eta_0$, we must have $E = 0$ and $\partial H/\partial \eta = 0$. When E and H are known the remaining components of the field may be computed from Maxwell's equations.

Special solutions of (4.3) (and (4.4)) are

$$\exp\,[i(\eta^2 - \xi^2)/2]\; U_n(\xi i^{1/2})\; U_n(\eta i^{-1/2}), \tag{4.5}$$

$$\exp\,[i(\eta^2 - \xi^2)/2]\; U_n(\xi i^{1/2})\; W_n(\eta i^{-1/2}), \tag{4.6}$$

where $i^{1/2}$ stands for $\exp\,(i\pi/4)$ and $U_n(z)$, $W_n(z)$ satisfy the equation

$$\frac{d^2 T_n(z)}{dz^2} - 2z\,\frac{dT_n(z)}{dz} + 2nT_n(z) = 0. \tag{4.7}$$

Another solution of (4.7) with which we shall be concerned is $V_n(z)$. These three solutions are defined by contour integrals of the form

$$(2\pi i)^{-1} \int \exp\,[f(t)]\, dt \qquad \text{where} \qquad f(t) = -t^2 + 2zt - (n + 1)\log t.$$

The path of integration for $U_n(z)$ comes in from $-\infty$ where $\arg t = -\pi$, encircles the origin counterclockwise and runs out to $-\infty$ with $\arg t = \pi$. The path for $V_n(z)$ runs from $-\infty$ where $\arg t = \pi$ to $+\infty$ where $\arg t = 0$, and the path for $W_n(z)$ runs from $+\infty$ to $-\infty$ where $\arg t = -\pi$. The integrals are written at greater length in equations (9.1) and the paths of integration are shown in Fig. 9.1. Since the paths may be joined to form a closed path containing no singularities of the integrand it follows that

$$U_n(z) + V_n(z) + W_n(z) = 0. \tag{4.8}$$

When n is a non-negative integer

$$U_n(z) = H_n(z)/n! = \frac{(-)^n}{n!}\, e^{z^2} \frac{d^n}{dz^n}\, e^{-z^2} \tag{4.9}$$

where $H_n(z)$ is Hermite's polynomial. When z becomes very large the leading terms in (9.17) and (9.16) give

$$U_n(z) \sim (2z)^n/n!, \tag{4.10}$$

$$W_n(\eta i^{-1/2}) \sim i(i^{1/2}/\eta)^{n+1}\, e^{-i\eta^2}/2\pi^{1/2}. \tag{4.11}$$

In order to obtain a series for the incident wave

$$\exp\,[-ix \sin\theta + iy \cos\theta]$$

shown in Fig. 4.1 we consider the special case $\theta = 0$. In this case the wave is simply $\exp(iy)$ or $\exp\,[i(\eta^2 - \xi^2)/2]$ and may be obtained by setting $n = 0$ in (4.5). This suggests that the incident wave may be expressed as the sum of terms like (4.5). The series turns out to be

$$\begin{aligned} \exp\,[-\, ix \sin\theta + iy\cos\theta] & \\ &= \exp\,[-\, i\xi\eta \sin\theta + i\cos\theta(\eta^2 - \xi^2)/2] \\ &= \exp\,[-\, izz' \sin\theta - \cos\theta(z^2 + z'^2)/2] \qquad (4.12) \\ &= e^{iy} \sec(\theta/2) \sum_{n=0}^{\infty} n!(-\, iw/2)^n U_n(z) U_n(z') \end{aligned}$$

where

$$\begin{aligned} w &= \tan(\theta/2), \\ z &= \xi i^{1/2}, \qquad (4.13) \\ z' &= \eta i^{-1/2}. \end{aligned}$$

This series has been studied by a number of writers. It goes back to Mehler[13] who obtained it by evaluating the integral

$$\pi^{-1/2}\, e^{x^2} \int_{-\infty}^{\infty} \exp\,[-\,(t - iy)^2 - (x + iat)^2]\, dt$$

first in closed form, and then as a series (by using the generating function $\exp\,[-\,(-iat)^2 + 2(-iat)x]$ for $H_n(x)$ and integrating termwise). This leads to

$$\begin{aligned} (1 - a^2)^{-1/2} \exp\left[\frac{2xya - (x^2 + y^2)a^2}{1 - a^2}\right] & \qquad (4.14) \\ &= \sum_0^{\infty} H_n(x) H_n(y)\; a^n/2^n n! \end{aligned}$$

which is equivalent to (4.12). Since (4.14) converges when $|a| < 1$, (4.12) converges when $|w| < 1$ or $|\theta| < \pi/2$.

---

[13] Reihenentwicklungen nach Laplaceschen Functionen höher Ordnung, J. Reine Angew., Math., **66,** pp. 161–176, 1866.

When the incident wave strikes the cylinder the reflected wave has some of the characteristics of a wave spreading radially outwards. Such a wave contains the factor $\exp(-ir) = \exp[-i(\xi^2 + \eta^2)/2]$. Consideration of the exponential factors in (4.6) and (4.11) suggests that the reflected wave may be expressed as the sum of terms of the form (4.6). The coefficients in this series are to be determined so that $E = 0$ or $\partial H/\partial\eta = 0$ at the surface $\eta = \eta_0$, the incident wave being represented by (4.12).

For the case of horizontal polarization this procedure gives

$$E = e^{iy} \sec(\theta/2) \sum_0^\infty n!(-iw/2)^n U_n(z)\, [U_n(z') - W_n(z')U_n(z_0')/W_n(z_0')] \tag{4.15}$$

$$E = \exp[-ix\sin\theta + iy\cos\theta] - e^{iy}\sec(\theta/2) \sum_0^\infty n!(-iw/2)^n U_n(z) W_n(z') U_n(z_0')/W_n(z_0') \tag{4.16}$$

for the complete field. These are special cases of Epstein's results. Here z_0' is the value of z' which corresponds to the surface of the cylinder:

$$z_0' = i^{-1/2}\eta_0 = (2h/i)^{1/2} \tag{4.17}$$

The entries for regions II and II′ (these are regions in the m-plane ($m = n + 1$) which, as Figs. 11.2 and 12.2 show, contain the large positive values of n) in Tables 12.2 and 12.4 of Section 12 may be used to show that as $n \to \infty$

$$\begin{aligned} V_n(z_0')/W_n(z_0') &\sim i^{-2n} \exp[2\eta_0(2in)^{1/2}], \\ U_n(z_0')/W_n(z_0') &= -1 - V_n(z_0')/W_n(z_0'), \\ U_n(z)W_n(z') &\sim -\frac{\exp[-iy - \eta(2n/i)^{1/2}]}{4[\Gamma(1 + n/2)]^2} \\ &\qquad \{\exp[-\xi(2n/i)^{1/2}] + i^{2n}\exp[\xi(2n/i)^{1/2}]\}. \end{aligned} \tag{4.18}$$

Since

$$n!/[\Gamma(1 + n/2)]^2 \sim 2^n\,(\pi n/2)^{-1/2}$$

the series in (4.15) and (4.16) converge if $|w| = |\tan\theta/2| < 1$.

Series for H similar to those of (4.15) and (4.16) may be obtained for the case of vertical polarization. The boundary condition at $\eta = \eta_0$ is now $\partial H/\partial\eta = 0$. It is convenient to introduce the functions $'U_n(z)$, $'V_n(z)$, $'W_n(z)$ defined by

$$'U_n(z) = -zU_n(z) + \partial U_n(z)/\partial z \tag{4.19}$$

and the two other equations obtained when U is replaced by V and W. The prime is placed in front of U instead of behind to avoid mistaking $'U_n(z)$ for $\partial U_n(z)/\partial z$. The function $'U_n(z')$ makes its appearance when $\partial H/\partial\eta$ is calculated for the boundary condition. Since $iy = -(z^2 + z'^2)/2$ we have

$$\frac{\partial}{\partial\eta}\, e^{iy}U_n(z') = i^{-1/2}e^{iy}\,'U_n(z'). \tag{4.20}$$

The analogues of (4.15) and (4.16) for vertical polarization are (assuming now that H for the incident wave is of unit amplitude).

$$H = e^{iy}\sec(\theta/2)\sum_0^\infty n!(-iw/2)^n U_n(z) \\ [U_n(z') - W_n(z')'U_n(z_0')/'W_n(z_0')], \tag{4.21}$$

$$= \exp[-ix\sin\theta + iy\cos\theta] \\ - e^{iy}\sec(\theta/2)\sum_0^\infty n!(-iw/2)^n U_n(z)W_n(z')'U_n(z_0')/'W_n(z_0'), \tag{4.22}$$

and these series converge if $|w| < 1$.

If the parabolic cylinder is merely a good conductor, instead of being perfect, the boundary conditions at $\eta = \eta_0$ are approximately[14] $E = -\zeta H_\xi$, $E_\xi = \zeta H$. Here E_ξ and H_ξ denote the ξ components of the electric and magnetic intensities and ζ is the intrinsic impedance

$$\zeta = [i\omega\mu/(g + i\omega\epsilon)]^{1/2} \tag{4.23}$$

of the cylinder material. ζ is assumed to be small compared to the intrinsic impedance $\zeta_0 = (\mu_0/\epsilon_0)^{1/2} = \omega\mu_0$ (since $\lambda = 2\pi$) of the external medium. In these expressions μ, ϵ, g are the permeability, dielectric constant, and conductivity of the cylinder; and μ_0 and ϵ_0 refer to the external medium.

When we set

$$\sigma = i^{-1/2}(\xi^2 + \eta_0^2)^{1/2}\,\zeta_0/\zeta, \\ \tau = i^{-1/2}(\xi^2 + \eta_0^2)^{1/2}\,\zeta/\zeta_0, \tag{4.24}$$

the boundary conditon for hp becomes $\sigma E = -\partial E/\partial z'$ at $z' = z_0'$. When σ is assumed to be constant we obtain

$$E = e^{iy}\sec(\theta/2)\sum_0^\infty n!(-iw/2)^n U_n(z) \\ \{U_n(z') - W_n(z')[\sigma U_n(z_0') + 'U_n(z_0')]/[\sigma W_n(z_0') + 'W_n(z_0')]\} \tag{4.25}$$

---

[14] *Electromagnetic Waves*, S. A. Schelkunoff, D. Von Nostrand Co., N. Y. (1943) p. 89. See also G. A. Hufford, Quart. Appl. Math. 9, pp. 391–403, 1952, where reference is made to the work of Leontovich and Fock.

which reduces to (4.15) when $\sigma \to \infty$. The constancy of σ may be achieved by either taking the properties of the cylinder material to change in a suitable way or, roughly, by taking η_0^2 (and hence h) to be so large that only the nearly constant values of σ at the crest of the cylinder have an effect on the result (assuming $\theta = \pi/2$, and restricting our attention to the region near the shadow boundary).

The corresponding expression for vertical polarization may be obtained from (4.25) by replacing E and σ by H and τ, respectively. We shall refer to (4.25) and its analogue later in connection with the field in the shadow (Section 7) and with Fock's[5] investigation of the surface currents on gently curved conductors (Section 6).

5. INTEGRALS FOR THE FIELD

When the curvature of the cylinder is small, i.e., when h is many wavelengths, the series of Section 4 converge slowly. The work initiated by G. N. Watson[15] on the smooth earth problem suggests that we convert the series into contour integrals with n as the complex variable of integration. When this is done we get an integral with the path of integration L_1 shown in Fig. 5.1. Thus, for example, expression (4.16) for E is transformed into

$$E = \exp\left[-ix \sin\theta + iy \cos\theta\right] - \frac{e^{iy} \sec \dfrac{\theta}{2}}{2i} \int_{L_1} \left(\frac{iw}{2}\right)^n \frac{\Gamma(n+1)}{\sin \pi n}\, U_n(z) W_n(z') U_n(z_0')\, dn / W_n(z_0'). \tag{5.1}$$

At first sight it seems that not much can be done with this integral because the integral obtained by deforming L_1 into L_2 does not converge (this is explained in the discussion of Table 5.1). However, some ex-

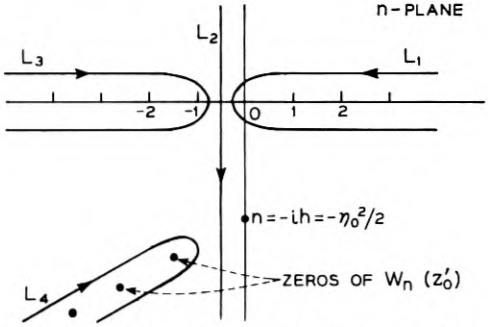

Fig. 5.1 — Paths of integration in the complex n-plane.

---

[15] Proc. Roy. Soc., London (A) **95**, p. 83, 1918.

perimentation shows that if we set $U_n(z_0') = -V_n(z_0') - W_n(z_0')$ in (4.16), the series splits into two series, one of which may be summed and the other may be converted into an integral along the path L_2 of Fig. 5.1:

$$\begin{aligned} E &= \exp\,[-ix \sin\theta + iy\cos\theta] + S_1 + S_2(h), \\ S_1 &= e^{iy} \sec(\theta/2) \sum_0^\infty n!(-iw/2)^n U_n(z) W_n(z'), \\ S_2(h) &= e^{iy} \sec(\theta/2) \sum_0^\infty n!(-iw/2)^n U_n(z) W_n(z') V_n(z_0')/W_n(z_0'). \end{aligned} \tag{5.2}$$

The series for S_1 may be summed by replacing $U_n(z)$ and $W_n(z')$ by their expressions (9.19) in terms of definite integrals, and interchanging the order of summation and integration. The resulting series may be summed and the integrations performed. The result is Sommerfeld's integral for a diffracted plane wave:

$$\begin{aligned} S_1 &= -(i/\pi)^{1/2} e^{-ix\sin\theta + iy\cos\theta} \int_{T_1}^\infty e^{-it^2}\,dt, \\ T_1 &= \eta\cos\frac{\theta}{2} - \xi\sin\frac{\theta}{2} = (2r)^{1/2}\sin\left(\frac{\varphi-\theta}{2} + \frac{\pi}{4}\right). \end{aligned} \tag{5.3}$$

The inversion of the order of summation and integration may be justified when $|\,w\,| = |\,\tan(\theta/2)\,| < 1$ (in which case the series in (5.2) converge) by using (1) the result that $|\,R_N\,| < |\,a^N/N!\,|$ when a is real in

$$\sum_0^{N-1} \frac{(ia)^n}{n!} = e^{ia} - R_N,$$

and (2) the inequality

$$\begin{aligned} &\left[\int_0^\infty t^N \exp\,[-t^2 + 2^{1/2}bt]\,dt\right]^2 \\ &\qquad < \int_0^\infty e^{-2(1-\alpha)t^2} t^{2N}\,dt \int_{-\infty}^\infty \exp\,[-2\alpha t^2 + 2^{3/2}bt]\,dt \\ &\qquad\qquad < A2^{-N} b^{-1/2} N^{-1/4} N! \exp(2bN^{1/2}) \end{aligned}$$

This inequality holds when $N \gg b^2$ and at the same time $N \gg 1$. The value of A is independent of N and b is a number which exceeds $|\,\xi\,|$. In this work the parameter α has been arbitrarily introduced; and has then been chosen so as to make the product of the two integrals a minimum when N is large. This value of α is $bN^{-1/2}$.

When the series (5.2) for $S_2(h)$ is converted into a contour integral taken along the path L_1, by the procedure used to obtain (5.1), it is seen that L_1 may be deformed into L_2 and we obtain

$$S_2(h) = \frac{e^{iy}\sec\frac{\theta}{2}}{2i}\int_{L_2}\left(\frac{iw}{2}\right)^n \frac{\Gamma(n+1)}{\sin \pi n} U_n(z)W_n(z')V_n(z_0')\, dn/W_n(z_0') \quad (5.4).$$

Whether a particular integrand, such as the one shown in (5.4), converges at the ends $n = \pm i\infty$ of L_2 can often be decided from Table 5.1. This table gives a rough idea of the behavior of the various functions in terms of powers of i. For example, if the integrand should turn out to be proportional to $i^n = \exp(i\pi n/2)$ at $n = i\infty$, the integral will converge like $\exp(-\pi \mid n \mid /2)$.

TABLE 5.1

Function	Order of Magnitude — Rough Approximation	
	near $n = i\infty$	near $n = -i\infty$
i^n	0	∞
i^{-n}	∞	0
$\sin \pi n$	i^{-2n}	i^{2n}
$\Gamma(n+1)$	i^n	i^{-n}
$U_n(z)$	$i^{-3n/2}$	$i^{3n/2}$
$V_n(z)$	$i^{-3n/2}$	$i^{-n/2}$
$W_n(z)$	$i^{n/2}$	$i^{3n/2}$

The approximations for $\Gamma(n+1)$ follow from its asymptotic expression, and those for the parabolic cylinder functions come from Tables 12.2 and 12.4. The entries for the cylinder functions may also be surmised from expressions (9.4) which hold for $z = 0$.

Table 5.1 may be used to show that the integrand in (5.1) is of the order of i^n as $n \to -i\infty$. Hence there is no hope of deforming L_1 into L_2 in this case. On the other hand, the integrand in (5.4) is of the order of i^n as $n \to i\infty$ and of i^{-n} as $n \to -i\infty$, and therefore (5.4) converges exponentially. In fact, it converges for all real positive values of $w = \tan \theta/2$. This enables us to obtain an expression for the field which holds for $0 < \theta < \pi$ (i.e. it is not subject to the restriction $\mid w \mid < 1$ required by (4.16)). This expression, which is fundamental for our work, has the form

$$E = \exp\left[-ix\sin\theta + iy\cos\theta\right] + S_1 + S_2\,(h). \quad (5.5)$$

Here S_1 and $S_2(h)$ are given by (5.3) and (5.4), respectively.

In working with (5.5) it is sometimes convenient to use the expression

$$\exp[-ix\sin\theta + iy\cos\theta] + S_1 = (i/\pi)^{1/2}\exp[-ix\sin\theta + iy\cos\theta]\int_{-\infty}^{T_1} e^{-it^2}\,dt \tag{5.6}$$

which follows from (5.3) and

$$\int_{-\infty}^{\infty}\exp(-it^2)\,dt = (\pi/i)^{1/2}. \tag{5.7}$$

The development leading to (5.5) shows that is satisfies the boundary condition $E = 0$ at $\eta = \eta_0$ for $0 < w < 1$. That (5.5) also satisfies the condition for the extended range $0 < w < \infty$ follows immediately from

$$\begin{aligned}\frac{e^{iy}\sec\frac{\theta}{2}}{2i}&\int_{L_2}\left(\frac{iw}{2}\right)^n\frac{\Gamma(n+1)}{\sin\pi n}U_n(z)V_n(z')\,dn\\ &= -(i/\pi)^{1/2}\exp[-ix\sin\theta + iy\cos\theta]\int_{-\infty}^{T_1}\exp(-it^2)\,dt\\ &= -\exp[-ix\sin\theta + iy\cos\theta] - S_1\end{aligned} \tag{5.8}$$

when we note that setting $z' = z_0'$ reduces $S_2(h)$ to the left hand side of (5.8) (with $z' = z_0'$).

Equation (5.8) is due to T. M. Cherry[16] who obtained it by expressing the cylinder functions as integrals and interchanging the order of integration (he works with the function $D_n(z)$ of our equations (9.2)). Substituting the integrals (9.19) for $U_n(z)$ and $V_n(z')$ in (5.8) and interchanging the order of integration leads to a similar derivation. Equation (5.8) may also be obtained by deforming L_2 into L_1 when $0 < w < 1$ and into L_3 when $1 < w < \infty$. This leads to the two series

$$e^{iy}\sec\frac{\theta}{2}\sum_{n=0}^{\infty}(-iw/2)^n n!\,U_n(z)V_n(z'), \tag{5.9}$$

$$-e^{iy}\sec\frac{\theta}{2}\sum_{n=-1}^{-\infty}(-iw/2)^n[\Gamma(n+1)U_n(z)]V_n(z') \tag{5.10}$$

which may be summed in much the same way as was (5.2) for S_1.

An expression for E which is useful in the study of the current density on the surface of the cylinder may be obtained from (5.5) by combining expression (5.8) for $\exp[-ix\sin\theta + iy\cos\theta] + S_1$ with expression (5.4)

---

[16] Expansions in Terms of Parabolic Cylinder Functions, Proc. Edinburgh Math. Soc., Ser. 2, **8**, pp. 50–65, 1948.

for $S_2(h)$:

$$E = \frac{e^{iy}\sec\frac{\theta}{2}}{2i}\int_{L_2}\left(\frac{iw}{2}\right)^n \frac{\Gamma(n+1)}{\sin\pi n}\,U_n(z)W_n(z') \left[\frac{V_n(z_0')}{W_n(z_0')} - \frac{V_n(z')}{W_n(z')}\right] dn. \tag{5.11}$$

When w exceeds unity (or when $w = 1$ and $\xi > \eta \geqq \eta_0 \geqq 0$) in (5.11), it may be verified with the help of Tables 12.2 and 12.4 that L_2 may be deformed into $L_3 + L_4$. When n is a negative integer the quantity within the brackets in (5.11) vanishes because of (4.8) and because $U_n(z) = 0$. The contribution of L_3 is zero since it encloses no poles. The contribution of L_4 is equal to the sum of the residues at the poles given by $W_n(z_0') = 0$. Hence, when $w > 1$,

$$E = -\pi e^{iy}\sec\frac{\theta}{2}\sum_{s=1}^{\infty}\left[\left(\frac{iw}{2}\right)^n \frac{\Gamma(n+1)U_n(z)W_n(z')V_n(z_0')}{\sin\pi n\,\partial W_n(z_0')/\partial n}\right]_{n=n_s} \tag{5.12}$$

where $n = n_s$ is the sth zero of $W_n(z_0')$. This series also converges when $w = 1$ and $\xi > \eta \geqq \eta_0 \geqq 0$ (which is roughly the shadow region). The preceding inequality does not necessarily specify the complete region of convergence.

Cherry[16] has also pointed out that the expression for a plane wave given by A. Erdélyi[17], namely (in our notation)

$$\exp\left[-ix\sin\theta + iy\cos\theta\right] = -\frac{e^{iy}\sec\frac{\theta}{2}}{2i}\int_{L_2}\left(\frac{iw}{2}\right)^n \frac{\Gamma(n+1)}{\sin\pi n}\left[U_n(z)V_n(z') + U_n(-z)V_n(-z')\right] dn, \tag{5.13}$$

may be regarded as the sum of the negative of (5.8) and a similar expression with ξ and η replaced by $-\xi$ and $-\eta$. In informal discussions with the writer, Prof. Erdélyi has pointed out that the work leading to our expression (5.5) for the field may be considerably shortened by starting with some known integral for the impressed field, such as (5.13) or a related result. One way of doing this is to take

$$\exp\left[-ix\sin\theta + iy\cos\theta\right] + S_1,$$

---

[17] Proc. Roy. Soc Edinburgh, **61**, pp. 61–70, 1941.

as given by the left hand side of (5.8), to be the impressed field in the equation

$$E = \text{impressed field} + \text{reflected field}$$

From the form of (5.8) and the discussion of expression (4.6) (given between equations (4.14) and (4.15)) we are led to assume the reflected field to be an outgoing wave of the form

$$\frac{e^{iy}\sec\frac{\theta}{2}}{2i}\int_{L_2}\left(\frac{iw}{2}\right)^n\frac{\Gamma(n+1)}{\sin\pi n}\,U_n(z)W_n(z')a(n)\,dn$$

where $a(n)$ must be chosen so as to make E vanish on the surface of the cylinder. This gives $a(n) = V_n(z_0')/W_n(z_0')$ and leads directly to the expression (5.11) for E.

When the incident wave is vertically polarized, integrals for H may be obtained from the series of Section 4 in much the same manner as were the integrals for E. The analogues of the earlier results are

$$H = \exp(-ix\sin\theta + iy\cos\theta)$$
$$-\frac{e^{iy}\sec\frac{\theta}{2}}{2i}\int_{L_1}\left(\frac{iw}{2}\right)^n\frac{\Gamma(n+1)}{\sin\pi n}\,U_n(z)W_n(z')'U_n(z_0')\,dn/'W_n(z_0'), \tag{5.14}$$

$$H = \exp(-ix\sin\theta + iy\cos\theta) + S_1 + S_3(h), \tag{5.15}$$

$$S_3(h) = \frac{e^{iy}\sec\frac{\theta}{2}}{2i}\int_{L_2}\left(\frac{iw}{2}\right)^n\frac{\Gamma(n+1)}{\sin\pi n}\,U_n(z)W_n(z') \tag{5.16}$$
$$'V_n(z_0')\,dn/'W_n(z_0'),$$

$$H = \frac{e^{iy}\sec\frac{\theta}{2}}{2i}\int_{L_2}\left(\frac{iw}{2}\right)^n\frac{\Gamma(n+1)}{\sin\pi n}\,U_n(z)W_n(z') \tag{5.17}$$
$$\left[\frac{'V_n(z_0')}{'W_n(z_0')} - \frac{V_n(z')}{W_n(z')}\right]dn,$$

$$H = -\pi e^{iy}\sec(\theta/2)\sum_{s=1}^{\infty}\left[\frac{(iw/2)^n\Gamma(n+1)U_n(z)W_n(z')'V_n(z_0')}{\sin\pi n\partial'W_n(z_0')/\partial n}\right]_{n=n_s'} \tag{5.18}$$

In these formulas $'U_n(z)$, etc. are defined by (4.19); w, z, z' by (4.13), z_0' by (4.17). In (5.14) w is restricted to $0 < w < 1$. In (5.15) $S_3(h)$ is given by (5.16), and w may be anywhere in $0 < w < \infty$. In (5.17) w

may also lie anywhere in $0 < w < \infty$, but in (5.18) it is restricted to $1 < w < \infty$ except when $\xi > \eta$ (roughly the shadow region) in which case w may be unity. In (5.18) $n = n_s'$ is the sth zero of $'W_n(z_0')$. The zeros of $'W_n(z_0')$ interlace those of $W_n(z_0')$ shown in Fig. 5.1.

When $h = \eta_0^2/2 = 0$ the parabolic cylinder degenerates into a half-plane and our solutions reduce to Sommerfeld's expressions for waves diffracted by a half-plane. It may be shown that if

$$T_2 = \eta \cos \frac{\theta}{2} + \xi \sin \frac{\theta}{2} = (2r)^{1/2} \sin \left(\frac{\varphi + \theta}{2} + \frac{\pi}{4} \right), \tag{5.19}$$

we have

$$\begin{aligned} S_2(0) &= -(i/\pi)^{1/2} \exp [ix \sin \theta + iy \cos \theta] \int_{T_2}^{\infty} e^{-it^2}\, dt, \\ S_3(0) &= -S_2(0). \end{aligned} \tag{5.20}$$

When this expression for $S_2(0)$ is added to (5.6) we obtain Sommerfeld's result for the case of horizontal polarization.

One may verify that the series (5.12) leads to Sommerfeld's result as z_0' approaches zero. By neglecting $0(z^2)$ terms in (9.3) and setting $n_s = -2s + p_s$ for the sth zero of $W_n(z_0')$ we may obtain the following relations which are needed in the course of the verification

$$\begin{aligned} p_s &= -4iz_0'\Gamma(s + 1/2)/\pi\Gamma(s) + \cdots, \\ \partial W_n(z_0')/\partial n \text{ at } n_s &= \Gamma(s)/4 + \cdots, \\ V_n(z_0') \text{ at } n_s &= -2iz_0'\Gamma(s + 1/2)/\pi + \cdots, \\ \left[\frac{V_n(z_0')}{\sin \pi n \partial W_n(z_0')/\partial n} \right]_{n=n_s} &= 2/\pi + \cdots. \end{aligned} \tag{5.21}$$

6. SURFACE CURRENTS ON THE CYLINDER

As shown in Fig. 6.1, the surface current J on the perfectly conducting cylinder $\eta = \eta_0$ is parallel to the crest of the cylinder (and to the electric intensity E) when the incident wave is horizontally polarized. We have from Maxwell's equations in parabolic coordinates

$$\mathrm{J} = [-H_\xi]_{\eta=\eta_0} = (i\zeta_0)^{-1}\, (2r)^{-1/2}\, [\partial E/\partial \eta]_{\eta=\eta_0}. \tag{6.1}$$

Here H_ξ is the component of magnetic intensity in the ξ-direction. ζ_0 is the intrinsic impedance of free space given by $\zeta_0 = (\mu_0/\epsilon_0)^{1/2} = \omega\mu_0$ where the second part of the equation follows from $2\pi/\lambda = \omega(\mu_0\epsilon_0)^{1/2}$

and $\lambda = 2\pi$. The E_0 and the H_0 of the incident wave are related by $H_0 = E_0/\zeta_0 = 1/\zeta_0$ since $E_0 = 1$. In rational MKS units $\zeta_0 = 120\pi$ ohms.

The derivative in (6.1) may be obtained by differentiating expression (5.11) for E and then setting $\eta = \eta_0$. Use of the Wronskian (9.9) for $V_n(z_0')$, $W_n(z_0')$ then takes (6.1) into

$$\zeta_0 J = M_0 \int_{L_2} \frac{dn}{\sin \pi n} (iw)^n U_n(z)/W_n(z_0') \tag{6.2}$$

where $w = \tan(\theta/2)$, L_2 is shown in Fig. 5.1, z and z_0' are given by (4.13) and (4.17), and

$$\begin{aligned} M_0 &= (i/8\pi r)^{1/2} e^{-ir} \sec \frac{\theta}{2}, \\ r &= (\xi^2 + \eta_0^2)/2. \end{aligned} \tag{6.3}$$

In this Section r will be restricted to mean a radius vector drawn to the trace of the cylinder on the (x, y) plane of Fig. 6.1.

Closing L_2 on the right and on the left gives the two series

$$\zeta_0 J = 2iM_0 \sum_{n=0}^{\infty} (-iw)^n U_n(z)/W_n(z_0'), \qquad 0 < w < 1, \tag{6.4}$$

$$\zeta_0 J = -2i\pi M_0 \sum_{s=1}^{\infty} \left[\frac{(iw)^n U_n(z)}{\sin \pi n \, \partial W_n(z_0')/\partial n} \right]_{n=n_s}, \qquad 1 < w < \infty, \tag{6.5}$$

where n_s is the sth zero of $W_n(z_0')$ regarded as a function of n.

For the half-plane case $\eta_0 = 0$, and (9.4) gives

$$W_n(0) = -i^n/2\Gamma(1 + n/2).$$

In this case the series (6.4) may be expressed as an infinite integral

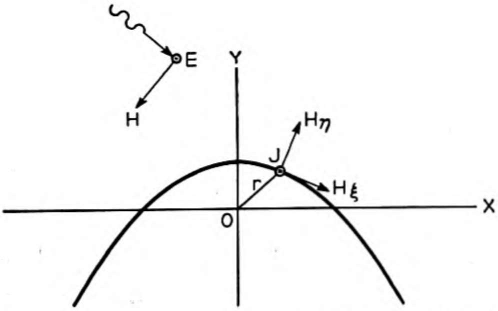

Fig. 6.1 — Relationship between surface current density J and electromagnetic field when incident wave is horizontally polarized. E and J are normal to the plane of the paper.

when the integral for $\Gamma(1 + n/2)$ is inserted and the sum (9.22) [i.e., the sum for the generating function of $U_n(z)$] used. Integrating part of the result gives

$$\zeta_0 J = (2/i\pi r)^{1/2} \cos\frac{\theta}{2}\Big[e^{-ir} - 2i\xi \sin\frac{\theta}{2}\, e^{-ir\cos\theta} \int_{\xi \sin(\theta/2)}^{\infty} \exp(-it^2)\, dt\Big]. \tag{6.6}$$

In (6.6) r is the distance along the half-plane as measured from the edge: $r = \xi^2/2 = |y|$. Positive values of ξ correspond to the shadowed side of the half-plane and negative values to the illuminated side. With this interpretation (6.6) agrees with the current density obtained from Sommerfeld's expression for the field.

Although (6.6) has been derived from (6.2) on the assumption that $0 < w < 1$ it also holds for $0 < w < \infty$ as may be shown by analytic continuation. Again, (6.6) may be obtained from (6.5).

Since the factor $r^{-1/2}$ comes from the multiplier M_0 in (6.4), it is possible that (6.6) may give one an idea of how the current density behaves near the crest of a thin cylinder which is almost, but not quite, a half-plane. Of course, r would have to be interpreted as shown in Fig. 6.1.

In order to study J when the radius of curvature of the cylinder is large compared to a wavelength we consider the case $\theta = \pi/2$, i.e. $w = 1$, in which the incident wave comes in horizontally. In this case most of the variation of the current density occurs near the crest of the cylinder where, as it turns out, ξ is of the order of $\eta_0^{1/3}$, η_0 being large.

At the beginning of the investigation rough calculations of the integrand in (6.2), based on the asymptotic expressions of Section 12, suggested that for small ξ and large η_0:

(a) Most of the contribution to the integral (6.2) comes from the neighborhood around point C shown on Fig. 6.2 where $m = n + 1 = z_0'^2/2 = -i\eta_0^2/2 = -ih$. Point C is a critical point associated with the asymptotic behavior of $W_n(z_0')$.

(b) The path of steepest descent for (6.2) roughly corresponds to the line ACD of Fig. 6.2, C being the high point of the path. Along this path $Im\,[f(t_0) - f(t_1)] = 0$ where $f(t) = -t^2 + 2zt - m \log t$, $m = n + 1$, is the function entering the definition (10.1) of the parabolic cylinder functions, and t_0, t_1 are the saddle points of $\exp\,[f(t)]$. This path in the n-plane separates the regions in which $W_n(z_0')$ has different asymptotic forms. It is the boundary of region III′ in Fig. 12.2 and has been studied in Sections 11 and 12.

Once (*b*) is verified the truth of (a) follows almost immediately since the path of integration L_2 may be deformed into ACD without passing over any singularities of the integrand of (6.2).

In order to verify (b), we note that the entries in Table 12.3 for $W_n(z_0')$ show that along ACD

$$W_n(z_0') \sim A_0' \approx \exp\,[f(t_0)]. \tag{6.7}$$

Here the expressions for $W_n(z_0')$ along ACD are taken to be those corresponding to the regions I'b and II$'$ shown in Fig. 12.2. In making the last approximation in (6.7) we have neglected the slowly varying coefficient of the exponential function in the expression (12.9) for A_0'. Since $|\,\xi\,| \ll \eta_0$ we set $\xi = 0$ in $U_n(z)$. Then upon using the values (9.4) for $U_n(0)$, (6.7) for $W_n(z_0')$, and unity for w, we see that the integrand of (6.2) behaves like

$$\frac{i^n \exp\,[-f(t_0)]}{2 \sin\,(\pi n/2)\Gamma(1 + n/2)}. \tag{6.8}$$

On ACD we have, in dealing with $W_n(z_0')$, $-3\pi/2 < \arg m \leqq -\pi/2$. Hence, from $t_0 + t_1 = i^{-1/2}\eta_0$ and from $f(t_0) + f(t_1)$ as calculated from (12.9), we have

$$\begin{aligned} \exp\,[f(t_0)] &= \exp\,(\tfrac{1}{2}[f(t_0) + f(t_1)] + \tfrac{1}{2}[f(t_0) - f(t_1)]) \\ &\sim i^{n+1}(2\pi)^{-1/2}\Gamma(-n/2) \exp\left(-\frac{i\eta_0^2}{2} + \tfrac{1}{2}[f(t_0) - f(t_1)]\right) \end{aligned} \tag{6.9}$$

where we have used the second of expressions (12.10) to evaluate $\exp\,[m(1 - \log\,(m/2))/2]$. Substitution of (6.9) in (6.8) shows that the integrand behaves roughly like

$$\exp\left(\frac{i\eta_0^2}{2} - \tfrac{1}{2}[f(t_0) - f(t_1)]\right). \tag{6.10}$$

The truth of statement (b) then follows from the fact that the lines of steepest descent of (6.10) in the n-plane are given by $Im\,[f(t_0) - f(t_1)] = 0$. To see that C is the high point of ACD we use (12.9) to show that near C we have

$$f(t_0) - f(t_1) \approx (2/3z_0')\,(z_0'^2 - 2m)^{3/2}$$

where $m = n + 1$. Consequently, $f(t_0) - f(t_1)$ is real and positive on AC [where, near C, $\arg\,(z_0'^2 - 2m) = -\pi/6$] and on CD [where $\arg\,(z_0'^2 - 2m) = -3\pi/2$, m being in region II$'$ according to the convention used in (6.7)]. That C is the high point now follows from (6.10).

In accordance with statement (a), we must study the form assumed by the integrand of (6.2) when n is near point C.

When (1) n is near C, (2) η_0 is large, and (3) $|\xi| \ll \eta_0$ we have for the various terms in (6.2)

$$\begin{aligned} i^n/\sin \pi n &\sim 2i^{1-n} \\ \Gamma(1 + n/2)W_n(z_0') &\sim (\eta_0/4)^{1/3}(2\pi)^{1/2}i^{7/6} \exp\left[-i\eta_0^2/2\right]Ai(\alpha), \end{aligned} \tag{6.11}$$

$$2\Gamma(1 + n/2)U_n(z) \sim i^n \exp\left[\frac{i\xi^2}{2} + \xi\left(\frac{2m}{i}\right)^{1/2} - \frac{\xi^3}{6}\left(\frac{i}{2m}\right)^{1/2}\right] \tag{6.12}$$

where $Ai\ (\alpha)$ denotes the Airy integral defined by (13.12), $m = n + 1$, $\arg m$ is near $-\pi/2$, and

$$\begin{aligned} \alpha &= (2/i\eta_0^2)^{1/3}\,(m + i\eta_0^2/2), \\ d\alpha &= (2/i\eta_0^2)^{1/3}\,dn. \end{aligned} \tag{6.13}$$

Expression (6.11) comes from (13.21) and expression (6.12) comes from region Ia of Table 12.2 (strictly speaking, region Ib should be used but point C is so close to $\arg m = -\pi/2$ that the simpler expression for Ia may be used). In obtaining (6.12) it is necessary to use the terms shown in the expansions (12.5) of t_0 and $\log t_1/t_0$. It may be shown that (6.12) also holds for negative values of ξ.

We now set $w = 1$ in (6.2) and change the variable of integration from n to α. Substituting for m in (6.12) its expression in terms of α, expanding in powers of α and neglecting higher order terms, converts the argument of the exponential function into

$$i\xi^2/2 - i\xi\eta_0 - i\gamma^3/3 + \alpha\gamma i^{1/3} \tag{6.14}$$

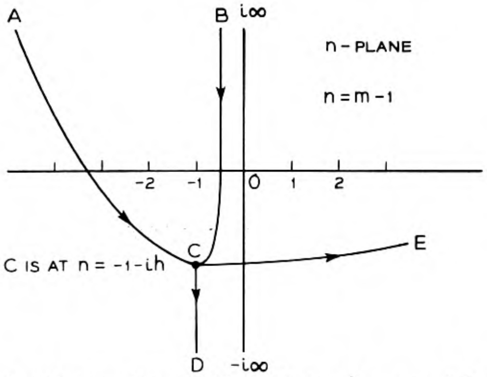

Fig. 6.2 — Paths of integration used in studying the current density and diffraction pattern when h is large. Path BCD is equivalent to path L_2 of Fig. 5.1. AC and CD are boundary lines which mark a change in the asymptotic behavior of $W_n(z_0')$. Far out towards A the line AC tends to become parallel to BC.

where

$$\gamma = \xi/(2\eta_0)^{1/3} = x/2h^{2/3} \tag{6.15}$$

When our approximations are set in (6.2) we obtain

$$\zeta_0 J \approx (i/2n_0)^{2/3}\pi^{-1} \exp\,[-i\xi\eta_0 - i\gamma^3/3] \int_{\infty \exp(i2\pi/3)}^{\infty \exp(-i2\pi/3)} \exp\,(i^{1/3}\gamma\alpha)\, d\alpha/Ai(\alpha). \tag{6.16}$$

Here we have taken the path of integration in the complex α-plane to be the transformed version of the path of steepest descent in the n-plane. That the path for (6.16) is still the one of steepest descent when $\gamma = 0$ and α is large follows from the asymptotic expansion (13.19) for $Ai(\alpha)$. It is interesting to note that near the crest of the cylinder $\xi\eta_0 + \gamma^3/3$ is approximately the distance along the cylinder as measured from the crest.

The expression (2.14) for $\zeta_0 J$ is obtained from (6.16) when $Ai(\alpha)$ is transformed by the relations (13.17).

When γ is positive the path of integration for α in (6.16) may be closed on the left to obtain a convergent series, the terms of which arise from the zeros of $Ai(\alpha)$. These zeros lie on the negative real α-axis starting with $\alpha = a_1 = -2.338 \cdots$, $a_2 = -4.087 \cdots$ The first fifty values of a_s and the corresponding values of the derivative $Ai'(a_s)$ have been tabulated*. Thus, when γ is positive,

$$\zeta_0 J \approx (2/i\eta_0^2)^{1/3} e^{-i\xi\eta_0 - i\gamma^3/3} \sum_{s=1}^{\infty} \frac{\exp\,(i^{1/3}\gamma a_s)}{Ai'(a_s)} \tag{6.17}$$

The leading term in this series leads to the approximation (2.19) when we use $Ai'(a_1) = .701 \cdots$ Expression (6.17) gives the form assumed by (6.5) when $w = 1$ and $h \to \infty$. For large values of s*

$$\begin{aligned} a_s &\sim -[3\pi(4s - 1)/8]^{2/3} \\ Ai'(a_s) &\sim -(-)^s \pi^{-1/2}(-a_s)^{1/4} \end{aligned} \tag{6.18}$$

When γ is large and negative an asymptotic expansion for $\zeta_0 J$ may be obtained by setting the asymptotic expansion (13.19) in (6.16) and using the method of steepest descent. It is found that the saddle point is at $\alpha = \alpha_0 = \gamma^2 i^{2/3}$ and the slope of the path of the steepest decent through it is given by arg $(d\alpha) = -5\pi/12$. This leads to the expression for $\zeta_0 J$ which appears in (2.17).

When the incident wave is vertically polarized the magnetic intensity

---

* **Reference 11, page 424.**

H is parallel to the crest of the parabolic cylinder. Since the cylinder is a perfect conductor, the current density J_v on the surface $\eta = \eta_0$ is equal in magnitude to H and its direction is that of increasing ξ. Thus setting $z' = z_0'$ in expression (5.17) for H and using the Wronskian (9.9) gives

$$\begin{aligned} J_v &= N \int_{L_2} \frac{dn}{\sin \pi n} (iw)^n U_n(z)/{}'W_n(z_0'), \\ N &= e^{-ir} \left(\sec \frac{\theta}{2}\right) \Big/ 2\pi^{1/2}, \qquad r = (\eta_0^2 + \xi^2)/2, \end{aligned} \tag{6.19}$$

where ${}'W_n(z_0')$ is defined by (4.19).

Closing L_2 on the right and left leads to the analogues of (6.4) and (6.5):

$$J_v = 2iN \sum_{n=0}^{\infty} (-iw)^n U_n(z)/{}'W(z_0'). \qquad 0 < w < 1, \tag{6.20}$$

$$J_v = -2i\pi N \sum_{s=1}^{\infty} \left[\frac{(iw)^n U_n(z)}{\sin \pi n \partial {}'W_n(z_0')/\partial n} \right]_{n=n_s'}, \qquad 1 < w < \infty, \tag{6.21}$$

where n_s' is the sth zero of ${}'W_n(z_0')$. The zeros of both ${}'W_n(z_0')$ and $W_n(z_0')$ are enclosed by the path of integration L_4 shown in Fig. 5.1.

The current density on a half-plane is obtained by setting $z_0' = 0$ in (6.20), using ${}'W_n(0) = W_n'(0) = -i^{n-1}/\Gamma(n/2 + \frac{1}{2})$, from (9.4), and the generating function series (9.22) for $U_n(z)$:

$$J_v = 2(i/\pi)^{1/2} e^{-ir \cos \theta} \int_{\xi \sin (\theta/2)}^{\infty} e^{-it^2} \, dt \tag{6.22}$$

where r has the same significance as in (6.6). This agrees with the expression obtained from Sommerfeld's result for the half-plane.

When $w = 1$ and h is large, the path of steepest descent for (6.19) becomes the same as that for the case of horizontal polarization, namely ACD of Fig. 6.2. This follows from the fact that, as may be seen from (12.2), the controlling exponential functions for ${}'W_n(z_0')$ and $W_n(z_0')$ are the same. The analogue of (6.16) is obtained by using the approximation (13.24) for ${}'W_n(z_0')$:

$$\begin{aligned} J_v \approx{} & (1/2\pi i) \exp \left[-i\xi\eta_0 - i\gamma^3/3\right] \\ & \int_{\infty \exp(i2\pi/3)}^{\infty \exp(-i2\pi/3)} \exp(i^{1/3}\gamma\alpha) \, d\alpha/Ai'(\alpha) \end{aligned} \tag{6.23}$$

where $Ai'(\alpha)$ denotes $dAi(\alpha)/d\alpha$ and γ is given by (6.15).

For positive values of γ (6.23) and $d^2Ai(\alpha)/d^2\alpha = \alpha Ai(\alpha)$ lead to

$$J_v \approx -\exp\,[-i\xi\eta_0 - i\gamma^3/3] \sum_{s=1}^{\infty} \frac{\exp\,(i^{1/3}\gamma a_s')}{a_s' Ai(a_s')} \tag{6.24}$$

where $a_1' = -1.019$, $a_2' = -3.248$, $\cdots$, etc. are the zeros of $Ai'(\alpha)$.* When we use $Ai(a_1') = 0.5357$ the leading term in (6.24) gives (2.19). For large values of s*

$$a_s' \sim -[3\pi(4s - 3)/8]^{2/3},$$

$$Ai(a_s') \sim -(-)^s(-a_s')^{-1/4}\pi^{-1/2}.$$

The expression (2.17) for J_v when γ is large and positive may be obtained by applying the method of steepest descent to (6.23). The asymptotic expression for $Ai'(\alpha)$ is obtained by differentiating (13.19).

When the cylinder is a good conductor, but not perfect, the expression for H analogous to (4.25) leads to an integral for J_v, obtained from (6.23) by substituting $Ai'(\alpha) + \ell Ai(\alpha)$ for $Ai'(\alpha)$, which is equivalent to one given by Fock.† Here $\ell = -(ih)^{1/3}\zeta/\zeta_0$ is assumed to be small compared to unity and ζ/ζ_0 is the ratio of the intrinsic impedance of the cylinder material to that of free space. Horizontal incidence, $\theta = \pi/2$, is assumed.

The analogue of (4.25) for H has the same form as (4.21) except that now $'U_n(z_0')$ is replaced by $'U_n(z_0') + \tau U_n(z_0')$, etc. The development leading from (4.21) through (5.15), (5.17), (6.19) to (6.23) may be carried out just as before. The work is also related to that given at the end of Section 7 where the effect of finite conductivity on the diffracted wave is briefly discussed.

A series corresponding to (6.24) may be derived from the integral. The exponential terms in this series are approximately $\exp\,[i^{1/3}\gamma(a_s' - \ell/a_s')]$, and are similar to those in (7.63). Since $\zeta_0 = (\mu_0/\epsilon_0)^{1/2}$ is real and $\zeta \approx (i\omega\mu/g)^{1/2}$ when $g \gg \omega\epsilon$ (the notation is explained in connection with (4.24); the g denoting conductivity should not be confused with the g defined by (7.20)) the quantity $-i^{1/3}\ell/a_s'$ has a positive part. Thus, the attenuation of J_v in the shadow is decreased slightly when the conductivity g of the cylinder is reduced from infinity to a large finite value.

7. FIELD AT A GREAT DISTANCE BEHIND THE PARABOLIC CYLINDER

The field at any point, for the case of horizontal polarization, is given by expression (5.5) with $S_2(h)$ given by (5.4). Since $S_2(h)$ is the

---

* Reference 11, page 424.
† Reference 5, page 418.

only troublesome term in (5.5) most of this section will be devoted to its study. Far behind the cylinder ξ and η are large and positive, and the corresponding terms in the integrand of (5.4) are

$$\Gamma(n + 1)U_n(z)W_n(z') = (2i\xi/\eta)^n i^{3/2} e^{-i\eta^2}(1 + f)/2\eta\pi^{1/2}, \tag{7.1}$$

where the asymptotic expressions (9.16) and (9.17) give

$$1 + f = 1 + \frac{in(n - 1)}{4\xi^2} + \frac{i(n + 1)(n + 2)}{4\eta^2} + 0(n^4/r^2). \tag{7.2}$$

In writing the "order of" term it is assumed that ξ and η are both $0(r^{1/2})$ with $r \gg n^2$.

When (7.1) is put in (5.4) we obtain

$$S_2(h) = M_1 \int_{L_2} \frac{\beta^n i^{2n} V_n(z_0')(1 + f)}{\sin \pi n W_n(z_0')}\, dn \tag{7.3}$$

where, from the expressions (4.1) for ξ and η,

$$M_1 = [(i/\pi)^{1/2} e^{-ir} \sec (\theta/2)]/4\eta, \tag{7.4}$$

$$\beta = \xi w/\eta = \xi[\tan (\theta/2)]/\eta = \cot (\varphi/2 + \pi/4) \tan (\theta/2).$$

Although it is not proved here, there is good reason to believe that (7.3) can be written as

$$S_2(h) = M_1 \int_{L_2} \frac{i^{2n}\beta^n V_n(z_0')}{\sin \pi n W_n(z_0')}\, dn + 0(h^3/r^{3/2}) \tag{7.5}$$

when r becomes large and we restrict ourselves to the region $|\varphi| < \pi/2$ in order to get $0(\xi^2) = 0(\eta^2) = 0(r)$. The first term contains r only through the factor M_1 and is of order $r^{-1/2}$. The "order of" term assumes h to be moderately large compared to unity but $h^2 \ll r$. When $h < 1$ the h^3 is to be replaced by unity.

The general idea leading to (7.5) is that (7.2) may be used over the portion of L_2 where the integrand is large and important. On the portion where (7.2) differs appreciably from unity the integrand is negligibly small. The important portion of L_2 runs from $n = \frac{1}{2}$ to $n = -\frac{1}{2} - ih$ (approximately). In particular the variation of $i^{2n}V_n(z_0')/\sin \pi n\, W_n(z_0')$ along L_2 may be summarized as follows: from $-\frac{1}{2}$ to $+ i\infty$ it decreases exponentially as i^{2n}, from $-\frac{1}{2}$ to $-ih$ it is equal to $-2i$ plus an oscillating function of order unity, and from $-ih$ to $-i\infty$ it decreases slowly at first and then more rapidly until it goes down like i^{-2n} (steepest descent behavior). This may be shown with the help of Fig. 12.2, the entries for regions $I'a$ and II' in Table 12.3, and the following items [see (12.9) and Figs. 10.1 and 10.2 for $z = i^{-1/2}\eta_0$ with $-3\pi/2 \leqq \arg\, (i\eta_0^2$

$- 2m) < \pi/2)]$:

(a) $Re\ [f(t_1) - f(t_0)]$ is almost zero between $-\tfrac{1}{2}$ and $-ih$.

(b) $Im\ [f(t_1) - f(t_0)]$ is almost zero between $-ih$ and $-i\infty$.

(c) t_1/t_0 runs from zero to unity as n goes from -1 to $-1-ih$.

Items (a) and (b) are consistent with $f(t_0) - f(t_1) \approx (\tfrac{2}{3} z_0')(z_0'^2 - 2m)^{3/2}$ which holds when n is near $-ih$ and which was mentioned in connection with (6.10).

This concludes our discussion of the reasons for believing that (7.5) is true for general values of h. Now we shall check it for the special case $h = 0$.

When we set $h = 0$ (i.e. $z_0' = 0$) in (7.3), use (9.4) and close L_2 by an infinite semicircle, we obtain

$$S_2(0) \sim \frac{i^{3/2} e^{-ir}}{\pi^{1/2} 2T_2}\left[1 - \frac{1}{2iT_2^2} + \cdots\right]. \tag{7.6}$$

This agrees with the first two terms in the asymptotic expansion of the Fresnel integral expression (5.20) for $S_2(0)$. In expanding (5.20) we need the first of the two asymptotic expansions (both of which hold for $T \gg 1$)

$$\int_T^\infty e^{-it^2}\,dt \sim -\frac{i \exp(-iT^2)}{2T}\left[1 - \frac{1}{2iT^2} + \cdots\right], \tag{7.7}$$

$$\int_{-\infty}^T e^{-it^2}\,dt \sim (\pi/i)^{1/2} + \frac{i \exp(-iT^2)}{2T}\left[1 - \frac{1}{2iT^2} + \cdots\right], \tag{7.8}$$

and also the first of the relations

$$\begin{aligned} x \sin\theta + y\cos\theta - T_2^2 &= -r, \\ T_2 &= \eta(1+\beta)\cos(\theta/2). \end{aligned} \tag{7.9}$$

In much of the following work we shall assume ξ and η to be so great that we can neglect the terms denoted by $0(h^3/r^{3/2})$ in (7.5). We shall use the asymptotic sign $\sim$ to acknowledge this omission.

From (7.4), β is equal to unity when $\varphi = \theta - \pi/2$. When r is very large this value of φ marks the shadow boundary. In the shadow $\beta > 1$ and in the illuminated region $\beta < 1$.

Closing L_2 on the right and on the left converts (7.5) into

$$S_2(h) \sim 2iM_1 \sum_{n=0}^{\infty} \beta^n V_n(z_0')/W_n(z_0'). \tag{7.10}$$

$$S_2(h) \sim 2iM_1\left\{(\beta - 1)^{-1} - \pi \sum_{s=1}^{\infty} \left[\frac{i^{2n}\beta^n V_n(z_0')}{\sin \pi n \, \partial W_n(z_0')/\partial n}\right]_{n=n_s}\right\} \tag{7.11}$$

It can be shown that (7.10) converges if $\beta < 1$ (see (4.18)) and that (7.11) converges if $\beta > 1$ (see (12.13)). The term $1/(\beta - 1)$ in (7.11) comes from the poles of csc πn inside the path L_3 shown in Fig. 5.1

From (7.7) and

$$\begin{aligned} -x \sin \theta + y \cos \theta - T_1^2 &= r, \\ T_1 &= \eta(1 + \beta) \cos (\theta/2) \end{aligned} \tag{7.12}$$

it may be shown that when $\beta > 1$, so that T_1 is negative, (5.6) has the asymptotic expression

$$\exp\,[-ix \sin \theta + iy \cos \theta] + S_1 \sim 2iM_1/(1 - \beta). \tag{7.13}$$

When this is added to (7.11) the $1/(1 - \beta)$ terms cancel leaving a series for E valid in the shadow where $\beta > 1$:

$$E \sim -2iM_1\pi \sum_{s=1}^{\infty} \left[\frac{i^{2n}\beta^n V_n(z_0')}{\sin \pi n \, \partial W_n(z_0')/\partial n}\right]_{n=n_s} \tag{7.14}$$

This series may also be obtained from the more general series (5.12) for E by using (7.1) and neglecting f.

We now take up the problem of finding the paths of steepest descent for the integral in (7.5) when β is near unity and h is large. When $\beta = 1$ and h is large, the integrand in (7.5) may be expressed in terms of $\exp\,[f(t_1) - f(t_0)]$ by using Table 12.3. In Section 6 it has been pointed out that the path of steepest descent for $\exp\,[f(t_1) - f(t_0)]$ is the path ACD of Fig. 6.2, with C being the high point. This suggests that the path ACD should be used to deal with the terms in (7.5) leading to $\exp\,[f(t_1) - f(t_0)]$. These terms are $U_n(z_0')/W_n(z_0')$ (introduced by the use of (4.8)) for the portion of L_2 between B and C, and $V_n(z_0')/W_n(z_0')$ for the portion between C and D. As a further argument supporting the use of the path AC we note that when n is on AC, i.e., on the edge of region $I'b$, Table 12.3 gives

$$U_n(z_0')/W_n(z_0') \sim -i(1 - i^{-4n})(t_1/t_0)^{1/2} \exp\,[f(t_1) - f(t_0)]. \tag{7.15}$$

Hence the variation of i^{2n} csc πn in the integrand of (7.5) is just cancelled by that of $(1 - i^{-4n})$ in (7.15). Consequently $i^{2n}U_n(z_0')/[\sin \pi n \, W_n(z_0')]$ varies as $\exp\,[f(t_1) - f(t_0)]$ along AC (the variation of t_1/t_0 is relatively small).

These considerations lead us to write (5.4) as

$$\begin{aligned} S_2(h) &= S_{21} + S_{22} + S_{23} \\ S_{21} &= -\int_B^C F\,dn, \\ S_{22} &= -\int_A^C FU_n(z_0')\,dn/W_n(z_0'), \\ S_{23} &= \int_C^D FV_n(z_0')\,dn/W_n(z_0'), \\ F &= e^{iy}\sec(\theta/2)(iw/2)^n\Gamma(n+1)U_n(z)W_n(z')/2i\sin\pi n. \end{aligned} \tag{7.16}$$

When instead of (5.4) the expression (7.5) for $S_2(h)$ is used we obtain

$$\begin{aligned} S_{21} &\sim -M_1\int_B^C i^{2n}\beta^n\,dn/\sin\pi n, \\ S_{22} &\sim -M_1\int_A^C i^{2n}\beta^n U_n(z_0')\,dn/[\sin\pi n W_n(z_0')], \\ S_{23} &\sim M_1\int_C^D i^{2n}\beta^n V_n(z_0')\,dn/[\sin\pi n W_n(z_0')]. \end{aligned} \tag{7.17}$$

In S_{22} it is permissible to swing AC from its original position BC because the zeros of $U_n(z_0')$ cancel those of $\sin\pi n$. When $\beta = 1$, AC and CD are the paths of steepest descent for S_{22} and S_{23} in (7.17) because $Im\,[f(t_1) - f(t_0)] = 0$ on ACD.

The asymptotic expression (7.17) for S_{21} may be evaluated by temporarily assuming β to be a complex number with $|\beta| < 1$ and $|\arg\beta| < \pi/2$. The integral along BC is the integral along BCE minus the integral along CE (see Fig. 6.2). Deforming BCE into L_1 of Fig. 5.1 shows that its contribution to S_{21} is $-2iM_1/(1-\beta)$. An infinite series for the integral along CE may be obtained by expanding $i^{2n}/\sin\pi n$ in powers of $\exp(-i2\pi n)$ and integrating termwise from $n = n_0 = -1-ih$ to $n = \infty - ih$, i.e., from C to E. In this way we obtain

$$S_{21} \sim -2iM_1\left[\frac{1}{1-\beta} + \sum_{t=0}^{\infty}\frac{\exp(n_0\log\beta - 2\pi th)}{\log\beta - 2\pi it}\right]. \tag{7.18}$$

Despite the appearance of the right hand side, it is analytic around $\beta = 1$ and analytic continuation may be used to show that (7.18) holds for $0 < \beta < \infty$.

When h is large only the first term in the series is important and we have

$$\begin{aligned} S_{21} &\sim 2iM_1[(\beta-1)^{-1} - \beta^{-1-ih}/\log\beta] \\ &= 2iM_1(\beta-1)^{-1} + iM_2\mathrm{g}^{-1} \end{aligned} \tag{7.19}$$

where we have introduced two quantities which will be used later:

$$M_2 = 2M_1h^{1/3}\beta^{-1-ih} = \left(\frac{i}{\pi}\right)^{1/2} \frac{h^{1/3}\exp\,[-ir + igh^{2/3}]}{2\xi \sin\,(\theta/2)}, \tag{7.20}$$

$$g = -h^{1/3}\log\beta.$$

When $\beta = 1$

$$S_{21} \sim 2iM_1(ih + \tfrac{1}{2}). \tag{7.21}$$

When h is large most of the contributions to the integrals (7.17) for S_{22} and S_{23} come from around $n = n_0 = -1-ih$, and we may use the approximations

$$U_n(z_0')/W_n(z_0') \sim i^{-4/3}Ai(\alpha i^{-4/3})/Ai(\alpha), \tag{7.22}$$

$$V_n(z_0')/W_n(z_0') \sim i^{4/3}Ai(\alpha i^{4/3})/Ai(\alpha), \tag{7.23}$$

$$\alpha = (ih)^{-1/3}(n + 1 + ih), \qquad n - n_0 = \alpha(ih)^{1/3},$$

which come from (13.21). Setting these in the integrals (7.17) and using the fact that $i^{2n}/\sin \pi n$ is nearly $2i$ around n_0 leads to

$$S_{22} \sim -M_2 \int_{\infty \exp\,(i2\pi/3)}^{0} \exp(\,-i^{1/3}\alpha g)Ai(\alpha i^{-4/3})\;d\alpha/Ai(\alpha), \tag{7.24}$$

$$S_{23} \sim -i^{2/3}M_2 \int_{0}^{\infty \exp\,(-i2\pi/3)} \exp\,(-i^{1/3}\alpha g)Ai(\alpha i^{4/3})\;d\alpha/Ai(\alpha), \tag{7.25}$$

$$S_{22} + S_{23} \sim iM_2\Psi(g), \tag{7.26}$$

where

$$\begin{aligned}\Psi(g) = i &\int_{\infty i^{4/3}}^{0} \exp\,(-i^{1/3}\alpha g)Ai(\alpha i^{-4/3})\;d\alpha/Ai(\alpha) \\ &+ i^{5/3}\int_{0}^{\infty i^{-4/3}} \exp\,(-i^{1/3}\alpha g)Ai(\alpha i^{4/3})\;d\alpha/Ai(\alpha).\end{aligned} \tag{7.27}$$

The expression (2.11) for $\Psi(g)$ is obtained from (7.27) by changing the variables of integration and using the transformations (13.17) for $Ai(\alpha)$.

Thus, when h is large and β near unity, (7.19) and (7.26) give

$$S_2(h) \sim 2iM_1(\beta - 1)^{-1} + iM_2[g^{-1} + \Psi(g)]. \tag{7.28}$$

In the shadow, where $\beta > 1$ and g is negative, (7.13) and (7.28) give

$$\begin{aligned}E &= \exp[-ix\sin\theta + iy\cos\theta] + S_1 + S_2(h) \\ &\sim iM_2\,[g^{-1} + \Psi(g)].\end{aligned} \tag{7.29}$$

This and the series (7.14) for E suggest that $\Psi(g) + 1/g$ may be expressed as a series in which the parabolic cylinder functions in (7.14) are replaced by Airy integrals. One way of obtaining this series from (7.14) is to use the Airy integral approximations (13.21). The zeros $n_1, n_2, \cdots$ of $W_n(z_0')$ go into the zeros $a_1, a_2, \cdots$ of $Ai(\alpha)$ by virtue of the relation $n - n_0 = \alpha(ih)^{1/3}$ and we have

$$E \sim i^{-2/3} M_2 \sum_{s=1}^{\infty} \frac{\exp\,[-a_s g i^{1/3}]}{[Ai'(a_s)]^2}, \tag{7.30}$$

$$\Psi(g) + 1/g = -i^{1/3} \sum_{s=1}^{\infty} \frac{\exp\,[-a_s g i^{1/3}]}{[Ai'(a_s)]^2}, \tag{7.31}$$

where $g < 0$. Here, as in (6.17), $a_1 = -2.338 \cdots$ and $Ai'(a_1) = .701 \cdots$ In obtaining these relations we have used $i^{2n}/\sin \pi n \approx 2i$, and

$$Ai(a_s i^{4/3}) = -i^{5/3} Bi(a_s)/2 = i^{5/3}/2\pi Ai'(a_s), \tag{7.32}$$

where the first equation follows from (13.17) and the second from the Wronskian

$$Ai(\alpha)Bi'(\alpha) - Ai'(\alpha)Bi(\alpha) = 1/\pi. \tag{7.33}$$

The equal sign in (7.31) holds even though the steps leading to it indicate that $\sim$ should be used. This may be seen from an alternative derivation of (7.31) in which $Ai(\alpha i^{-4/3})$ in the first integral of (7.27) is replaced by the right hand side of*

$$Ai(\alpha i^{-4/3}) = -i^{4/3} Ai(\alpha) - i^{-4/3} Ai(\alpha i^{4/3}). \tag{7.34}$$

In the first portion the $Ai(\alpha)$'s cancel and the resulting integral contributes $-1/g$ to (7.27) (g must be negative for convergence). The second portion combines with the second integral in (7.27) to give a contour integral which leads to the series in (7.31) when the path of integration in the α-plane is closed on the left. The closure may be justified by the asymptotic expressions (13.19) and (13.20) for $Ai(\alpha)$ (again g must be negative).

Since the integrals in (7.27), and their equivalents in (2.11), converge uniformly for all finite values of g, $\Psi(g)$ is an integral function of g. When g is negative $\Psi(g)$ may be computed from the series (7.31). When g is positive I have not been able to find a practicable method of obtaining $\Psi(g)$ other than the numerical integration of (2.11). The results are shown in Table 2.1. Since $\Psi(g)$ is an integral function its Taylor's series about, say, $g = -.5$ converges for all values of g. The coefficients in this series may be computed from (7.31). However, I was unable to

---

* Reference 11, page 424.

obtain useful results by this method because the computation of the coefficients becomes more and more difficult.

When g is large and positive it may be shown that

$$\Psi(g) \sim -g^{-1} + (i\pi g)^{1/2} \exp(-ig^3/12). \tag{7.35}$$

The procedure used to establish (7.35) is much the same as that used to establish the more general result

$$\begin{aligned} S_{22} + S_{23} \sim & -iM_2 g^{-1} \\ & - \left[\frac{h(1-\beta)}{r(1+\beta)}\right]^{1/2} \frac{\exp[-ir + 2ih(1-\beta)/(1+\beta)]}{\sin\frac{1}{2}(\varphi + \theta + \pi/2)}, \end{aligned} \tag{7.36}$$

$$\frac{1-\beta}{1+\beta} = \frac{\sin\frac{1}{2}(\varphi - \theta + \pi/2)}{\sin\frac{1}{2}(\varphi + \theta + \pi/2)},$$

which holds when $h^{1/3}(1-\beta)$ is large and positive.

When φ is near $-\pi/2 + \theta$, (7.36) gives the same result as (7.26) plus (7.35). For φ near $-\pi/2 + \theta$,

$$g \approx h^{1/3}(1-\beta) \approx [2h^{1/3}/\sin\theta] \sin\frac{1}{2}\left(\varphi - \theta + \frac{\pi}{2}\right), \tag{7.37}$$

which shows that g is proportional to the cube root of the radius of curvature $2h/\sin^3\theta$ at the point where the incident ray is tangent to the cylinder.

When $\beta < 1$, (7.36) may be obtained from

$$S_{22} + S_{23} \sim -M_1 \int_C^E \frac{i^{2n}\beta^n}{\sin\pi n}\,dn - M_1 \int_{ACE} \frac{i^{2n}\beta^n U_n(z_0')}{\sin\pi n W_n(z_0')}\,dn. \tag{7.38}$$

The second integral in (7.38) represents, asymptotically, the wave reflected by the cylinder. This interpretation is suggested by the fact that, when the expression (7.1) for $\Gamma(n+1)U_n(z)W_n(z')$ is substituted in expression (5.1) for E, the resulting integral may be written as the second integral in (7.38).

The first term in (7.36) is obtained when $i^{2n}/\sin\pi n$ in the first integral of (7.38) is approximated by $2i$ and the result integrated. When the integrand of the second integral is examined with the help of Table 12.3, it is found to have a saddle point* at $m = m_1$ on the imaginary axis between $m = 0$ and $m = -ih$. Near m_1 the integrand is approximately

$$2\beta^{-1}(t_1/t_0)^{1/2} \exp[F(m)] \tag{7.39}$$

---

* It is interesting to note that a saddle point also appears in the study of reflection from a sphere. See page 86 of reference.[7]

where $F(m) = f(t_1) - f(t_0) + m \log \beta$ and $F'(m) = \log (t_0\beta/t_1)$. Here t_0 and t_1 are functions of m defined by (12.9). At m_1 we have $t_0\beta = t_1$ and this leads to

$$m_1 = -4ih\beta/(1 + \beta)^2, \qquad F(m_1) = 2ih(1 - \beta)/(1 + \beta),$$
$$F''(m_1) = -(1 + \beta)/m_1(1 - \beta). \tag{7.40}$$

When we attempt to deform the path of integration ACE of the second integral in (7.38) into a path of steepest descent, we encounter no trouble near m_1 in regions $I'a$ and $I'b$. The path passes through m_1 with $\arg (dm) = -\pi/4$. Soon after passing through m_1 the path of steepest descent strikes the boundary between $I'a$ and II' at a point we shall call G. At G the imaginary part of m is $2h(1 - \beta)/(1 + \beta) \log \beta$. The asymptotic approximation to the integrand changes its form at this point. The choice of the path from G out to ∞ is not important since it contributes little to the value of the integral. However, if we insist on following paths of steepest descent, it turns out that we must split the path of integration at G.

When $h^{1/3}(1 - \beta) \gg 1$, it may be shown that the value of second integral in (7.38) is nearly equal to

$$-2M_1[-2\pi/\beta F''(m_1)]^{1/2} \exp [F(m_1)]$$

and this gives the second term in (7.36).

So far, in this section, we have been dealing with the case of horizontal polarization. Since the work for the case of vertical polarization (in which H plays the role of the wave function) follows much the same lines, we shall merely list the formulas corresponding to those already obtained for horizontal polarization. M_1, β and M_2, g are still given by (7.4) and (7.20), respectively.

$$S_3(h) = M_1 \int_{L_2} \frac{i^{2n}\beta^n \, 'V_n(z_0')}{\sin \pi n' W_n(z_0')} \, dn + 0(h^3/r^{3/2}), \tag{7.41}$$

$$S_3(0) = -S_2(0), \tag{7.42}$$

$$S_3(h) \sim 2iM_1 \sum_{n=0}^{\infty} \beta^n \, 'V_n(z_0')/'W_n(z_0'), \qquad \beta < 1 \tag{7.43}$$

$$\begin{gathered} S_3(h) \sim 2iM_1 \left\{ (\beta - 1)^{-1} - \pi \sum_{s=1}^{\infty} \left[\frac{i^{2n}\beta^n \, 'V_n(z_0')}{\sin \pi n \, \partial 'W_n(z_0')/\partial n} \right]_{n=n_s'} \right\}, \\ \beta > 1 \text{ (shadow region)}, \\ n_s' = s\text{th zero of } 'W_n(z_0'), \end{gathered} \tag{7.44}$$

$$H \sim -2iM_1\pi \sum_{s=1}^{\infty} \left[\frac{i^{2n}\beta^{n}\,{}'V_n(z_0')}{\sin \pi n\, \partial' W_n(z_0')/\partial n} \right]_{n=n_s'}, \qquad \beta > 1 \qquad (7.45)$$

$$\begin{aligned} S_3(h) &= S_{31} + S_{32} + S_{33}, \\ S_{31} &= S_{21} \text{ defined by (7.16)}, \\ S_{32} &= S_{22} \text{ with } {}'U_n(z_0')/{}'W_n(z_0') \text{ in place of } U_n(z_0')/W_n(z_0'), \\ S_{33} &= S_{23} \text{ with } {}'V_n(z_0')/{}'W_n(z_0') \text{ in place of } V_n(z_0')/W_n(z_0'), \end{aligned} \qquad (7.46)$$

$$S_{32} \sim i^{2/3} M_2 \int_{\infty \exp(i2\pi/3)}^{0} \exp(-i^{1/3}\alpha g) Ai'(\alpha i^{-4/3})\, d\alpha / Ai'(\alpha), \qquad (7.47)$$

$$S_{33} \sim M_2 \int_{0}^{\infty \exp(-i2\pi/3)} \exp(-i^{1/3}\alpha g) Ai'(\alpha i^{4/3})\, d\alpha / Ai'(\alpha), \qquad (7.48)$$

$$S_{32} + S_{33} \sim iM_2 \Psi_v(g), \qquad (7.49)$$

$$\begin{aligned} \Psi_v(g) = i^{-1/3} &\int_{\infty \exp(i2\pi/3)}^{0} \exp(-i^{1/3}\alpha g) Ai'(\alpha i^{-4/3})\, d\alpha / Ai'(\alpha) \\ &- i \int_{0}^{\infty \exp(-i2\pi/3)} \exp(-i^{1/3}\alpha g) Ai'(\alpha i^{4/3})\, d\alpha / Ai'(\alpha), \end{aligned} \qquad (7.50)$$

$$H \sim iM_2[g^{-1} + \Psi_v(g)], \qquad g < 0 \qquad (7.51)$$

$$H \sim i^{-2/3} M_2 \sum_{s=1}^{\infty} \frac{\exp(-a_s' g i^{1/3})}{(-a_s')[Ai(a_s')]^2}, \qquad g < 0 \qquad (7.52)$$

$$\Psi_v(g) + g^{-1} = -i^{1/3} \sum_{s=1}^{\infty} \frac{\exp(-a_s' g i^{1/3})}{(-a_s')[Ai(a_s')]^2}, \qquad g < 0 \qquad (7.53)$$

$$\begin{aligned} &a_s' = s\text{th zero of } Ai'(\alpha), \qquad a_1' = -1.019, \qquad Ai(a_1') = 0.5357, \\ &Ai'(a_s' i^{4/3}) = -i^{1/3} Bi'(a_s')/2 = -i^{1/3}/[2\pi Ai(a_s')], \\ &\quad Ai''(\alpha) = \alpha Ai(\alpha). \end{aligned} \qquad (7.54)$$

When g is large and positive,

$$\Psi_v(g) \sim -g^{-1} - (i\pi g)^{1/2} \exp(-ig^3/12), \qquad (7.55)$$

$$\begin{aligned} S_{32} + S_{33} \sim &-iM_2 g^{-1} \\ &+ \left[\frac{h(1-\beta)}{r(1+\beta)} \right]^{1/2} \frac{\exp[-ir + 2ih(1-\beta)/(1+\beta)]}{\sin \frac{1}{2}(\varphi + \theta + \pi/2)}. \end{aligned} \qquad (7.56)$$

The change in sign of the second term on the right in going from (7.36) to (7.56) comes from (12.2) and the analogous expression for ${}'W_n(z_0')$

(only t_1 contributes to $U_n(z_0')$ and only t_0 to $W_n(z_0')$ at the saddle point m_1 of the second integral in (7.38)).

So far in this section the parabolic cylinder has been assumed to possess infinite conductivity. When the cylinder has a finite (but very large) conductivity, it may be shown that the field far out in the shadow is approximately

$$E \sim M_1 \int_{L_4} \frac{i^{2n}\beta^n}{\sin \pi n} \frac{V_n(z_0') + \sigma^{-1}\,'V_n(z_0')}{W_n(z_0') + \sigma^{-1}\,'W_n(z_0')}\, dn. \tag{7.57}$$

Equation (7.57) is suggested by (7.14) and (4.25). The analogue of (7.57) for vertical polarization may be obtained by replacing E, σ in (7.57) by H, τ so that $'V_n(z_0') + \tau V_n(z_0')$ appears in place of $V_n(z_0') + \sigma^{-1}\,'V(z_0')$, and so on.

When the parabolic cylinder functions are replaced by Airy integrals according to (13.21) and (13.24), equation (7.57) may be written as

$$E \sim i^{8/3} M_2 \int_{L_4'} \frac{[\exp(-\alpha g i^{1/3})] Ai[(\alpha + k)i^{4/3}]}{Ai(\alpha + k)}\, d\alpha \tag{7.58}$$

where g and M_2 are given by (7.20), α by (7.23) and

$$k = -(ih)^{-1/3}\zeta/\zeta_0. \tag{7.59}$$

$| k |$ is small compared to unity. L_4' is a path of integration in the α plane which encloses the zeros of $Ai(\alpha + k)$ in a clockwise direction. Changing the variable of integration in (7.58) to $u = \alpha + k$ enables us to conclude that

$$\begin{bmatrix} E \text{ for finite} \\ \text{conductivity} \end{bmatrix} \approx \left[\exp\left(-\frac{\zeta\psi}{\zeta_0}\right)\right] \begin{bmatrix} E \text{ for infinite} \\ \text{conductivity} \end{bmatrix}. \tag{7.60}$$

Since we have assumed $\theta = \pi/2$, the relation (7.60) holds in the region where the angle ψ defined by Fig. 2.3 is negative.

The analogue of (7.58) for vertical polarization is obtained by replacing E by H, omitting the $i^{8/3}$, and replacing the ratio of the Airy integrals by

$$Ai'[(\alpha + \ell/\alpha)i^{4/3}]/Ai'(\alpha + \ell/\alpha) \tag{7.61}$$

where

$$\ell = -(ih)^{1/3}\zeta/\zeta_0. \tag{7.62}$$

Even though h is large, ζ/ζ_0 is assumed to be so small that ℓ is small compared to unity. The path of integration L_4' must now enclose the zeros of $Ai'(\alpha + \ell/\alpha)$ which are close to those of $Ai'(\alpha)$ at $\alpha = a_s'$, $s = 1$, 2, $\cdots$. It must not pass close to $\alpha = 0$ since the work leading to (7.61) assumes ℓ/α to be a small number. Changing the variable of integration to $v = \alpha + \ell/\alpha$, approximating ℓ/α, ℓ/α^2 by ℓ/v, ℓ/v^2, and evaluating the integral by considering the residues of the poles at $v = a'_s$ gives

$$H \approx i^{-2/3} M_2 \sum_{s=1}^{\infty} \left(1 - \frac{\ell}{a_s'^2}\right)^{-1} \frac{\exp\,[-i^{1/3} g(a'_s - \ell/a'_s)]}{(-a'_s)[Ai(a'_s)]^2}. \qquad (7.63)$$

This shows, to a first approximation, how the expression (7.52) is modified when the cylinder is a very good, but not perfect, conductor. Of course g must be negative in (7.63). Since ℓ in (7.62) varies as $h^{1/3}$ while k in (7.59) varies as $h^{-1/3}$ it appears that the field for vertical polarization is much more sensitive to changes in the conductivity than it is for horizontal polarization.

It may be verified that the change in the exponential terms in the series (7.30) and (7.52) produced by finite conductivity, namely

$$\begin{aligned} &a_s \text{ changes to } a_s - k \\ &a'_s \text{ changes to } a'_s - \ell/a'_s, \end{aligned} \qquad (7.64)$$

agrees, to a first approximation, with the change produced in the corresponding series (given, for example, by the series (27) and (28) on page 45 of Reference 7) for the propagation of radio waves over the earth's surface.

8. FIELD AT A GREAT DISTANCE BEHIND THE PARABOLIC CYLINDER WHEN $\theta = \pi/2$ AND h IS LARGE

In the work of Section 7 the angle of incidence θ may lie anywhere between 0 and π. Here we take $\theta = \pi/2$, which corresponds to the case shown in Fig. 2.3 and described in Section 2. Some simplification is obtained thereby. For example, the incident wave is now simply $\exp(-ix)$. We shall write the expressions for the horizontal and vertical polarization cases as

$$E = (e^{-ix} + S_1)_r + S_{21} + (S_{22} + S_{23}), \qquad (8.1)$$

$$H = (e^{-ix} + S_1)_r + S_{21} + (S_{32} + S_{33}), \qquad (8.2)$$

respectively. Here S_{21}, $\cdots$ are defined by (7.16) and (7.46) in which

$$\begin{aligned} &\theta = \pi/2, \qquad w = 1, \\ &\beta = \xi/\eta = \cot(\varphi/2 + \pi/4) = 1 - \varphi + \varphi^2/2 - \varphi^3/3 + \cdots \end{aligned} \qquad (8.3)$$

Throughout this section β will be defined by (8.3), i.e., by (7.4) with

$\theta = \pi/2$. Also, from (5.3) and (5.6)

$$\begin{aligned}(e^{-ix} + S_1)_r = (i/\pi)^{1/2} e^{-ix} \int_{-\infty}^{T_1} e^{-it^2}\, dt, \qquad T_1 &= 2^{-1/2}(\eta - \xi) \\ &= (2r)^{1/2} \sin (\varphi/2).\end{aligned} \tag{8.4}$$

The subscript r is used to denote correspondence to a half-plane with its edge at $r = 0$.

When h is large, physical reasons lead us to expect a similarity between our field and the one behind a half-plane with its edge at the crest of the cylinder where $\rho = 0$ (see Fig. 2.3). The main part of this field is the analogue of (8.4):

$$(e^{-ix} + S_1)_\rho = (i/\pi)^{1/2} e^{-ix} \int_{-\infty}^{T_3} e^{-it^2}\, di, \qquad T_3 = (2\rho)^{1/2} \sin (\psi/2), \tag{8.5}$$

where the subscript ρ indicates that $[\exp(-ix) + S_1]_\rho$ corresponds to diffraction behind the half-plane just mentioned.

In order to make use of the similarity between the field behind the cylinder and the half-plane with its edge at the crest of the cylinder, we change the polar coordinates from (r, φ) to (ρ, ψ). From

$$\rho e^{i\psi} = r e^{i\varphi} - ih \tag{8.6}$$

it may be shown that, when h^2/r is small,

$$\begin{aligned}(e^{-ix} + S_1)_r - (e^{-ix} + S_1)_\rho &= (i/\pi)^{1/2} e^{-ix} \int_{T_3}^{T_1} e^{-it^2}\, dt \\ &= \frac{2iM_1}{\beta - 1} [e^{ih \sin \varphi} - 1] + 0(h^3/r^{3/2})\end{aligned} \tag{8.7}$$

where M_1 is obtained by putting $\theta = \pi/2$ in (7.4).

When we combine (8.7) and the expression (7.19) for S_{21} the $2iM_1/(\beta - 1)$ terms cancel leaving

$$\begin{aligned}(e^{-ix} + S_1)_r + S_{21} = (e^{-ix} + S_1)_\rho + \frac{2iM_1}{\beta - 1} e^{ih \sin \varphi} + i \frac{M_2}{g} \\ + 0(h^3/r^{3/2}) + 0[M_1 \exp(-2\pi h)].\end{aligned} \tag{8.8}$$

The sum of the terms involving M_1 and M_2 may be expressed in a form which contains the expression $c(r)$ defined by (2.5) and the quantity b defined by

$$\begin{aligned} b &= -\log \beta = \log \tan\left(\frac{\varphi}{2} + \frac{\pi}{4}\right) = \varphi + \varphi^3/6 + \cdots \\ &= h^{-1/3} g, \\ \tanh b &= \sin \varphi. \end{aligned} \tag{8.9}$$

Replacing $c(r) \exp(ih \sin \varphi)$ by $c(\rho)$ plus a correction term then converts (8.8) into

$$\begin{aligned} (e^{-ix} + S_1)_r + S_{21} &= (e^{-ix} + S_1)_\rho \\ &+ \frac{c(\rho)[1 + \exp(2b_\rho)]^{1/2}}{2^{1/2}} \left[\frac{1}{1 - e^b} + \frac{\exp(ihb - ih \tanh b)}{b}\right]_\rho \\ &+ 0(h^3/r^{3/2}) + 0(r^{-1/2} e^{-2\pi h}), \end{aligned} \tag{8.10}$$

where the subscript ρ on the square brackets indicates that b is to be replaced by b_ρ defined by

$$b_\rho = \log \tan(\psi/2 + \pi/4) = \psi + \psi^3/6 + \cdots \tag{8.11}$$

The quantity within the square brackets in (8.10) is continuous at $b = 0$ where it behaves like (neglecting $0(b)$ terms but retaining $0(hb^2)$)

$$\tfrac{1}{2} + ihb^2/3 = \tfrac{1}{2} + ih^{1/3} g^2/3. \tag{8.12}$$

Expression (8.10) is to be used with $(S_{22} + S_{23})$ and $(S_{32} + S_{33})$ obtained from (7.17) and (7.46) (with $\theta = \pi/2$ and $w = 1$), respectively.

When ψ is small, expression (8.10) becomes

$$\begin{aligned} (e^{-ix} + S_1)_r + S_{21} &= (e^{-ix} + S_1)_\rho \\ &+ c(\rho)\left[\frac{1}{2} - \frac{1}{\psi} + \frac{h^{1/3} \exp(ig^3/3)}{g}\right]_\rho + \cdots . \end{aligned} \tag{8.13}$$

The subscript ρ on the square bracket indicates that g is to be replaced by g_ρ defined by

$$g_\rho = h^{1/3} b_\rho = h^{1/3}(\psi + \psi^3/6 + \cdots). \tag{8.13}$$

When, in accordance with (8.1) and (8.2), we add to (8.13) the approximations (7.26) and (7.49), namely

$$\begin{aligned} S_{22} + S_{23} &\sim iM_2 \Psi(g), \\ S_{32} + S_{33} &\sim iM_2 \Psi_v(g), \end{aligned} \tag{8.14}$$

we obtain

$$E = (e^{-ix} + S_1)_\rho + c(\rho)\left[\frac{1}{2} - \frac{1}{\psi} + \left\{\frac{1}{g} + \Psi(g)\right\} h^{1/3} \exp\,(ig^3/3)\right]_\rho + \cdots, \tag{8.15}$$

$$H = (e^{-ix} + S_1)_\rho + c(\rho)\left[\frac{1}{2} - \frac{1}{\psi} + \left\{\frac{1}{g} + \Psi_v(g)\right\} h^{1/3} \exp\,(ig^3/3)\right]_\rho + \cdots. \tag{8.16}$$

The terms neglected in (8.15) and (8.16) are the "order of" terms in (8.10), plus those neglected by virtue of ψ being small, plus the errors in (8.14) The errors in (8.14) are of two kinds namely those of $0(h^3/r^{3/2})$ and those due to approximating the parabolic cylinder functions by Airy integrals.

It is interesting to observe the forms assumed by (8.15) and (8.16) when $h = 0$ even though they are not supposed to hold for small values of h. In this case ρ, ψ go into r, φ and the right hand sides of (8.15) and (8.16) become the same, namely

$$(e^{-ix} + S_1)_r + c(r)/2. \tag{8.17}$$

The half plane results given in Section 2 become, for small values of φ,

$$\left.\begin{matrix} E \\ H \end{matrix}\right\} = (e^{-ix} + S_1)_r \pm c(r)/2 \tag{8.18}$$

where the upper sign corresponds to E and the lower one to H. Comparison of (8.17) and (8.18) shows that (8.15) for E reduces to the proper value but (8.16) for H fails to do so because the signs of $c(r)/2$ do not agree.

The discrepancy is apparently related to the approximations we have made in obtaining the expression (7.19) for S_{21} from (7.18) and to the errors introduced by approximating the parabolic cylinder functions by the Airy integrals. As we let $h \to 0$ in the more complete expression (7.18) for S_{21}, the value obtained for $S_{21} \to \infty$. This is explained by the fact that the upper limit of integration $-1 - ih$ (at point C) approaches the pole of the integrand of (7.17) at $n = -1$. This large value of S_{21} tends to be cancelled by the large value of S_{23} (for horizontal polarization). On the other hand our approximation (7.19) yields via (7.21) the value iM_1 for S_{21} and S_{31} when $h = 0$ and $\beta = 1$. The factor $h^{1/3}$ in M_2 makes our approximations for S_{22}, S_{23}, S_{32}, S_{33} in terms of Airy integrals vanish when $h = 0$.

Incidentally, if, instead of taking the point C of Fig. 6.2 to be at $-1 - ih$, we take it to be at $-\frac{1}{2} - ih$ (a choice which receives some support from the Airy integral representation obtained from the viewpoint of the differential equations discussed in the first part of Section 13), the approximate integrals of (7.17) and (7.46) may be integrated directly when $h = 0$ and $\beta = 1$. It is found that

$$S_{21} \sim -\frac{M_1}{\pi} \log 2, \qquad S_{22} \sim \frac{M_1}{\pi} \log 2 + \frac{iM_1}{2}, \qquad S_{23} \sim +iM_1/2,$$

$$S_{31} \sim -\frac{M_1}{\pi} \log 2, \qquad S_{32} \sim \frac{M_1}{\pi} \log 2 - \frac{iM_1}{2}, \qquad S_{33} \sim -iM_1/2,$$

and these add to give the values $S_2(0) \sim iM_1$, $S_3(0) \sim -iM_1$ required by the half-plane case.

It is seen that a rather thorough investigation of the errors introduced by our approximations would be required to resolve the discrepancy between (8.17) and (8.18). Since we do not intend to go into this subject, and since the errors we have made may be as large as the $\frac{1}{2}$ which appears within the square brackets of (8.15) and (8.16), we shall "split the difference" between the two polarizations and omit the $\frac{1}{2}$ altogether. This is done in Section 2 where $\tau \approx g_\rho$.

9. THE FUNCTIONS $U_n(z)$, $V_n(z)$, $W_n(z)$

The functions $U_n(z)$, etc., are defined for all values of z and n by the integrals

$$\begin{aligned} U_n(z) &= \frac{1}{2\pi i} \int_U t^{-n-1} e^{-t^2+2zt}\, dt, \\ V_n(z) &= \frac{1}{2\pi i} \int_V t^{-n-1} e^{-t^2+2zt}\, dt, \qquad (9.1) \\ W_n(z) &= \frac{1}{2\pi i} \int_W t^{-n-1} e^{-t^2+2zt}\, dt. \end{aligned}$$

where the paths of integration U, V, W in the complex t-plane are shown in Fig. 9.1. The cut in the t-plane runs from $-\infty$ to 0 and has been introduced in order to make the function t^{-n-1} one-valued. In some of the later work the paths of integration will cross this cut. Of course, this requires close attention to arg t.

The initial and final points of the various paths (denoted in Fig. 9.1 by the subscripts i and f) are located at infinity. Arg $t = -\pi$ at U_i and W_f and $+\pi$ at U_f and V_i.

We shall give a summary of the properties of the functions (9.1) which will be needed in our work. These functions are related to the parabolic cylinder function $D_n(z)$[18,19] through the equations

$$\begin{aligned} U_n(z) &= 2^{n/2}\, e^{z^2/2}\, D_n(2^{1/2}z)/\Gamma(n+1), \\ V_n(z) &= -i^{-n}\, 2^{n/2}\, e^{z^2/2}\, D_{-n-1}\,(-iz2^{1/2})/(2\pi)^{1/2}, \\ W_n(z) &= -i^{n}\, 2^{n/2}\, e^{z^2/2}\, D_{-n-1}\,(iz2^{1/2})/(2\pi)^{1/2}. \end{aligned} \tag{9.2}$$

We use the functions $U_n(z)$, etc., here instead of $D_n(z)$ because they seem to be more convenient for the particular problem we have to deal with.

From the definitions (9.1) it follows that $U_n(z)$, $V_n(z)$, $W_n(z)$ are one-valued analytic functions of z and n. By expanding $\exp(2zt)$ in (9.1) and integrating termwise it may be shown that

$$\begin{aligned} U_n(z) &= 2A\cos(\pi n/2) + 4zB\sin(\pi n/2), \\ V_n(z) &= -Ai^{-n} - 2zi^{-n+1}B, \\ W_n(z) &= -Ai^{n} - 2zi^{n-1}B, \end{aligned} \tag{9.3}$$

$$A = {}_1F_1\left(-\frac{n}{2};\frac{1}{2};z^2\right)\Big/ 2\Gamma\left(1+\frac{n}{2}\right),$$

$$B = {}_1F_1\left(\frac{1-n}{2};\frac{3}{2};z^2\right)\Big/ 2\Gamma\left(\frac{1+n}{2}\right).$$

When $z = 0$ and $U_n'(z) = d\,U_n(z)/dz$, etc.,

$$U_n(0) = \frac{\cos(\pi n/2)}{\Gamma(1+n/2)}, \qquad V_n(0) = \frac{-i^{-n}}{2\Gamma(1+n/2)},$$

$$W_n(0) = \frac{-i^{n}}{2\Gamma(1+n/2)},$$

$$U_n'(0) = \frac{2\sin(\pi n/2)}{\Gamma\left(\frac{n+1}{2}\right)}, \qquad V_n'(0) = \frac{-i^{-n+1}}{\Gamma\left(\frac{n+1}{2}\right)}, \tag{9.4}$$

$$W_n'(0) = \frac{-i^{n-1}}{\Gamma\left(\frac{n+1}{2}\right)}.$$

---

[18] See E. T. Whittaker and G. N. Watson, *Modern Analysis*, Fourth Edition (1927) Cambridge Univ. Press pp. 347–354.

[19] W. Magnus and F. Oberhettinger, Formeln und Sätze für Speziellen Funktionen, 2nd Ed., Springer, 1948 Chap. 6 Section 3, and p. 227. A comprehensive account of $D_n(z)$ is given in the forthcoming work, *Higher Transcendental Functions*, compiled by the staff of the Bateman Manuscript Project.

Let $T_n(z)$ denote any one of $U_n(z)$, $V_n(z)$, $W_n(z)$, let primes denote differentiation with respect to z, and let asterisks denote complex conjugates. Then we have the following relations

$$T_n''(z) - 2zT_n'(z) + 2nT_n(z) = 0, \tag{9.5}$$

$$\frac{d}{dz}\left[e^{-z^2}T_n'(z)\right] + 2ne^{-z^2}T_n(z) = 0, \tag{9.6}$$

$$\frac{d^2}{dz^2}\left[e^{-z^2/2}T_n(z)\right] + (2n + 1 - z^2)e^{-z^2/2}T_n(z) = 0, \tag{9.7}$$

$$\begin{aligned} T_n'(z) &= 2T_{n-1}(z), \\ nT_n(z) &= 2zT_{n-1}(z) - 2T_{n-2}(z), \end{aligned} \tag{9.8}$$

$$\begin{aligned} U_n'(z)\,V_n(z) - U_n(z)\,V_n'(z) &= i2^n e^{z^2}/\pi^{1/2}\,\Gamma(n+1), \\ V_n'(z)\,W_n(z) - V_n(z)\,W_n'(z) &= i2^n e^{z^2}/\pi^{1/2}\,\Gamma(n+1), \\ W_n'(z)\,U_n(z) - W_n(z)\,U_n'(z) &= i2^n e^{z^2}/\pi^{1/2}\,\Gamma(n+1), \end{aligned} \tag{9.9}$$

$$U_n(z) + V_n(z) + W_n(z) = 0, \tag{9.10}$$

$$\begin{aligned} &[V_n(z)]^* = W_{n^*}(z^*),\ [W_n(z)]^* = V_{n^*}(z^*), \\ &[U_n(z)]^* = U_{n^*}(z^*), \end{aligned} \tag{9.11}$$

$$\begin{aligned} &V_n(-z) = i^{-2n}\,W_n(z),\ W_n(-z) = i^{2n}\,V_n(z), \\ &U_n(-z) = -i^{2n}\,V_n(z) - i^{-2n}\,W_n(z), \end{aligned} \tag{9.12}$$

$$V_{-n-1}(iz) = -i^{n+1}KU_n(z), \qquad W_{-n-1}(iz) = -i^{-n-1}KU_n(-z),$$

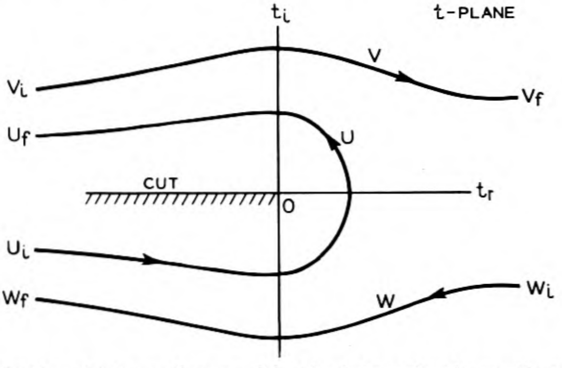

Fig. 9.1 — Paths of integration used in the integrals of equations (9.1) which define the functions $U_n(z)$, $V_n(z)$ and $W_n(z)$. The subscripts i and f stand for the "initial" and "final" points of the paths.

$$\begin{aligned} U_{-n-1}(iz) &= i^{-n-1}(i^{2n} - i^{-2n})KW_n(z) = -(2i)^{-n}\pi^{1/2}e^{-z^2}W_n(z)/\Gamma(-n), \\ U_{-n-1}(-iz) &= i^{n-1}(i^{2n} - i^{-2n})KV_n(z), \\ K &= e^{-z^2}\Gamma(n+1)/\pi^{1/2}2^{n+1} \end{aligned} \tag{9.13}$$

Equation (9.5) may be obtained from (9.1) by forming $T_n''(z) - 2zT'(z)$ and integrating by parts. Equation (9.10) follows from (9.1) upon joining the paths U, V, W to obtain a closed path of integration. From (9.11) it follows that when we have an expression for $V_n(z)$ which holds for all values of z and n, replacing i by $-i$ (or i^{-1}) gives the corresponding expression for $W_n(z)$. Equations (9.13) may be obtained by using the fact that $U_{-n-1}(iz)$ exp (z^2) etc. are solutions of the differential equations (9.5) and (9.7).

The relations (9.11) and (9.13) enable us to compute the values of $U_n(z)$, $V_n(z)$, $W_n(z)$ for $z = i^{1/2}\rho$ and $z = i^{-1/2}\rho$ and all n when the values of any two are given for $z = i^{1/2}\rho$ and $Re(n) \geqq -\frac{1}{2}$.

It may be verified that as z becomes large and n remains fixed the differential equation (9.5) has the asymptotic solutions

$$\begin{aligned} s_1(n, z) &= \frac{2^n z^n}{\Gamma(n+1)}\, {}_2F_0\left(-\frac{n}{2}, \frac{1-n}{2}\,;\,;-1/z^2\right), \\ s_2(n, z) &= \frac{z^{-n-1}e^{z^2}}{2\sqrt{\pi}}\, {}_2F_0\left(\frac{n+1}{2}, \frac{n+2}{2}\,;\,;1/z^2\right), \end{aligned} \tag{9.14}$$

where

$$|\arg z| < \pi \text{ and } s_2(-n-1, iz) = i^n K s_1(n, z),$$

K being given by (9.13). In terms of these functions we have

$$\begin{aligned} V_n(z) &\sim -is_2(n, z), & 0 < \arg z < \pi \\ &\sim -s_1(n, z) - is_2(n, z), & -\pi/2 < \arg z < 0 \\ &\sim -s_1(n, z) - i^{-4n+1}s_2(n, z), & -\pi < \arg z < -\pi/2 \end{aligned} \tag{9.15}$$

$$W_n(z) \sim is_2(n, z), \qquad -\pi < \arg z < 0 \tag{9.16}$$

$$U_n(z) \sim s_1(n, z), \qquad -\pi/2 < \arg z < \pi/2. \tag{9.17}$$

The first expression for $V_n(z)$ in (9.15) follows when we note that the leading term may be obtained from (9.1) by choosing the path of integration V to be $t = z + \tau$ where τ runs from $-\infty$ to $+\infty$, and $|z|$ is supposed to be large. (9.17) follows from the first of (9.15) and the relation (9.13) between $V_{-n-1}(iz)$ and $U_n(z)$. Asymptotic expressions for $W_n(z)$ may be obtained by taking the conjugate complex of those for $V_n(z)$. The second and third expressions for $V_n(z)$ follow from the other asymptotic expressions and (9.11), (9.12).

When $R(n) < 0$, the theory of gamma functions and (9.1) lead to

$$\begin{aligned}\Gamma(n+1)\Gamma(-n)U_n(z) &= -\pi \csc \pi n U_n(z) \\ &= \int_0^\infty \tau^{-n-1} \exp(-\tau^2 - 2\tau z)\, d\tau.\end{aligned} \tag{9.18}$$

By expressing $\sqrt{\pi} \exp[-(z-t)^2]$ as the integral of

$$\exp[-\tau^2 + 2i(z-t)\tau]$$

taken from $\tau = -\infty$ to $+\infty$ and substituting in (9.1) it may be shown that, when $R(n) > -1$,

$$\begin{aligned}U_n(z) &= Fi^n \int_{-\infty}^{\infty} e^{-t^2-2izt} t^n\, dt, \\ V_n(z) &= -Fi^{-n} \int_0^\infty e^{-\tau^2+2iz\tau} \tau^n\, d\tau, \\ W_n(z) &= -Fi^n \int_0^\infty e^{-\tau^2-2iz\tau}\, \tau^n\, d\tau, \\ F &= 2^n e^{z^2}/\Gamma(n+1)\pi^{1/2}.\end{aligned} \tag{9.19}$$

When n is not an integer the path of integration in the integral (9.19) for $U_n(z)$ is indented downward at the origin. Equations (9.19) mav also be obtained from (9.1) by using (9.13) and (9.18).

When n is an integer

$$U_n(-z) = (-)^n\, U_n(z), \qquad V_n(-z) = (-)^n\, W_n(z), \tag{9.20}$$

and when n is a positive integer

$$\begin{aligned}U_n(z) &= s_1(n, z) = (-)^n \frac{e^{z^2}}{n!} \frac{d^n}{dz^n} e^{-z^2}, \\ U_{-n}(z) &= 0, \\ V_{-n}(z) = -W_{-n}(z) &= -is_2(-n, z) = -\frac{i}{\sqrt{\pi} 2^n} \frac{d^{n-1}}{dz^{n-1}} e^{z^2}.\end{aligned} \tag{9.21}$$

From Maclaurin's expansion and (9.21),

$$\sum_{n=0}^{\infty} t^n U_n(z) = \exp[-t^2 + 2zt]. \tag{9.22}$$

10. FORMULAS FOR THE SADDLE-POINT METHOD

Much of our work involves the behavior of the parabolic cylinder functions as functions of n when n is a large complex number. Although this subject has been studied by several writers,[20, 21, 22] their results are not in the form we require. As the work of Sections 6 and 7 shows, the paths of steepest descent for the integrals in our electromagnetic problem are intimately connected with the function $f(t_0) - f(t_1)$. In turn, this function is closely related to the saddle point method of evaluating $U_n(z)$, etc., for large values of n. For the sake of completeness, we shall outline this method. We shall pay special attention to the relative importance of the two saddle points as n moves about in its complex plane.

When we write the integrand of the integrals (9.1) as exp $[f(t)]$ we obtain expressions of the form

$$U_n(z) = \frac{1}{2\pi i}\int_U \exp\,[f(t)]\,dt, \qquad f(t) = -t^2 + 2zt - m\log t, \qquad m = n + 1. \tag{10.1}$$

The saddle points of the integrand are at the points t_0 and t_1 in the complex t-plane where $f'(t)$ is zero:

$$\begin{aligned} 2t_0^2 - 2zt_0 + m &= 0, & t_0^2 - zt_0 &= -m/2, \\ t_0 &= \frac{z + (z^2 - 2m)^{1/2}}{2}, & t_0 + t_1 &= z, \\ t_1 &= \frac{z - (z^2 - 2m)^{1/2}}{2}, & 2t_0t_1 &= m. \end{aligned} \tag{10.2}$$

Let the path of integration U of (10.1), for example, be deformed so as to pass through a saddle point, say t_0, along a path of steepest descent. Let

$$f(t) = f(t_0) - \sum_2^\infty b_k(t - t_0)^k/k!. \tag{10.3}$$

Then, if b_2 is not too small, the contribution of the region around t_0

---

[20] Nathan Schwid, The Asymptotic Forms of the Hermite and Weber Functions, Amer. Math. Soc. Trans. **37,** pp. 339–362, 1935. References to earlier work will be found in this paper. Schwid's work is based on R. Langer's study of the asymptotic solutions of second order differential equations.

[21] O. E. H. Rydbeck, The Propagation of Radio Waves, Trans. of Chalmers Univ. of Tech. **34,** 1944.

[22] G. N. Watson, Harmonic Functions Associated with Parabolic Cylinder Functions, Proc. London Math. Soc. (2) **17,** pp. 116–148, 1918.

to the value of the integral is exp $[f(t_0)]$ times

$$\frac{1}{2\pi}\int \exp\left[-\sum_{2}^{\infty} b_k(t-t_0)^k/k!\right]dt \sim (2\pi b_2)^{-1/2}[1+\{-b_4B_2+10b_3^2B_3\} \tag{10.4}$$
$$+\{-b_6B_3+[35b_4^2+56b_3b_5]B_4-2100b_3^2b_4B_5+55(280)b_3^4B_6\} + \cdots]$$

where $B_k = (2b_2)^{-k}/k!$. The sign of $(2\pi b_2)^{-1/2}$ is chosen so that the argument of the right hand side of (10.4) is equal to arg (dt) at $t = t_0$ on the path of steepest descent. The derivatives of $f(t)$ at t_0 give

$$b_2 = 2(t_0-t_1)/t_0, \qquad b_3 = 4t_1/t_0^2, \qquad b_4 = -12t_1/t_0^3,$$
$$-b_4B_2+10b_3^2B_3 = \frac{t_1(t_1+9t_0)}{24t_0(t_0-t_1)^3}. \tag{10.5}$$

The values of these quantities at the saddle point t_1 may be obtained by interchanging t_0 and t_1. If more terms of (10.4) are desired they may be obtained from the formal result

$$\frac{1}{2\pi}\int_{-\infty}^{\infty} \exp\left[-\sum_{k=2}^{\infty}\alpha_k t^k/k!\right]dt \sim (2\pi\alpha_2)^{-1/2}\left[1+\sum_{k=2}^{\infty} Y_{2k}(0,0,-\alpha_3,-\alpha_4,\cdots,-\alpha_{2k})/k!(2\alpha_2)^k\right] \tag{10.6}$$

where $Y_n\,(a_1, a_2, \ldots, a_n)$ is the Bell exponential polynomial.[23] It is necessary to rearrange the terms given by (10.6) in order to get them in groups having the same order of magnitude. A more careful treatment of the terms in the asymptotic expansions for $D_n(z)$ has been given by Watson.[22] His method is similar to that used by Debye for Bessel functions.

In our work we shall deal with two different complex planes, and the reader is cautioned against confusing them. One is the complex t-plane, shown in Fig. 10.1, which contains the paths of integration for integrals such as (10.1). The other is the complex m-plane, shown in Fig. 10.2, which is introduced because we are often more interested in $U_n(z)$, etc., as functions of $m = n + 1$ than as functions of z. In the earlier sections

---

[23] E. T. Bell, Exponential Polynomials, Ann. of Math. **35,** pp. 258–279, 1934. The polynomials are tabulated up to $n = 8$ by John Riordan, Inversion Formulas in Normal Variable Mapping, Annals of Math. Stat. **20,** pp. 417–425, 1949.

we have spoken of the complex n-plane, but this is essentially the m-plane shifted by unity.

Since we are going to deal with a fixed value of z ($i^{1/2}\xi$ or $i^{-1/2}\eta$) but with a variable value of m, we make t_0 and t_1 one-valued functions of m by cutting the m-plane as shown in Fig. 10.2.

It may be shown that t_0 and t_1 lie in the opposite half-planes indicated in Fig. 10.1. This restricts arg t_0 to lie between arg $z - \pi/2$ and arg $z + \pi/2$. Arg t_1 is restricted to lie between arg $z - \pi$ and arg $z + \pi$ by the cut shown in Fig. 10.1. It may also be shown that

$$| t_0 | \geqq | t_1 |, \qquad | \arg t_0 - \arg t_1 | \leqq \pi. \tag{10.7}$$

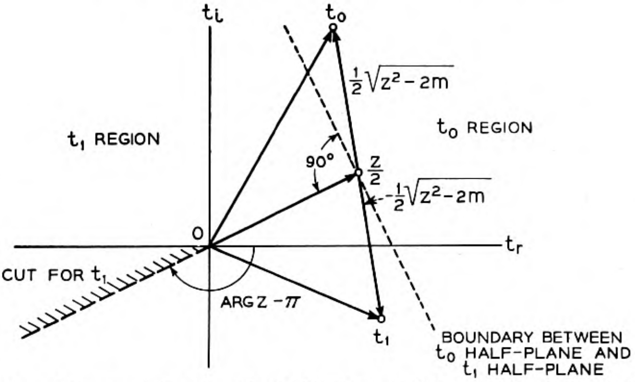

Fig. 10.1 — Diagram showing the half-plane regions to which the saddle points t_0 and t_1 are confined in the t-plane.

One might wonder why cuts in the m-plane are required since it has already been pointed out that $U_n(z)$, etc., are one-valued functions of $m = n + 1$. The trouble is that the asymptotic expressions for $U_n(z)$ are many-valued functions of m even though $U_n(z)$ itself is not.

Now that we have considered the saddle points t_0 and t_1, we turn to a consideration of the paths of steepest descent in the t-plane which pass through them.* The path of steepest descent which passes through t_0, for example, is that branch of the curve

$$Im\,[f(t) - f(t_0)] = 0 \tag{10.8}$$

for which t_0 is the highest point (i.e., $Re\,[f(t) - f(t_0)] \leqq 0$ on it). The

---

* Watson[22] has studied paths corresponding to $Re(n) > 0$ when z is any complex number, and has given curves which are related to some of those shown in Section 11.

paths of steepest descent may be shown to have the following properties:

1. Let $t = t_r + it_i = r \exp(i\theta)$. Then the paths of steepest descent either run out to $t_r = \pm\infty$ with $t_i \to Im\, z$ or spiral in to $t = 0$ as $r =$ (constant) $\exp(-m_r\theta/m_i)$.

2. The steepest descent path through t_0 may be computed by a graphical method based on*

$$\arg(dt) = \arg t - \arg(t - t_0) - \arg(t - t_1). \tag{10.9}$$

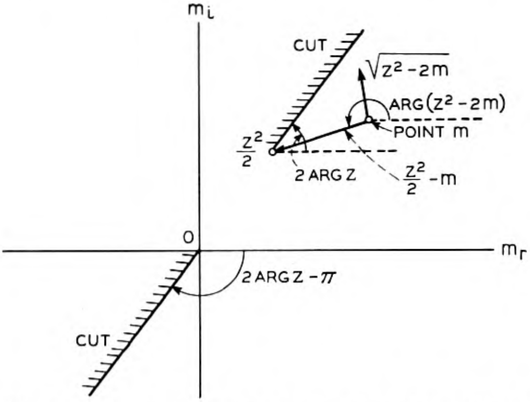

Fig. 10.2 — Diagram showing the cuts in the complex m-plane, $m = n + 1$.

If we draw the triangle $t_0\ 0\ t_1$ and bisect the interior angle at t_0 by the line b_0t_0 then

$$\arg(dt) \text{ at } t_0 = \text{angle } t_1t_0b_0. \tag{10.10}$$

If one goes clockwise in traveling from the side t_0t_1 to t_0b_0 then arg dt is negative. Likewise, arg (dt) at t_1 (on the path through t_1) is the angle between the side t_1t_0 and the bisector t_1b_1 of the interior angle at t_1.

3. When m has the critical value $z^2/2$ the saddle points coincide: $t_0 = t_1 = z/2$, and the paths of steepest descent start out from $t = z/2$ in the three directions $\arg(t - z/2) = (\arg z)/3 + \delta$ where δ is 0, $2\pi/3$, or $-2\pi/3$.

4. Some of the paths of steepest descent change their character as m goes from one region of the m-plane to another. This is illustrated in Section 11 for the case $z = \rho \exp(i\pi/4)$ where it is shown that the

---

* A similar method was used in 1938 by A. Erdélyi in an unpublished study of the asymptotic behavior of confluent hypergeometric functions.

boundaries are given by

$$Im\,[f(t_0) - f(t_1)] = 0, \tag{10.11}$$

or a similar equation involving another pair of saddle points, e.g., t_1 and $t_1 \exp(i2\pi)$. In this equation z is regarded as fixed and t_0, t_1 are functions of m defined by (10.2). It should be noted that although (10.8) defines a path of steepest descent in the t-plane, (10.11) defines curves (boundaries of regions) in the m-plane.

5. If m is such that the path of integration for a particular function, say $U_n(z)$, passes through both t_0 and t_1, each one will contribute to the value of $U_n(z)$. Furthermore, if m is such that

$$Re\,[f(t_0) - f(t_1)] = 0, \tag{10.12}$$

t_0 and t_1 have the same height and the two contributions have a chance of cancelling each other and giving a value of zero for $U_n(z)$. Thus (10.12) or some similar equation defines the lines in the m-plane along which the zeros of $U_n(z)$, etc., (regarded as functions of m) are asymptotically distributed.

6. The lines in the m-plane defined by (10.11) and (10.12) may be obtained by substituting the values (10.2) for t_0 and t_1 in

$$f(t_0) - f(t_1) = t_0^2 - t_1^2 - 2t_0t_1 \log(t_0/t_1), \tag{10.13}$$

and setting the imaginary and real parts, respectively, to zero. However, instead of dealing with m directly it is easier to use $w = u + iv$ defined by

$$w = \log(t_0/t_1) = \log|t_0/t_1| + i(\arg t_0 - \arg t_1), \tag{10.14}$$

$$m = z^2/(\cosh w + 1), \tag{10.15}$$

where (10.15) follows from (10.14) and (10.2). Then (10.13) becomes

$$\begin{aligned} f(t_0) - f(t_1) &= m(\sinh w - w) \\ &= \frac{z^2(\sinh w - w)}{\cosh w + 1}. \end{aligned} \tag{10.16}$$

The inequalities (10.7) show that

$$u \geqq 0, \ |v| \leqq \pi.$$

7. For the special case $z = \rho \exp(i\pi/4)$, (10.16) gives

$$(\cosh u + \cos v - v \sin v) \sinh u = (\cosh u \cos v + 1)\,u, \tag{10.17}$$

$$(\cos v + \cosh u + u \sinh u) \sin v = (\cosh u \cos v + 1)\,v,$$

respectively, for $Im[f(t_0) - f(t_1)] = 0$ and $Re\,[f(t_0) - f(t_1)] = 0$. These equations are plotted in Fig. 10.3. It will be noted that a curve is shown for $v > \pi$ even though this puts w outside the allowed rectangle. This is done because one of the paths of integration, W, passes through both t_0 and $t_1 \exp(-i2\pi)$ when m is in a certain region, and the corresponding zeros of $W_n(z)$ lie on the curve defined by

$$Re\,[f(t_0) - f(t_1 \exp\{-i2\pi\})] = 0.$$

It may be shown that a curve corresponding to

$$f(t_0) - f(t_1 \exp\{-i2\pi\})$$

with $-\pi < v < \pi$ may be obtained from the curve corresponding to $f(t_0) - f(t_1)$ with $\pi < v < 3\pi$ by simply subtracting 2π from v. This is done on Fig. 10.3.

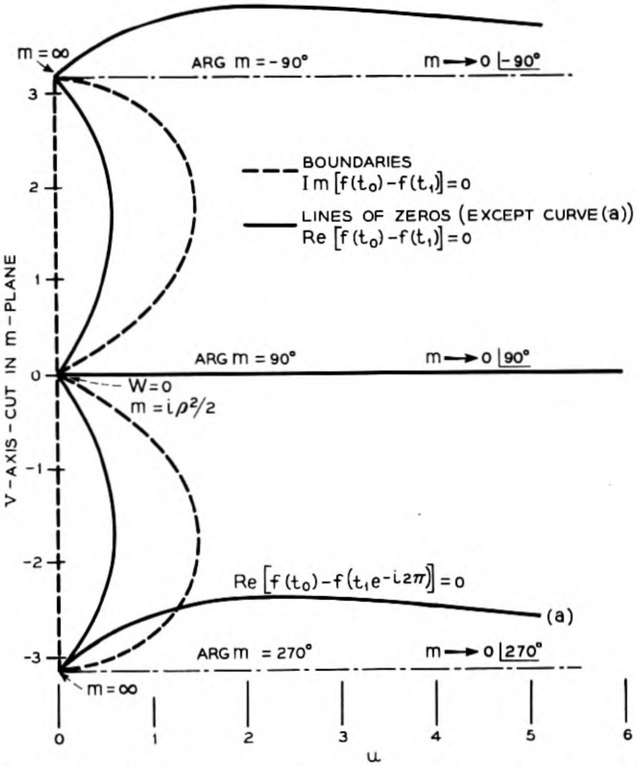

Fig. 10.3 — Boundaries of the regions shown in Fig. 11.2 and lines of zeros shown in Fig. 12.1 as they appear on the $w = u + iv$ plane when $z = i^{1/2}\rho$.

TABLE 11.1 — SADDLE POINT VALUES FOR REPRESENTATIVE VALUES OF m WHEN $z = i^{1/2}\rho$

Point Number	m/ρ^2		t_0/ρ		t_1/ρ		$\dfrac{f(t_0) + m \log \rho}{\rho^2}$	$\dfrac{f(t_1) + m \log \rho}{\rho^2}$
	Mod.	Arg.	Mod.	Arg.	Mod.	Arg.		
1	0.5	0°	1.07	57°	0.23	−57°	$-0.013 + i0.550$	$1.21 + i0.450$
2	1	0	1.20	64	0.42	−64	$-0.080 + i0.021$	$1.77 + i0.979$
3	0.550	0	1.09	58	0.25	−58	$-0.017 + i0.500$	$1.28 + i0.500$
4	0.005	0	1.00	45.1	0.0025	−45.1	$-0.000 + i0.996$	$0.035 + i0.004$
6	0.005	90	0.997	45	0.0025	45	$0.004 + i1.000$	$0.004 + i0.035$
8	0.005	180	1.00	44.9	0.0025	135.1	$+0.000 + i1.004$	$-0.035 + i0.012$
9	0.005	270	1.00	45	0.0025	225	$-0.004 + i1.000$	$-0.020 - i0.035$
10	0.005	−90	1.00	45	0.0025	−135	$-0.004 + i1.000$	$0.012 - i0.035$
11	0.550	180	1.09	32	0.25	148	$0.017 + i1.36$	$-1.28 + i1.36$
12	1	180	1.20	26	0.42	154	$0.077 + i1.59$	$-1.77 + i2.55$
13	1	$90-\epsilon$ $\arg(z^2 - 2m) = 270$	0.71	90	0.71	0	$1.07 + i1.35$	$0.5 + i1.35$
—	1	$90+\epsilon$ $\arg(z^2 - 2m) = -90$	0.71	0	0.71	90	$0.5 + i1.35$	$1.07 + i1.35$
14	0.5	90	0.5	45	0.5	45	$0.39 + i1.10$	$0.39 + i1.10$
—	1	270	1.37	45	0.37	225	$-0.784 + i1.18$	$-3.93 - i1.87$
—	1	−90	1.37	45	0.37	−135	$-0.784 + i1.18$	$+2.35 - i1.87$

The entries in this table must satisfy $t_0/\rho + t_1/\rho = i^{1/2}$. Equations (12.8) show that when all of the entries are replaced by their complex conjugates, a table for $z = i^{-1/2}\rho$ is obtained.

3. $m = (0.54953\ldots)\rho^2 \sim 0.55\rho^2$. Fig. 11.1 (b). This value of m marks the change in type of path. Since $\operatorname{Im} f(t_1) = \operatorname{Im} f(t_0)$ is satisfied, the paths through t_0 and t_1 have the same equation [see (11.2)], and there is a chance for a situation like that at t_0 in Fig. 11.1 (b) to occur. The high point of the path U is at t_1, and it goes continually downhill on either side of t_1 although its direction changes sharply by 90° at t_0. The point $m = 0.55\rho^2$ is just one point on the boundary between regions in the m-plane corresponding to various types of paths. The boundary lines are obtained by solving condition (10.11) for m as outlined in Items 6 and 7 of Section 10. Mapping the boundary lines

$$\operatorname{Im}\,[f(t_0) - f(t_1)] = 0$$

from the auxiliary w-plane (shown in Fig. 10.3) to the m-plane with the help of $m = i\rho^2/(\cosh w + 1)$ gives the boundaries between the regions

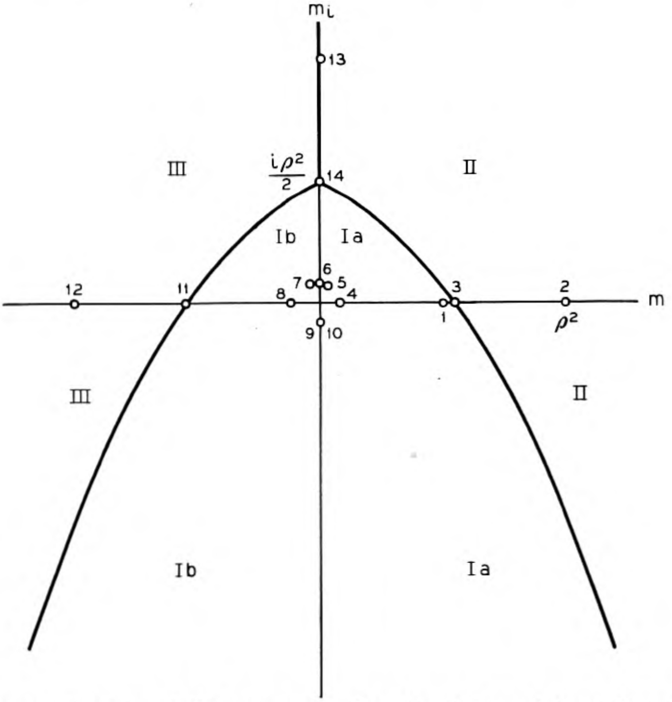

Fig. 11.2 — Regions of different types of paths of steepest descent, and hence different types of asymptotic expansions, when $z = i^{1/2}\rho$. Points numbered 1, 2, 3, are values of m corresponding to the paths of Figs 11.1 (a), (c), (b). Points designated by 5, 6, 7 correspond to Fig. 11.3(b). Points 4, 8, 9 correspond to Fig. 11.5 and points 11, 12, 13, 14 to Figs. 11.6 (a), (b), (c), (d).

I, II, III shown in Fig. 11.2. It may be verified that for large negative values of m_i the boundary lines in Fig. 11.2 are given approximately by

$$m_r = \pm 2^{3/2}\pi^{-1}\rho \mid m_i \mid^{1/2}. \tag{11.4}$$

There was a period, while these curves were being worked out, during which it appeared that the regions I, II, III told the entire story. However, when small values of m were studied it was found that region I splits up into the two sub-regions, Ia and Ib, such that the boundary between them is given by

$$\mathrm{Im}\,[f(t_1) - f(t_1e^{-2\pi i})] = 0. \tag{11.5}$$

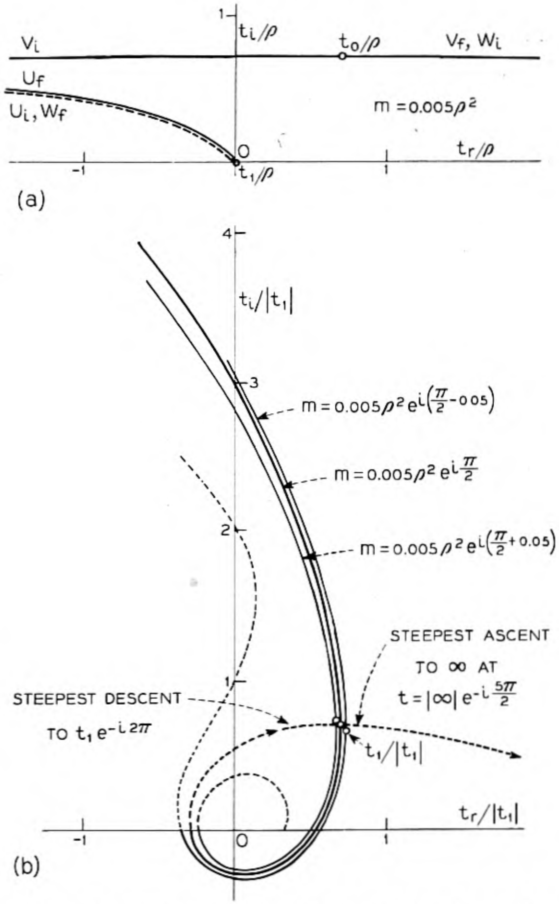

Fig. 11.3 — Paths of steepest descent for $| m | = 0.005\,\rho^2$, $z = i^{1/2}\rho$. Away from $t = t_1$ all paths look much like Fig. 11.3(a).

This is of the same form as (10.11). That $t_1 \exp(-2\pi i)$ is a saddle point follows from differentiation of the equation

$$f(te^{-2\pi i}) = f(t) + 2\pi i m_r - 2\pi m_i. \tag{11.6}$$

Combining (11.5) and (11.6) shows that the boundary between Ia and Ib is given by $m_r = 0$. This is indicated on Fig. 11.2.

We now examine the paths of steepest descent when m is small. Fig. 11.3 (a) gives a large view of all the paths, irrespective of arg m, when m^2/ρ is small.

4. $m = 0.005\rho^2$. Fig. 11.5 shows the vicinity around t_1.

5. $|m| = 0.005\rho^2$, arg $m = \pi/2 - 0.05$. Fig. 11.3 (b).

6. $|m| = 0.005\rho^2$, arg $m = \pi/2$. Fig. 11.3 (b). After passing through t_1 the path encircles the origin clockwise and runs down into the saddle point at $t = t_1 \exp(-2\pi i)$. Since m_i is positive, (11.6) shows that $t_1 \exp(-2\pi i)$ is lower than t_1. The path for arg $m = \pi/2 - 0.05$ suggests that from $t_1 \exp(-2\pi i)$ the path runs out to $\infty \exp(-\pi i)$ along the path of steepest descent which lies directly under (on the Riemann sheet for $-3\pi < \arg t < -\pi$) the path which runs from t_1 to $t = \infty \exp(i\pi)$. It follows from (11.6) that, as t traces out a path of steepest descent through t_1, $t \exp(-2\pi i)$ traces out a path of steepest descent through $t_1 \exp(-2\pi i)$ directly under the path through t_1.

7. $|m| = 0.055\rho^2$, arg $m = \pi/2 + 0.05$. Fig. 11.3 (b) shows that after passing through t_1 the path of steepest descent spirals in to $t = 0$. According to (11.3), the spiral is given by

$$r \approx (\text{constant}) \exp(-m_r\theta/m_i) \tag{11.7}$$

when r is small and θ large. Two things are to be noted. First, the type of path is different from that for arg $m = \pi/2 - 0.05$. Hence arg $m = \pi/2$ marks a change of type similar to that shown in Fig. 11.1 (b), except that here $t_1 \exp(-2\pi i)$ takes the place of t_0. Condition (11.5) takes the place of condition (10.11), and is satisfied by virtue of $m_r = 0$ when arg $m = \pi/2$.

The second thing to be noted is that up until now all of the paths of steepest descent have ended at $\pm\infty$ and U, V, W could be deformed into them without difficulty. How can we deform U, for example, into a path of steepest descent when the path through t_1 spirals in to $t = 0$? The way to deal with this problem is shown in Fig. 11.4 where U is continuously deformed into two portions, one coinciding with the path through t_1, as shown in Fig. 11.3 (b), and the other with the path of steepest descent through $t_1 \exp(-2\pi i)$. The second portion lies directly "underneath" the first portion.

In Fig. 11.4 the dashes mean, as before, that the path of steepest descent is on a sheet of the Riemann surface other than $| \arg t | < \pi$. The alternate dots and dashes are used to indicate that $| \arg t | > \pi$ and that in addition the path lies directly under the curve it parallels. Although in Fig. 11.4 the two kinds of dashed curves are joined at about $\arg t = -3\pi - \pi/4$, they actually should spiral in to $t = 0$ before they connect.

8. $| m | = 0.005\rho^2$, $\arg m = \pi$. Fig. 11.5. For $\arg m = \pi$, (11.6) shows that t_1 and $t_1 \exp(-2\pi i)$ are of the same height.

9. $m = 0.005\rho^2$, $\arg m = 3\pi/2$. For $\pi < \arg m < 3\pi/2$, $t_1 \exp(-2\pi i)$ is higher than t_1 and the paths spiral into $t = 0$ counterclockwise. At $\arg m = 3\pi/2$ the rate of spiralling is zero and we have the path shown in Fig. 11.5 (which is the path for $\arg m = \pi/2$ rotated by 180 degrees). Here $\arg t_1 = 5\pi/4$.

10. $m = 0.005\rho^2$, $\arg m = -\pi/2$. The paths for $\arg m$ equal to $-\pi/2$

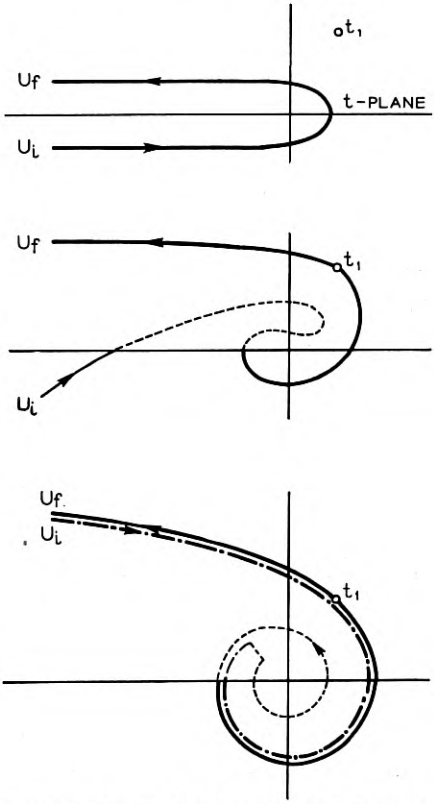

Fig. 11.4 — Deformation of path of integration U into path of steepest descent through t_1 when $m = 0.005\,\rho^2 \exp(i\pi/2 + i0.05)$.

and $3\pi/2$ have the same shape and both are highest at the saddle point whose argument is $-3\pi/4$. In both cases the contributions are the same and hence the value of $U_n(z)$, for example, is the same for arg $m = -\pi/2$ as for $3\pi/2$ (as it must be since our parabolic cylinder functions are one-valued functions of m).

Before leaving the region around $m = 0$ we point out that when $|m/\rho^2| \ll 1$ the path of steepest descent through t_0 is almost independent of arg m. Also, the curves of steepest descent for

$$1/\Gamma(m) = \frac{1}{2\pi i}\int_U e^t t^{-m}\, dt \tag{11.8}$$

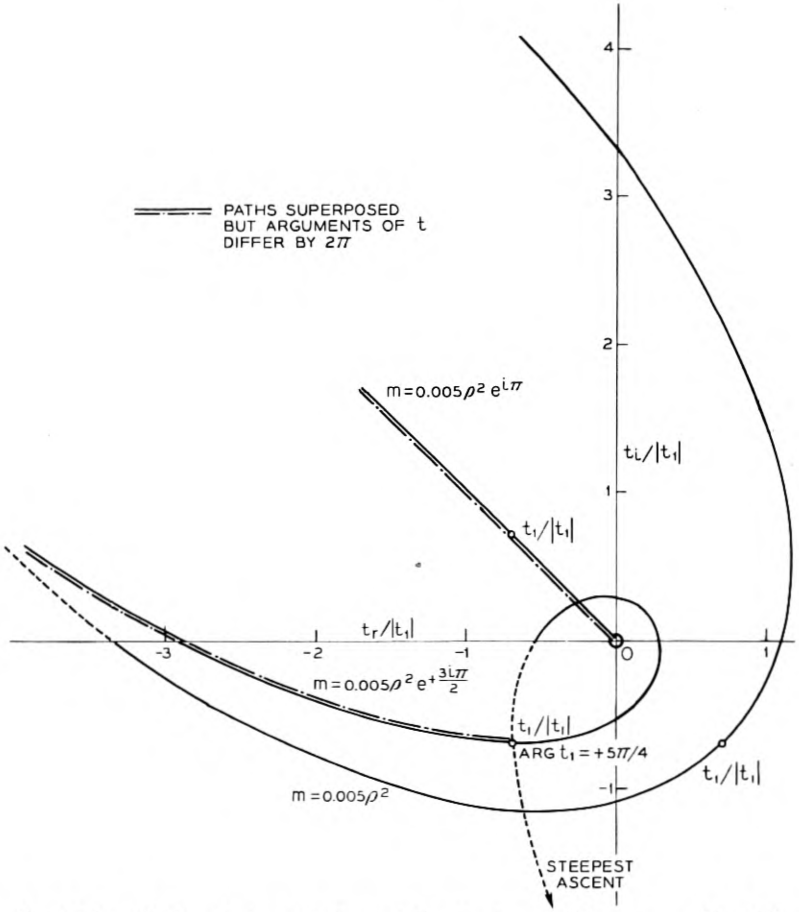

Fig. 11.5 — Paths of steepest descent for $|m| = 0.005\,\rho^2$, $z = i^{1/2}\rho$. These curves are much the same as those in Fig. 11.3(b) except for the values of arg m.

behave in much the same way as those just described. The line $m_r = 0$ divides the m-plane into two regions corresponding to different types of paths, and the negative real axis is a line of zeros corresponding to $Re\ [f(t_1) - f(t_1 \exp(-2\pi i))] = 0$ where $t_1 = m$ is the saddle point.

11. $|m| = 0.55\rho^2$, $\arg m = \pi$. Fig. 11.6 (a). This value of m marks a change in the type of path.

12. $|m| = \rho^2$, $\arg m = \pi$. Fig. 11.6 (b).

13. $|m| = \rho^2$, $\arg m = \pi/2$, $\arg (i\rho^2 - 2m) = 3\pi/2$. Fig. 11.6 (c). The complication of the paths in Fig. 11.6 (c) is due to the superposition of two boundaries in the m-plane. Im $f(t_0) =$ Im $f(t_1)$ accounts for

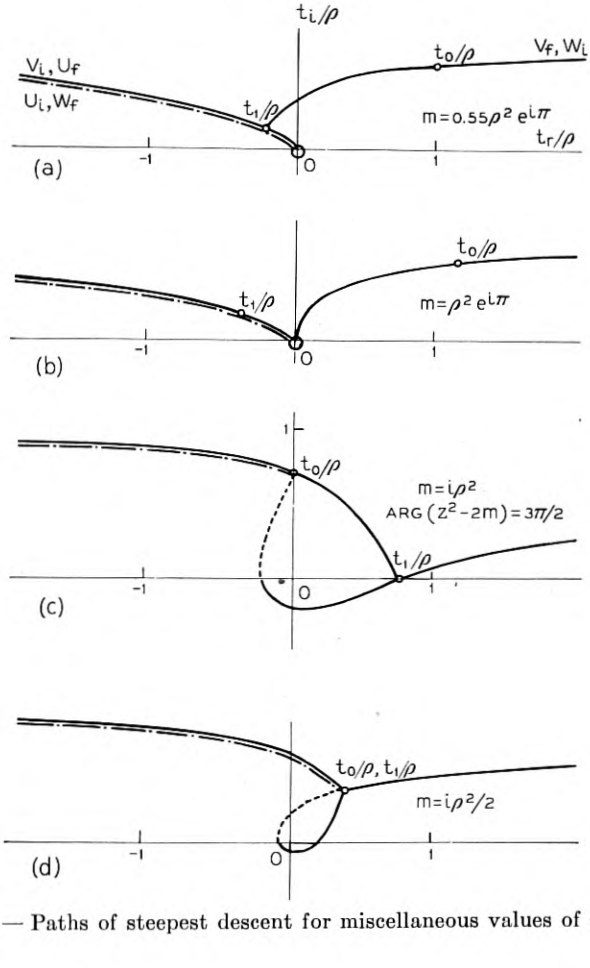

Fig. 11.6 — Paths of steepest descent for miscellaneous values of m with $z = i^{1/2}\rho$.

the path running from t_0 to t_1, and $\operatorname{Im} f(t_1) = \operatorname{Im} f[t_0 \exp(-2\pi i)]$ for the one running from t_1 to $t_0 \exp(-2\pi i)$. The saddle points in order of their height are t_0, t_1, $t_0 \exp(-2\pi i)$, t_0 being the highest.

14. $m = i\rho^2/2$. Fig. 11.6 (d). Here $t_0 = t_1$ and the dashed lines go into the saddle point at $t_1 \exp(-2\pi i)$. The paths of steepest descent change their directions upon passing through the saddle points.

12. ASYMPTOTIC EXPRESSIONS FOR $U_n(z)$, $V_n(z)$, $W_n(z)$

The asymptotic expressions given here are for $z = i^{1/2}\rho$ and $z = i^{-1/2}\rho$ [with $i^{1/2} = \exp(i\pi/4)$] when n is not too close to $z^2/2$. As mentioned earlier, there is a close relation between our results and those given by Schwid.* The main difference is that we regard n as variable and z as fixed while Schwid regards z as variable with n fixed. Another point of difference is that in place of the $m = n + 1$ which appears in our expressions for t_0 and t_1 the quantity $n + \frac{1}{2}$ appears in Schwid's work. The quantity $2n + 1$ appears to enter naturally when the asymptotic values are obtained from the differential equations. This is seen when the *WKB* method is applied to equation (9.7).

By examining the paths of steepest descent shown in the figures of Section 11 we can determine the saddle points corresponding to $U_n(z)$, etc., (for $z = i^{1/2}\rho$) for various values of n. The contributions to the integral (10.1) from the saddle points t_0 to t_1 were discussed in Section 10. The contribution from the saddle point $t_1 \exp(-2\pi i)$ (which enters when $z = i^{1/2}\rho$) is, from (11.6), $\exp(i2\pi m)$ times the contribution from t_1.

Although we shall be concerned mainly with asymptotic expressions for the parabolic cylinder functions themselves, expressions for their derivatives may be readily obtained. Thus $U_n'(z) = dU_n(z)/dz$ has the asymptotic expression

$$\begin{aligned} U_n'(z) \sim\ & 2t_0 \,[\text{contribution of } t_0 \text{ to } U_n(z)] \\ & + 2t_1 \,[\text{contribution of } t_1 \text{ to } U_n(z)] \qquad (12.1) \\ & + 2t_1 \,[\text{contribution of } t_1 \exp(-2\pi i) \text{ to } U_n(z)] \end{aligned}$$

and similar expressions hold for $V_n'(z)$, $W_n'(z)$. These follow when we note that differentiation of the integrals (9.1), which define the functions, introduces a factor $2t$ into the integrand. Of course, if the path of integration does not pass throught a particular saddle point, its contribution to (12.1) is zero. Upon replacing t_0 and t_1 by their expressions

---

* Reference 20, page 478.

(10.2) and subtracting the corresponding expression for $zU_n(z)$ we obtain

$$
\begin{aligned}
'U_n(z) &= U_n'(z) - z\,U_n(z) \\
&\sim (z^2 - 2m)^{1/2}\,[(t_0 \text{ contribution}) - (t_1 \text{ contribution}) \qquad (12.2) \\
&\qquad - (t_1 e^{-2\pi i} \text{ contribution})]
\end{aligned}
$$

where $'U_n(z)$ is the function defined by (4.19). The same is true for $'V_n(z)$ and $'W_n(z)$.

Consideration of the various paths of integration shown in Section 11 leads to the results shown in Table 12.1. The leading terms of the asymptotic expansions are listed for the various regions of the m-plane shown in Fig. 11.2. If the next order terms are required, they may be obtained from (10.4) and (10.5).

TABLE 12.1 — LEADING TERMS IN THE ASYMPTOTIC EXPANSIONS FOR $U_n(z)$, $V_n(z)$, $W_n(z)$ WHEN $z = i^{1/2}\rho$, $\rho > 0$

Region in m-plane $m = n + 1$	$U_n(i^{1/2}\rho)$	$V_n(i^{1/2}\rho)$	$W_n(i^{1/2}\rho)$
Ia	A_1	A_0	$-A_0 - A_1$
II	$A_1 - A_0$	A_0	$-A_1$
Ib	$(1 - i^{4n})A_1$	A_0	$-A_0 - A_1 + i^{4n}A_1$
III	$(1 - i^{4n})A_1$	$A_0 - A_1$	$-A_0 + i^{4n}A_1$

The notation used in Table 12.1 is as follows:

$$z = i^{1/2}\rho, \qquad m = n + 1, \qquad i = \exp(i\pi/2),$$

$$-\pi/2 < \arg m \leqq 3\pi/2, \qquad -\pi/4 < \arg t_0 \leqq 3\pi/4,$$

$$-\pi/2 < \arg(i\rho^2 - 2m) \leqq 3\pi/2, \qquad -3\pi/4 < \arg t_1 \leqq 5\pi/4,$$

$$t_0 = [i^{1/2}\rho + (i\rho^2 - 2m)^{1/2}]/2, \qquad t_1 = [i^{1/2}\rho - (i\rho^2 - 2m)^{1/2}]/2,$$

$$
\begin{aligned}
A_0 &= [t_0^{1/2}(i\rho^2 - 2m)^{-1/4}/2i\pi^{1/2}]\exp f(t_0), \qquad (12.3) \\
A_1 &= [t_1^{1/2}(i\rho^2 - 2m)^{-1/4}/2\pi^{1/2}]\exp f(t_1),
\end{aligned}
$$

$$f(t_0) = zt_0 + \frac{m}{2} - m\log t_0 = \frac{m}{2}\left(1 - \log\frac{m}{2} - \log\frac{t_0}{t_1}\right) + i^{1/2}\rho t_0,$$

$$f(t_1) = zt_1 + \frac{m}{2} - m\log t_1 = \frac{m}{2}\left(1 - \log\frac{m}{2} - \log\frac{t_1}{t_0}\right) + i^{1/2}\rho t_1.$$

Sometimes it is helpful to use

$$(2\pi)^{-1/2}\exp\left[\frac{m}{2}\left(1-\log\frac{m}{2}\right)\right]$$

$$\sim\begin{cases} 1/\Gamma\left(\dfrac{m+1}{2}\right) = 1/\Gamma(1+n/2) \qquad \text{for} \\ \qquad\qquad -\pi/2 < \arg m < \pi/2, \\ i^{-m}\Gamma\left(\dfrac{1-m}{2}\right)/2\pi = i^{-n-1}\Gamma(-n/2)/2\pi, \\ \qquad\qquad \pi/2 < \arg m < 3\pi/2, \end{cases} \tag{12.4}$$

where the last line is obtained by setting $m \exp(-\pi i)$ for m in the second line.

The asymptotic expansions for regions *Ib* and *III* may be obtained from those for *Ia* and *II* by using equations (9.11) and (9.13). However, the work is more difficult than one might suspect at first glance.

Incidentally, the leading terms in the asymptotic expansions (9.15) and (9.17), which hold when $\rho \to \infty$ and n remains fixed, may be obtained by considering the entries for *Ia* and *Ib* in Table 12.1.

It is sometimes convenient to use the limiting forms of the asymptotic expressions when $|m| \gg \rho^2$. In this case, for $z = i^{1/2}\rho$,

$$\begin{aligned} 2t_0 &\to z \pm i(2m)^{1/2}\left[1-\frac{z^2}{2m}\right] + 0(m^{-3/2}), \\ 2t_1 &\to z \mp i(2m)^{1/2}\left[1-\frac{z^2}{2m}\right] + 0(m^{-3/2}), \\ \log t_1/t_0 &\to \mp i\pi \pm iz(2m)^{-1/2}\left[2+\frac{z^2}{6m}\right] + 0(m^{-5/2}), \end{aligned} \tag{12.5}$$

where the upper signs hold when $-\pi/2 < \arg m < \pi/2$ and the lower ones when $\pi/2 < \arg m < 3\pi/2$. Substituting (12.5) in (12.3), neglecting the higher order terms, and setting

$$\begin{aligned} B &= 2^{-3/2}\pi^{-1/2}\exp\left[\frac{m}{2}\left(1-\log\frac{m}{2}\right)+i\rho^2/2\right], \\ \alpha_0 &= \exp\,[-\rho(2m/i)^{1/2}], \\ \alpha_1 &= \exp\,[\rho(2m/i)^{1/2}] = 1/\alpha_0, \end{aligned} \tag{12.6}$$

converts Table 12.1 into Table 12.2.

In this table B, α_0, α_1, are defined by (12.6); $m = n + 1$; $-\pi/2$

TABLE 12.2 — LEADING TERMS IN THE ASYMPTOTIC EXPANSIONS FOR $U_n(z)$, $V_n(z)$, $W_n(z)$ WHEN $z = i^{1/2}\rho$ AND $|2n| \gg \rho^2$

Region in m-plane ($m = n + 1$)	$U_n(i^{1/2}\rho)$	$V_n(i^{1/2}\rho)$	$W_n(i^{1/2}\rho)$
Ia	$i^n B\alpha_1$	$-i^{-n}B\alpha_0$	$B(i^{-n}\alpha_0 - i^n\alpha_1)$
II	$B(i^{-n}\alpha_0 + i^n\alpha_1)$	$-i^{-n}B\alpha_0$	$-i^n B\alpha_1$
Ib	$(1 - i^{4n})i^{-n}B\alpha_0$	$i^n B\alpha_1$	$B(i^{3n}\alpha_0 - i^{-n}\alpha_0 - i^n\alpha_1)$
III	$(1 - i^{4n})i^{-n}B\alpha_0$	$B(i^n\alpha_1 - i^{-n}\alpha_0)$	$B(i^{3n}\alpha_0 - i^n\alpha_1)$

$< \arg m \leqq 3\pi/2$; and in regions *Ia* and *Ib* arg m is approximately $-\pi/2$ and $3\pi/2$, respectively. Gamma functions may be introduced into the expression for B with the help of (12.4). It may be verified that the functions do not change, except for negligible terms, in crossing over the boundary from *Ia* to *Ib* (α_0 and α_1 are interchanged and B is changed by the factor $\exp(-m\pi i)$).

Since the zeros of our functions, regarded as functions of n, occur (asymptotically) when the contributions from two saddle points cancel each other, we may look at Table 12.1 and pick out regions which may possibly contain zeros. Thus, A_0 may equal A_1 along the line $|A_0| = |A_1|$, i.e. very nearly $Re[f(t_0) - f(t_1)] = 0$, in the m-plane. These lines were discussed in Item 7 of Section 10 and are plotted on the auxiliary w-plane in Fig. 10.3 When plotted on the m-plane the lines appear as shown in Fig. 12.1 The condition $Re[f(t_0) - f(t_1 \exp(-2\pi i))] = 0$ gives the line $|A_0| \approx |i^{4n}A_1|$ for some of the zeros of $W_n(i^{1/2}\rho)$.

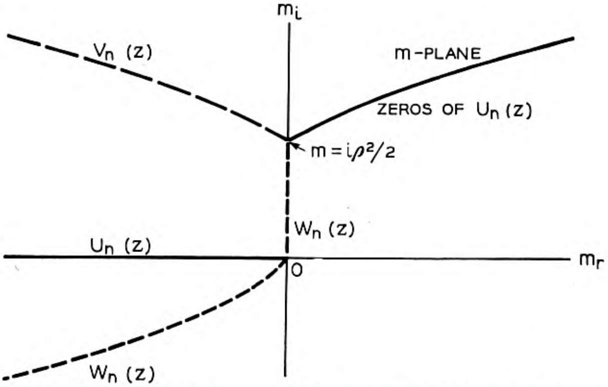

Fig. 12.1 — When $U_n(z)$, $V_n(z)$, and $W_n(z)$ are regarded as functions of n their zeros lie on the lines indicated when $z = i^{1/2}\rho$. The three branches coming out from $m = i\rho^2/2$ are lines along which $|A_0| \approx |A_1|$ and the branch for $W_n(z)$ coming down from $m = 0$ is a line along which $|A_0| \approx |i^{4n}A_1|$ where A_0 and A_1 appear in Table 12.1.

The location of the zeros far out on the lines of Fig. 12.1 may be obtained by writing the appropriate expressions of Table 12.2 as proportional to B times a cosine or sine. Examination of the trigonometrical terms shows that

$$\begin{aligned} &U_n(i^{1/2}\rho) \text{ has zeros at } n \approx 2k + 1 + i^{1/2}4\rho k^{1/2}/\pi, \\ &V_n(i^{1/2}\rho) \text{ has zeros at } n \approx -2k + i^{3/2}4\rho k^{1/2}/\pi, \\ &W_n(i^{1/2}\rho) \text{ has zeros at } n \approx -2k + i^{-1/2}4\rho k^{1/2}/\pi, \end{aligned} \qquad (12.7)$$

where k is a large positive integer. Of course, $U_n(z)$ also is zero when n is a negative integer.

So far we have been dealing with $z = i^{1/2}\rho$. Now we consider the case $z = i^{-1/2}\rho$.

Asymptotic expressions which hold when $z = i^{-1/2}\rho$ may be obtained from Table 12.1 by using the relations (9.11) between functions of z and of its complex conjugate z^*. Thus, for example, $V_{a+ib}(i^{-1/2}\rho)$ is equal to the complex conjugate of $W_{a-ib}(i^{1/2}\rho)$. These relations, and relations such as

$$\begin{aligned} &[t_0 \text{ for } z = i^{1/2}\rho,\ n = a - ib]^* = t_0 \text{ for } z = i^{-1/2}\rho,\ n = a + ib \\ &[f(t_0) \text{ for } z = i^{1/2}\rho,\ n = a - ib]^* = f(t_0) \text{ for } z = i^{-1/2}\rho,\ n = a + ib \end{aligned} \qquad (12.8)$$

have been used in constructing Tables 12.3 and 12.4 from Tables 12.1 and 12.2 The interchange of $V_n(z)$ and $W_n(z)$ should be noted. The

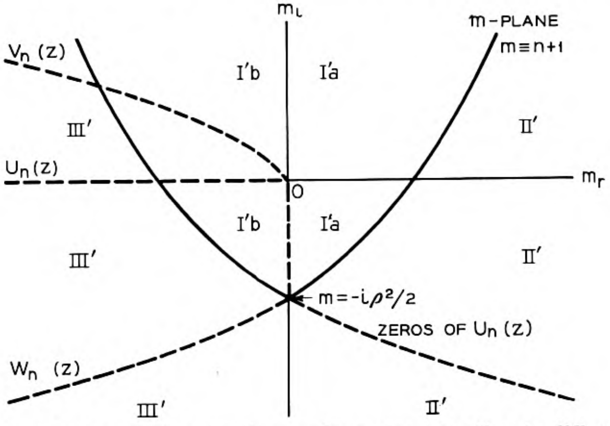

Fig. 12.2 — Regions in the complex m-plane corresponding to different asymptotic expressions when $z = i^{-1/2}\rho$. The lines on which the zeros of the various functions lie are shown by the dashed lines. The corresponding information for $z = i^{1/2}\rho$ is shown on Figs. 11.2 and 12.1.

TABLE 12.3 — LEADING TERMS IN THE ASYMPTOTIC EXPANSIONS FOR $U_n(z)$, $V_n(z)$, $W_n(z)$ WHEN $z = i^{-1/2}\rho$, $\rho > 0$

Region in m-plane $m = n + 1$	$U_n(i^{-1/2}\rho)$	$V_n(i^{-1/2}\rho)$	$W_n(i^{-1/2}\rho)$
Ia′	A_1'	$-A_0' - A_1'$	A_0'
II′	$A_1' - A_0'$	$-A_1'$	A_0'
Ib′	$(1 - i^{-4n})A_1'$	$-A_0' - (1 - i^{-4n})A_1'$	A_0'
III′	$(1 - i^{-4n})A_1'$	$-A_0' + i^{-4n}A_1'$	$A_0' - A_1'$

regions in the $m = n + 1$ plane corresponding to the different asymptotic expressions are shown in Fig. 12.2. The boundaries are simply those of Fig. 11.2 reflected in the real m-axis. The lines of zeros are also shown in Fig. 12.2, and are reflections of those of Fig. 12.1 except for the interchange of $V_n(z)$ and $W_n(z)$.

Table 12.3 may also be constructed by returning to the paths of integration shown in Section 11. It may be shown that corresponding to every path of steepest descent for $z = i^{1/2}\rho$, $n = n_1$ there is another path, obtained from the first by reflection in the real t-axis, which gives the path of steepest descent for $z = i^{-1/2}\rho$, $n = n_1^*$.

The notation used in Table 12.3 is as follows:

$$z = i^{-1/2}\rho,\ m = n + 1, \qquad i = \exp(i\pi/2),$$

$$-3\pi/2 \leqq \arg m < \pi/2, \qquad -3\pi/4 \leqq \arg t_0 < \pi/4,$$

$$-3\pi/2 \leqq \arg(-i\rho^2 - 2m) < \pi/2, \qquad -5\pi/4 \leqq \arg t_1 < 3\pi/4,$$

$$t_0 = [i^{-1/2}\rho + (-i\rho^2 - 2m)^{1/2}]/2, \qquad t_1 = [i^{-1/2}\rho - (-i\rho^2 - 2m)^{1/2}]/2,$$

$$A_0' = [t_0^{1/2}(-i\rho^2 - 2m)^{-1/4}/(-2i\pi^{1/2})] \exp f(t_0), \tag{12.9}$$

$$A_1' = [t_1^{1/2}(-i\rho^2 - 2m)^{-1/4}/2\pi^{1/2}] \exp f(t_1),$$

$$f(t_0) = zt_0 + \frac{m}{2} - m \log t_0 = \frac{m}{2}\left(1 - \log\frac{m}{2} - \log\frac{t_0}{t_1}\right) + i^{-1/2}\rho t_0,$$

$$f(t_1) = zt_1 + \frac{m}{2} - m \log t_1 = \frac{m}{2}\left(1 - \log\frac{m}{2} - \log\frac{t_1}{t_0}\right) + i^{-1/2}\rho t_1.$$

Sometimes it is helpful to use

$$(2\pi)^{-1/2} \exp\left[\frac{m}{2}\left(1 - \log\frac{m}{2}\right)\right]$$

$$\sim \begin{cases} 1/\Gamma\left(\dfrac{m+1}{2}\right) = 1/\Gamma(1 + n/2) \text{ for } -\pi/2 < \arg m < \pi/2, & (12.10) \\ i^m\Gamma\left(\dfrac{1-m}{2}\right)\Big/ 2\pi = i^{n+1}\Gamma(-n/2)/2\pi, \quad -3\pi/2 < \arg m < -\pi/2. & \end{cases}$$

TABLE 12.4 — LEADING TERMS IN THE ASYMPTOTIC EXPANSIONS FOR $U_n(z)$, $V_n(z)$, $W_n(z)$ WHEN $z = i^{-1/2}\rho$ AND $|2n| \gg \rho^2$

Region in m-plane $m = n + 1$	$U_n(i^{-1/2}\rho)$	$V_n(i^{-1/2}\rho)$	$W_n(i^{-1/2}\rho)$
Ia′	$i^{-n}B'\alpha_1'$	$B'(i^n\alpha_0' - i^{-n}\alpha_1')$	$-i^nB'\alpha_0'$
II′	$B'(i^n\alpha_0 + i^{-n}\alpha_1')$	$-i^{-n}B'\alpha_1'$	$-i^nB'\alpha_0'$
Ib′	$(1 - i^{-4n})i^nB'\alpha_0'$	$B'(i^{-3n}\alpha_0' - i^n\alpha_0' - i^{-n}\alpha_1')$	$i^{-n}B'\alpha_1'$
III′	$(1 - i^{-4n})i^nB'\alpha_0'$	$B'(i^{-3n}\alpha_0' - i^{-n}\alpha_1')$	$B'(i^{-n}\alpha_1' - i^n\alpha_0')$

The notation used in Table 12.4 is as follows:

$$
\begin{gathered}
m = n + 1,\ i = \exp(i\pi/2), \qquad -3\pi/2 \leqq \arg m < \pi/2, \\
B' = 2^{-3/2}\pi^{-1/2} \exp\left[\frac{m}{2}\left(1 - \log\frac{m}{2}\right) - \frac{i\rho^2}{2}\right], \\
\alpha_0' = \exp[-\rho(2im)^{1/2}], \qquad (12.11) \\
\alpha_1' = \exp[\rho(2im)^{1/2}] = 1/\alpha_0',
\end{gathered}
$$

B' may be expressed in terms of gamma functions with the help of (12.10.).

Approximate expressions for the zeros are given by the complex conjugates of (12.7). For example, if k be a large positive integer such that $2k \gg \rho^2$, the zeros of $W_n(i^{-1/2}\rho)$ are at $n = n(k)$ where $i^{-n}\alpha_1' = \exp(i\pi k)$ and

$$n(k) \approx -2k + i^{-3/2}4\rho k^{1/2}/\pi - 4i\rho^2/\pi^2. \qquad (12.12)$$

Here the approximation has been carried out one step further than in (12.7) We also have for the quantities in (7.11)

$$
\begin{gathered}
[\partial W_n(i^{-1/2}\rho)/\partial n]_{n=n(k)} \approx (-)^{k+1}B'i[\pi - \rho(i/k)^{1/2}], \qquad (12.13) \\
[i^{2n}V_n(i^{-1/2}\rho)/\sin \pi n]_{n=n(k)} \approx (-)^{k+1}2B'i.
\end{gathered}
$$

13. ASYMPTOTIC EXPRESSIONS FOR $U_n(z)$, ETC., WHEN n IS NEAR $z^2/2$

The asymptotic expressions given in Section 12 fail when n is near $z^2/2$. Expressions for the parabolic cylinder functions which hold for this region have been given by Schwid.* More recent studies of this sort, based on differential equations, have been made by T. M. Cherry[24] and F. Tricomi.[25] Their results suggest the possibility that our expressions

---

* Reference 20, page 478.

[24] Uniform Asymptotic Expansions, J. Lond. Math. Soc., **24**, pp. 121–130, 1949. Uniform Asymptotic Formulae for Functions with Transition Points, Am. Math. Soc. Trans., **68**, pp. 224–257, 1950.

[25] Equazioni Differenziali, Einaudi, Torino, pp. 301–308, 1948.

for the electromagnetic field which contain Airy integrals may be replaced by more accurate, but also more complicated, expressions. In dealing with our functions we shall work with the integrals and our procedure is somewhat similar to that used by Rydbeck.* First however, we point out that when we write (as suggested by the work of Cherry and Tricomi)

$$y = e^{-z^2/2} T_n(z), \qquad ax = z - (2n+1)^{1/2}, \qquad 2(2n+1)^{1/2} a^3 = 1, \tag{13.1}$$

the differential equation (9.7) for the parabolic cylinder functions goes into

$$\frac{d^2y}{dx^2} - xy = 2^{-4/3}(2n+1)^{-2/3} x^2 y. \tag{13.2}$$

The Airy integrals $Ai(x)$ and $Bi(x)$ (and also $Ai[x \exp(\pm i2\pi/3)]$) discussed later in this section are solutions of

$$\frac{d^2y}{dx^2} - xy = 0, \tag{13.3}$$

and therefore we expect that approximate solutions of (13.2) are given by, for example,

$$y = c_1 Ai(xi^{\nu})[1 + 0(n^{-2/3})] \tag{13.4}$$

where the $0(n^{-2/3})$ term corresponds to the particular integral of (13.2) when the y on the right hand side is replaced by its approximate value $Ai(xi^{\nu})$. Here c_1 is independent of x (or z) but may depend on n, and ν may be 0 or $\pm 4/3$.

Since the labor of computing c_1 is considerable, we shall work out the approximations directly from the integrals.

We shall consider the case $z = i^{1/2}\rho$, $\rho > 0$, first. When $n + 1 = m = m_0 \equiv i\rho^2/2$ the saddle points t_0 and t_1 coincide at $t_2 \equiv i^{1/2}\rho/2$. Consequently only those portions of the paths of steepest descent which lie near t_2 are of importance. This is true even if m is not exactly equal to m_0. We therefore regard

$$f(t) = -t^2 + 2zt - m \log t \tag{13.5}$$

in (10.1) as a function of the two variables t and m (linear in m) with z fixed at $i^{1/2}\rho$. Expanding (13.5) about $t = t_2$, $m = m_0$ gives

$$\begin{aligned} f(t) = \frac{z^2}{2} + \left[\frac{m_0}{2} - \frac{m_0}{2}\log\frac{m_0}{2} - \frac{(m - m_0)}{2}\log\frac{m_0}{2}\right] \\ - 4(t - t_2)^3/3z - 2(m - m_0)(t - t_2)/z + \cdots \end{aligned} \tag{13.6}$$

---

* Page 87 of Reference 21 cited on page 478.

where we have used

$$t_2 = z/2 = i^{1/2}\rho/2 = (m_0/2)^{1/2} \tag{13.7}$$

and have arranged the terms within the brackets so that they represent the first two terms in the expansion of

$$\frac{m}{2} - \frac{m}{2}\log\frac{m}{2} \sim \log\left[(2\pi)^{1/2}\Big/\Gamma\left(\frac{m+1}{2}\right)\right] \tag{13.8}$$

about m_0.

The paths of steepest descent in the t-plane when $m = m_0$ are shown in Fig. 11.6(d). The three branches start out from $t = t_2$ in the directions $\arg(t - t_2) = 15°, 135°$, and $-105°$. In this section we take the paths of integration to be those of Fig. 11.6(d) even when m is not exactly equal to m_0. Since we are dealing with asymptotic expressions we may confine our attention to the region around $t = t_2$ where the paths of integration are essentially straight lines [the contributions from $t_2 \exp(-2\pi i)$ are negligible].

When (13.6) is set in the integral

$$(1/2\pi i)\int \exp\,[f(t)]\,dt \tag{13.9}$$

we see that the initial directions of the branches are such as to make $(t - t_2)^3/z$ positive ($\arg z = 45°$). Some study of (13.6) and of the Airy integrals we intend to use suggests that we change the variable of integration from t to s and introduce the parameter b where

$$t - t_2 = s(z/4)^{1/3}, \qquad b = (m - m_0)(2/z^2)^{1/3} = (m - m_0)/m_0^{1/3}. \tag{13.10}$$

This and (13.6) converts the integral (9.1) for $V_n(i^{1/2}\rho)$ into

$$V_n(i^{1/2}\rho) = \frac{(z/4)^{1/3}e^{z^2/2}}{i(2\pi)^{1/2}\Gamma\left(\dfrac{m+1}{2}\right)}\int_{\infty \exp(i2\pi/3)}^{\infty} \exp\,[-bs - s^3/3 + \cdots]\,ds. \tag{13.11}$$

When we use the Airy integral defined by

$$\begin{aligned} Ai(x) &= \pi^{-1}\int_0^{\infty} \cos\,(xt + t^3/3)\,dt \\ &= (i^{1/3}/2\pi)\int_{\infty \exp(i2\pi/3)}^{\infty} \exp\,[-i^{-2/3}xs - s^3/3]\,ds, \end{aligned} \tag{13.12}$$

we obtain

$$V_n(i^{1/2}\rho) \sim \frac{(z/4)^{1/3}e^{z^2/2}}{i(2\pi)^{1/2}\Gamma\left(\dfrac{m+1}{2}\right)}\,\frac{2\pi}{i^{1/3}}\,Ai(bi^{2/3}). \tag{13.13}$$

In order to obtain expressions corresponding to (13.13) for $U_n(z)$, $W_n(z)$ we examine Fig. 11.6(d). We have already seen that the limits of integration for s, in the integral (13.11) for $V_n(i^{1/2}\rho)$, are $[\infty \exp (i2\pi/3), \infty]$. In the same way it follows that the limits for $U_n(i^{1/2}\rho)$ and $W_n(i^{1/2}\rho)$ are $[\infty \exp (-i2\pi/3), \infty \exp (i2\pi/3)]$ and $[\infty, \infty \exp (-i2\pi/3)]$, respectively. When we take $s' = s \exp (\mp i2\pi/3)$ as new variables of integration (with the upper sign for $U_n(z)$ and the lower one for $W_n(z)$), the integrals corresponding to (13.11) go into Airy integrals.

We can write our results for $z = i^{1/2}\rho$, when n is close to $i\rho^2/2$, as follows:

$$\begin{aligned} U_n(i^{1/2}\rho) &\sim C i^{1/6} Ai(b i^{6/3}), \\ V_n(i^{1/2}\rho) &\sim C i^{-7/6} Ai(b i^{2/3}), \\ W_n(i^{1/2}\rho) &\sim C i^{9/6} Ai(b i^{-2/3}), \end{aligned} \tag{13.14}$$

where

$$\begin{aligned} C &= (\rho/4)^{1/3}(2\pi)^{1/2}e^{i\rho^2/2}/\Gamma\left(\frac{m+1}{2}\right), \\ b &= (2/\rho^2)^{1/3}(m - i\rho^2/2)i^{-1/3}, \\ i &= \exp (i\pi/2), \qquad m = n + 1. \end{aligned} \tag{13.15}$$

The asymptotic expansions whose leading terms are given by (13.14) may be obtained by the method used by F. W. J. Olver[26] to study Bessel functions.

$Ai(x)$ and its derivative have been tabulated for positive and negative values of x.* Here we shall use the definitions and results as set forth in Reference 11. These tables and (13.14) enable us to obtain values of $U_n(i^{1/2}\rho)$ along the rays in the m-plane defined by $\arg (m - i\rho^2/2) = \pi/6$ and $-5\pi/6$. Along the $\pi/6$ ray $bi^{6/3}$ is negative. Since the tables show that the zeros of $Ai(x)$ occur when x is negative, it follows that the zeros of $U_n(i^{1/2}\rho)$ occur on the $\pi/6$ ray. In the same way it is seen that the zeros of $V_n(i^{1/2}\rho)$ and $W_n(i^{1/2}\rho)$ occur on the $5\pi/6$ and the $-\pi/2$ rays, respectively. This agrees with Fig. 12.1.

The Airy integral defined by

---

* Reference 11, page 424.

[26] Some New Asymptotic Expansions for Bessel Functions of Large Orders, Proc. Cambridge Phil. Soc., **48,** pp. 414–427, 1952.

$$\begin{aligned} Bi(x) &= \frac{i^{-2/3}}{2\pi}\left[\int_{\infty \exp(-i2\pi/3)}^{\infty \exp(i2\pi/3)} \right. \\ &\qquad \left. + \int_{\infty \exp(-i2\pi/3)}^{\infty}\right] \exp\,[-i^{-2/3}xs - s^3/3]\,ds \\ &= \frac{1}{\pi}\int_0^\infty \left[\exp\left(-\frac{t^3}{3} + xt\right) + \sin\left(\frac{t^3}{3} + xt\right)\right] dt \end{aligned} \tag{13.16}$$

is also tabulated in Reference 11 where it is shown that

$$\begin{aligned} Ai(xi^{4/3}) &= i^{2/3}[Ai(x) - iBi(x)]/2, \\ Ai(xi^{-4/3}) &= i^{-2/3}[Ai(x) + iBi(x)]/2. \end{aligned} \tag{13.17}$$

With the help of these relations we may evaluate the expressions (13.14) for $U_n(i^{1/2}\rho)$, etc., on any one of the six rays

$$\arg\,(m - i\rho^2/2) = \pm 5\pi/6,\ \pm/\pi/2,\ \pm\pi/6.$$

When b is a general complex number the expressions (13.14) may be evaluated with the help of the modified Hankel functions $h_1(\alpha)$, $h_2(\alpha)$ tabulated in Reference 27 for complex values of α. The relation needed is

$$\begin{aligned} Ai(\alpha) &= \frac{1}{2k}\,h_1(-\alpha) + \frac{1}{2k^*}\,h_2(-\alpha), \\ k &= (12)^{1/6}i^{-1/3}. \end{aligned} \tag{13.18}$$

When $|\arg\alpha| < \pi$ we have the asymptotic expansion

$$Ai(\alpha) \sim 2^{-1}\pi^{-1/2}\alpha^{-1/4}\,(\exp\,[-(2/3)\alpha^{3/2}])(1 - 5/48\alpha^{3/2} + \cdots) \tag{13.19}$$

and when $|\arg(-\alpha)| < 2\pi/3$ we have

$$Ai(\alpha) \sim \pi^{-1/2}(-\alpha)^{-1/4}\sin\,[(2/3)(-\alpha)^{3/2} + \pi/4]. \tag{13.20}$$

Both of these expansions follow from the discussion of the asymptotic behavior of $h_1(\alpha)$ and $h_2(\alpha)$ given by W. H. Furry and H. A. Arnold.[27]

Asymptotic expressions for $U_n(i^{-1/2}\rho)$, $\cdots$ valid when n is near $-i\rho^2/2$ may be obtained by applying the relations $U_n(z^*) = [U_{n*}(z)]^* \cdots$ given by (9.11) to the expressions (13.14) for $U_n(i^{1/2}\rho)$, $\cdots$:

$$\begin{aligned} U_n(i^{-1/2}\rho) &\sim C'i^{-1/6}Ai(b'i^{-6/3}), \\ V_n(i^{-1/2}\rho) &\sim C'i^{-9/6}Ai(b'i^{2/3}), \\ W_n(i^{-1/2}\rho) &\sim C'i^{7/6}Ai(b'i^{-2/3}), \end{aligned} \tag{13.21}$$

---

[27] Tables of the Modified Hankel Functions of Order One-Third and of Their Derivatives, Harvard Univ. Press, 1945.

where

$$\begin{aligned} C' &= (\rho/4)^{1/3}(2\pi)^{1/2}e^{-i\rho^2/2}/\Gamma\left(\frac{m+1}{2}\right), \\ b' &= (2/\rho^2)^{1/3}(m + i\rho^2/2)i^{1/3}, \\ i &= \exp\,(i\pi/2), \qquad m = n + 1. \end{aligned} \tag{13.22}$$

In (13.14) $bi^{6/3} = -b$ and in (13.21) $b'i^{-6/3} = -b'$ since $Ai(\alpha)$ is a single-valued function of α. It is interesting to note that the factor $i^{1/6}$ in the expression for $U_n(i^{1/2}\rho)$ gives the direction of that one of the three paths of steepest descent (in the t-plane) which is *not* traversed in getting $U_n(i^{1/2}\rho)$. The same sort of thing is true for the remaining expressions in (13.14) and (13.21).

The functions

$$'U_n(z) = \exp\,(z^2/2)\partial[U_n(z)\exp\,(-\,z^2/2)]/\partial z,$$

defined by (4.19), may be computed from (13.21) when $z = i^{-1/2}\rho$. We need the relations $\partial/\partial z = i^{1/2}\partial/\partial\rho$ and

$$\begin{aligned} m &= -i\rho^2/2 + b'(\rho^2/2i)^{1/3}, \\ \partial b'/\partial\rho &= (2/3)(2i\rho)^{1/3}(i - m/\rho^2) = i(2i\rho)^{1/3} - 2b'/3\rho, \end{aligned} \tag{13.23}$$

which follow from the definition of b'. When the differentiations are carried out we obtain

$$\begin{aligned} 'U_n(i^{-1/2}\rho) &\sim (2\rho)^{1/3}C'i^{-1/3}Ai'(b'i'^{-6/3}), \\ 'V_n(i^{-1/2}\rho) &\sim (2\rho)^{1/3}C'i^{3/3}Ai'(b'i^{2/3}), \\ 'W_n(i^{-1/2}\rho) &\sim (2\rho)^{1/3}C'i^{7/3}Ai'(b'i^{-2/3}), \end{aligned} \tag{13.24}$$

In these expressions the prime on the Airy integral denotes its derivative:

$$Ai'(\alpha) = dAi(\alpha)/d\alpha. \tag{13.25}$$

Abstracts of Bell System Technical Papers* Not Published in this Journal

AIKENS, A. J.,[1] and C. S. THAELER.[2]

Control of Noise and Crosstalk on N1 Carrier Systems, A.I.E.E. Trans., Commun. & Electronics, **9,** pp. 605–611, Nov., 1953.

BENEDICT, T. S.[1]

Microwave Observation of the Collision Frequency of Holes in Germanium, Letter to the Editor, Phys. Rev., **91,** pp. 1565–1566, Sept. 15, 1953.

BENNETT, W.[1]

Telephone System Applications of Recorded Machine Announcements, Elec. Eng., **72,** pp. 975–980, Nov., 1953.

Applications of voice-recording equipment discussed in some detail can be divided into four general groups: Announcements made directly to and providing a service to subscribers, such as weather forecasts and the time of day; announcements to assist subscribers in connection with telephone service, that is, intercept announcements when an individual calls a vacant or disconnected terminal, or emergency announcements if an unusual condition prevents normal service; announcements to expedite service and assist operators in completing calls, including completion of calls from a dial to a non-dial phone, and advising operators of the time delay for completing long distance calls; and specialized announcement or recording services, such as price quotation and ticket reservation.

---

* Certain of these papers are available as Bell System Monographs and may be obtained on request to the publication Department, Bell Telephone Laboratories, Inc., 463 West Street, New York 14, N. Y. For papers available in this form, the monograph number is given in parentheses following the date of publication, and this number should be given in all requests.

[1] Bell Telephone Laboratories.

[2] American Telephone and Telegraph Company.

BRIGGS, H. B.,[1] and R. C. FLETCHER.[1]

Absorption of Infrared Light by Free Carriers in Germanium, Phys. Rev., **91,** pp. 1342–1346, Sept. 15, 1953.

The absorption of infrared light associated with the presence of free carriers in germanium has been measured by injecting these carriers across a p-n junction at room temperature. The absorption is found to be proportional to the concentration of carriers. The absorption as a function of wavelength shows the same rather sharp maxima previously observed in normal p-type germanium. These bands are found to change with temperature. An explanation of this absorption is offered in terms of a degenerate energy band scheme.

BRIGGS, H. B., see M. TANENBAUM.

CARLITZ, L.,[1] and J. RIORDAN.[1]

Congruences for Eulerian Numbers, Duke Math. J., **20,** pp. 339–343, Sept., 1953.

CLARK, M. A., see H. C. MONTGOMERY.

CRABTREE, J.,[1] and B. S. BIGGS.[1]

Cracking of Stressed Rubber by Free Radicals, Letter to the Editor, J. Polymer Sci., **11,** pp. 280–281, Sept., 1953.

DICKINSON, F. R., see L. H. MORRIS.

FELCH, E. P.,[1] and J. L. POTTER.[1]

Preliminary Development of a Magnettor Current Standard, A.I.E.E. Trans., Commun. & Elec., **9,** pp. 524–531, Nov., 1953.

In the wartime development of the air-borne magnetometer, a method of detecting extremely small changes in magnitudes of magnetic fields was developed. The principle involved was the use of a second-harmonic type of magnetic modulator now known as a magnettor. This instrument can detect changes in magnetic fields in the order of 10^{-5} oersted. A study was made at Rutgers University under the sponsorship of Bell Telephone Laboratories to determine the feasibility of obtaining a standard of current using the magnettor principle.

FLETCHER, R. C., see H. B. BRIGGS.

---

[1] Bell Telephone Laboratories, Inc.

GOERTZ, M., see H. J. WILLIAMS.

GRAY, M. C.[1]

Legendre Functions of Fractional Order, Quart. Appl. Math., **11,** pp. 311–318, Oct., 1953.

GRISDALE, R. O.[1]

Formation of Black Carbon, J. Appl. Phys., **24,** pp. 1082–1091, Sept., 1953.

Electron microscopic evidence is presented in support of the hypothesis that black carbon resulting from pyrolysis of gaseous hydrocarbons is produced through the intermediate formation of droplets of complex hydrocarbons. Electron diffraction studies further confirm the hypothesis if, as has been found for particles of carbon blacks, the droplets consist in part of graphitic nuclei arranged with their basal planes tangential to the droplet surface. The carbonization of small solid spherules of highly cross-linked organic polymers is described, and it is shown that the morphology of the carbonization products is wholly analogous to those for pyrolytic carbon and carbon blacks. It is suggested, therefore, that the formation of carbon by the carbonization of solids and by deposition from the gas phase occurs through similar mechanisms and that the two processes are simply two extremes in an infinite series of processes which are all fundamentally alike.

GRISDALE, R. O.[1]

Properties of Carbon Contacts, J. Appl. Phys., **24,** pp. 1288–1296, Oct., 1953.

Microphone carbon has been produced by deposition of pyrolytic carbon films over the surfaces of small spherules of silica. The properties of contacts between these spherules are shown to be dependent on the structure and geometry of the carbon surface as determined by electron diffraction and microscopic studies. The graphite-like crystallites in pyrolytic carbon surfaces are more or less preferentially oriented with their basal planes parallel to the surface, and the contact properties depend systematically on the degree of orientation. This is explained in terms of the anisotropy in properties of these crystallites which are closely approximated by those of single crystal graphite which were determined. The contact resistance and its temperature coefficient and the "burning voltage" for carbon contacts are explicable on this basis. However, the microphonic sensitivity of carbon contacts is independent of the surface structure and depends only on the surface geometry.

---

[1] Bell Telephone Laboratories, Inc.

HARRIS, C. M.[1]

Speech Synthesizer, Acoust. Soc. Am., J., **25,** pp. 970–975, Sept., 1953.

"Standardized speech" constructed from building blocks called speech modules has been described; it was synthesized by piecing together bits of magnetic tape containing recorded speech sounds. An electromagnetic device, a "speech module synthesizer," is described here which performs the synthesis automatically. When buttons on a keyboard are pressed, a sequence of corresponding speech modules are automatically recorded on tape exactly in tandem. The modules are selected from a group "stored" on a rotating magnetic drum. The pressing of a button causes an electrical signal corresponding to a module to be reproduced — the electrical switching is so arranged that only one complete module is reproduced for a single button-pressing. This electrical signal is amplified, biased, and then fed into a constantly rotating head which makes contact with stationary magnetic tape and records the signal on it. A 10-kc signal superposed on each stored speech module controls an electromagnetic clutch which (a) measures the length of the recording accurately, and (b) advances the tape at the completion of the recording by the correct amount so that the next recording forms a connected sequence with it. The same module may be used any number of times and in combination with different stored modules, thereby introducing wider experimental control in standardized speech studies. The principle of this type of device could be applied to other classes of problems involving communication of information, as the conversion into speech of typing or of electronically-red printed matter.

HARRIS, C. M.[1]

Study of the Building Blocks in Speech, Acoust. Soc. Am., J., **25,** pp. 962–969, Sept., 1953.

Identification of the information-bearing elements of speech is important in applying recent thinking on information theory to speech communication. One way to study this problem is to select groups of building blocks and use them to form standardized speech which then may be evaluated; a method having the advantage of simplicity is described. Individual recordings of the building blocks were made on magnetic tape and then various pieces of tape were joined together to form words. Experiments indicated that speech based upon one building block for each vowel and consonant not only sounds unnatural but is mostly unintelligible because the influences on vowel and consonants are missing which ordinarily occur between adjacent speech sounds. To synthesize speech with reasonable naturalness, the influence factor should be included. Here these influences can be approximated by employing more than one building block to represent each linguistic element and by selecting these blocks properly, taking into account the spectral characteristics of adjacent sounds so as to approximate the

---

[1] Bell Telephone Laboratories, Inc.

time pattern of the formant structure occurring in ordinary speech. There is no *a priori* method of determining how many building blocks are required to produce intelligible standardized speech. This can only be determined from experiments involving listening tests. Such tests are described.

HOLDAWAY, V. L.[1]

Bulb Puncture in Gas Tubes, Electronics, **26,** pp. 208, 210, 212, Nov., 1953.

HOPKINS, I. L.[1]

Ferry Reduction and the Activation Energy for Viscous Flow, J. Appl. Phys., **24,** pp. 1300–1304, Oct., 1953.

The relationship proposed by Ferry and his co-workers for the effects of frequency and temperature on the dynamic properties of certain polymers is shown to lead to a method for calculating the activation energy of viscous flow from relaxation, creep, and dynamic test data, the results agreeing with those obtained in steady-state flow. The Ferry reduction explains, and is supported by, observed increases in dynamic modulus and viscosity with increasing temperature.

JONES, T. A.,[1] and W. A. PHELPS.[1]

A Level Compensator for Telephotograph Systems, A.I.E.E. Trans. Commun. and Electronics, **9,** pp. 537–541, Nov., 1953.

KARNAUGH, M.[1]

Map Method for Synthesis of Combinational Logic Circuits, A.I.E.E. Trans., Commun. and Electronics, **9,** pp. 593–598, disc. pp. 598–599, Nov., 1953.

KOMPFNER, R.,[1] and N. T. WILLIAMS.[1]

Backward-Wave Tubes, I.R.E., Proc., **41,** pp. 1602–1611, Nov., 1953.

It has been surmised for some time that a traveling-wave tube in which backward-traveling field components can be excited — such as for instance the "Millman" tube — may oscillate in a backward mode, the RF power emerging at the gun-end of the tube and its frequency depending only on the beam voltage. Experiments with the "Millman" tube show this to be so and oscillations have been observed in the first and second backward spatial-harmonic modes. The latter is excited between 600 and 900 volts, the tube oscillating between 5.9 and 6.4 mm. The former more power-

---

[1] Bell Telephone Laboratories, Inc.

ful mode is excited between 1,600 and 4,000 volts, the tube tuning continuously between 6.0 and 7.5 mm, thus covering a frequency band of 10,000 mc. Power output of about 10 mw has been measured at 6.4 mm. The tube has also been studied as an amplifier and more than 20-db stable backward gain has been obtained. A simple theory of backward gain and of oscillation starting conditions is given.

LANDER, J. J.[1]

Auger Peaks in the Energy Spectra of Secondary Electrons from Various Materials, Phys. Rev., **91,** pp. 1382–1387, Sept. 15, 1953.

The energy spectra of secondary electrons from carbon, beryllium, aluminum, nickel, copper, barium, platinum, and the oxides of beryllium, aluminum, nickel, copper, and barium have been measured with equipment of high stability and sensitivity. Characteristic peaks due to Auger electrons emitted as a result of absorption of a valence electron by an excited x-ray level were observed for all these materials. The peaks exhibit structure which is of some theoretical interest. The structure can be related to the distribution in energy of electrons in the valence band, and it complements that observed in soft x-ray emission work. Since the emission of the Auger electron is not subject to the selection rules governing the emission of x-radiation, additional information can be obtained from the Auger electron energy distribution. Excitation of Auger peaks by a beam of low velocity electrons provides an interesting technique for surface analysis. "Plasma" peaks of the type reported by Ruthemann, and interpreted by Pines and Bohm, were also observed.

LOVELL, G. H., see L. H. MORRIS.

MONTGOMERY, H. C.[1] and M. A. CLARK.[1]

Shot Noise in Junction Transistors, Letter to the Editor, J. Appl. Phys., **24,** pp. 1337–1338, Oct., 1953.

MORRIS, L. H.,[1] G. H. LOVELL[1] and F. R. DICKINSON.[1]

L3 Coaxial System — Amplifiers, A.I.E.E. Trans., Commun. & Electronics, **9,** pp. 505–517, Nov., 1953 (Monograph 2090).

The line amplifiers for the L3 coaxial system are designed to compensate for the loss of the 4 miles of cable which separate the repeaters; the flat amplifiers are used to compensate for equilizer loss and as transmitting amplifiers. The two types are basically similar, consisting of two feedback amplifiers in tandem, separated by an interamplifier network; in the line amplifier, this network is variable, and is automatically adjusted to com-

---

[1] Bell Telephone Laboratories, Inc.

pensate for variations in cable temperature, and for small deviations from the nominal 4-mile spacing.

PIERCE, J. R.[1]

Spatially Alternating Magnetic Fields for Focusing Low-Voltage Electron Beams, Letter to the Editor, J. Appl. Phys., **24,** p. 1247, Sept., 1953.

PIERCE, J. R.,[1] and L. R. WALKER.[1]

"Brillouin Flow" with Thermal Velocities, J. Appl. Phys., **24,** pp. 1328–1330, Oct., 1953.

A type of electron flow in a constant magnetic field is described. The beam of electrons is supposed to be everywhere in thermal equilibrium and the usual Brillouin flow is found when the equilibrium temperature tends to zero. Some considerations are put forward bearing on the choice of a suitable beam temperature in specific problems.

POTTER, J. L., see E. P. FELCH

READ, W. T., JR.[1]

Dislocations and Plastic Deformation, Physics Today, **6,** pp. 10–14, Nov., 1953.

Small and exceedingly rare defects in the structure of solids are the "weak links" that determine the strength of materials. The article reviews some fundamental concepts concerning plastic deformation in certain ductile metals.

RIORDAN, J., see L. CARLITZ.

ROMIG, H. G., see R. I. WILKINSON.

SCHNETTLER, F. J., see H. J. WILLIAMS.

SHERWOOD, R. C., see H. J. WILLIAMS.

SHOCKLEY, W.[1]

Some Predicted Effects of Temperature Gradients on Diffusion in Crystals, Letter to the Editor, Phys. Rev., **91,** pp. 1563–1564, Sept. 15, 1953.

---

[1] Bell Telephone Laboratories, Inc.

STEENECK, W. R.[1]

N1 Carrier Equipment Design, Commun. Eng., **13,** pp. 26–28, Sept.–Oct., 1953.

Progress in telephone apparatus and in radio equipment design seem to follow converging paths, each contributing something to the other. Bell Laboratories started in the telephone field and adopted radio as an accessory means of transmission. More recently, radio manufacturers have borrowed telephone-circuit techniques for remote controls and multiplexing. The N1 equipment, while it looks more like radio than telephone apparatus, is a most interesting example of economy in manufacture, testing, service, and also in cubic contents. And those gains have been achieved, it should be noted, as part of a program to increase reliability and to reduce the duration of outages.

TANENBAUM, M.[1] and H. B. BRIGGS.[1]

Optical Properties of Indium Antimonide, Letter to the Editor, Phys. Rev., **91,** pp. 1561–1562, Sept. 15, 1953.

THAELER, C. S., see A. J. AIKENS.

TIEN, P. K.[1]

Traveling-Wave Tube Helix Impedance, I.R.E., Proc., **41,** pp. 1617–1623, Nov., 1953.

The impedance parameter of a circular helix, from which the gain of a helix-type traveling wave amplifier is computed, is investigated for a "Tape-Helix" model. Results obtained in this paper indicate that the impedance has a smaller value than for the "Sheath-Helix" model, and is considerably reduced at larger values of ka, the ratio of the helix circumference to the free space wavelength. A tape helix surrounded by a dielectric medium is analyzed. It is shown that the results obtained from the theory can be used to evaluate the helix impedance for usual types of traveling wave tubes. They have been found to be in agreement with measurements on many tube designs.

WALKER, L. R., see J. R. PIERCE.

WILKINSON, R. I.[1] and H. G. ROMIG.[1]

Random Picture Spacing with Multiple Camera Installations, S.M.P.T.E. J., **61,** pp. 605–618, Nov., 1953.

When several high-speed cameras are operated simultaneously, but independently, it is possible that the aggregate of pictures obtained will

---

[1] Bell Telephone Laboratories, Inc.

satisfactorily cover the space between the pictures provided by any one camera. This paper gives a method for estimating the probability that the longest interval without a picture will not exceed a selected value.

WILLIAMS, H. J.,[1] R. C. SHERWOOD,[1] M. GOERTZ[1] and F. J. SCHNETTLER.[1]

Stressed Ferrites Having Rectangular Hysteresis Loops, A.I.E.E. Trans., Commun. & Electronics, **9,** pp. 531–537, Nov., 1953.

A study has been made of the effect of stress on the magnetic properties of ferrites. Rectangular hysteresis loops were obtained by encasing toroidal specimens in plastics which shrink during polymerization. Ferrites having this type of hystersis loop are useful in magnetic switching and magnetic memory devices.

WILLIAMS, N. T., see R. KOMPFNER.

WRIGHT, S. B.[1]

Higher Frequencies, Aero Digest, 67, pp. 66, 70, 72, Nov., 1953. Spectrum crowding plus new techniques has moved USAF ground-air communications into the ultra-high-frequency bands.

Correction

On page 878 of the July, 1953, issue of the JOURNAL, an error was made in quoting the number of P. H. Richardson's patent in Reference 5. It should have been 2,348,572.

Contributors to this Issue

John T. Bangert, B.S. in E.E., University of Michigan, 1942; M.S. in E.E., Stevens Institute of Technology, 1947; doctoral studies, Columbia University, 1951–. Bell Telephone Laboratories, 1942–. Following design work on various military systems and test equipment during World War II, Mr. Bangert turned his attention to investigations of fundamental problems in transmission and communication theory. Recently he has been exploring new methods of analysis and synthesis of active and passive networks in the time and frequency domain. Member of Sigma Xi, Tau Beta Pi, Phi Kappa Phi, Eta Kappa Nu, I.R.E., and Association for Computing Machinery.

Clayton B. Brown, B.S. in E.E., Polytechnic Institute of Brooklyn, 1952; Bell Telephone Laboratories, 1937–1940; Western Electric Company, 1940–1943; Bell Telephone Laboratories, 1943–. During World War II he worked on the development of precision potentiometers, later doing test work on the automatic trouble recorder; magnet design and test work on the card translator. He is presently concerned with the planning, analysis, and testing of switching apparatus and solderless wrapped connections.

Donald F. Johnston, B.S. in E.E., Catholic University of America, 1922; Western Electric Company, 1922–1925; Bell Telephone Laboratories, 1925–. From 1922 to 1924, Mr. Johnston prepared literature describing methods of circuit operation. With the Laboratories he has been concerned with testing and development of toll testing and switching circuits.

J. A. Lewis, B.S., Worcester Polytechnic Institute, 1944; Sc.M., Brown University, 1948; Ph.D., Brown University, 1950; Corning Glass Works, 1950–1951; Bell Telephone Laboratories, 1951–. With the Laboratories, he has been concerned with mathematical research in theoretical mechanics, piezoelectric crystal vibrations, heat transfer, and stress analysis. Member American Mathematical Society, Sigma Xi.

STEPHEN O. RICE, B.S., Oregon State College, 1929; California Institute of Technology, Graduate Studies, 1929–30 and 1934–35. Bell Telephone Laboratories, 1930–. In his first years at the Laboratories, Mr. Rice was concerned with non-linear circuit theory, with special emphasis on methods of computing modulation products. Since 1935 he has served as a consultant on mathematical problems and in investigations of telephone transmission theory, including noise theory, and applications of electromagnetic theory. Fellow, I.R.E.

WILLIAM W. RIGROD, B.S. in E.E., Cooper Union Institute of Technology, 1934; M.S. in Engineering, Cornell University, 1941; D.E.E., Polytechnic Institute of Brooklyn, 1950; Westinghouse Electric Corporation, 1941–1951; Bell Telephone Laboratories, 1951–. Since 1935 he has been concerned principally with the design of electron tubes. Member of American Physical Society, Sigma Xi.

MILTON E. TERRY, B.Sc., Acadia, 1937; Ph.D. University of North Carolina, 1951; associate professor in mathematical statistics, Virginia Polytechnic Institute, 1949–1952; Bell Telephone Laboratories, 1952–. With the Laboratories, he is a consulting statistician with the mathematics group, special problems section, working on such projects as sampling, L-3 apparatus development, and the transistor. Member of American Society for Quality Control, Institute of Mathematical Statistics, American Statistical Association, Virginia Academy of Science, Sigma Xi.

C. J. TRUITT, B.S. in Chemistry, Harvard University 1924; New York Telephone Company, Traffic Engineering, 1924–1943. Mr. Truitt transferred to the Long Island area when it was formed in 1927, becoming Trunk Traffic Engineer for that area in 1941. In 1943, he transferred to the toll line engineering group, Operating and Engineering Department, American Telephone and Telegraph Company, where he has since been engaged in developing traffic engineering procedures involving the theory and practice of intertoll trunking.

BOGUMIL M. WOJCIECHOWSKI, Polytechnic Institute of Warsaw, E.E., 1936; Research Staff, Physical Department, Polit. Inst., 1936–1938; Technical Advisor, Polish Stratospheric Board, 1937–1939; National Institute of Telecommunication (Warsaw) 1937–1939; Research Bureau, Industrièlle des Téléphones (Paris) 1939–1940; Test Set Development Department, Western Electric Co., 1942–. While working for the Western

Electric Company, Mr. Wojciechowski has been engaged in the development of electrical measuring apparatus. Particularly, his work has been concerned with the industrial precision measuring problems growing out of war and post-war changes in electronic techniques. Some of his contributions are: the development of bridges for temperature coefficient measurements of capacitance; inductance measurements of quartz crystal plates; unbalance measurements of four-branch networks; phase sensitive detectors; and digital frequency combining and selecting systems. Mr. Wojciechowski is a Member of the American Institute of Electrical Engineers and a Senior Member of the Institute of Radio Engineers.